Quantum cascade laser absorption studies of nitric oxide production by nanosecond pulsed discharges in air and in combustible mixtures

Marien Simeni Simeni

CentraleSupélec

THÈSE

présentée par

Marien SIMENI SIMENI

pour l'obtention du

GRADE DE DOCTEUR

Formation doctorale : Energétique et Physique

Laboratoire d'accueil : Laboratoire d'Energétique Moléculaire et Macroscopique, Combustion (EM2C) du CNRS et de CentraleSupélec

Quantum Cascade Laser Absorption Studies of Nitric Oxide Production by Nanosecond Pulsed Discharges in Air and in Combustible Mixtures

Soutenue le 22 juin 2015

Jury :

Mme	Pascale	Desgroux	Dir. de Recherche CNRS, PC2A
M.	Nicolas	Gherardi	Dir. de Recherche CNRS, LAPLACE
M.	Jun	Hayashi	Associate Professor, Osaka University
M.	Christophe	Laux	Professeur à l'ECP, EM2C
M.	Ajmal	Mohamed	Ingénieur de Recherche, ONERA
M.	Juergen	Roepcke	Professeur, INP Greifwald
M.	Gabi-Daniel	Stancu	Maître de Conf. à l'ECP, EM2C

2015ECAP0033

Remerciements

Au terme de ce travail de thèse, je tiens à remercier en tout premier mes encadrants Gabi-Daniel Stancu et Christophe Laux qui ont chacun apporté leur touche à ce rendu. Leurs leitmotivs respectifs “Learning by doing” et “Savoir perdre du temps pour en gagner” ont été les clés de voûte face aux difficultés rencontrées au fur et à mesure de l'avancée des travaux. Je remercie particulièrement Gabi pour son sens de la pédagogie, sa rigueur, sa capacité à unir connaissances théoriques et expérimentales et sa disposition pour le partage de sa culture scientifique. Je remercie chaleureusement Christophe pour sa minutie, ses astuces scientifiques de tous les instants et sa grande implication quant à la finalisation de ce manuscrit.

Je pense aussi aux autres chercheurs avec lesquels j'ai eu la chance de travailler, notamment ceux du LPGP à Orsay, Simon Dap, Olivier Leroy, Caroline Boisse-Laporte et Tiberiu Minea. Je suis aussi reconnaissant de l'aide offerte par Henrik Zimmermann de Neoplas Control pour l'optimisation des outils de spectroscopie moyen-infrarouge, mis à disposition par Q-MACS.

Je remercie également les rapporteurs de ma thèse, Nicolas Gherardi et Juergen Roepcke, qui a fait le déplacement depuis Greifswald, qui ont accepté de rapporter cette thèse dans des délais assez courts et dont les remarques pertinentes ouvrent de nouvelles perspectives à mes travaux. Bien évidemment, ma gratitude va aussi a l'endroit des autres membres du jury, Pascale Desgroux, Jun Hayashi et Ajmal Mohamed qui ont accepté d'être examinateurs de cette thèse et qui m'ont permis d'apprécier l'échange constitué par la séance des questions-réponses de la soutenance.

J'exprime également ma gratitude envers le personnel de l'EM2C. D'abord le personnel technique dont le support a été indispensable pour réaliser les pièces nécessaires aux différentes expériences. Je dis donc merci à Jérome Beaunier, Sid Bouamama, Erika Jean-Bart, Yannick Le Teno, Dedit Mushatsi et Alain Walton mais aussi à Anne-Cécile Aiach, Matthieu Boileau, David Charalampous, Brigitte Llobel, Nathalie Rodrigues et Sébastien Turgis pour les si précieux supports administratifs et informatiques !

Il ne faudrait pas oublier l'Ecole Doctorale ! Un grand MERCI à Geraldine Carbonel, Catherine Lhopital, Catherine Di Costanzo, Emmanuelle Coplo et à Benoît Goyeau !

Une thèse serait bien triste sans les autres thésards pour construire un beau microcosme en vue de garder un esprit sain ! Je remercie donc tous les doctorants post-doctorants et stagiaires de l'EM2C que j'ai pu côtoyer (je m'excuse d'avance

pour les oublis). Parmi eux, d'abord ceux dont j'ai eu la chance de partager le bureau, Francois Doisneau (Souviens-toi des Vendéens), Sylvain Heitz (de Germanie), Kevin Prieur ("On est ensemble" !), Fabien Tholin (Chorégraphe sur techno-chicken) et Laurent Tranchant (A la recherche du Mont Perdu). Ensuite les membres de l'équipe plasma : Farah Kaddouri, Diane Rusterholtz-Duval, Adrien Lemal (The Big Guy), Florent Sainct, Da Xu, Francois Pechereau, Aurélien Guy (Le prince de Wurtemberg), Carolyn Jacobs, Megan MacDonald, Umar Sheikh, Gilles Bailet, Sara Lovascio, Arthur Salmon (nouvel ami de la QCLAS), Christopher James et Erwan Pannier (Toujours saucé !). Et enfin, Benedetta Franzelli, Aymeric Vié, Layal Hakim, Raphael Baudoin (l'homme très fort du basket !), Antoine Renaud, Pierre-Edouard Bossard, Benjamin Robbes, Wenjie Tao, Gizem Okyay, Haoxue Han, Macole Sabat, Maxime Philip, Manuel Gonzalez-Flesca (Kendrick Lamar), Marie Zarrouati, Vincent Leroy (Morsay en force !), Nicolas Dumont (Tonton !!), Prasanna Swaminathan, Laurent Soucasse, Quentin Bilnaud, Théa Lancien, Davy Nayigizente, Abigail Cervantes, Lantao Yu, Benoît Latour (alley-oop !!), Chai Koren, Wafa Bendhaou, Jordan Soussi, Yann Dauvois, Marek Mazur, Diana Tudorache, Sorour Refahi, Thibault Guiberti, Florence Drui, Maria Castela, Renaud Mercier, Wassim Kassem, Clément Mirat, Alaric Sibra, Yuxiang Ni, Mihaela Cirisan, José Ordonez-Miranda, Jean-François Bourgoin, Mélanie Rochoux, Benoît Cheneau, Paul Jourdaine, Jordan Andrieu et la liste continue...

Pour finir en beauté, j'aimerais dédicacer cette thèse à tous ceux qui oeuvrent pour l'éducation. C'est grâce à ces personnes (parents, enseignants, éducateurs, qui se reconnaîtront...), qui n'ont pas été citées plus haut que le sens du travail et la passion pour les sciences naissent chez les plus jeunes. Plus particulièrement, il n'existe pas de mots assez fort en langue française pour exprimer ma reconnaissance envers mes parents, ma famille et mes proches, qui m'ont toujours soutenu et à qui je dois simplement tout !

Abstract

Atmospheric pressure plasmas have numerous potential applications. These applications include for instance biomedicine, material processing, environmental biodecontamination and plasma-assisted combustion. The versatility of plasma discharges results from their ability to produce high quantities of active species without increasing the temperature of the gas appreciably. Nanosecond Repetitively Pulsed discharges (NRP) have received great attention owing to their capacity to generate high electron densities, which lead to the creation of a high density of active species such as atomic oxygen. Optical Emission Spectroscopy (OES) showed that excited nitric oxide (NO) was released by NRP discharges in air or in air/fuel mixtures.

Although NRP discharges have already been the object of several investigations, the kinetic mechanisms of NO production by NRP discharges at atmospheric pressure remain somewhat unclear. This is one of the motivations for the investigations conducted in this thesis. In addition, NRP discharges were found to produce large amounts of atomic oxygen, which is of great interest for applications such as plasma-assisted combustion. It was shown in particular that thanks to this high production of active species, NRP discharges can effectively stabilize lean flames at atmospheric pressure. However, the production of NO in NRP discharges and in plasma-stabilized flames remains to be investigated. This is the second purpose of this thesis.

Absolute and *in-situ* NO density measurements in atmospheric pressure plasma or/and flame environments are very challenging. Fluorescence-based techniques such as Laser Induced Fluorescence (LIF) require complex calibration methods. These techniques also require the knowledge of the quenching rates of the excited states (particularly at atmospheric pressure), which strongly depend on the temperature, density and nature of the species and can be very different for plasma or/and flame environments. Other techniques, such as chemiluminescence probe sampling also have quenching and calibration issues, and *ex-situ* UV and IR absorption-based gas analyzers can lead to errors, in particular for radicals.

In this study, we developed Quantum Cascade Laser Absorption Spectroscopy (QCLAS) for *in-situ* nitric oxide absolute density measurements in open-air and in combustion environments. This technique overcomes the difficulties of the previous ones by using high-resolution (10^{-3} cm^{-1}) rotational-vibrational absorption spectroscopy. This technique presents the advantages of high spectral selectivity, no calibration requirement, and high sensitivity.

Two experimental setups were developed to measure NO densities and temperature, (1) within a NRP discharge in air, with 300-µm spatial resolution, and (2) downstream of NRP discharges in air and in plasma-assisted methane/air flames, using multi pass cell.

The first study aims to determine the spatial profiles of NO produced by the discharges, and to measure reference values of time-averaged NO density and temperature, for kinetics modeling of the NRP discharge.
We implemented two methods: two-line intensity ratios and spectra width analysis. Each method was combined with an Abel inversion. We found a radial distribution of the NO density with a maximum of about 2 x 10^{15} cm^{-3} at discharge center and a FWHM of about 6 mm. The diagnostic also enabled us to determine the time-averaged gas temperature, with a 300-µm spatial resolution. The maximum mean gas temperature was found to be 800 K at discharge center.

The second study was devoted to post-discharge characterization downstream of a discharge in air, and then downstream of a plasma-assisted methane/air flame.
For the air post-discharge, we demonstrated that the NO density downstream of the NRP discharges is controlled by several parameters including, the voltage amplitude, pulse repetition frequency, gap distance, air flow rate and gas temperature. Carrying out this parametric investigation in ambient air flows, we recorded a maximum NO density about 6 x 10^{15} cm^{-3} and a maximum NO production rate of 2 x 10^{18} molecule/s. We found that the NO density in the post-discharge is only a function of two parameters: the number of pulses seen by the gas, which is the dimensionless parameter $d\ f/v$ (where d, f and v are the gap distance, the repetition frequency and the flow velocity, respectively) and of the applied voltage amplitude. The same two parameters dependency was also found for NRP discharges operating in 1000 K preheated air flows, with the difference that the maximum NO production rate was only about 6 x 10^{17} molecule/s. Surprisingly, we also found that the NO mole fraction released by the NRP discharges was approximately independent of the gas temperature (for gas temperatures between 300 and 1000 K). Then, the results of the parametric study combined with a simple kinetic analysis and with previous measurements in the NRP *reference case* enabled us to conclude that NO in NRP discharges is created by the reactions of electronically excited nitrogen states with oxygen atoms. 90 % of the NO arises actually from the $N_2(B)$ state. In addition, NO is lost by quenching with N and O atoms.
For the post-discharge of the combustible mixture, for several selected experimental configurations, we compared the NO densities in plasma, plasma-assisted combustion and combustion cases at various values of the fuel equivalent ratio in the lean regime. For all configurations the NO mole fractions in the plasma case were always greater than those in plasma-assisted combustion and combustion. Moreover, the NO

densities produced by plasma-assisted combustion were found to be always comparable with the NO densities produced by a stoichiometric flame. Thus, the NO densities produced in plasma-assisted flames are much lower than in pure air, and are not higher than those produced in stoichiometric flames. A method was proposed to control the NO production by NRP discharges in air. This method is not effective to reduce the NO production in plasma-assisted flame below the level obtained in stoichiometric flames. More work is required to understand the differences between the kinetic mechanisms in air and in combustion.

Résumé

Les plasmas d'air à pression atmosphérique ont de nombreuses applications, comme par exemple dans le domaine biomédical, le traitement des matériaux, la bio-décontamination environnementale et la combustion assistée par plasma. La polyvalence des décharges plasma résulte de leur capacité à produire des densités élevées d'espèces actives, sans toutefois chauffer substantiellement le gaz. Les décharges nanosecondes répétitivement pulsées (NRP) ont particulièrement reçu une grande attention en raison de leur capacité à produire des densités électroniques élevées, qui conduisent à la création de fortes densités d'espèces actives telles que l'oxygène atomique (O). Par ailleurs, des mesures de spectroscopie d'émission ont montré que le monoxyde d'azote (NO) dans ses états excites est produit par les décharges NRP opérant dans l'air ou dans des mélanges combustibles.

Bien que les décharges NRP aient déjà fait l'objet de plusieurs investigations, les mécanismes cinétiques conduisant à la production de NO sont toujours incertains. C'est la motivation première des travaux menés dans le cadre de cette thèse. En outre, les décharges NRP se sont avérées produire une grande quantité d'oxygène d'atomique, espèce de grande importance pour la combustion assistée par plasma. Il a été en particulier démontré que grâce à la production élevée d'espèces actives, les décharges NRP peuvent stabiliser efficacement des flammes pauvres, à pression atmosphérique. Cependant la production de NO par les décharges NRP et par les flammes stabilisées à l'aide des décharges NRP reste à étudier. Cela constitue le second objectif de cette thèse.

Les mesures *in-situ* de densités absolues de NO à pression atmosphérique dans les décharges plasmas et/ou en combustion sont difficiles. Les techniques de fluorescence telle que la fluorescence induite par laser (LIF) nécessitent de complexes méthodes de calibration. Ces techniques requièrent également la connaissance des taux de quenching des états excités (en particulier à pression atmosphérique). Or ces taux de quenching sont très fortement dépendants de la température, de la nature des espèces en présence et de leur densité, et peuvent donc fortement différer entre un plasma opérant dans l'air et en combustion. D'autres techniques telles que l'utilisation des sondes à chimiluminescence sont tout aussi sujettes aux problèmes de calibration et de quenching des états excités tandis que les mesures *ex-situ* à l'aide d'analyseurs à gaz réalisant de l'absorption dans l'UV et l'IR peuvent conduire à des erreurs, surtout lorsqu'il s'agit de mesurer des radicaux.

Dans cette étude, nous avons développé la spectroscopie d'absorption par laser à cascade quantique (QCLAS), pour des mesures *in-situ* de densités de NO dans l'air et

en combustion. Cette technique permet de surmonter les difficultés des autres méthodes par utilisation d'une spectroscopie rotationnelle-vibrationnelle de haute résolution spectrale (10^{-3} cm^{-1}). La QCLAS a les avantages d'être spectralement sélective, d'avoir une grande sensibilité et de ne pas nécessiter de calibration.
Deux dispositifs expérimentaux ont été développés pour mesurer des densités de NO et des températures (1) dans une décharge NRP dans l'air, avec une résolution spatiale de 300 µm, et (2) en aval de la décharge NRP opérant dans l'air et dans des flammes méthane/air assistée par plasma, par utilisation d'une cellule multi-passages.

La première étude vise à déterminer les profils spatiaux de NO produit par les décharges NRP et à donner des valeurs de référence des moyennes temporelles de densité de NO et de température, pour les besoins de la modélisation de la cinétique de la décharge NRP.
Deux méthodes ont été implémentées : le rapport des intensités d'absorption de deux raies et l'analyse de la largeur des spectres. Chacune de ces méthodes a été combinée à une inversion d'Abel. Nous avons ainsi trouvé une distribution radiale de la densité de NO avec un maximum d'environ 2 x 10^{15} cm^{-3}, au centre de la décharge et une FWHM d'environ 6 mm. Le diagnostic nous a également permis de terminer la température moyenne du gaz avec une résolution spatiale de 300-µm. Nous avons ainsi déterminé une température moyenne maximale de 800 K au centre de la décharge.

La seconde étude a été consacrée à la caractérisation de la post-décharge, en aval de la décharge dans l'air, puis en aval de la décharge d'une flamme méthane/air assistée par plasma.
Pour la post-décharge dans l'air, nous avons démontré que la densité de NO en aval des décharges NRP est contrôlée par plusieurs paramètres dont l'amplitude de tension, la fréquence de répétition, la distance interélectrodes, le débit d'air et la température du gaz. Réalisant cette étude paramétrique dans des écoulements d'air à température ambiante, nous avons mesuré un maximum de densité de NO d'environ 6 x 10^{15} cm^{-3} et un maximum du taux de production de 2 x 10^{18} molécule/s. Nous avons montré que la densité de NO dans la post-décharge est uniquement fonction de deux paramètres: le nombre d'impulsions vu par le gaz, qui est le paramètre sans dimension $d\ f/v$ (où d, f et v sont respectivement la distance interélectrode, la fréquence de répétition et la vitesse de l'écoulement) et de l'amplitude de la tension appliquée. La dépendance à ces deux paramètres a également été observée pour les décharges NRP opérant dans des écoulements d'air préchauffé à 1000 K, avec la différence que le taux de production maximum de NO était seulement d'environ 6 x 10^{17} molécule/s. De manière surprenante, nous avons constaté que la fraction molaire de NO produit par les décharges NRP est approximativement indépendante de la température du gaz (pour des températures de gaz comprises entre 300 et 1000 K).

Ensuite, les résultats de l'étude paramétrique combinés avec une analyse cinétique simple et avec les mesures précédentes d'un cas de « référence » NRP, nous ont permis de conclure que le NO des décharges NRP est créé par les réactions des états électroniquement excités de N_2 avec des atomes d'oxygène. 90% du NO produit provient en fait de l'état (B) de N_2. En outre, le NO est perdu par quenching avec les atomes N et O. Pour la post-décharge du mélange combustible, nous avons comparé les densités de NO, pour plusieurs configurations expérimentales, dans les cas plasma, combustion assistée par plasma et combustion, et ceci à différentes valeurs de richesse de carburant dans le régime de flamme pauvre. Pour toutes les configurations, les fractions molaires de NO dans le cas plasma étaient toujours supérieures à celles en combustion assistée par plasma et en combustion. De plus, les densités de NO produites par la combustion assistée par plasma étaient toujours comparables aux densités du NO produit par une flamme stoechiométrique. Ainsi, les densités de NO produit par les flammes assistées par plasma sont beaucoup plus faibles que dans l'air pur, et ne sont pas supérieures à celles produites dans les flammes stoechiométriques. Une méthode a été proposée pour contrôler la production de NO par les décharges NRP dans l'air. Cette méthode s'est avérée inefficace pour réduire la production de NO dans la flamme assistée par plasma en dessous du niveau des flammes stoechiométriques. Des études supplémentaires sont nécessaires pour comprendre les différences entre les mécanismes cinétiques dans l'air et dans la combustion.

Contents

Chapter 1

Introduction

1.1 A brief introduction to plasma and to laser-matter interaction

The plasma state of matter represents 99.9 % of the "visible" universe [*Moisan and Pelletier*, 2006]. The sun is one of the well-known examples of plasma. Closer to human beings, on Earth, other typical examples of plasmas are neon signs, which are used for lighting. The transition from the gas state of matter to the plasma state can be accomplished either by heating the gas or by applying an intense electromagnetic field. This transition is accompanied by a significant increase of the number densities of charged species (positive and negative). Plasma can hence be regarded as a big "soup" of gas, in which charged species are in "suspension". Irving Langmuir used the latter image in 1928 when he coined the name "plasma", by analogy with "blood plasma", which carries red and white corpuscules as well as germs [*Langmuir*, 1928]. The presence of charged species is not sufficient to define a plasma. A collective behavior of the charged species is also required (see section 2.3 of chapter 2). Consequently, many chemical and electrodynamics effects take place in plasma and this results in many potential applications (see chapter 2).

However, a deep understanding of the plasma is necessary to optimize its properties for the different types of application. Up to now, laser photons appear to be one of the more advanced interaction tools with plasma constituents (atoms, molecules, ions, electrons...) [*Hutchinson*, 2005]. The big advantage of these photons is their selectivity for the choice of the "interlocutor(s)". Since 2000s, laser-matter interaction has been improved by Quantum Cascade Lasers (QCLs), owing to their narrow spectral width and to their tuneability, respectively. We will use these new devices to study the production of nitric oxide by NRP plasma discharges.

1.2 Thesis outline

This thesis starts with **chapter 2,** which describes the various fields of application of atmospheric pressure discharges. Then, the specific case of Nanosecond Repetitively Pulsed (NRP) discharges is detailed and recent experimental results are presented together with the results of numerical modeling. Both support our understanding of the physics of NRP discharges. Further, we discuss the role of nitric oxide released by

atmospheric pressure discharges in air as key species for applications ranging from biomedicine to combustion. Finally, a review of the NO detection techniques employed in literature, in plasma and plasma-assisted combustion environments is performed. We discuss the advantages of the Quantum Cascade Laser Absorption Spectroscopy technique used in this thesis in comparison with literature techniques but also the challenges required to carry out the diagnostic.

Chapter 3 deals with the theoretical background necessary to extract quantitative information from the measurements performed in this thesis. It also quantifies the limitations of the performed diagnostics. For this purpose, the principles of discharge energy measurements, Mid-IR laser absorption spectroscopy in uniform and axisymmetric environments and gas temperature determination using QCLAS are presented. **Chapter 4** gives the specifics of all electrical and optical experimental arrangements used in this work. The QCLAS diagnostic set up is particularly highlighted.

The goal of **chapter 5** is to characterize NRP discharges in terms of NO density and gas temperature in the discharge. We present radial NO density profiles in the NRP discharge in ambient flowing air. But prior to the density profiles, the temperature profiles are displayed, in order to take into account the line strength change with the temperature. In **chapter 6,** we conduct parametric studies of the NO density in the post-discharge (downstream the discharge) in ambient air and 1000 K preheated air flows, respectively, as a function of the parameters of the NRP discharge. Then, we investigate numerically the main routes of NO formation and loss in NRP discharges.

In chapter 7, we apply the QCLAS technique to detect NO in combustion and in plasma-assisted combustion environments. The NO density is detected in post-combustion, post-discharge and post-NRP assisted combustion as a function of the flame equivalence ratio. Using the developed optimization method in air, a trade-off study between lean flames stabilization by NRP discharges and NO production by NRP-assisted combustion is conducted.

References

[1] Hutchinson, I. H. (2005). *Principles of plasma diagnostics*. Cambridge university press.

[2] Langmuir, I. (1928). Oscillations in ionized gases. *Proceedings of the National Academy of Sciences of the United States of America*, *14*(8), 627.

[3] Moisan, M., & Pelletier, J. (2006). *Physique des plasmas collisionnels: application aux décharges haute fréquence*. EDP sciences.

Chapter 2

Nitric oxide in atmospheric pressure air discharges, detection and applications

2.1 Introduction

In this chapter we present the role of nitric oxide in atmospheric pressure air discharges. An overview of the different applications of these discharges is first given (section 2.2). Then in section 2.3, the plasma sources used in atmospheric pressure air are presented. In section 2.4 we focus our attention to the nanosecond repetitively pulsed discharges, which were employed in this thesis. Recent results and features are given. The role of nitric oxide for biomedical and combustion applications is highlighted in section 2.5. Finally, a review of the techniques used in the literature for the detection of nitric oxide in plasma and plasma-assisted combustion is presented together with the method implemented in this thesis.

2.2 Applications of atmospheric pressure air discharges

Plasmas discharges are ionized gases containing positive, negative ions, electrons, radicals, metastables as well as atoms and molecules in the ground and in the excited states. Transitions from excited states lead to the production of photons and the charged particles from discharges also generate electric fields. Most of these plasma "species" are chemically active, therefore they are very interesting for applications. Running the plasma at atmospheric pressure has the advantage of simpler apparatus. This has led to a large variety of plasma sources and applications, especially for non-thermal plasmas. The application fields of non-thermal plasma discharges are presented in the interesting recent review "*The 2012 Plasma Roadmap*" by *Samukawa et al.* [2012]. For each field, the role of non-thermal plasma, the advantages/drawbacks of the different plasma techniques, the various kind of plasma sources, the possible drawbacks of the plasma techniques and the current challenges related to the development of plasma-based techniques are presented.

2.2.1 Plasma medicine

Plasma medicine is a relatively new field of application, with strong growth in the last few years. As stated by *Kong et al.* [2009], at the early ages of plasma medicine, plasmas were essentially used for medical equipment sterilization [*Laroussi*, 2005] and for biological decontamination in the process of packaging in the food industry

[*Moisan et al.*, 2001]. These achievements were possible due to the efficiency of plasmas for killing bacteria and the ability to access narrow spaces. Recently, the development of low-temperature plasmas made possible the direct application of plasma discharges on living tissues (in vitro) and on treatment of internal diseases (in vivo).
For instance, using a Floating Electrode Dielectric Barrier Discharge (FE-DBD), *Fridman et al.* [2006] demonstrated improved blood coagulation on a human spleen tissue. Authors also mentioned non-damaging effects on living tissue even after 5 minutes of treatment. What is important in these experiments is that the treatment area remains at room temperature. In this case, the key species responsible for blood coagulation was found to be nitric oxide (NO). Its influence will be detailed in section 2.5.

Another remarkable result is related to the treatment of cancer cells. *Vandamme et al.* [2012] reported not only inhibition of tumor cells proliferation but also apoptosis of those cells following the application of plasma discharges operating in open air. The study was carried out on mice, which received beforehand injections of tumor cells into their hind legs. The treatment was implemented on the skin of the mice, in open air. A photograph of their DBD discharge is given in the left side of figure 2.1. In this case, microsecond pulses of 23-kV were applied at 2 kHz repetition frequency. The duration of the treatment was about 15 seconds. Authors attributed the apoptosis of tumor cells to the creation of Reactive Oxygen Species (ROS) by the non-thermal plasma (NTP).

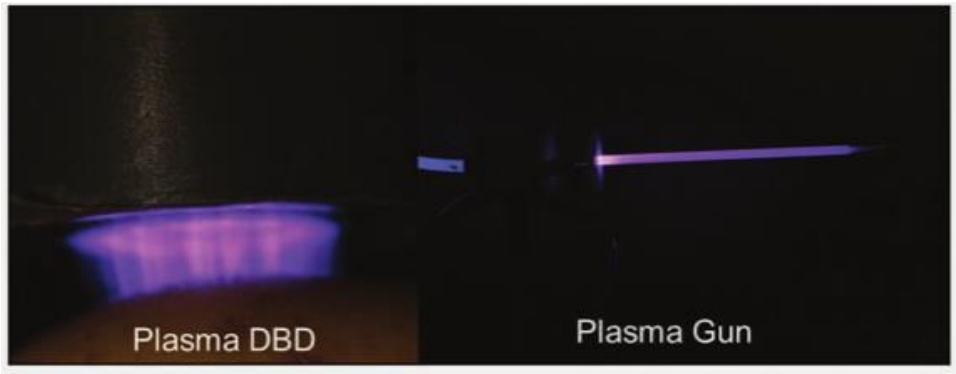

Figure 2.1: Non-thermal plasmas for the treatment of tumor cells. The plasma generated at the extremity of one of the capillaries in presented at the right side. Figure taken from [*Vandamme et al.*, 2012].

Although many in vitro and in vivo studies are performed, a deep understanding of the interaction between plasma and living organisms is required in order to apply

plasmas in large-scale medical treatments. Many novel questions are open, for instance, the long-term side effects of the plasma treatment on humans.

2.2.2 Plasma for environmental applications

One of the key characteristics of the NTP discharges in atmospheric pressure air is the fact that their highly energetic electrons create free radicals (O_3, O, N, OH…). These radicals can decompose pollutants such as volatile organic compounds (VOC) [*Oda et al.*, 1996]. Historically, the first application of NTP for environmental control was dedicated to ozone production. In the early 1857, Siemens invented a DBD generating ozone used for disinfecting water plants [*Kim*, 2004]. Since that time, NTP have been used for dust removal in air [*Cottrell*, 1911], for nitrogen oxides (NO_x) and sulphur oxides (SO_x) abatement [*Tamaki et al.*, 1979; *Mizuno et al.*, 1986], for fuel reforming and even for carbon sequestration [*Fridman et al.*, 2006]. Figure 2.2 (taken from [*Kim*, 2004]) presents some key dates of applications of NTP in the environment field. It is remarkable that various types of discharges are used: DBD, corona, microwave and radio-frequency (RF) plasmas, operating in different types of regimes: DC, AC or pulsed.

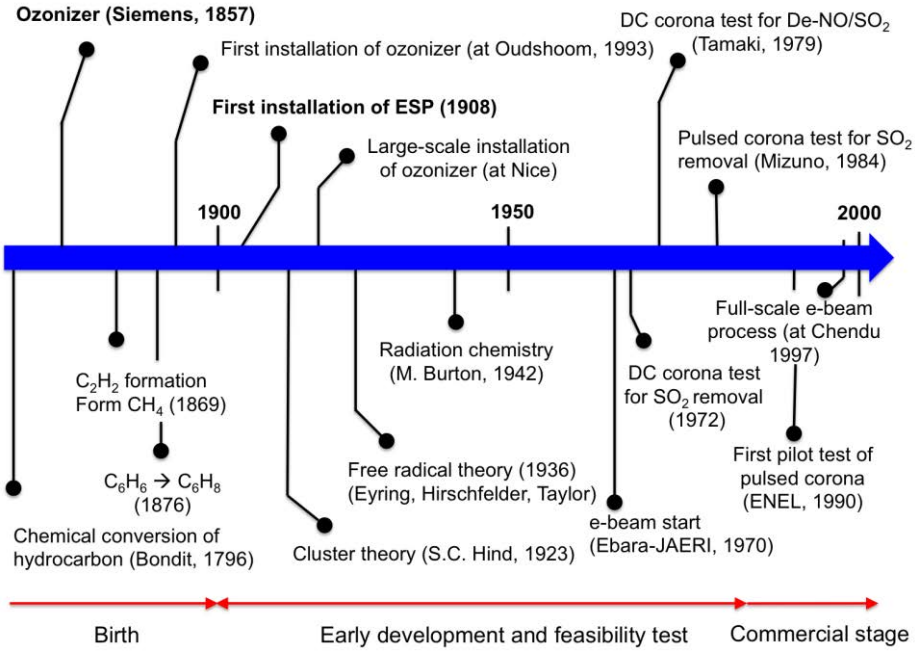

Figure 2.2: Timeline for non-thermal plasmas applications to environmental concerns. Figure taken from [*Kim*, 2004].

Currently, research on NTP pollution abatement takes the direction of combining NTP with other methods. An example is plasma-enhanced catalysis in which the plasma increases catalytic effects. This process improves energy efficiency and optimizes the distribution of the by-products [*Kim*, 2004]. For instance, figure 2.3

displays the energy efficiency of the decomposition of 200 ppm of benzene using various types of NTP reactors. The most efficient decomposition is achieved by a pulsed corona discharge combined with a catalytic process. The efficiency of the combination of NTP with photocatalyst for C_2H_2 removal was also demonstrated by *Rouseau et al.* [2005]. They found an improved activation of the oxidation processes of C_2H_2 when the photocatalytic material (TiO_2) was combined with their low pressure NTP discharge.

Current challenges for the application of environmental plasmas include the scaling-up of energy efficiency and energy conversion of these processes. Another key point is the deep understanding of the interaction between plasma and liquids.

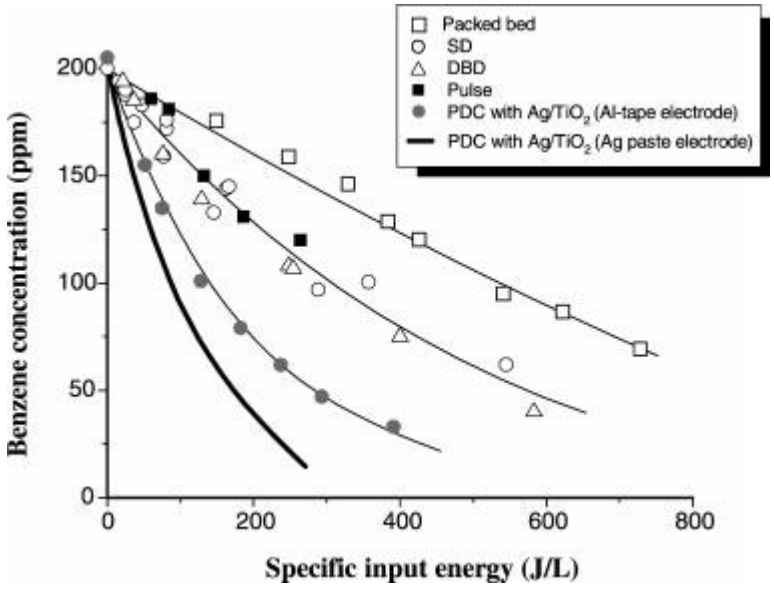

Figure 2.3: Decomposition of 200 ppm of benzene using different types of non-thermal plasmas reactors. Figure taken from [*Kim*, 2004].

2.2.3 Plasma material processing

Since 1960s, plasmas have been widely used for the purpose of modifying surface properties of materials. However, historically, plasma-based material processes such as sputtering were already used for the fabrication of mirror surfaces since the late 19th century [*Donnelly and Kornblit*, 2013]. Atmospheric pressure DBD have been for instance applied to surface modifications and deposition (thin film growths) [*Massines et al.*, 2005]. Nowadays, plasmas have been mostly applied to the manufacturing of integrated circuits in the electronic industry [*Lieberman and Lichtenberg*, 1994]. The surface treatment is achieved through the chemically reactive plasma species, which react with the surface, or which react with each other to produce secondary chemical precursors needed for thin film deposition [*Selwyn et al.*, 2001]. Here, the key

advantage of non-thermal plasmas is their non-destructive capability as a result of the low gas temperature. Plasma processes represent about one third of the steps required for the manufacture of integrated circuits [*Lieberman and Lichtenberg*, 1994]. These steps include film deposition, material doping and surface etching (as sketched in figure 2.4) of materials such as silicon, aluminium and silicon dioxide. An illustration of some examples of plasma-surface interaction with desired components and products is given in table 2.1.
Another important point is the fact that the plasma-based processes are capable to etch materials anisotropically. This allowed the introduction of smaller (submicrometer) feature size and spacing in the electronic industry [*Donnelly and Kornblit*, 2013].

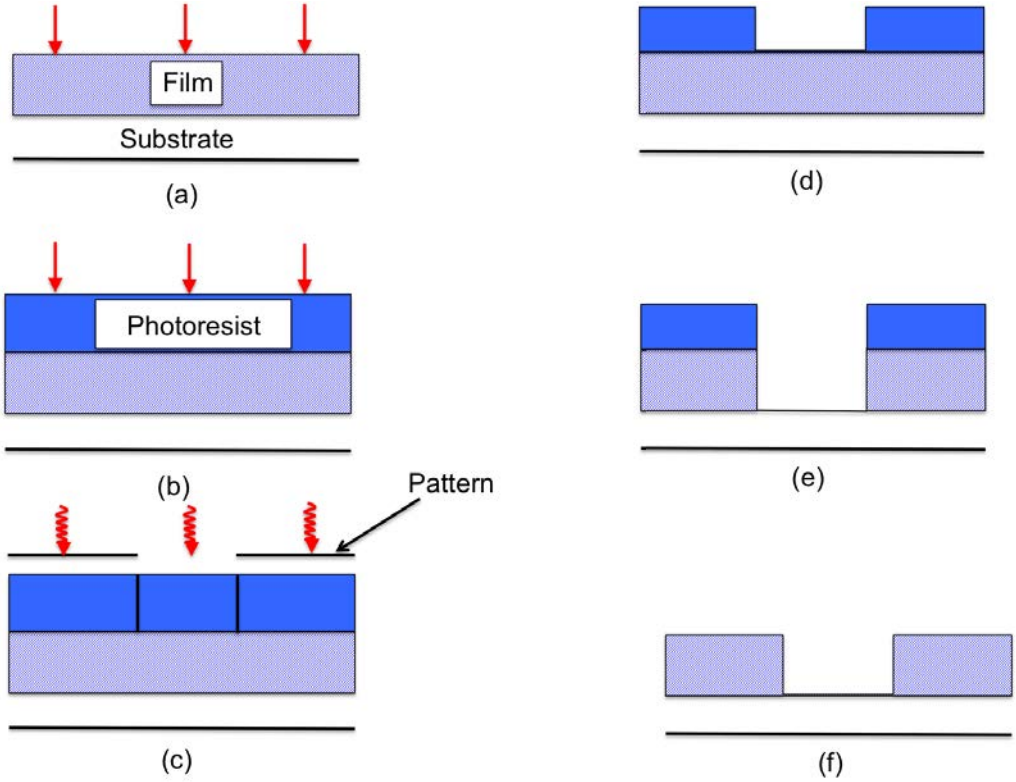

Figure 2.4: Manufacturing of an integrated circuit, deposition and pattern transfer: (a) metal deposition; (b) photoresist deposition; (c) optical exposure through a pattern; (d) photoresist development; (e) anisotropic plasma etch; (f) remaining photoresist removal. Figure adapted from [*Lieberman and Lichtenberg*, 1994].

Table 2.1: Examples of applications of NTP for materials processing. Adapted from [*Selwyn et al.*, 2001].

Material/Substrate	Desired component	Desired product
Semiconductor substrates	Active neutral and ionic species generated by electron impact	Etching, thin film deposition, stripping, cleaning
Magnetic storage media	Sputtered atoms generated by ion bombardment of the target	Magnetic thin films, anticorrosive coatings
Glass	Thin film chemical precursors, neutrals	Energy efficient coatings
Textiles	Ion bombardment, active neutrals	Increased wettability, wear properties
Industrial cleaning	Oxygen atoms, ions	Oxidation and removal of organic films

Common plasma sources for material processing include RF capacitively and inductively coupled plasma discharges (CCP and ICP).

Nowadays one of the challenges of plasma processing is to manufacture sub-10 nm devices. To achieve this breakthrough, there is a need to tackle damaging effects due to UV radiation and charge accumulation during the plasma processing.

2.2.4 Plasma-assisted combustion and ignition

Another important field of NTP at atmospheric pressure is the plasma-assisted combustion and ignition. A interesting review of the field is given by *Starikovskiy and Aleksandrov*, [2013]. Here we will underline some of the important aspects.
A plasma discharge can interact with a flame by thermal or/and non-thermal mechanisms. Firstly, for the thermal mechanisms, the heat release from the discharge increases the gas temperature and hence improves chemical reactions. Besides increasing chemical reaction rates, inhomogeneous gas heating also fosters flow mixing. Secondly, for non-thermal mechanisms, the mixing of reagents can also be induced by the electric field of the discharge, which generates an ionic wind. The ionic wind entrains charged particles from the discharge or/and from the flame and hence enhances flame stability and mixing. Another non-thermal effect is the formation of chemically active species and radicals, which can initiate combustion reactions, even at low temperature. These reactive species can be produced directly by electronic impact excitation, dissociation and ionization or indirectly through the reactions of excited atoms and molecules with neutrals.

As will be shown later, the ability of plasma discharges to assist combustion systems depends first on the coupling of the discharge energy through the internal degrees of freedom of the mixture molecules, second on the relaxation time of these excited states and third on the response of the system (plasma + flame) to this excitation.
The use of plasmas for combustion started with the advent of the spark ignition systems in the automobile industry. Apart from non-equilibrium plasma-based ignition systems, which are still up-to-date, current topics of research concern ignition of high-speed gas flows [*Esakov et al.*, 2006; *Adamovich et al.*, 2009], plasma-enhancement of lean flames and control of combustion dynamics [*Pilla et al.*, 2006; *Pancheshnyi*, 2006; *Adamovich et al.*, 2008; *Barbosa et al.*, 2009; *Sun et al.*, 2012; *Lacoste et al.*, 2013]. We propose to detail here the applications to flame ignition and stabilization, closely related to the work of this thesis and for which recent results have been obtained using NRP discharges.

Plasma-assisted ignition

Sparks ignite internal combustion engines thanks to their heat release. However, they are not efficient to ignite large gas volume since they lead to considerable energy consumption to heat the whole volume. The current interest is for igniting using discharges with limited joule heating in comparison with the chemical heat released in the whole gas volume [*Starikovskii*, 2005].
One of the promising solution is the use of the nanosecond pulsed discharges. According to *Starikovskiy and Aleksandrov*, [2013], the requirements for nanosecond plasma discharges to provide a high ignition efficiency are:

- High reduced electric field value ($E/n > 200$ Td) to enhance the dissociation of molecular oxygen by electron impact and by the quenching of the electronically excited nitrogen states).
- High voltage rise rate ($dU/dt > 0.3$ kV/ns) to induce a homogeneous gas excitation.
- The typical time of creation of active species to be less than the typical ignition time.

Amongst plasma sources, the nanosecond repetitively pulsed discharges (NRP discharges) are interesting candidates (see details in section 2.4) for the achievement of efficiency fuel ignition.
For instance, using a train of ten nanosecond pulses (up to 10 kV pulse amplitude, 10 ns pulse duration, 30 kHz repetition frequency) to ignite lean propane-air mixtures, *Pancheshnyi et al.* [2006] observed experimentally a significant reduction of the ignition delay and some acceleration of the combustion process. Figure 2.5 is an example of light emission during the flame ignition and propagation stages. It consists in a sequence of images taken at a frame rate of 1.5 ms^{-1} with an exposure

time of 33 µs. In addition to the reduced ignition delay, from spectroscopic measurements at 1-bar in air, authors observed the presence of numerous species (N, N^+, O, O^+) in the afterglow (after 300 µs) combined with an increase of the gas temperature of up to 3000 K, limited to a short time following each pulse.

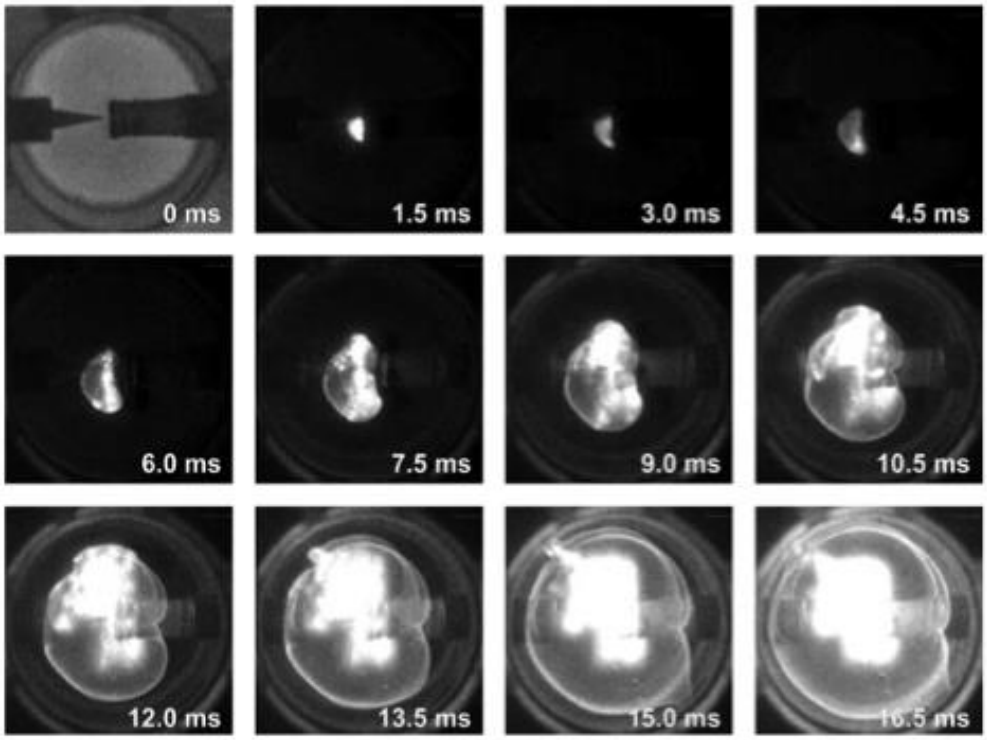

Figure 2.5: Flame propagation in a lean propane-air mixture ($\phi = 0.7$) at 2-bar ignited by a train of 10 high-voltage nanosecond pulses at 30 kHz repetition frequency. Gap distance: 1.5 mm, ignition energy: 1 mJ/pulse. Image taken from [*Pancheshnyi et al.*, 2006].

To understand the non-equilibrium ignition mechanism following a nanosecond pulse, *Wu et al.* [2011] compared their spatially resolved OH density dynamics obtained by PLIF with the discharge emission dynamics in air (recorded with a sequence of ICCD images). These authors found a spatial similarity between both, which led them to suggest that the excitation of nitrogen electronic states is related to the production of atomic oxygen, which afterward turns to the formation of hydroxyl radicals. Note that the nanosecond pulsed discharge (20 kV, 10 ns, 10 kHz) was generated between electrodes in a point-to-point configuration and separated by an inter-electrode gap distance of 8 mm. OH density measurements were performed using various hydrocarbon fuels (methane, ethane, propane and butane). Similar conclusions were drawn by *Aleksandrov et al.* [2009-a]; *Aleksandrov et al.* [2009-b], who conducted numerical simulation of the ignition dynamics of a CH_4:O_2:Ar mixture by a high-

voltage nanosecond discharge. These authors also demonstrated that gas heating by the action of the discharge was insufficient to explain the reduced ignition delay.

Up to now, the standard combustion mechanisms mostly fail to reproduce the (experimental) temporal evolution of densities of the main radicals in plasma-assisted combustion cases. This is because there is no validated kinetic mechanism of ignition at low initial temperature and for complex hydrocarbons (the cross-sections of the collisions of electrons with complex hydrocarbons are lacking). Current researches in plasma-assisted combustion and ignition are going toward combining detailed (highly space and time resolved) *in-situ* measurements of plasma and combustion parameters with the validation of chemical mechanisms [*Laux et al.*, 2014; *Adamovich and Lempert*, 2015].

Plasma-stabilization of lean flames

There is an increasing interest on lean premixed combustion to reduce of NO_x emissions in combustion engines. This interest is motivated by the fact that European emission standards for light commercial vehicles regarding NO_x emissions were restricted from 150 mg/km in 2000 (norm Euro 3) to 60 mg/km in 2014 (norm Euro 6). Because NO_x released by the combustion systems increases exponentially with flame temperature, the designed strategy consists in reducing the flame temperature. This can be achieved by lean premixed combustion [*Lefebvre*, 1998]. However, lean flames tend to be unstable. Flame instability manifests itself by self-oscillating combustion regimes with fluctuating heat release rate as well as mechanical oscillations, which can damage the combustion chamber. A convenient method to tackle these drawbacks is to use non-equilibrium plasma discharges to stabilize lean flames.

One of the early investigations of plasma-assisted stabilization was conducted by *Choi et al.* [2004], who reported a significant extension of the flammability limit of lean propane-air mixtures at atmospheric pressure using a Microsecond Repetitively Pulsed (MRP) discharge to stabilize the flame. In this case, pulses of 100 µs duration at 9 kHz repetition frequency were used. The authors estimated the required plasma power to be about 5 % of flame power. However, the flame power was relatively low (up to 300 W). This result was confirmed and improved by *Pilla et al.* [2006]. Here, stabilization and lean flammability limit extension at atmospheric pressure were achieved using NRP discharges (10 kV, 10 ns, 30 kHz). This time the power of the lean turbulent ($Re_D = 3 \times 10^4$) premixed propane-air flame was about 25 kW and that of the plasma used was 75 W, which represents only 0.3 % of the flame power.

Figure 2.6 displays the influence of the addition of NRP discharges on the burner regimes. Region 1 represents burner stability domain without plasma. Then region 2 corresponds to the extension of the flame stability domain following the application

of the 30 kHz NRP discharges. Region 3 is the domain of flames in the intermittent regime while the large region 4 corresponds to the domain of the pilot flame. The pilot flame is a small flame confined in the recirculation zone behind the bluff-body, in the vicinity of the electrodes (see figure 2.7, which presents the locations of the bluff-body and electrodes). Then finally, the flame extinction domain is shown in zone 5. Figure 2.6 also reports lean-flammability results obtained by *Choi et al.* [2004]. The comparison between results obtained with the microsecond repetitively pulsed discharge and those obtained with the NRP discharge demonstrates a more efficient flame enhancement by NRP discharges. Performing Optical Emission Spectroscopy (OES) with and without the NRP discharges in order to identify radicals present in combustion and in plasma-assisted combustion, *Pilla et al.* [2006] observed for instance an increased OH emission with the discharge applied. Figure 2.7 represents the comparison of OH emissions without (left part of the image) and with (right part of the discharge) NRP discharge.

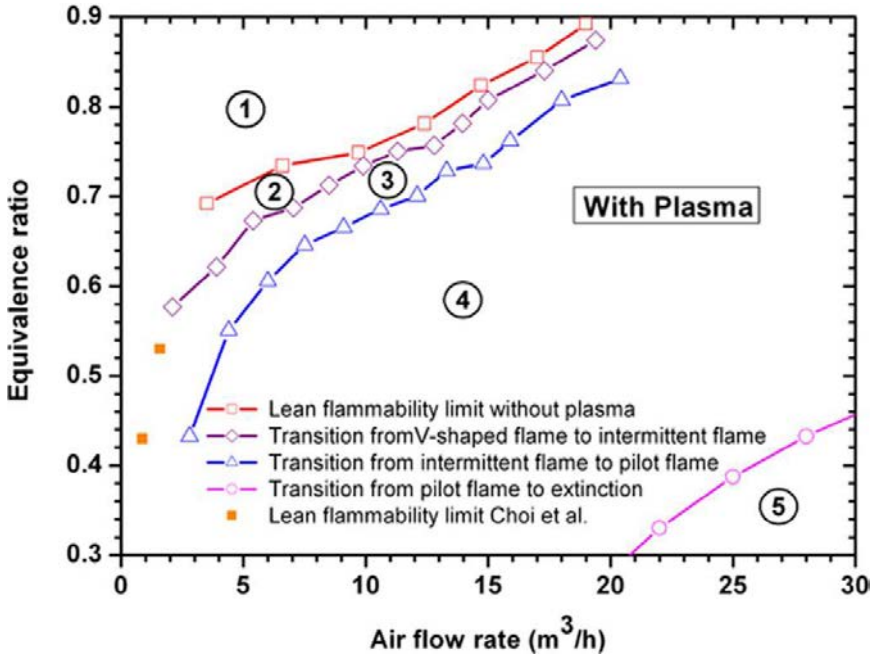

Figure 2.6: Burner regimes with a NRP spark discharge applied at 30 kHz repetition frequency. Figure taken from [*Pilla et al.*, 2006].

For diffusion flames (partially premixed flames more exactly), *Sun et al.* [2012] conducted both experimental (performing TALIF, FTIR and chromatography measurements) and simulation investigations of the extension of diffusion methane-air flames extinction limits when enhanced by a NRP discharge. Measurements were carried out at 60 Torr pressure with discharge pulses of 32 kV amplitude, 12 ns duration and repetition frequencies up to 50 kHz. These authors concluded that the

extension of the flammability limit was due to the improvement of fuel oxidation by O atoms produced by the discharge.
Current researches on PAC focus on the understanding of the role of the different internal degrees of freedom at various values of E/n. Others key points of interest include the development of kinetic mechanisms for the PAC of complex fuels and for PAC with initial temperature below the self-ignition point. In this thesis, we address as well comparative studies of nitric oxide emission in methane-air lean flame assisted by NRP discharges [*Stancu et al.*, 2013]. The corresponding results are presented in chapter 7.

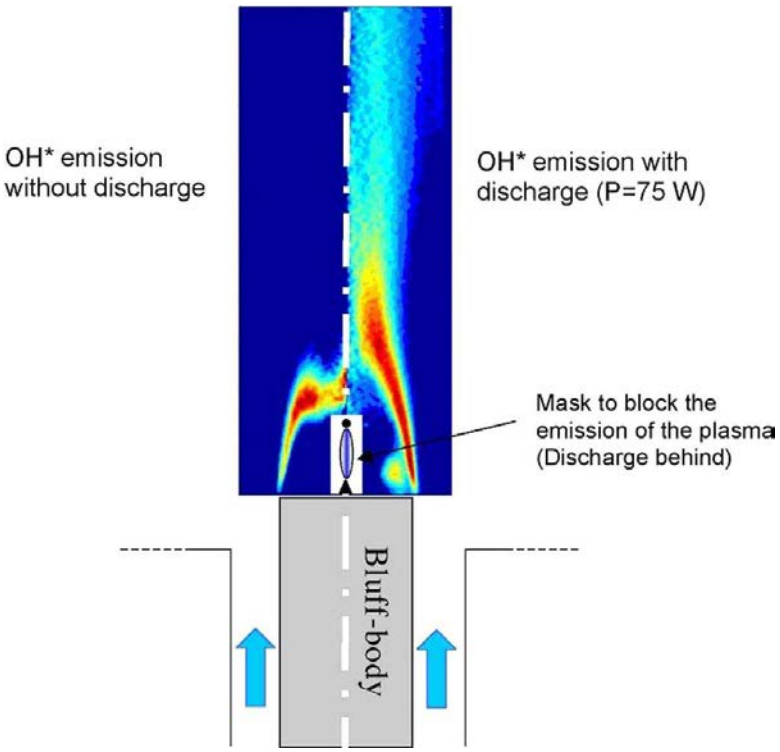

Figure 2.7: OH (A-X) emission with and without plasma discharge. Conditions: ϕ = 0.83, propane flow rate = 0.5 m^3/h, flame power = 12.5 kW and discharge power = 75 W. Figure taken from [*Pilla et al.*, 2006].

2.3 Types of atmospheric pressure air plasmas

In this section we briefly introduce the types of plasmas at atmospheric pressure.
Different types of classification and sources for plasma discharges operating in air at atmospheric pressure are presented.

A key parameter of atmospheric pressure air plasmas is the ionization degree α, which is described as:

$$\alpha = \frac{n_e}{n_e + n} \tag{2.1}$$

where n_e and n are the electrons and total neutral densities, respectively.

Following *Delcroix and Bers*, [1994], regarding their ionization degrees, plasmas can be classified as it follows:

- **Weakly-ionized plasmas**, whose dynamics are dominated by electron collisions with neutrals. In these plasmas, the collision frequency between electrons and neutrals is higher than that between electrons or between electrons and ions.

- **Highly-ionized plasmas**, in which Coulomb interactions between charged species dominate plasma dynamics. Unlike the former case, here the collision frequency between electrons or between electrons and ions is greater than that between electrons and neutrals.

It should be noticed that a relatively low ionization degree could be sufficient for a plasma to be in the "highly-ionized" category. This arises from the long-range Coulomb interaction potential (~1/r). Consequently, Coulomb interaction cross-sections between charged species are many orders of magnitude greater than cross-sections of interactions between electrons and neutrals.
However, for the purpose of predicting the reactive behavior of plasma species, we need to determine densities of all these species together with the distribution of particles in the various internal states. This task is not possible for realistic plasmas. Another approach consists in characterizing the thermodynamic state of the plasma, in term of deviation from an equilibrium distribution. Indeed, as it will be shown, plasmas can attain some types of equilibrium.

2.3.1 Thermal plasmas

When all the states of particles of a plasma follow the Boltzmann distribution at a same temperature T and when the radiation field for all possible transitions is described by the blackbody radiation at the same temperature T, the plasma is described as in Complete Thermodynamic Equilibrium (CTE). The state of the plasma is then entirely described by the gas pressure and temperature. Nevertheless, the CTE case is never achieved in laboratory plasmas since the finite size of these plasmas allows radiation to escape. Accordingly, the radiation field cannot longer be a blackbody radiation.
The so-called Local Thermodynamic Equilibrium (LTE) gives a less constraining type of equilibrium. In this case, populations of quantum states of plasma species follow

Boltzmann distribution but the radiation field is not necessary Blackbody radiation [*Hutchinson*, 2005].

In general, discharge plasmas depart from LTE conditions because of the finite rates of ionization and recombination processes. The distributions of particle densities among the energy levels depart from a Boltzmann distribution, as illustrated in figure 2.8.

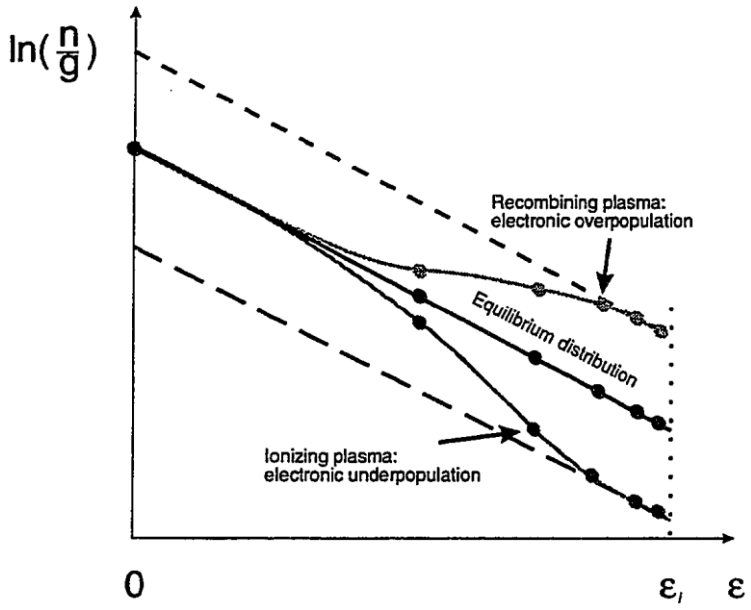

Figure 2.8: Electronic populations distribution in equilibrium, ionizing and recombining plasmas. Figure taken from [*Laux*, 1993].

Thermal plasma sources

Thermal plasma sources include first DC discharges, which are the easiest way to produce thermal plasmas at atmospheric pressure. Another possibility is to use radio-frequency inductively coupled (RF-ICP) torches. The latter can for instance create thermal plasmas with 5-cm typical diameter and a temperature up to 10^4 K [*Laux*, 1993]. Microwave plasma torches (often at 2.45 GHz) can also be used. For instance, *Machala et al.*, [2004] produced a thermal plasma with a temperature up to 5 x 10^3 K, in a 10-cm^3 volume.
Thermal plasmas are widely used for welding, cutting, spraying, sputtering, and for waste processing.

2.3.2 Non-thermal plasmas

Non-thermal plasmas exhibit a non-equilibrium behavior. Accordingly, the gas temperature can be many orders of magnitude lower than the electrons temperature ($T_e >> T_g$). This makes non-thermal plasmas interesting for many types of applications as shown in section 2.2. Non-thermal plasmas depart from LTE distribution since in this case, collisions do not dominate all the transitions between internal states. It is possible to demonstrate that for a two-level atom, LTE prevails only if [*Hutchinson*, 2005]:

$$n_e \gg 10^{13}(T/e)^{1/2}(\Delta E/e)^3 \tag{2.2}$$

where T/e and ΔE/e are respectively the temperature and energy level difference in eV.

Non-thermal plasma sources

It is more difficult to maintain the non-equilibrium state of air plasmas at atmospheric pressure than at low pressure. As the gas pressure increases, the number of collisions between electrons and neutrals increases and gas tends to thermalize. Gas heating will then promote the transition to the arc regime. Methods for generating non-thermal plasmas (low gas temperature) at atmospheric pressure rely on various strategies to prevent the transition to arc [*Tendero et al.*, 2006]. Amongst them, we can quote:

- **DC discharges** combined with a current-limiting resistance in series with the discharge. The outcome of the combination prevents the glow-to-arc transition [*Yu et al.*, 2002]. Their average electron densities can reach 10^{15} cm^{-3}, for gas temperatures between 1000 and 3000 K.

- **Dielectric Barrier Discharges** (DBD) in which a dielectric layer covers plane electrodes to capacitively limit the current in the plasma filaments and hence preventing arcing. Although they produce plasmas with low gas temperature (from 300 to 1000 K), DBDs tend to generate non-uniform randomly distributed plasma filaments [*Massines et al.*, 2003], especially in air, for gas distance greater than 2 mm. They also produce electron densities about 10^9 – 10^{11} cm^{-3}.

- **Micro plasmas,** which are plasmas of size from µm up to 1-mm. They allow providing low temperature plasmas thanks to their small size, which favors large heat losses to the surroundings (in comparison with heat losses in the volume) [*Karanassios*, 2004].

- **Atmospheric Pressure Plasma Jets** (APPJs) are different from others plasma sources, which are mostly confined between two electrodes, limiting the area of application. APPJs are generated mainly in rare gases and can propagate out of tubes in which they are produced (hence the name "jets"), entraining active species with them. These plasmas operate mostly with RF and microwave frequencies. The transition to the thermal state is prevented by a special care on the combination of driving frequency, plasma power and gas flows [*Van Gessel*, 2013]. Note however that APPJs running on air do not propagate significantly outside of the tube in which they are generated.

- **Nanosecond Repetitively Pulsed Discharges** (NRPD), which were studied in this thesis is another important technique to produce non-thermal plasma. Details are presented in the following section.

2.4 Nanosecond Repetitively Pulsed (NRP) discharges

2.4.1 Principles, advantages and regimes

Introduced at Stanford in the early 2000s, the NRP strategy to circumvent transition to arc consists in generating plasmas by applying repeated short voltage pulses (in the range of 10 ns duration) [*Nagulapally et al.*, 2000]. In this way, the pulse duration is shorter than the characteristic time for the transition to arc. As shown by figure 2.9, during the pulse, electron number density rises exponentially thanks to the effective ionization of the gas in high-reduced electric fields (greater than 100 Td). Then, between pulses, the electron number density decreases as a result of recombination processes. In order to enable accumulation of plasma species, the pulse repetition frequency of NRP discharges is adjusted so that the duration of the inter-pulse is shorter or comparable to the recombination time of the electrons. *Packan*, [2003], found a recombination time about 90 µs at 2000 K. The author claimed that the dominant ion at the end of the pulse is NO^+ and that the principal recombination process after the pulse is $NO^+ + e^- \rightarrow N + O$. Accordingly, a repetition frequency higher than 12 kHz fulfills the necessity of an inter-pulse duration shorter than the recombination time.

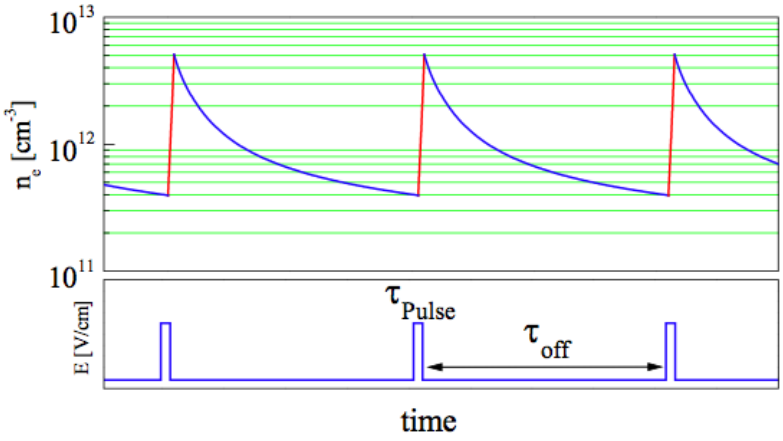

Figure 2.9: NRP electron density and reduced electric field as functions of time. Figure taken from [*Packan*, 2003].

Figure 2.10 represents calculations of the fraction of electrons energy branching in the various degrees of freedom in an air-like mixture as a function of the reduced electric field in Townsend units (1 Td = 10^{-17} V-cm^2). It is shown that for E/n > 100 Td, the energy is mainly transferred to the electronically excited levels of nitrogen. Moreover, for E/n > 200 Td, the fraction of energy going to O_2 dissociation (by electron impact) and the gas ionization increase significantly.
A notable point is the fact that thanks to the pulsed strategy, the instantaneous power during the pulse is high (up to 100 kW) whereas the average power dissipated power is low (100 kW x duty cycle ~ 30 W for a 33 µs inter-pulse duration), thus energetically interesting for applications.

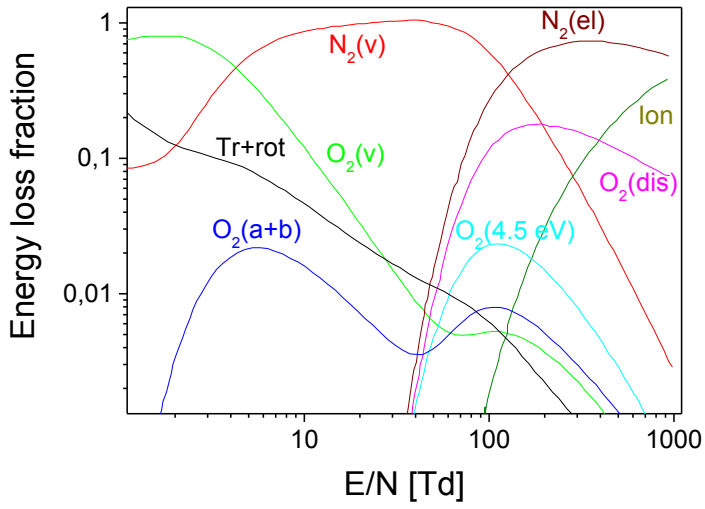

Figure 2.10: Fraction of electrons energy transferred in the various channels of a N_2:O_2 = 4:1 mixture as a function of the reduced electric field in Townsend (1 Td = 10^{-17} V.cm^2). Figure taken from [*Starikovskiy and Aleksandrov*, 2013].

NRP discharges regimes

When increasing the voltage amplitude, *Pai*, [2008] observed three regimes of NRP discharges operating in air at atmospheric pressure and at gas temperatures ranging between 300 and 1000 K. These 3 regimes are shown in figure 2.11. They differ one from another in terms of the deposited energy, conduction current and gas heating.

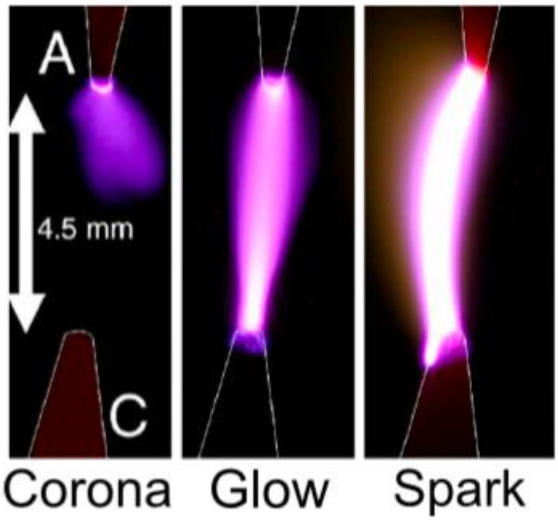

Figure 2.11: NRP discharge regimes at 1000 K gas temperature, for 10 kHz PRF, 4.5-mm gap distance and 1 m/s flow rate. Figure taken from [*Pai*, 2008].

These regimes have been called NRP corona, glow and spark, by analogy with their DC counterparts. The NRP corona is characterized by low emission levels and is present only near the anode. This regime gives very little energy to the gas (below 10 µJ) and it does not significantly heat the gas. The NRP glow appears to be diffuse. This regime is of primary interest since it is able to create active species with reduced gas heating (ΔT <200 K). Finally the NRP spark regime, which exhibits a filamentary appearance, is characterized by an intense emission in the gap, hot spots at electrode tips and a high conduction current (20-40 A).
The NRP spark produces large amounts of active species and a significant heat release. Accordingly, this regime meets the requirements for plasma-assisted combustion. All the experiments of this thesis were conducted in the spark regime. Properties of the spark regime are detailed in 2.4.2. Table 2.2 summarizes the major features of these three regimes.

Table 2.2: Main features of NRP discharge regimes at 1000 K. Table adapted from [*Pai*, 2008].

Appearance	Energy deposited per pulse	Gas heating	Name
Corona	< 10 µJ	~0	NRP corona
Diffuse	10-100 µJ	200 K	NRP glow
Filamentary	> 100 µJ	2000-4000 K	NRP spark

2.4.2 NRP spark discharges in air

In this subsection we review the principal properties of NRP spark discharges operating in air, at atmospheric pressure.

Oxygen atoms production and ultrafast heating

Conducting time-resolved Two-photons Absorption Laser-Induced Fluorescence (TALIF) measurements of oxygen atoms during (and after) a nanosecond discharge pulse, [*Stancu et al.*, 2009; *Kaddouri*, 2011] found a peak O density about 1.5 x 10^{18} cm^{-3}, which corresponds to a 50 % dissociation of molecular oxygen (the gas temperature was about 2000 K). Such high O-atoms density is of considerable importance for plasma-assisted combustion and other O atoms related applications as explained in section 2.2. Furthermore, the peak O density was found to appear after the discharge pulse (see figure 2.12). The two-step mechanism introduced by *Popov*, [2001] was considered to be an explanation of the previous observations. It consists in two reactions:

$$N_2(X) + e^- \rightarrow N_2(A, B, C, a', B'\ldots) + e^- \quad (2.3)$$

$$N_2(A, B, C, a', B'\ldots) + O_2 \rightarrow N_2(X) + O + O + \text{heat} \quad (2.4)$$

The rapid heating predicted by the previous mechanism was first observed by *Pai*, [2008] and was further validated by *Kaddouri*, [2011] and *Rusterholtz*, [2012]. For instance, in the latter reference under operating conditions of the "reference case" (see chapter 6 for more details), a 900 K gas temperature increase in about 20 ns was measured (temperature increased from 1500 to 2400 K). This corresponds to a heating rate of 4.5 x 10^{10} K/s, hence the name "ultrafast heating". Note that the gas temperature was inferred from emission spectra of the first and second nitrogen positive systems ($N_2(B \rightarrow A)$ and $N_2(C \rightarrow B)$) [*Kaddouri*, 2011; *Rusterholtz et al.*, 2013]. This mechanism was further validated by [*Stancu et al.*, 2009; *Stancu et al.*,

2010-b], which performed absolute density measurements using synchronized TALIF for O atoms, Optical Emission Spectroscopy (OES) for N_2(B) and N_2(C) and Cavity Ring-Down Spectroscopy for N_2(A). These authors observed that the increase of O atoms density was synchronized with the decrease of populations of N_2(B, C) states as shown in figure 2.12.

Finally, *Rusterholtz et al.* [2013] refined measurements of [*Stancu et al.*, 2010; *Kaddouri*, 2011] (for the same operating conditions) in particular the N_2(B, C), the gas temperature and completed with electron densities, gas temperature and electrical measurements. It was concluded that about 35 % of the NRP discharge energy was spent on O_2 dissociation and about 21 % on gas heating.

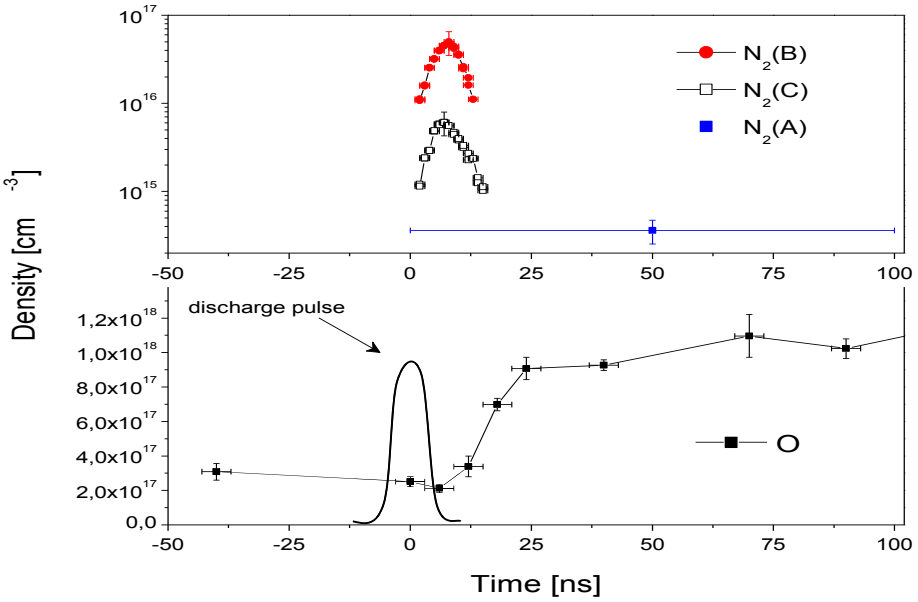

Figure 2.12: Temporal evolution of N_2(A, B, C) and O densities during first 100 ns. Figure taken from [*Stancu et al.*, 2009].

Recently *Popov*, [2013] performed numerical simulations of the NRP discharges kinetics in the reference case using a detailed kinetics model taking into account the ultrafast mechanism (equations 2.5 and 2.6). Figure 2.13 shows that a good agreement was found between experimental and simulation results in terms of temporal evolutions of O atoms density and gas temperature. Furthermore, this kinetic model allowed Popov to estimate that about 35 % of O atoms density arises from the direct dissociation of molecular oxygen by electron impact.

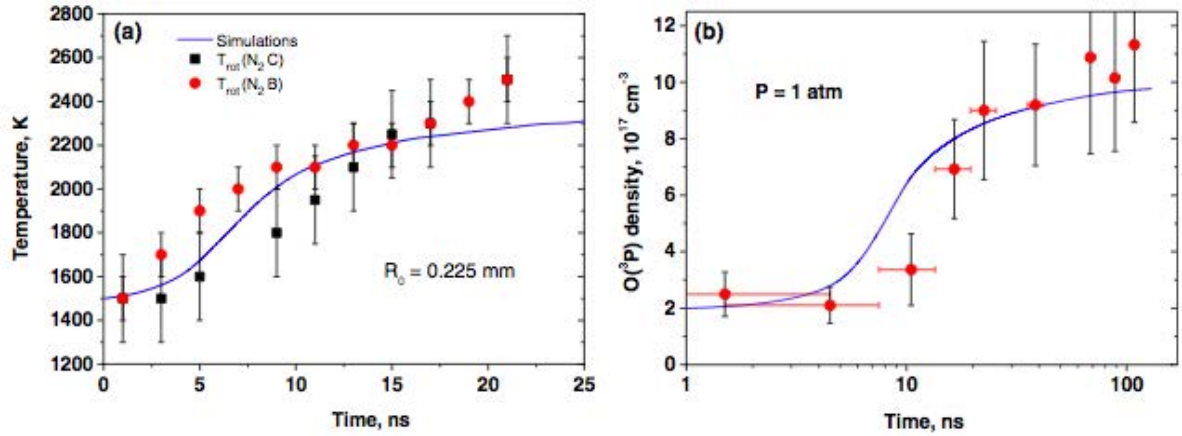

Figure 2.13: Comparison between experimental (dots) and simulation results (lines) of temporal evolution of gas temperature (a) and O density (b). Figure taken from [*Popov*, 2013].

Thermal and hydrodynamic effects

Regarding hydrodynamic effects of the NRP discharges on the flow, [*Xu et al.*, 2011; *Xu*, 2013; *Xu et al.*, 2014] evidenced the expansion of the gas-heated channel, preceded by the propagation of a shock wave. These observations were carried out using to time-resolved single-shot Schlieren imaging of the discharge (see figure 2.14). These authors observed that initially, the shock-wave and the heated channel both extends with a cylindrical shape. Then, beyond the heated channel, the shock-wave propagates as a spherical wave (see figure 2.14) at sound speed. Comparing experimental results to those obtained by performing numerical Schlieren enabled the authors to infer the fraction of energy transferred into gas heating. More specifically it was found that the energy transferred into heating increases with increasing reduced electric field and gas temperature (see table 2.3). For instance, for the case 1, where NRP discharges operate in ambient air flows, the reduced electric field at peak conduction current was found to be about 164 Td and it was estimated that about 25 % of the energy was transferred into the heating of the gas. In a 1000 K preheated air flow, the measured reduced electric field at peak conduction current was found to be about 270 Td leading to about 75 % of the energy transferred into heating. Because previous pulses heated the gas, the initial gas temperature effects on the velocity of the shock-wave were also taken into consideration by the authors. They used OES of the second N_2 positive system to determine this initial gas temperature. Moreover, due to the microsecond timescale of gas dynamics, the authors also demonstrated that the discharge could be considered as isochoric over 50 ns after the beginning of pulse.

Table 2.3: Fraction of energy transferred into gas heating. Taken from [*Xu et al.*, 2014].

	Initial temperature [K]	E/n at I_{max} [Td]	Fraction of energy into heating	Hydrodynamics characteristic time [µs]
Case 1	400	164	25 %	0.50
Case 3	2000	270	75 %	0.54

Regarding numerical simulations, the fraction of energy transferred into gas heating in the case 1 of *Xu*, [2013] (25 %) is consistent with the results of *Aleksandrov et al.* [2010] where 20-23 % of the energy was found. In addition, *Tholin*, [2012] numerically simulated the ultrafast heating, thermal and hydrodynamics effects of the NRP discharges. Multi-pulses discharge dynamics were also well simulated [*Tholin at al.*, 2011].

Although many kinetic and dynamic aspects of NRP have been investigated, the NO production and kinetics mechanisms remain somewhat unclear [*Uddi et al.*, 2009], and therefore one of the reasons of the investigations in this thesis.

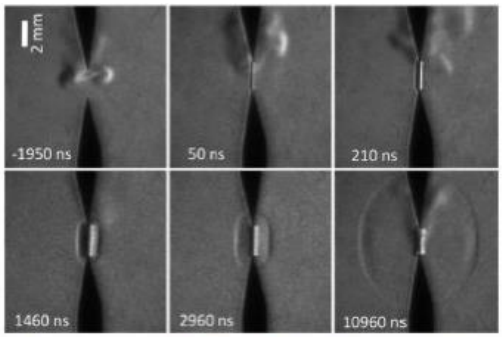

(a) Case 1: $T_g = 300$ K, $d = 2$ mm, $PRF = 1$ kHz and $v \approx 1.6$ m.s^{-1}

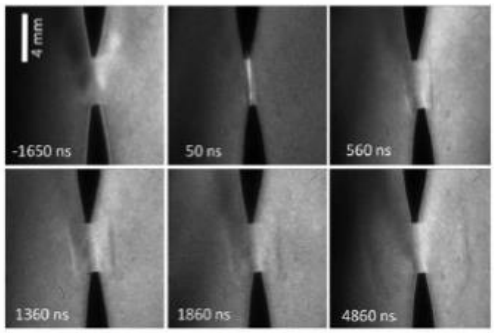

(b) Case 3: $T_g = 1000$ K, $d = 4$ mm, $PRF = 10$ kHz and $v \approx 1.6$ m.s^{-1}

Figure 2.14: Single shot Schlieren images of the NRP discharges. Figures taken from [*Xu*, 2013].

2.5 Nitric oxide (NO) role for biomedical and combustion applications

Three decades ago, NO was mainly regarded as an environmental pollutant released in engine exhaust. However in the early 1990s, it was found that NO is an important biological messenger in mammals [*Palmer et al.*, 1987; *Culotta and Koshland*, 1992]. Besides that, NO was also found to be involved in the regulation of biological processes at the crossroad of neuroscience, physiology and immunology fields. Consequently, NO was proclaimed "Molecule of the year 1992" and the 1998 Nobel prize of "physiology or medicine" was awarded to three scientists who discovered the role of nitric oxide as a cardiovascular signaling molecule. In the following subsections, we will shortly review the role of the NO molecule for biomedical applications and we will discuss the role of NO for combustion-related applications.

2.5.1 NO for biomedical applications

In the nineties it was demonstrated that nitric oxide acts like a neurotransmitter in the nervous system. According to [*Culotta and Koshland*, 1992], NO is the first discovered biological gas messenger. It was proven that nitric oxide molecule is related to learning and remembering mechanisms [*Redy and Kulkarny*, 1998]. Furthermore, the NO molecule possesses also the potential of a defensive weapon. For instance, *Fridman et al.* [2008] observed a reduced bacterial load following seven to fourteen days NO-therapy implementation on 318 patients suffering from trophic ulcers at their lower extremities. If NO is known to favor wound healing by modulating human skin cells proliferation [*Weller*, 2003; *Liebmann et al.*, 2011], it can at the contrary block certain cells growth or either kill those cells [*Culotta and Koshland*, 1992]. NO defense mechanism against invaders cells consists in attacking iron groups of enzymes, which synthetize invader cells DNA and those, which help these cells to respire.

Physiology is another important domain here, the key point is of course the role played by NO as a ubiquitous intercellular messenger in vertebrates. This is possible due to the rapid diffusion of NO through most of tissues with little consumption or direct reaction [*Beckman and Koppenol*, 1996].

Finally, regarding biomedical applications, we should first note that *Liebmann et al.* [2011] demonstrated non-toxicity exposure time of NO up to 10 min for mole fraction about 200 ppm (at atmospheric pressure). This extends the NO mole fraction range of interest for biomedical applications between 5 and 200 ppm. Second, NO is shown to be cytotoxic when combined with superoxide (O_2^-) to create the peroxynitrite ($ONOO^-$).

2.5.2 NO in atmosphere and combustion

Nitric oxide, as mentioned before is a by-product of combustion processes whose emissions are regulated by international norms. Here we will shortly present the impact of NO on the atmosphere and then we will discuss the different mechanisms of the formation of NO in combustion environment.

Nitric oxide is responsible for ozone and nitrogen dioxide production in the troposphere (up to 10 to 15 km altitude), which both contribute to the photochemical smog [*Bowman*, 1992]. Besides, nitrogen dioxide is a precursor of acid rains. Important reactions contributing to the photochemical smog are:

$$NO_2 + h\nu \rightarrow NO + O \tag{2.5}$$

$$O_2 + O + M \rightarrow O_3 + M \tag{2.6}$$

$$NO + O_3 \rightarrow NO_2 + O_2 \tag{2.7}$$

For acid rain formation, the other key reaction involves nitrogen dioxide and hydroxyl radicals to produce nitric acid:

$$NO_2 + OH \rightarrow HNO_3 \tag{2.8}$$

NO also affects the stratosphere (from 15 to 50 km altitude) by destroying the ozone layer via reactions:

$$NO + O_3 \rightarrow NO_2 + O_2 \tag{2.9}$$

$$NO_2 + O \rightarrow NO + O_2 \tag{2.10}$$

As a conclusion, NO contributes to ozone formation in the troposphere where ozone is a pollutant but destroys the same ozone in the stratosphere where it provides a protective layer from sun's UV radiation, hence the strict regulations nowadays for the carmakers industry.

NO released from premixed combustion exhaust arises mainly from four processes: thermal, nitrous oxide, prompt mechanisms and fuel-NO.
The Zel'dovich thermal mechanism is the dominant route for NO formation in combustion processes with at gas temperatures above 1800 K [*Sarofim and Pohl*, 1973; *Bowman*, 1992]. The process involves the following reactions:

$$N_2 + O \rightarrow NO + N \tag{2.11}$$

$$N + O_2 \rightarrow NO + O \tag{2.12}$$

In addition to these reactions, the thermal mechanism can be extended to a third reaction to provide the so-called "extended Zel'dovich mechanism":

$$N + OH \rightarrow NO + H \tag{2.13}$$

Under fuel-lean conditions and for gas temperatures lower than 1800 K accompanied with intense turbulence, *Malte and Pratt*, [1974] found that **nitrous oxide** (N_2O) is an important intermediate for NO formation via reactions:

$$N_2 + O_2 \rightarrow N_2O + O \tag{2.14}$$

$$N_2 + OH \rightarrow N_2O + H \tag{2.15}$$

$$N_2O + O \rightarrow NO + NO \tag{2.16}$$

The Zel'dovich thermal mechanism occurs mainly in the post-flame region because the thermal mechanism is slow. However, *Fenimore*, [1971] observed NO emissions in the flame zone. He proposed **the prompt mechanism** to explain this unexpected rapid formation rate. This mechanism starts with the reaction of CH_x radicals (released in fuel-rich conditions) with N_2 to produce HCN (or NCN):

$$CH + N_2 \rightarrow HCN + N \tag{2.17}$$

$$C + N_2 \rightarrow CN + N \tag{2.18}$$

Then HCN reacts with oxygen containing radicals (OX) to produce NO and others products:

$$HCN + OX \rightarrow NO + \text{others products} \tag{2.19}$$

Finally, when the fuel contains nitrogen, HCN is quickly formed and then, following the prompt mechanism, NO is produced. It is called **fuel-NO**.

2.6 NO detection techniques in plasma and plasma-assisted combustion at atmospheric pressure

In this section, we review the main techniques applied in the literature to detect NO in plasmas, combustion and plasma-assisted combustion fields at atmospheric

pressure. We highlight the principles, advantages and difficulties of these techniques and we emphasize our choice for QCLAS technique. The results and the conclusions of the literature studies presented in this section are discussed in chapters 6 and 7 to better understand NO kinetics in NRP discharges in air and in combustion, respectively.

2.6.1 Optical Emission Spectroscopy (OES)

The ideal non-intrusive method to detect NO either in combustion or in plasma field is OES. However, OES only gives access to exited states, which are statistically less populated than the ground state. In this case, the recovery of NO ground state population is only possible using complex Collisional Radiative Models (CRM).

2.6.2 Chemiluminescence

Common gas analyzers capable of detecting NO rely on the principle of the chemiluminescence reaction between NO and ozone [*Fontijn et al.*, 1970]:

$$NO + O_3 \rightarrow NO_2 + O_2 + h\nu \tag{2.20}$$

The recorded light emission intensity is proportional to the NO density. *Kim et al.* [2007], for instance used a chemiluminescence-based gas analyzer to measure the NO mole fraction produced by a nanosecond pulsed plasma discharge operating in atmospheric pressure air and in combustion environments. The main advantage of this technique is the fact that it is fast and easy to implement. However, this method is not in-situ, since the gas samples are collected and analyzed elsewhere, most of the time in a specific vessel where the second reactant (ozone) is added. Moreover, the collection of the samples can also be regarded as intrusive and the method needs to be calibrated to yield absolute densities. Besides, at atmospheric pressure the fluorescence of the NO_2^* molecules depends strongly of the quenching rate of these excited molecules and these rates are strongly dependent of the gas composition and temperature. Accordingly, since the latter parameters change from plasma to plasma-assisted combustion cases, chemiluminescence could lead to large errors in absolute densities.

2.6.3 Laser-Induced Fluorescence (LIF)

NO detection by LIF in combustion, plasma discharges and in plasma-assisted combustion is very attractive [*Di Rosa et al.*, 1996; *Schultz et al.*, 1997; *Jamette et al.*, 2001; *Uddi et al.*, 2009; *Rao et al.*, 2009; *Van Gessel et al.*, 2013; *Burnette et al.*, 2014] because the technique can provide highly space and time resolved measurements (~50 µm and few ns). Authors usually implement this technique by

recording the (laser-induced) UV fluorescence signal of the NO-γ band (NO A $^2\Sigma^+ \rightarrow$ NO X $^2\Pi$) around 226 nm (for the transition (NO A $^2\Sigma^+$, $v' = 0$) $\rightarrow$ (NO X $^2\Pi$, $v'' = 0$)) or around 247 nm (for the transition (NO A $^2\Sigma^+$, $v' = 0$) $\rightarrow$ (NO X $^2\Pi$, $v'' = 2$)). Many lines can be excited. In the plasma community, the transitions $P_{11}(4.5) + P_{11}(13.5) + R_{22}(10.5)$ [*Uddi et al.*, 2009] and $P_{11}(3.5) + P_{11}(14.5)$ [*Burnette et al.*, 2014] are commonly used. For the combustion community, one of the commonly used excitation line is composed of $P_1(23.5) + Q_1 + P_{21}(14.5) + Q_2 + R_{12}(20.5)$. A review of the different excitation schemes for the detection of NO by LIF in high-pressure flames is given by *Bessler et al.* [2003].

The total measured fluorescence signal S_{LIF} as a function of the excitation laser frequency ν can be written as:

$$S_{LIF}(\nu) = \frac{C_{opt} E_p A_{\nu'=0 \rightarrow \nu"=2}}{\left[\sum_{\nu"} A_{\nu'\nu"} + Q(P,T)\right]} \sum_i \{f_{B_i}(T)\, B_i\, g_i(\nu, P, T)\}\, n_{NO} \tag{2.21}$$

where the summation is carried out over all transitions I that are excited by the laser. C_{opt} is a constant that describes the efficiency of the optical collection. E_p is the laser pulse energy. A and B_i are the Einstein coefficients for spontaneous emission and stimulated absorption, respectively. f_{Bi} is the Boltzmann factor. $Q(P, T)$ is the quenching rate of the NO(A) state. $g_i(P, T)$ is the lineshape function and n_{NO} is the NO absolute density.

The determination of the ground-state absolute density under steady-state conditions hence requires an absolute calibration to determine each of the factors of equation 2.23. The absolute calibration method can be complex when dealing with short-lived radicals. But as NO is a long-lived radical, authors in the literature [*Uddi et al.*, 2009; *Van Gessel et al.*, 2013] manage to implement the calibration procedure using a known NO/N_2 and NO/He sample mixtures, respectively, in reference cells:

$$n_{NO,disch} = n_{NO,calib} \frac{S_{f,disch}}{S_{f,calib}} \frac{\left[\sum_{\nu"} A_{\nu'\nu"} + Q\right]_{disch}}{\left[\sum_{\nu"} A_{\nu'\nu"} + Q\right]_{calib}} \tag{2.22}$$

Then they derived the unknown discharge NO density ($n_{NO,\,disch}$) as a function of the known NO density of the calibration mixture ($n_{NO,\,calib}$), of the ratio of the temporally and spectrally integrated fluorescence signals of the NO in the discharge ($S_{f,\,disch}$/ $S_{f,\,calib}$) and in the calibration mixture, of the sum of the Einstein spontaneous emission coefficients over all the excited transitions by the laser and of the quenching rate. Apart from the quenching rate, the foregoing parameters are well known. The

quenching rate strongly depends on the gas pressure, temperature and composition. At low pressure, quenching is slow, it can hence be measured from time-resolved measurements of the fluorescence signal. But at atmospheric pressure, the quenching is fast and sometimes it cannot be measured even with ultrafast detectors. This is a major drawback for the implementation of the LIF at atmospheric pressure. Other issues affecting the measurement of absolute NO density by LIF, especially in combustion are the possible interferences with O_2 (in lean non-premixed flames) and CO_2 (in high-pressure methane-air flames for instance) spectra, as well as the distortion of the fluorescence signal due to the temperature field.

2.6.4 Fourier-Transform InfraRed (FTIR) spectroscopy

(Incoherent) FTIR uses a broadband IR source to perform broadband absorption spectroscopy. However, before passing through the target gas sample, the IR light passes through an interferometer (typically a Michelson interferometer, which is made of a fixed mirror and another motor moveable mirror). Consequently, the signal exiting from the interferometer consists in the intensity of the light interference as a function of the retardation induced by the moving mirror. This signal, which is called an interferogram, has the property that every data point (i.e. for each mirror position) contains information about every infrared wavelength that comes from the source. Thus, once the interferogram is measured, all the wavelengths are being measured simultaneously. After passing through the gas sample, raw data are collected by an IR detector and then analyzed by means of fast Fourier transform algorithms, which turn light absorption as a function of the mirror position into light absorption as a function of the wavelength. As for laser absorption spectroscopy, a background spectrum must be also measured to determine absolute densities.
As a result of the properties listed above, FTIR offers a wide spectral range so that many lines of the desired species can be used and the detection of other plasma/combustion species can be performed simultaneously with the NO detection. Under some conditions, the "multiplexed measurements" can improve the signal-to-noise ratio (in comparison with an equivalent scanning monochromator). This is sometimes referred as the multiplex or Fellgett's advantage. Another advantage over dispersive spectrometers sometimes referred as the Jaquinot's advantage is the improvement of the sensitivity, owing to a higher optical throughput. Unlike a dispersive spectrometer whose throughput is limited by its entrance and exits slits, the throughput of a FTIR interferometer is only limited by the size of the collimated beam coming from the IR source. In addition, FTIR spectroscopy can also provide high spectral resolution ~10^{-3} cm^{-1}, for a 10 m maximum retardation (the spectral resolution is equal to the reciprocal of the maximum retardation) and it does not require a calibration. Nevertheless, the time resolution of FTIR spectroscopy is limited by the displacement speed of the moving mirror, part of the interferometer.

The advantages and the limitations of the FTIR spectroscopy are further detailed and discussed by *Griffiths and Haseth*, [2007].
In the literature one can find examples of the detection of NO by FTIR spectroscopy in plasmas [*Penetrante et al.*, 1995; *Zhao et al.*, 2005] and in combustion [*Goode et al.*, 2000].

2.6.5 Quantum Cascade Laser Absorption Spectroscopy (QCLAS)

The principle of QCLAS is detailed in chapter 4. The main benefits of this method are that **(1)** it does not require any calibration procedure and **(2)** it allows species selectivity (to distinguish close absorbing lines) thanks to a spectral resolution of about $\sim 10^{-3}$ cm^{-1}. This technique can also provide highly sensitive results (down to 1 ppm) when coupled with a multi-pass cell. For the disadvantages of the QCLAS, we can note that it is a difficult technique to implement (invisible laser); it is limited in time resolution to about 1 µs at atmospheric pressure as shown by *Welzel et al.*, [2010]. In the literature, absolute NO density measurements by QCLAS have been conducted in low-pressure plasmas [*Welzel et al.*, 2007; *Welzel et al.*, 2011], and in atmospheric pressure combustion environments with gas temperatures of up to 700 K [*Wysocki et al.*, 2005; *Chao et al.*, 2011; *Chao et al.*, 2012].

In the field of trace gas detection, NO detection sensitivity was improved up to sub-ppb by coupling quantum cascade laser with others techniques such as Cavity Ring Down Spectroscopy (CRDS) [*Kosterev et al.*, 2001] or Integrated Cavity Output Spectroscopy (ICOS) [*Bakhirkin et al.*, 2004; *Bakhirkin et al.*, 2006].

Even though it is less encountered in the literature, NO ground-state densities could also be detected using classical CRDS [*Pillier at al.*, 2002; *Sepman et al.*, 2003], Electronic Resonance Enhanced Coherent Anti-Stokes Raman Scattering (ERE-CARS) [*Hanna et al.*, 2003] and broadband UV absorption spectroscopy.

Besides the selectivity, another key reason of using QCLAS technique is the precision of the measured absolute density. Below 1 % error on absolute density of NO in uniform gas environments is easily achievable with this technique. However, in situ diagnostics in combustion environments remain very challenging because of the presence of large amounts of hot water as will be shown later.

2.7 Conclusions

In this chapter, we first presented the application fields of non-thermal plasmas, emphasizing the benefits of their non-equilibrium character. Then we overviewed the usual techniques to create non-thermal plasmas in air, at atmospheric pressure.

Afterward, we focused our attention to the particular case of NRP discharges. Finally, we compared several methods implemented for NO detection. For each technique, we highlighted the characteristics such as the sensitivity, spatial and temporal resolutions, intrusiveness and calibration requirements.

References

[1] Adamovich, I. V., Lempert, W. R., Rich, J. W., Utkin, Y. G., & Nishihara, M. (2008). Repetitively pulsed nonequilibrium plasmas for magnetohydrodynamic flow control and plasma-assisted combustion. *Journal of Propulsion and Power*, *24*(6), 1198-1215.

[2] Adamovich, I. V., Choi, I., Jiang, N., Kim, J. H., Keshav, S., Lempert, W. R., ... & Uddi, M. (2009). Plasma assisted ignition and high-speed flow control: non-thermal and thermal effects. *Plasma Sources Science and Technology*, *18*(3), 034018.

[3] Adamovich, I. V., & Lempert, W. R. (2015). Challenges in understanding and development of predictive models of plasma assisted combustion. *Plasma Physics Controlled Fusion*, *56*.

[4] Aleksandrov, N. L., Kindysheva, S. V., Kosarev, I. N., Starikovskaia, S. M., & Starikovskii, A. Y. (2009). Mechanism of ignition by non-equilibrium plasma. *Proceedings of the Combustion Institute*, *32*(1), 205-212.

[5] Aleksandrov, N. L., Kindysheva, S. V., Kukaev, E. N., Starikovskaya, S. M., & Starikovskii, A. Y. (2009). Simulation of the ignition of a methane-air mixture by a high-voltage nanosecond discharge. *Plasma physics reports*, *35*(10), 867-882.

[6] Aleksandrov, N. L., Kindysheva, S. V., Nudnova, M. M., & Starikovskiy, A. Y. (2010). Mechanism of ultra-fast heating in a non-equilibrium weakly ionized air discharge plasma in high electric fields. *Journal of Physics D: Applied Physics*, *43*(25), 255201.

[7] Bakhirkin, Y. A., Kosterev, A. A., Roller, C., Curl, R. F., & Tittel, F. K. (2004). Mid-infrared quantum cascade laser based off-axis integrated cavity output spectroscopy for biogenic nitric oxide detection. *Applied optics*, *43*(11), 2257-2266.

[8] Bakhirkin, Y. A., Kosterev, A. A., Curl, R. F., Tittel, F. K., Yarekha, D. A., Hvozdara, L., ... & Faist, J. (2006). Sub-ppbv nitric oxide concentration

measurements using cw thermoelectrically cooled quantum cascade laser-based integrated cavity output spectroscopy. *Applied Physics B*, *82*(1), 149-154.

[9] Barbosa, S., Pilla, G., Lacoste, D., Scouflaire, P., Ducruix, S., Laux, C., & Veynante, D. (2009). Influence of a repetitively pulsed plasma on the flame stability domain of a lab-scale gas turbine combustor. In *Fourth European Combustion Meeting* (pp. 1-6).

[10] Beckman, J. S., & Koppenol, W. H. (1996). Nitric oxide, superoxide, and peroxynitrite: the good, the bad, and ugly. *American Journal of Physiology-Cell Physiology*, *271*(5), C1424-C1437.

[11] Bessler, W. G., Schulz, C., Lee, T., Jeffries, J. B., & Hanson, R. K. (2003). Strategies for laser-induced fluorescence detection of nitric oxide in high-pressure flames. III. Comparison of A–X excitation schemes. *Applied optics*, *42*(24), 4922-4936.

[12] Bowman, C. T. (1992, December). Control of combustion-generated nitrogen oxide emissions: technology driven by regulation. In *Symposium (International) on Combustion* (Vol. 24, No. 1, pp. 859-878). Elsevier.

[13] Burnette, D., Montello, A., Adamovich, I. V., & Lempert, W. R. (2014). Nitric oxide kinetics in the afterglow of a diffuse plasma filament. *Plasma Sources Science and Technology*, *23*(4), 045007.

[14] Cottrell, F. G. (1911). The Electrical Precipitation of Suspended Particles. *Industrial & Engineering Chemistry*, *3*(8), 542-550.

[15] Chao, X., Jeffries, J. B., & Hanson, R. K. (2011). In situ absorption sensor for NO in combustion gases with a 5.2 μm quantum-cascade laser. *Proceedings of the Combustion Institute*, *33*(1), 725-733.

[16] Chao, X., Jeffries, J. B., & Hanson, R. K. (2012). Wavelength-modulation-spectroscopy for real-time, in situ NO detection in combustion gases with a 5.2 μm quantum-cascade laser. *Applied Physics B*, *106*(4), 987-997.

[17] Choi, W. S., Neumeier, Y., & Jagoda, J. (2004). Stabilization of a combustion process near lean blow off (LBO) by an electric discharge. *AIAA paper*, *982*, 2004.

[18] Culotta, E., & Koshland, D. E. (1992). NO news is good news. *Science*, *258*(5090), 1862-1865.

[19] Delcroix, J. L., & Bers, A. (1994). Physique des plasmas, Tome 1. *InterEditions/CNRS Editions*.

[20] Di Rosa, M. D., Klavuhn, K. G., & Hanson, R. K. (1996). LIF spectroscopy of NO and O2 in high-pressure flames. *Combustion science and technology*, *118*(4-6), 257-283.

[21] Donnelly, V. M., & Kornblit, A. (2013). Plasma etching: Yesterday, today, and tomorrow. *Journal of Vacuum Science & Technology A*, *31*(5), 050825.

[22] Esakov, I. I., Grachev, L. P., Khodataev, K. V., Vinogradov, V. A., & Van Wie, D. M. (2006, January). Efficiency of propane-air mixture combustion assisted by deeply undercritical MW discharge in cold high-speed airflow. In *44th AIAA aerospace sciences meeting and exhibition (Reno, Nevada, USA) AIAA-2006-1212*.

[23] Fenimore, C. P. (1971, December). Formation of nitric oxide in premixed hydrocarbon flames. In *Symposium (International) on Combustion* (Vol. 13, No. 1, pp. 373-380). Elsevier.

[24] Fontijn, A., Sabadell, A. J., & Ronco, R. J. (1970). Homogeneous chemiluminescent measurement of nitric oxide with ozone. Implications for continuous selective monitoring of gaseous air pollutants. *Analytical chemistry*, *42*(6), 575-579.

[25] Fridman, G., Peddinghaus, M., Balasubramanian, M., Ayan, H., Fridman, A., Gutsol, A., & Brooks, A. (2006). Blood coagulation and living tissue sterilization by floating-electrode dielectric barrier discharge in air. *Plasma Chemistry and Plasma Processing*, *26*(4), 425-442.

[26] Fridman, A., Gutsol, A., Dolgopolsky, A., & Shtessel, E. (2006). CO2-free energy and hydrogen production from hydrocarbons. *Energy & fuels*, *20*(3), 1242-1249.

[27] Fridman, G., Friedman, G., Gutsol, A., Shekhter, A. B., Vasilets, V. N., & Fridman, A. (2008). Applied plasma medicine. *Plasma Processes and Polymers*, *5*(6), 503-533.

[28] Goode, J. G., Yokelson, R. J., Ward, D. E., Susott, R. A., Babbitt, R. E., Davies, M. A., & Hao, W. M. (2000). Measurements of excess O3, CO2, CO, CH4,

C2H4, C2H2, HCN, NO, NH3, HCOOH, CH3COOH, HCHO, and CH3OH in 1997 Alaskan biomass burning plumes by airborne Fourier transform infrared spectroscopy (AFTIR). *Journal of Geophysical Research: Atmospheres (1984–2012)*, *105*(D17), 22147-22166.

[29] Griffiths, P. R., & De Haseth, J. A. (2007). *Fourier transform infrared spectrometry* (Vol. 171). John Wiley & Sons.

[30] Hanna, S. F., Kulatilaka, W. D., Arp, Z., Opatrný, T., Scully, M. O., Kuehner, J. P., & Lucht, R. P. (2003). Electronic-resonance-enhanced coherent anti-Stokes Raman spectroscopy of nitric oxide. *Applied Physics Letters*, *83*(9), 1887-1889.

[31] Hutchinson, I. H. (2005). *Principles of plasma diagnostics*. Cambridge university press.

[32] Jamette, P., Ricordeau, V., Deschamps, B., & Desgroux, P. (2001). *Laser Induced Fluorescence Detection of NO in the Combustion Chamber of an Optical GDI Engine with AX (0, 1) Excitation* (No. 2001-01-1926). SAE technical paper.

[33] Kaddouri, F. (2011). *Development of advanced optical diagnostics for the study of ultrafast kinetics of oxygen production by nanosecond discharges in atmospheric pressure air* (Doctoral dissertation, Ecole Centrale Paris).

[34] Karanassios, V. (2004). Microplasmas for chemical analysis: analytical tools or research toys?. *Spectrochimica Acta Part B: Atomic Spectroscopy*, *59*(7), 909-928.

[35] Kim, H. H. (2004). Nonthermal plasma processing for air-pollution control: a historical review, current issues, and future prospects. *Plasma Processes and Polymers*, *1*(2), 91-110.

[36] Kim, W., Do, H., Mungal, M. G., & Cappelli, M. A. (2007). Investigation of NO production and flame structure in plasma enhanced premixed combustion. *Proceedings of the Combustion Institute*, *31*(2), 3319-3326.

[37] Kong, M. G., Kroesen, G., Morfill, G., Nosenko, T., Shimizu, T., Van Dijk, J., & Zimmermann, J. L. (2009). Plasma medicine: an introductory review. *New Journal of Physics*, *11*(11), 115012.

[38] Kosterev, A. A., Malinovsky, A. L., Tittel, F. K., Gmachl, C., Capasso, F., Sivco, D. L., ... & Cho, A. Y. (2001). Cavity ringdown spectroscopic detection of

nitric oxide with a continuous-wave quantum-cascade laser. *Applied optics*, *40*(30), 5522-5529.

[39] Lacoste, D. A., Xu, D. A., Moeck, J. P., & Laux, C. O. (2013). Dynamic response of a weakly turbulent lean-premixed flame to nanosecond repetitively pulsed discharges. *Proceedings of the Combustion Institute*, *34*(2), 3259-3266.

[40] Laroussi, M. (2005). Low temperature plasma-based sterilization: overview and state-of-the-art. *Plasma processes and polymers*, *2*(5), 391-400.

[41] Laux, C. O. (1993). *Optical diagnostics and radiative emission of air plasmas* (Doctoral dissertation, Stanford University).

[42] Laux, C.O., Adamovich, I., Aleksandrov, N., Cappelli, M., Coulombe, S., Ju, Kim, W., Leonov, S., Miles, R., Pasquiers, S., Sommerer, T., Starikovskaya, S., Starikovskyi, A., Veynante, D., Vincent, A., and Yetter, R., "Plasma-Enhanced Combustion," invited contribution to the white paper entitled "Plasma Aerodynamics: Current Status and Future Directions," edited by J. Poggie, T. McLaughlin, S. Leonov, AIAA Plasma-Aerodynamics Working Group, AIAA Technical Committee on Plasmadynamics & Lasers, published in *Aerospace America*, Nov. 2014.

[43] Lefebvre, A. H. (1998). *Gas turbine combustion*. CRC press.

[44] Lieberman, M. A., & Lichtenberg, A. J. (1994). Principles of plasma discharges and materials processing. *MRS Bulletin*, *30*, 899-901.

[45] Liebmann, J., Scherer, J., Bibinov, N., Rajasekaran, P., Kovacs, R., Gesche, R., ... & Kolb-Bachofen, V. (2011). Biological effects of nitric oxide generated by an atmospheric pressure gas-plasma on human skin cells. *Nitric Oxide*, *24*(1), 8-16.

[46] Machala, Z., Laux, C., Kruger, C., & Candler, G. (2004). Atmospheric Air and Nitrogen DC Glow Discharges with Thermionic Cathodes and Swirl Flow. *AIAA 2004*, *355*.

[47] Malte, P. C., & Pratt, D. T. (1974). The role of energy-releasing kinetics in NOx formation: fuel-lean, jet-stirred CO-air combustion. *Combustion Science and Technology*, *9*(5-6), 221-231.

[48] Massines, F., Segur, P., Gherardi, N., Khamphan, C., & Ricard, A. (2003). Physics and chemistry in a glow dielectric barrier discharge at atmospheric pressure: diagnostics and modelling. *Surface and Coatings Technology*, *174*, 8-14.

[49] Massines, F., Gherardi, N., Fornelli, A., & Martin, S. (2005). Atmospheric pressure plasma deposition of thin films by Townsend dielectric barrier discharge. *Surface and Coatings Technology*, *200*(5), 1855-1861.

[50] Mizuno, A., Clements, J. S., & Davis, R. H. (1986). A method for the removal of sulfur dioxide from exhaust gas utilizing pulsed streamer corona for electron energization. *Industry Applications, IEEE Transactions on*, (3), 516-522.

[51] Moisan, M., Barbeau, J., Moreau, S., Pelletier, J., Tabrizian, M., & Yahia, L. H. (2001). Low-temperature sterilization using gas plasmas: a review of the experiments and an analysis of the inactivation mechanisms. *International journal of Pharmaceutics*, *226*(1), 1-21.

[52] Nagulapally, M., Candler, G. V., Laux, C. O., Yu, L., Packan, D., Kruger, C. H., ... & Schoenbach, K. H. (2000). Experiments and simulations of dc and pulsed discharges in air plasmas. *AIAA Paper*, *2417*.

[53] Oda, T., Yamashita, R., Haga, I., Takahashi, T., & Masuda, S. (1996). Decomposition of gaseous organic contaminants by surface discharge induced plasma chemical processing-SPCP. *Industry Applications, IEEE Transactions on*, *32*(1), 118-124.

[54] Packan, D. (2003). *Repetitive nanosecond glow discharge in atmospheric pressure air* (Doctoral dissertation, Stanford University).

[55] Pai, D. Z. (2008). Nanosecond repetitively pulsed plasmas in preheated air at atmospheric pressure. *PhD Report, Ecole Centrale Paris, France*.

[56] Palmer RM, Ferrige AG, Moncada S. Nitric oxide release accounts for the biological activity of endothelium-derived relaxing factor. Nature 1987; 327: 524-6.

[57] Pancheshnyi, S. V., Lacoste, D. A., Bourdon, A., & Laux, C. O. (2006). Ignition of propane–air mixtures by a repetitively pulsed nanosecond discharge. *Plasma Science, IEEE Transactions on*, *34*(6), 2478-2487.

[58] Penetrante, B. M., Hsiao, M. C., Merritt, B. T., Vogtlin, G. E., & Wallman, P. H. (1995). Comparison of electrical discharge techniques for nonthermal plasma processing of NO in N 2. *Plasma Science, IEEE Transactions on*, *23*(4), 679-687.

[59] Pilla, G., Galley, D., Lacoste, D. A., Lacas, F., Veynante, D., & Laux, C. O. (2006). Stabilization of a turbulent premixed flame using a nanosecond repetitively pulsed plasma. *Plasma Science, IEEE Transactions on*, *34*(6), 2471-2477.

[60] Pillier, L., Moreau, C., Mercier, X., Pauwels, J. F., & Desgroux, P. (2002). Quantification of stable minor species in confined flames by cavity ring-down spectroscopy: application to NO. *Applied Physics B*, *74*(4-5), 427-434.

[61] Popov, N. A. (2001). Investigation of the mechanism for rapid heating of nitrogen and air in gas discharges. *Plasma physics reports*, *27*(10), 886-896.

[62] Popov N A 2013 Fast gas heating initiated by pulsed nanosecond discharge in atmospheric pressure air *51st AIAA Aerospace Sciences Meeting (Grapevine, TX, 7–10 January)* AIAA 2013-1052.

[63] Rao, X., Matveev, I. B., & Lee, T. (2009). Nitric oxide formation in a premixed flame with high-level plasma energy coupling. *Plasma Science, IEEE Transactions on*, *37*(12), 2303-2313.

[64] Reddy, D. S., & Kulkarni, S. K. (1998). Possible role of nitric oxide in the nootropic impairment. *Brain research*, *799*(2), 215-229.

[65] Rousseau, A., Guaitella, O., Gatilova, L., Thevenet, F., Guillard, C., Ropcke, J., & Stancu, G. D. (2005). Photocatalyst activation in a pulsed low pressure discharge. *Applied Physics Letters*, *87*(22), 221501-221501.

[66] Rusterholtz, D. (2012). *Nanosecond repetitively pulsed discharges in atmospheric pressure air* (Doctoral dissertation, Ecole Centrale Paris).

[67] Rusterholtz, D. L., Lacoste, D. A., Stancu, G. D., Pai, D. Z., & Laux, C. O. (2013). Ultrafast heating and oxygen dissociation in atmospheric pressure air by nanosecond repetitively pulsed discharges. *Journal of Physics D: Applied Physics*, *46*(46), 464010.

[68] Samukawa, S., Hori, M., Rauf, S., Tachibana, K., Bruggeman, P., Kroesen, G., ... & Mason, N. (2012). The 2012 plasma roadmap. *Journal of Physics D: Applied Physics*, *45*(25), 253001.

[69] Sarofim, A. F., & Pohl, J. H. (1973, December). Kinetics of nitric oxide formation in premixed laminar flames. In *Symposium (International) on Combustion* (Vol. 14, No. 1, pp. 739-754). Elsevier.

[70] Schulz, C., Sick, V., Heinze, J., & Stricker, W. (1997). Laser-induced-fluorescence detection of nitric oxide in high-pressure flames with A–X (0, 2) excitation. *Applied optics*, *36*(15), 3227-3232.

[71] Selwyn, G. S., Herrmann, H. W., Park, J., & Henins, I. (2001). Materials processing using an atmospheric pressure, RF-generated plasma source. *Contributions to Plasma Physics*, *41*(6), 610-619.

[72] Sepman, A. V., van Essen, V. M., Mokhov, A. V., & Levinsky, H. B. (2003). Cavity ring-down measurements of seeded NO in premixed atmospheric-pressure H2/air and CH4/air flames. *Applied Physics B*, *77*(1), 109-117.

[73] Stancu, G. D., Kaddouri, F., Lacoste, D. A., & Laux, C. O. (2009, June). Investigations of rapid plasma chemistry generated by nanosecond discharges in air at atmospheric pressure using advanced optical diagnostics. In *47th AIAA Aerospace Sciences Meeting*.

[74] Stancu, G. D., Janda, M., Kaddouri, F., Lacoste, D. A., & Laux, C. O. (2009). Time-Resolved CRDS Measurements of the N2 (A3Σ u+) Density Produced by Nanosecond Discharges in Atmospheric Pressure Nitrogen and Air. *The Journal of Physical Chemistry A*, *114*(1), 201-208.

[75] Stancu, G. D., Kaddouri, F., Lacoste, D. A., & Laux, C. O. (2010). Atmospheric pressure plasma diagnostics by OES, CRDS and TALIF. *Journal of Physics D: Applied Physics*, *43*(12), 124002.

[76] Stancu, G. D., M. Simeni Simeni, and C. O. Laux. (2013). Study of nitric oxide and carbon monoxide production in plasma assisted combustion by Quantum Cascade Laser Absorption Spectroscopy. *21st ISPC.*

[77] Starikovskii, A. Y. (2005). Plasma supported combustion. *Proceedings of the Combustion Institute*, *30*(2), 2405-2417.

[78] Starikovskiy, A., & Aleksandrov, N. (2013). Plasma-assisted ignition and combustion. *Progress in Energy and Combustion Science*, *39*(1), 61-110.

[79] Sun, W., Uddi, M., Won, S. H., Ombrello, T., Carter, C., & Ju, Y. (2012). Kinetic effects of non-equilibrium plasma-assisted methane oxidation on diffusion flame extinction limits. *Combustion and Flame*, *159*(1), 221-229.

[80] Tamaki, K., Kawamura, K., Yoshida, H., Katayama, T., & Kaido, C. (1979). OXIDATION OF NITROGEN MONOXIDE BY CORONA DISCHARGE. 3. EFFECTS OF TEMPERATURE, WATER-VAPOR, SULFUR-DIOXIDE AND AMMONIA ON THE DISCHARGE OXIDATION OF NITROGEN MONOXIDE. *Nippon Kagaku Kaishi*, (11), 1597-1603.

[81] Tendero, C., Tixier, C., Tristant, P., Desmaison, J., & Leprince, P. (2006). Atmospheric pressure plasmas: A review. *Spectrochimica Acta Part B: Atomic Spectroscopy*, *61*(1), 2-30.

[82] Tholin, F., Rusterholtz, D. L., Lacoste, D. A., Pai, D. Z., Celestin, S., Jarrige, J., ... & Laux, C. O. (2011). Images of a nanosecond repetitively pulsed glow discharge between two point electrodes in air at 300 k and at atmospheric pressure. *IEEE Transactions on Plasma Science*, *39*(11), 2254.

[83] Tholin, F. (2012). *Numerical simulation of nanosecond repetitively pulsed discharges in air at atmospheric pressure: Application to plasma-assisted combustion* (Doctoral dissertation, Châtenay-Malabry, Ecole centrale de Paris).

[84] Uddi, M., Jiang, N., Adamovich, I. V., & Lempert, W. R. (2009). Nitric oxide density measurements in air and air/fuel nanosecond pulse discharges by laser induced fluorescence. *Journal of Physics D: Applied Physics*, *42*(7), 075205.

[85] Vandamme, M., Robert, E., Lerondel, S., Sarron, V., Ries, D., Dozias, S., ... & Pape, A. L. (2012). ROS implication in a new antitumor strategy based on non-thermal plasma. *International Journal of Cancer*, *130*(9), 2185-2194.

[86] Van Gessel, A. F. H., Hrycak, B., Jasiński, M., Mizeraczyk, J., Van der Mullen, J. J. A. M., & Bruggeman, P. J. (2013). Temperature and NO density measurements by LIF and OES on an atmospheric pressure plasma jet. *Journal of Physics D: Applied Physics*, *46*(9), 095201.

[87] Van Gessel, A. F. (2013). Laser diagnostics on atmospheric pressure plasma jets.

[88] Welzel, S., Gatilova, L., Röpcke, J., & Rousseau, A. (2007). Time-resolved study of a pulsed dc discharge using quantum cascade laser absorption spectroscopy: NO and gas temperature kinetics. *Plasma Sources Science and Technology*, *16*(4), 822.

[89] Welzel, S., Hempel, F., Hübner, M., Lang, N., Davies, P. B., & Röpcke, J. (2010). Quantum cascade laser absorption spectroscopy as a plasma diagnostic tool: An overview. *Sensors*, *10*(7), 6861-6900.

[90] Welzel, S., Guaitella, O., Lazzaroni, C., Pintassilgo, C. D., Rousseau, A., & Röpcke, J. (2011). NO kinetics in pulsed low-pressure plasmas studied by time-resolved quantum cascade laser absorption spectroscopy. *Plasma Sources Science and Technology*, *20*(1), 015020.

[91] Wu, L., Lane, J., Cernansky, N. P., Miller, D. L., Fridman, A. A., & Starikovskiy, A. Y. (2011). Plasma-assisted ignition below self-ignition threshold in methane, ethane, propane and butane-air mixtures. *Proceedings of the Combustion Institute*, *33*(2), 3219-3224.

[92] Wysocki, G., Kosterev, A. A., & Tittel, F. K. (2005). Spectroscopic trace-gas sensor with rapidly scanned wavelengths of a pulsed quantum cascade laser for in situ NO monitoring of industrial exhaust systems. *Applied Physics B*, *80*(4-5), 617-625.

[93] Xu, D. A., Lacoste, D. A., Rusterholtz, D. L., Elias, P. Q., Stancu, G. D., & Laux, C. O. (2011). Experimental study of the hydrodynamic expansion following a nanosecond repetitively pulsed discharge in air. *Applied Physics Letters*, *99*(12), 121502.

[94] Xu, D. (2013). *Thermal and Hydrodynamic effects of a Nanosecond Discharges in air and application to Plasma-Assited Combustion* (Doctoral dissertation, Ecole Centrale Paris).

[95] Xu, D. A., Shneider, M. N., Lacoste, D. A., & Laux, C. O. (2014). Thermal and hydrodynamic effects of nanosecond discharges in atmospheric pressure air. *Journal of Physics D: Applied Physics*, *47*(23), 235202.

[96] Yu, L., Laux, C. O., Packan, D. M., & Kruger, C. H. (2002). Direct-current glow discharges in atmospheric pressure air plasmas. *Journal of Applied Physics*, *91*(5), 2678-2686.

[97] Zhao, G. B., Garikipati, S. V. B., Hu, X., Argyle, M. D., & Radosz, M. (2005). Effect of oxygen on nonthermal plasma reactions of nitrogen oxides in nitrogen. *AIChE journal*, *51*(6), 1800-1812.

Chapter 3

Theoretical background

3.1 Introduction

The understanding of NO creation and destruction pathways in NRP discharges is a key to optimize the amount of NO released for the various applications. For this purpose, optical and electrical characterizations of the NRP discharges were performed. Here the theoretical background is given in order to:

- Extract quantities from measurements, in order to compare them with numerical modelling.

- Quantify uncertainties or/and inaccuracies introduced by the measurements methods.

Among interesting comparable quantities, the principle of the measurements of energy transferred by the discharge to the gas is presented in section 3.2. Then section 3.3 presents Mid-IR laser absorption technique in uniform environments (such as post-NRP discharge in ambient or preheated air). NRP discharge exhibits a cylindrical symmetry for temperature and NO density in the discharge, the principle of Mid-IR laser absorption measurements in axisymmetric environments is given in section 3.4. Furthermore section 3.5 describes the choice of selected absorption lines for this thesis, as well as major features of the chosen lines. Finally, using results from the previous section, section 3.6 outlines two methods for gas temperature determination.

3.2 Discharge energy measurements

The NRP discharge can be modelled as a parallel RC circuit (see figure 3.1). Essentially, before the breakdown, the two-electrodes separated by the gap act like a capacitor leading therefore to a displacement current proportional to the time derivative of the voltage difference across the electrodes. When the breakdown happens, following ionization waves propagation, charge carriers fill the gap [*Célestin*, 2008; *Pai*, 2008; *Pai et al.*, 2009]. As a result the gap becomes conductive, enabling a conduction current to pass through it. The measured current is the sum of the displacement and conduction currents:

$$I_{meas} = I_{disp} + I_{cond} \tag{3.1}$$

where I_{disp} and I_{cond} are the displacement and conduction currents, respectively. The displacement current can be declined as follows:

$$I_{disp} = C_{eq}\frac{dU}{dt} \tag{3.2}$$

where C_{eq} is the equivalent capacitance of the electrodes and U is the measured voltage across the electrodes.

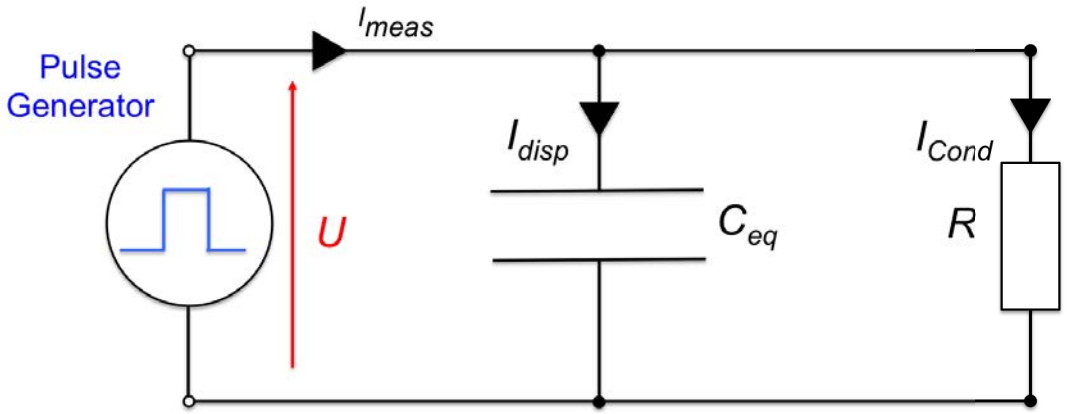

Figure 3.1: Electrical model for the filamentary discharge.

The total current *I(t)* and voltage *U(t)* signals are recorded simultaneously so that the instantaneous power *P(t)* can be determined by multiplying both signals. Sample current and voltage measurements for the NRP spark discharge are displayed in figure 3.2.

The measured current signal exhibits successively in time a peak of about 8 A, a second peak of about 18 A and then several oscillations. The oscillations result from inductive effects in the transmission line as well as from impedance mismatch between the pulse generator and the transmission line (see [*Pai*, 2008] for more details). The measured duration (FWHM) of the main current peak is about 11.5 ns. The sample voltage trace shown in figure 3.2 has an amplitude of 6.2 kV, a 6 ns rise time, a 10 ns duration at 90 % of amplitude and an 8 ns fall time. Here again one can observe the oscillations trend after the pulse.

The voltage and current signals must be synchronized. Indeed, NRP discharges have a characteristic duration of a few nanoseconds, which is comparable to the duration of signals propagation in coaxial cables of length around one meter (the speed of such

electromagnetic waves can reach 90 % of the speed of light, depending on the dieletric constant of the cable core). In addition, differences in the lengths of the cables used for voltage and current probes as well as differences in the response time of the various instruments lead to additional delays.
The procedure of synchronization consists in measuring the delay between the current signal and the time derivative of the voltage signal before the breakdown. Then, the current signal is shifted by the measured delay value in order to be phased with the time derivative of the voltage. Figure 3.3 displays the total current shifted by the measured 3.1 ns delay relative to the time derivative of the voltage trace. Moreover we observe that once the time base is adjusted, the first peak of the total NRP spark current signal and the one of the time derivative of the voltage are phased. Hence, it follows that the first peak (of about 8 A amplitude) is a capacitive peak. Owing to this identification, we can deduce the equivalent capacitance of the NRP discharge by matching the two peaks and therefore obtain the displacement (or capacitive) current using equation 3.2. This is depicted in figure 3.4. The best match is found for a 4.8 pF equivalent capacitance. Following equation 3.1, the conduction current is obtained by subtracting the displacement current from the total current. The total current, together with the deduced displacement current and calculated conduction current are displayed figure 3.4.

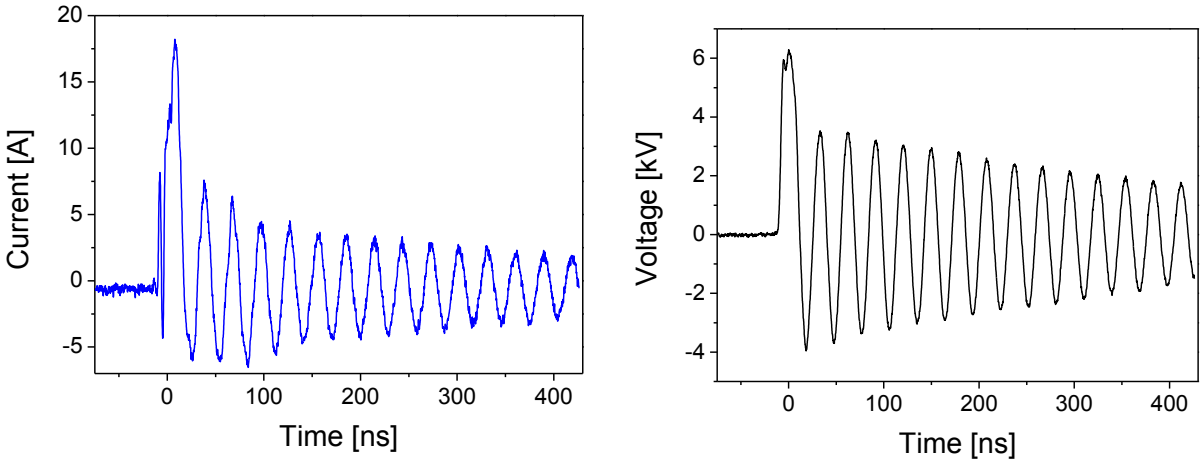

Figure 3.2: Current and voltage sample measurements. $PRF = 30$ kHz, $d = 4$ mm, $U = 6$ kV, v = 8.63 m/s.

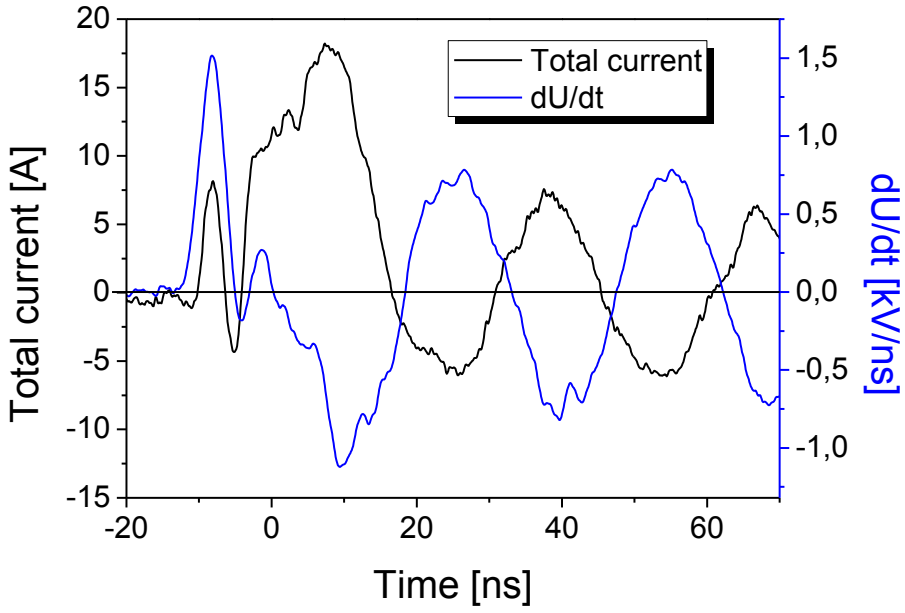

Figure 3.3: Total current synchronized with the time derivative of the voltage signal. Determination of the equivalent capacitance.

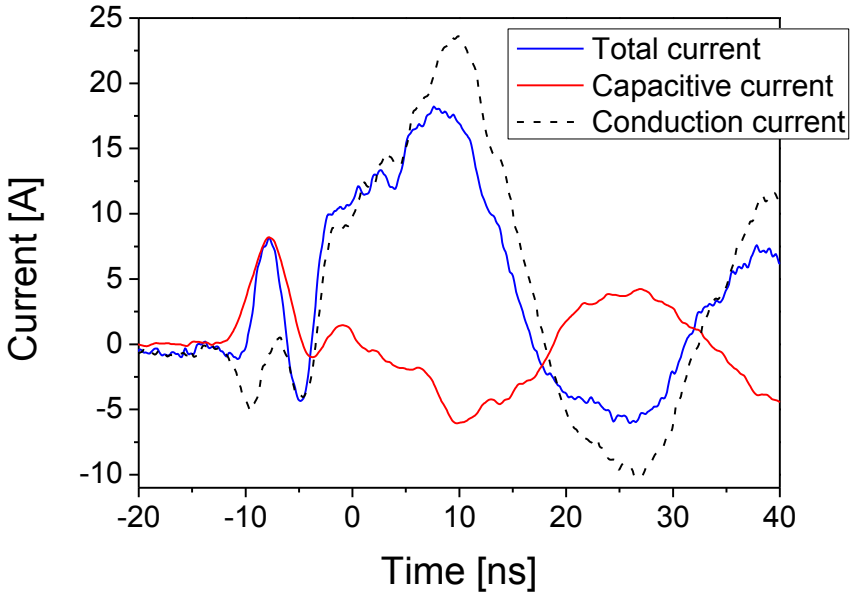

Figure 3.4: Time evolutions of the total capacitive and conduction currents. The conduction current is obtained by subtracting the capacitive current from the total current.

The instantaneous power is obtained by multiplying the voltage and the synchronized conduction current. Thereafter, integrating the instantaneous power over the pulse

duration then yields the energy deposited by the discharge in the gap during the pulse, as outlined by equation 3.3.

$$E_{pulse} = \int_{pulse} P(t)dt = \int_{pulse} U(t)I(t+\Delta t)dt \qquad (3.3)$$

Figure 3.5 shows the time evolution of the discharge power and energy. It appears that secondary pulses also give energy to the gas. This contribution can reach up to 40 % of the pulse energy for the displayed case.
The pulse energy, measured voltage and current during an NRP spark discharge pulse are summarized in figure 3.6. The energy per pulse is found to be about 1 mJ.

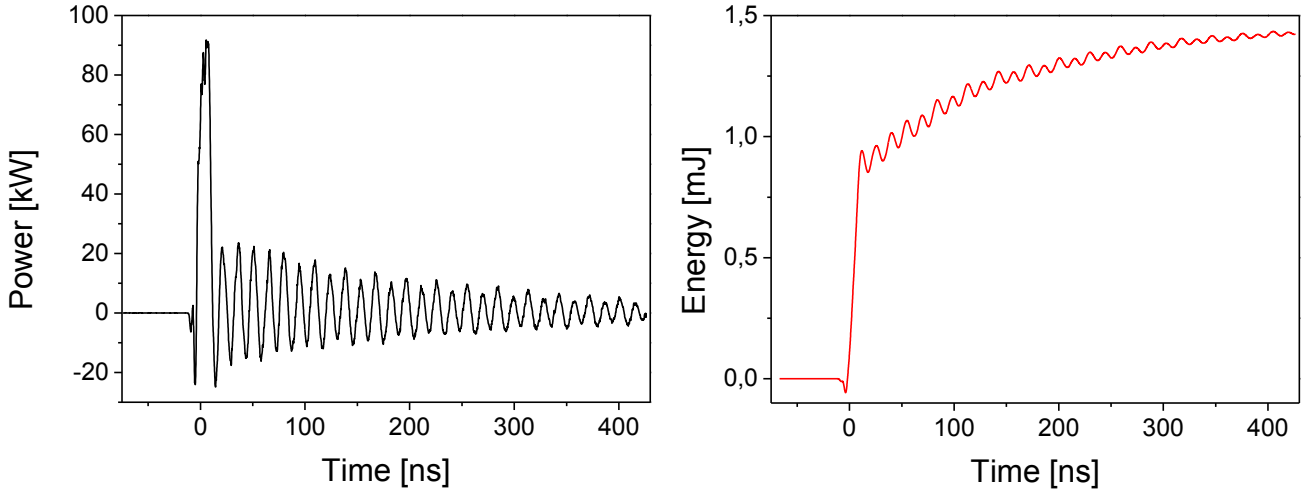

Figure 3.5: Time evolution of discharge power and energy. The instantaneous power of the discharge reaches up to 90 kW and the energy deposited in the gas is about 1.4 mJ. $PRF = 30$ kHz, $d = 4$ mm, $U = 6$ kV, v = 8.63 m/s.

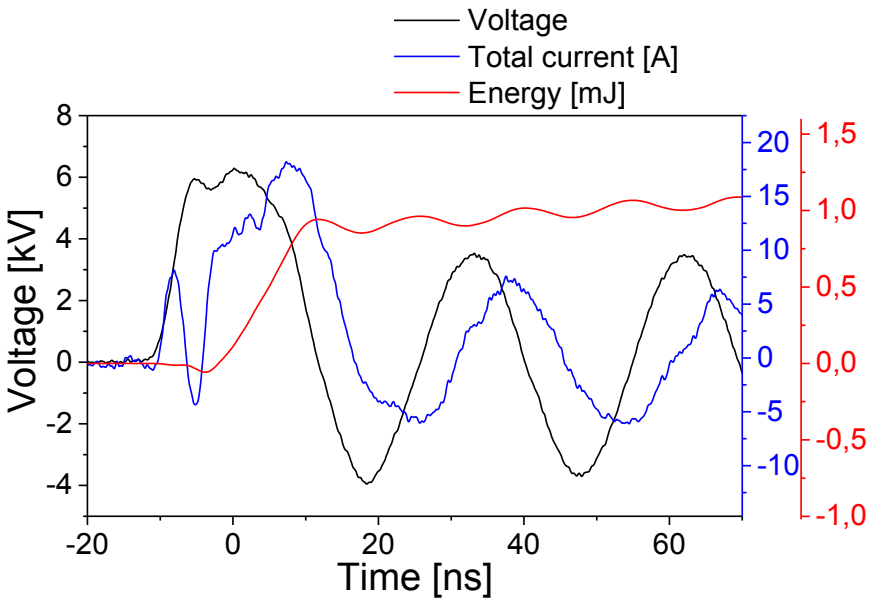

Figure 3.6: Voltage, total current and energy measured during a discharge pulse.

3.3 Mid-IR laser absorption in uniform environments

The interaction of a radiation beam with a gas sample can result in different types of phenomena:

- Photons of the beam can be deviated by gas particles with a possible change in frequency and polarization. This is referred to as **scattering.**

- Beam photons can induce the gas to emit photons with the same frequency, direction and polarization as the beam. It is called **stimulated emission**. This process increases the beam intensity.

- On the contrary, the gas sample along the beam path can also be stimulated to absorb beam photons. In this case, the beam intensity is decreased by **stimulated absorption.**

- In addition, the gas along beam optical path can spontaneously emits photons, which will increase beam intensity. It is **spontaneous emission.**

Spontaneous emission does not dependent on the beam intensity contrary to scattering, stimulated emission and stimulated absorption. Scattering can be neglected in the Mid-IR (in comparison with the UV or the visible), as it is proportional to the fourth power of the frequency. Neglecting scattering, the energy conservation along a ray gives the following radiative transfer equation [*Griem*, 2005; *Hutchinson*, 2005]:

$$\frac{dI(\nu)}{ds} = -k(\nu)I(\nu) + j(\nu) \tag{3.4}$$

where $I(\nu)$ is the frequency-dependent beam intensity, ds an elementary travelling distance, $k(\nu)$ the absorption coefficient (accounting for both stimulated emission and absorption) and $j(\nu)$ the emission coefficient. At sufficient laser intensity, spontaneous emission becomes negligible in comparison with absorption. As a result, for a homogeneous optically thin medium of absorption length L, the measured transmitted intensity through the medium is:

$$I(\nu) = I_0(\nu)\exp(-k(\nu)L) \tag{3.5}$$

This is Beer-Lambert's law, which expresses the exponential reduction with distance travelled of the incident radiation when passing through a uniform absorber, as sketched in figure 3.7. The gas sample absorption coefficient results actually from a summation over the absorption coefficients of all absorption features probed by the incident beam:

$$k(\nu) = \sum_i k_i(\nu) = \sum_i N_i\sigma_i(\nu) \tag{3.6}$$

where k_i, N_i and σ_i are the absorption coefficient, the characteristic density and the cross section of the i^{th} absorption feature, respectively.

When a narrow spectral source of radiation is used, a "single" transition between two levels (a ground and an excited state) can be probed. This consists of two features: the stimulated absorption ("positive" absorption) and the stimulated emission ("negative" absorption). In this configuration the absorption coefficient is written as follows:

$$k(\nu) = N_1\sigma_{abs}(\nu) - N_2\sigma_{emi}(\nu) = \frac{h\nu_0}{4\pi}f(\nu)(N_1B_{12} - N_2B_{21}) \tag{3.7}$$

where N_1 and N_2 are respectively the ground and excited states densities. σ_{abs} and σ_{emi} are the stimulated absorption and emission cross-sections. ν_0 is the central frequency of the transition. B_{12} and B_{21} are the Einstein coefficients for stimulated absorption and emission, respectively (this will be detailed in section 4.5.5) and $f(\nu)$ is the normalized absorption line shape function, which is centered at ν_0. Statistical weights (degeneracy factors) g_1 and g_2 of levels 1 and 2 are linked by the relation:

$$g_1 B_{12} = g_2 B_{21} \tag{3.8}$$

Equation 3.7 combined with equation 3.8 leads to:

$$k(\nu) = \sigma_{abs}(\nu)\left(N_1 - \frac{g_1}{g_2} N_2\right) \tag{3.9}$$

The first term on the right side accounts of course for stimulated absorption whereas the second one represents stimulated emission.

The absorption cross-section σ_{abs} can be defined as the product of the temperature-dependent line strength of the absorption line $S(T)$ by the normalized absorption line shape function $f(\nu\text{-}\nu_0)$:

$$\sigma_{abs}(\nu) = S(T) f(\nu - \nu_0) \tag{3.10}$$

Note that T is the temperature along the line of sight (assuming here that the system is at thermal equilibrium). Line strengths of Mid-IR nitric oxide transitions and of many others molecules at 296 K are tabulated in the HITRAN database [*Rothman et al.*, 2005]. Calculations must be carried out to determine the line strength at the appropriate temperature (see section 3.5.3).

In our investigations we use the following expression arising from the combined Beer-Lambert law (equation 3.5) with expressions 3.9 and 3.10.

$$k(\nu) = \frac{1}{L} \ln\left(\frac{I_0}{I}\right) = S(T) f(\nu - \nu_0) N \tag{3.11}$$

The spectrally integrated absorption coefficient is therefore:

$$K(T) = \int_{\nu} k(\nu) d\nu = \frac{1}{L} \int_{\nu} \ln\left(\frac{I_0}{I}\right) d\nu = N S(T) \tag{3.12}$$

For a uniform environment, the total density N is determined from measurements of $I(\nu)$ and $I_0(\nu)$:

$$N = \frac{\int_\nu \ln\left(\frac{I_0}{I}\right) d\nu}{S(T)L} \tag{3.13}$$

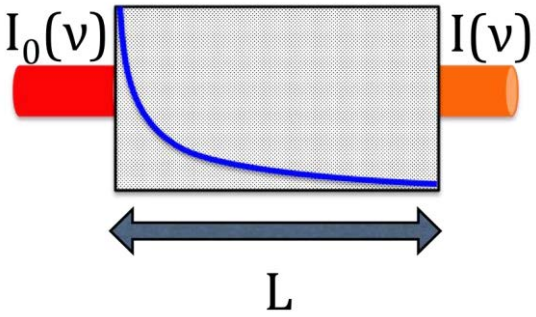

Figure 3.7: Absorption in a uniform environment. Exponential decay of the radiation intensity when passing through the absorbing medium of absorption length L.

The principle described here was applied to measurements in the post-discharge region where the gas density and the temperature are uniform due to mixing [*Stancu et al.*, 2013].

3.4 Mid-IR laser absorption in axisymmetric environments

In the previous section the principle of density measurements in a uniform absorbing medium was presented. To perform spatially resolved density measurements in non-uniform environments, local absorption coefficients $k(x, y, z)$ are needed. NRP discharges exhibit a cylindrical symmetry (see figure 4.1). The gas density and the temperature are no longer uniform over the volume but just on concentric rings of radius r. Note that NRP discharges have a typical diameter of 400 µm, which is much smaller than the spread of NO created by the discharge (up to 5 mm distance from axis) as will be shown latter. Lateral absorbance measurements $\tau(x)$ are line-of-sight integrated. For an axisymmetric, optically thin absorbing medium, radial profiles of absorption coefficient can be inferred from lateral absorbance profiles by a method called the Abel-inversion. The lateral scanning strategy is illustrated in figure 3.8.

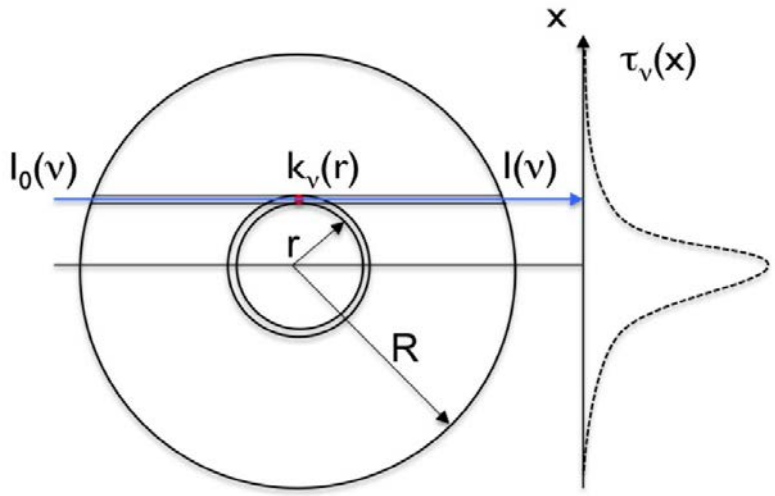

Figure 3.8: Schematic diagram for lateral scanning in spatially resolved measurements.

3.4.1 Spectrally resolved Abel inversion

At lateral position x, the line-of-sight integrated absorbance results from the summation of all the infinitely small absorbance elements $k(r)dy$ along the line of sight:

$$\tau_\nu(x) = \int_{-\infty}^{+\infty} k_\nu(r)dy = 2\int_0^{+\infty} k_\nu\left(\sqrt{x^2+y^2}\right)dy \qquad (3.14)$$

We convert the y integral into an r integral to get [*Bracewell*, 1999]:

$$\tau_\nu(x) = 2\int_0^{+\infty} k_\nu(r)\frac{r}{(r^2-x^2)^{\frac{1}{2}}}dr = 2\int_0^{R} k_\nu(r)\frac{r}{(r^2-x^2)^{\frac{1}{2}}}dr \qquad (3.15)$$

where R is a radial position far from discharge center, such that k(R)=0, τ(R)=0.

The spectrally resolved radial absorption coefficient is related to the spectrally resolved lateral absorbance by the inverse Abel transform:

$$k_\nu(r) = -\frac{1}{\pi}\int_r^R \frac{d\tau_\nu(x)}{dx}\frac{dx}{(x^2-r^2)^{\frac{1}{2}}} \qquad (3.16)$$

3.4.2 Spectrally integrated Abel inversion

From equation 3.16, the spectrally integrated radial absorption coefficient can therefore be derived as:

$$\int_{\nu_1}^{\nu_2} k_\nu(r)d\nu = -\frac{1}{\pi}\int_{\nu_1}^{\nu_2}\left(\int_r^R \frac{d\tau_\nu(x)}{dx}\frac{dx}{(x^2-r^2)^{\frac{1}{2}}}\right)d\nu \quad (3.17)$$

Here ν_1 and ν_2 are the lower and upper wavenumber limits of the spectral integration selected upon the criterion that the spectrally resolved radial absorption coefficient is zero at these limits. Then applying successively Fubini's theorem (to switch the order of integration) and Leibniz integral rule (to derive the equality with the differentiation under the integral sign) yields:

$$\int_{\nu_1}^{\nu_2} k_\nu(r)d\nu = -\frac{1}{\pi}\int_r^R \frac{d\left(\int_{\nu_1}^{\nu_2}\tau_\nu(x)d\nu\right)}{dx}\frac{dx}{(x^2-r^2)^{\frac{1}{2}}} \quad (3.18)$$

Thereafter, if the radial temperature distribution $T(r)$ is known, then the radial species density can be inferred from the radial absorption coefficient:

$$N(r) = \frac{\int_\nu k_\nu(r)d\nu}{S(T(r))} \quad (3.19)$$

Therefore, to obtain local densities, we can either choose to apply the inverse transform to the spectrally resolved absorbance measurements (equation 3.16) or to the spectrally integrated ones (equation 3.18). In the latter case the spectral information is lost. Both integration strategies will be applied in chapter 5 for spatially resolved gas temperature and nitric oxide density determinations.

Nevertheless the singularity of both equations 3.16 and 3.18 at $x = r$ and their dependence on the first derivative of measured absorbance, which implies smoothing the data to avoid discontinuities are two major problems posed by Abel inversion algorithms. Another problem, which arises from equation 3.16 is the finite number of measurements absorbance point measurements. Therefore integral calculation requires an interpolation scheme of raw data.

Cremers and Birkebak, [1966] reported two general categories of methods to compute equation 3.16:

- **Analytical methods**, which allow direct integration of Abel inversion by fitting experimental data to an analytical function. In this case, the analytical function must be chosen carefully to reproduce the raw data accurately.

- **Numerical methods**, which use transformed forms of the Abel inversion equation into summation in order to be able to compute discrete sets of data. These methods tend to be more sensitive to data scatter.

Cremers and Birkebak, [1966] compared several inversion techniques and pointed out the advantage of the polynomial least-square curve fitting methods in comparison with exact fitting techniques. A notable advantage of polynomial fits is that they permit the calculation of uncertainty propagation, which can be in this case analytically performed. Later in the time, *Smith et al.*. [1988] reformulated Abel inverse transforms in terms of Fourier and Hankel integral transforms and showed that the new expression was singularity and derivative-free besides being faster to compute and noise filtered.

In the present work the Fourier approach of *Pretzler*, [1991] was employed. It consists in using a Fourier-series-like expansion of the unknown radial distribution. It should be noted that in our experiments, the axis of symmetry was experimentally determined by joining the anode and cathode tips and verifying that no laser signal was transmitted. Then lateral measurements were performed on a half-profile. Many reasons motivated our choice of the Pretzel's approach. First, it is derivative-free, thus it reduces sensitivity to measurements errors. Second, the method can be used as a noise-filter by choosing upper and lower frequency limits (UPF and LOF) to reduce the noise and thus smooth the data. Third, the computer time, (which is strongly dependent on the UPF value) required to invert a half-set of 600 points is on the order of 10 seconds at UPF=10 (and 100 s at UPF=100). Finally to reduce effects of under sampling, measurements data were interpolated by fifth order polynomial prior to Abel inversion treatment. A validation of the used method is presented in appendix A.

3.5 Choice of lines of interest and analysis of absorption lines profiles

This section deals with the physics of the selected lines profiles (in terms of lines strengths and lines widths) with respect to the temperature. The gained knowledge will be used in section 3.6 to derive two methods for gas temperature determination in the NRP discharge. But first, we examine how to choose the lines.

3.5.1 Selection of spectral lines

Equation 3.13 states that the system's sensitivity (i.e. its ability to detect small particle densities) can be improved by increasing the product of the line strength *S(T)* by the length of absorption *L*. High-L will be achieved using a multiple pass (or multipass) absorption cell. We also choose the NO line with the strongest line strength for our laser spectral range available. In addition, the selected line should not spectrally overlap with lines from other combustion species (H_2O, CH_4 and CO_2). Simulations using HITRAN and HITEMP [*Rothman et al.*, 2010] databases (for room temperature and high temperature respectively) are presented in figures 3.9 and 3.10. Simulations at room temperature are for NO detection in the post-NRP discharge in ambient air whereas simulations at high temperature are for measurements in combustion environments or in preheated air. At stoichiometric conditions, the typical composition of methane-air combustion products is 20 % of water vapour, 10 % of CO_2 and gas temperature over 1000 K.

The NO absorption line at 1900.076 cm^{-1} has high line strength at room temperature (see figure 3.9) and exhibits less overlapping with combustion species at high temperature (see figure 3.10). For these reasons this line was chosen for NO measurements. This line corresponds to a rovibrational transition between the vibrational levels $\nu = 0$ and $\nu = 1$ in NO ground-state (NO X $^2\Pi$): ($X_{1/2}$, ν=0)→ ($X_{1/2}$, ν=1) R(6.5). For the purpose of gas temperature determination while performing spatially resolved NO density measurements in the NRP discharge, we adjoined a second line at 1900.517 cm^{-1}, which has good line strength too at room temperature. It corresponds to the ($X_{3/2}$, ν=0)→ ($X_{3/2}$, ν=1) R(6.5) transition.

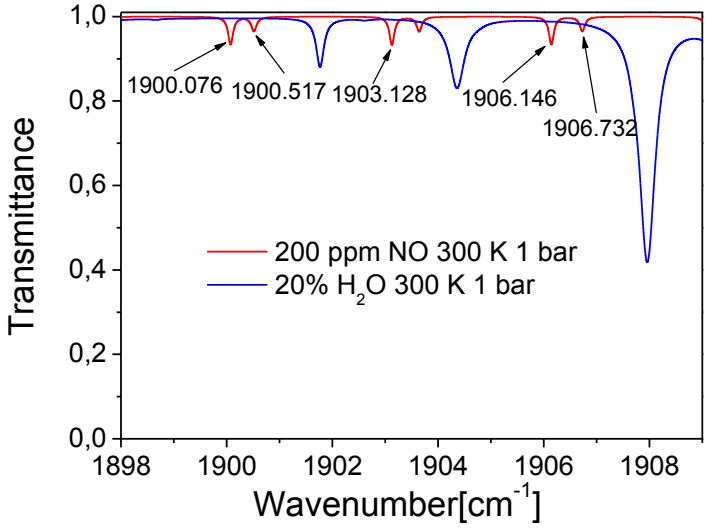

Figure 3.9: HITRAN simulations at room temperature. No superimposition between water and NO lines at 1900.076 and 1900.517 cm^{-1}. The useful spectral range of our laser is between 1899 and 1909 cm^{-1}.

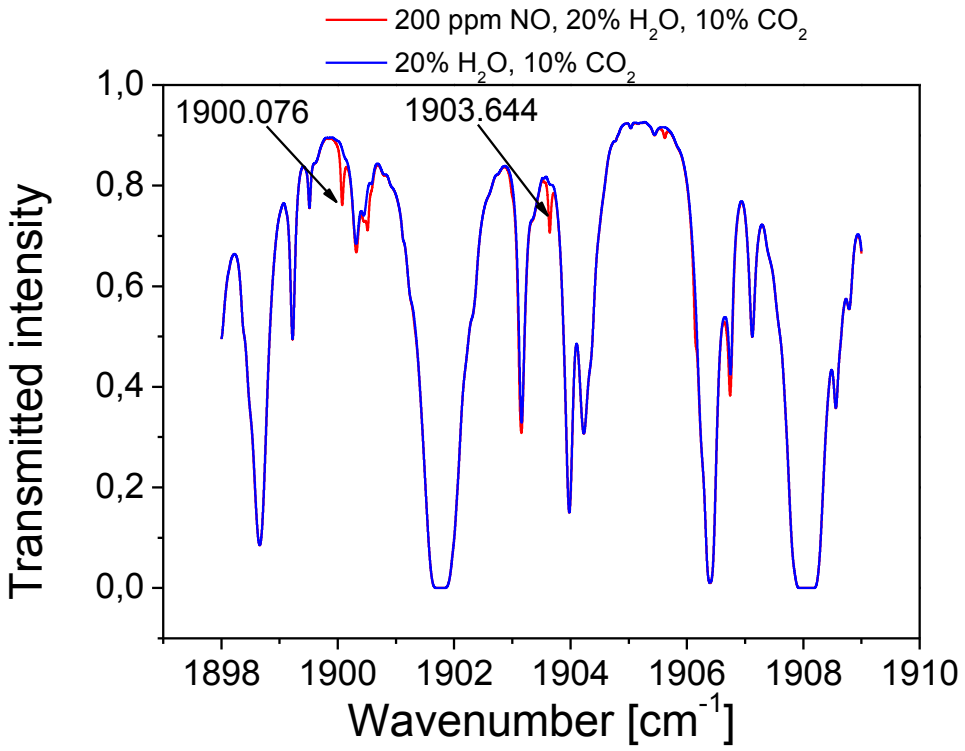

Figure 3.10: HITEMP simulations at 1000 K and 1bar. NO detection is feasible at 1900.076 cm^{-1}.

3.5.2 NO ground-state

Since the major fraction of the particles is in the ground state (assuming a Boltzmann distribution at equilibrium for the investigated range of gas temperatures), we conducted experiments to measure absolute densities of NO-ground state (NO ($X\ ^2\Pi$)).

The spin-orbit coupling (LS coupling) between the electronic spin angular momentum (S = ½) and the electronic angular momentum (L = 1) splits the ground state into two states: $\Pi_{1/2}$ and $\Pi_{3/2}$. Electrons spin orientation in parallel or anti-parallel directions with respect to the orbital angular momentum gives rise to the two foregoing configurations. Both electronic configurations are subdivided in vibrational states with vibrational quantum numbers v and rotational states with rotational quantum numbers J. J is the total angular momentum and takes the values J=0.5, 1.5, 2.5... The rotational energy levels of NO ground state as described by Hund's coupling case (a) [*Herzberg*, 1950] and the exploited transitions are displayed in figure 3.11.

The HITRAN database provides the hyperfine rotational structure of the energy levels. They consist in closely separated pairs of opposite parity (e and f), which are themselves made of six components each. As a result, transitions $R(6.5)_{1/2}$ and

$R(6.5)_{3/2}$ in the band (v = 1← v = 0) consists in twelve components each. A plot of both lines fine structure is presented in figure 3.12. Tables 3.1 and 3.2 respectively summarize features the hyperfine structure components of lines 1 and 2.
Figure 3.13 shows the selected lines for various combinations of instrumental broadening and pressure. Laser spectral width of the laser was found to be 6 x 10^{-3} cm^{-1} and simulations were performed using a Gaussian instrumental function with this FWHM. At low pressure, with a negligible instrumental broadening the e and f components of the line at 1900.076 cm^{-1} are resolved, whereas the components of the line at 1900.517 cm^{-1} merge. Moreover considering laser broadening, the transmittance at peak decreases and the spectral profiles are wider, in order to preserve the area under the curves (which can be regarded as an image of particles density). Finally, at atmospheric pressure all the twelve components are merged for both lines. Furthermore, pressure broadening at atmospheric pressure results in much wider Lorentzian profiles.

Table 3.1: Components of the line at 1900.076 cm^{-1}. (HITRAN datase).

Transition [cm^{-1}]	**Line intensity [cm]**	**Lower level energy [cm^{-1}]**	**Transition type**
1900.070578	2.028E-20	80.21880	R 6.5e
1900.070593	2.322E-20	80.21880	R 6.5e
1900.070596	1.770E-20	80.21880	R 6.5e
1900.072052	3.670E-22	80.21880	R 6.5e
1900.072147	3.670E-22	80.21880	R 6.5e
1900.073620	1.638E-24	80.21880	R 6.5e
1900.077163	1.638E-24	80.30030	R 6.5f
1900.079250	3.669E-22	80.30030	R 6.5f
1900.079550	3.669E-22	80.30030	R 6.5f
1900.081594	2.322E-20	80.30030	R 6.5f
1900.081628	1.769E-20	80.30030	R 6.5f
1900.081636	2.027E-20	80.30030	R 6.5f

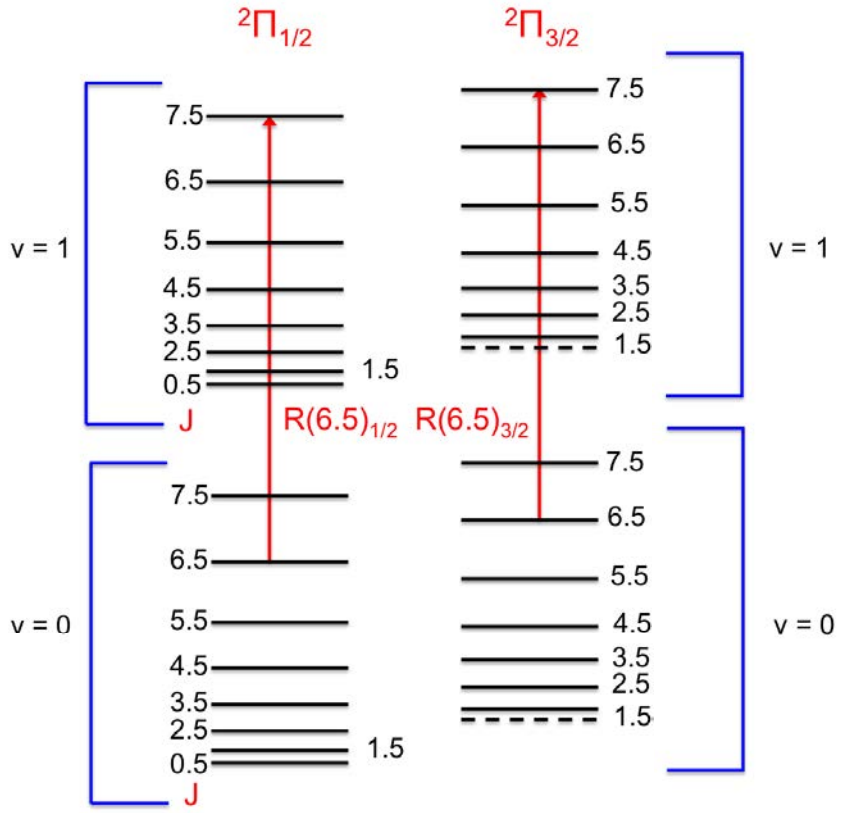

Figure 3.11: Rotational energy levels of the NO ground state.

Table 3.2: Components of the line at 1900.517 cm^{-1}. (HITRAN datase).

Transition [cm^{-1}]	Line intensity [cm]	Lower level energy [cm^{-1}]	Transition type
1900.516490	8.730E-25	202.29840	R 6.5e
1900.516783	1.956E-22	202.29840	R 6.5e
1900.516903	1.956E-22	202.29840	R 6.5e
1900.517093	1.238E-20	202.29840	R 6.5e
1900.517185	8.730E-25	202.30010	R 6.5f
1900.517196	1.080E-20	202.29840	R 6.5e
1900.517276	9.429E-21	202.29840	R 6.5e
1900.517453	1.956E-22	202.30010	R 6.5f
1900.517688	1.956E-22	202.30010	R 6.5f
1900.517870	1.238E-20	202.30010	R 6.5f
1900.517956	1.080E-20	202.30010	R 6.5f
1900.518033	9.429E-21	202.30010	R 6.5f

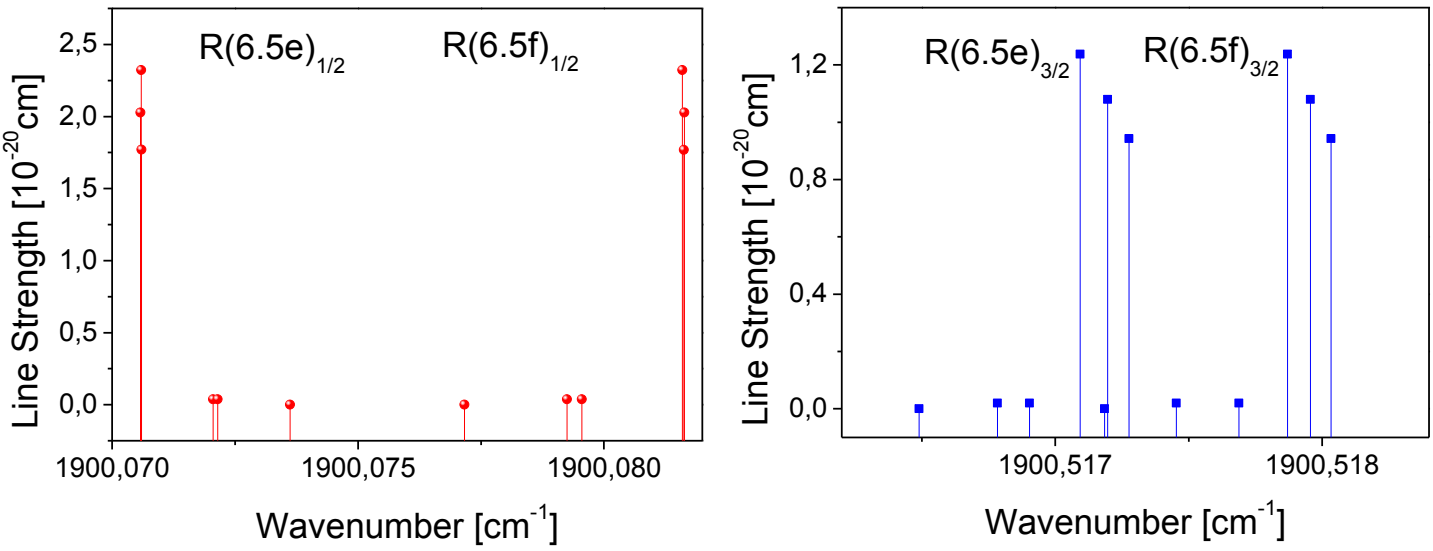

Figure 3.12: Fine structures of the lines 1900.076 cm^{-1} and 1900.517 cm^{-1}. Twelve components each.

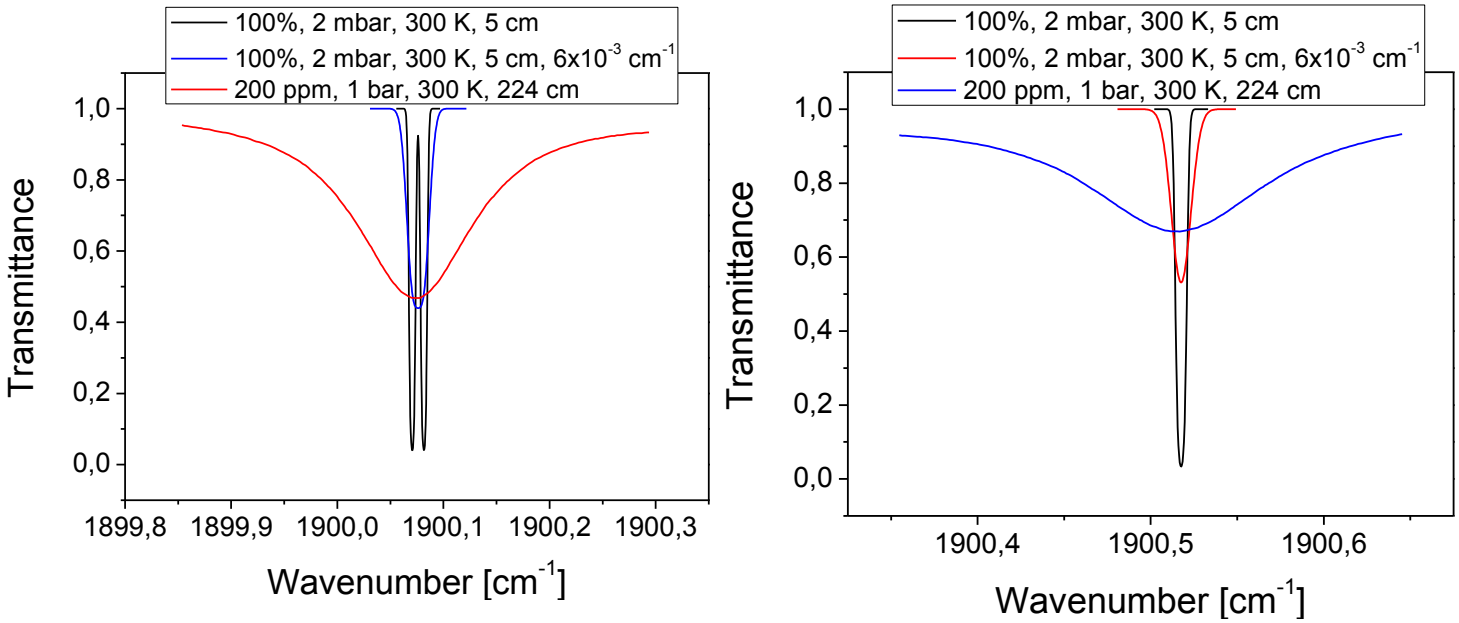

Figure 3.13: HITRAN simulation of both lines. Effects of laser and pressure broadening.

3.5.3 Lines strengths evolution with temperature

From equation 3.13, the NO absolute density (in the case of a uniform environment) is inferred from the knowledge of the area under the absorbance spectrum, the length of absorption and the line strength (also called line intensity) at the measured gas temperature. The area under the absorbance spectrum is calculated directly from absorbance measurements, length of absorption is deduced from the knowledge of the number of passes. But the calculation of the line intensity as a function of gas temperature must be carried out. This also applies for measurements in an axisymmetric environment with the difference this time that the temperature field must be known radially as requested by equation 3.19.

The spectral line intensity between two states of a vibrational-rotational system is defined by radiative transfer theory [*Penner*, 1959] as:

$$S_{12} = \frac{h\nu_{12}}{c}\frac{n_1}{N}\left(1 - \frac{g_1 n_2}{g_2 n_1}\right)B_{12} \tag{3.20}$$

where n_1 and n_2 are the population of the lower and upper states, respectively, g_1 and g_2 are the statistical weights, N is the molecular number density and B_{12} (here in $cm^3/(ergs\ s^2)$) is the Einstein coefficient for stimulated absorption. The term in parentheses accounts for the effect of stimulated emission.
Assuming local thermodynamic equilibrium at temperature T, the populations of the lower and upper states follow a Boltzmann distribution:

$$\frac{n_1}{N} = \frac{g_1 e^{-\frac{c_2 E_1}{T}}}{Q(T)} \qquad \frac{g_1 n_2}{g_2 n_1} = e^{-\frac{c_2 \nu_{12}}{T}} \tag{3.21}$$

where E_1 is the lower state energy in cm^{-1}, c_2 is the second radiation constant ($c_2 \approx 1.44$ cm. K) and Q(T) the Total Internal Partition Sum (TIPS), which is given by:

$$Q(T) = \sum_{\eta} g_\eta e^{-\frac{c_2 E_\eta}{T}} \tag{3.22}$$

where η represents the index of lower energy states. $Q(T)$ represents the number of quantum states thermally accessible to the molecular system. Incorporating equations 3.22 and 3.21 into equation 3.20 yields the line intensity as a function of the temperature and of the Einstein stimulated absorption coefficient:

$$S_{12}(T) = \frac{h\nu_{12}}{c} g_1 \frac{e^{-\frac{c_2 E_1}{T}}}{Q(T)} (1 - e^{-\frac{c_2 \nu_{12}}{T}}) B_{12} \tag{3.23}$$

Using the Einstein spontaneous emission coefficient (in s^{-1}) listed in the HITRAN database for rovibrational transitions, we can express the line intensity as follows:

$$S_{12}(T) = \frac{1}{8\pi c \nu_{12}^2} g_2 \frac{e^{-\frac{c_2 E_1}{T}}}{Q(T)} (1 - e^{-\frac{c_2 \nu_{12}}{T}}) A_{21} \tag{3.24}$$

The latter expression results from the relation between B_{12} and A_{21}:

$$B_{12} = \frac{1}{8\pi h \nu_{21}^3} \frac{g_2}{g_1} A_{21} \tag{3.25}$$

Equation 3.24 is sufficient to carry out line strength calculations on individual rotational-vibrational transitions using the data provided by HITRAN. But since in addition to transitions wavenumbers (in cm^{-1}), Einstein spontaneous emission coefficients (in s^{-1}) and statistical weights, HITRAN also provides line strength at 296 K. It is then convenient to derive the line intensity as a function of temperature as follows:

$$S_{12}(T) = S_{12}(T_{ref}) \frac{Q(T_{ref})}{Q(T)} \frac{e^{-\frac{c_2 E_1}{T}}}{e^{-\frac{c_2 E_1}{T_{ref}}}} \frac{1 - e^{-\frac{c_2 \nu_{12}}{T}}}{1 - e^{-\frac{c_2 \nu_{12}}{T_{ref}}}} \tag{3.26}$$

The first term of the product is the line intensity at 296 K, the second one is the ratio of TIPS, the third term is related to the ratio of Boltzmann populations and the fourth one accounts for stimulated emission. As the temperature increases, both second and fourth terms decrease but at the same time the third term of the previous expression increases. Actually, for $T > T_{ref}$, $Q(T) > Q(T_{ref})$ as more internal states are thermally accessible, the population of the lower state decreases with increasing temperature and the increase of the upper state population leads to a decrease of stimulated emission factor (see figure B.2 of appendix B for an example of compared contributions).

Apart from the ratio of TIPS, other terms are easily computable. Then since the line strength is additive, contributions of the twelve line components can be summed to

yield the line intensity at atmospheric pressure. Nevertheless, we first need to calculate the second term, which is fortunately the same for all the components.
Assuming separability of electronic, vibrational and rotational energies of the molecule, Q(T) can be approximated as the product of electronic, vibrational and rotational partition sums:

$$Q(T) = Q_{el}(T)Q_{vib}(T)Q_{rot}(T) \tag{3.27}$$

For large molecules with fine structure spectrally resolvable, a nuclear spin partition function may appear in the product [*Stancu et al.*, 2005]. Analytical calculations of the evolution with temperature of the TIPS and both selected line intensities are performed in appendix B.

In the present work, the line strengths were calculated as a function of the gas temperature using the HITRAN and HITEMP-based Q-MACS simulation tool, which is based on the total internal partition sum calculated by the TIPS program [*Fischer et al.*, 2003] integrated into the HITRAN package. From equation 3.13 we know that the line intensity is related to the particle density N by:

$$S(T) = \frac{\int_{\tilde{\nu}} \ln\left(\frac{I_0}{I}\right) d\tilde{\nu}}{NL} \tag{3.28}$$

By simulating absorbance spectra at different temperatures for fixed length of absorption, pressure and density, we obtain the line strength as a function of gas temperature. Note that these simulations were carried out at low pressure to minimize errors due to calculation of the area under absorbance curves (overlapping issues at high pressure, see section 3.5.4). Some absorbance simulations are presented in figure 3.14 and results for both lines are displayed in figure 3.15. The intensities of both lines decrease with increasing temperature. More specifically, for the transition at 1900.076 cm^{-1}, the line intensity decreases by more than a factor 3 from room temperature to 1400 K whereas transition at 1900.517 cm^{-1} decreases by a factor of 2 for the same range of temperature.

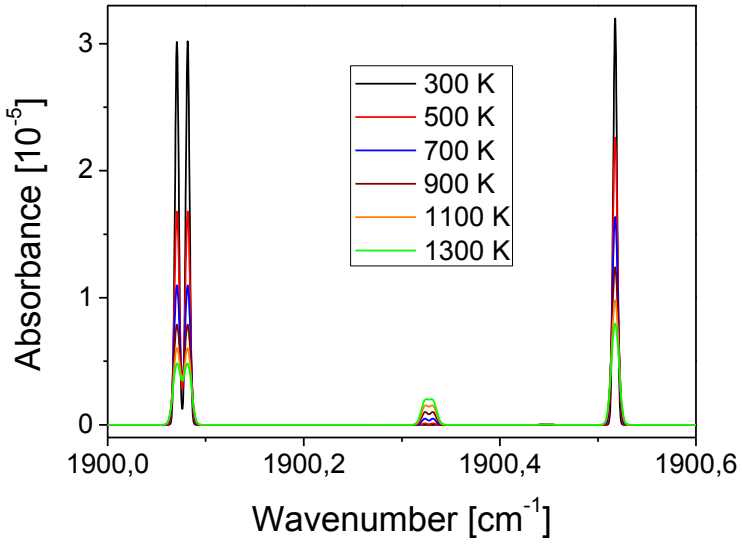

Figure 3.14: Absorbance spectra of both transitions for temperatures from 300 to 1300 K. $P = 1$ mbar, $L = 1$ mm, $N = 2.45$ x 10^{13} cm^{-3}.

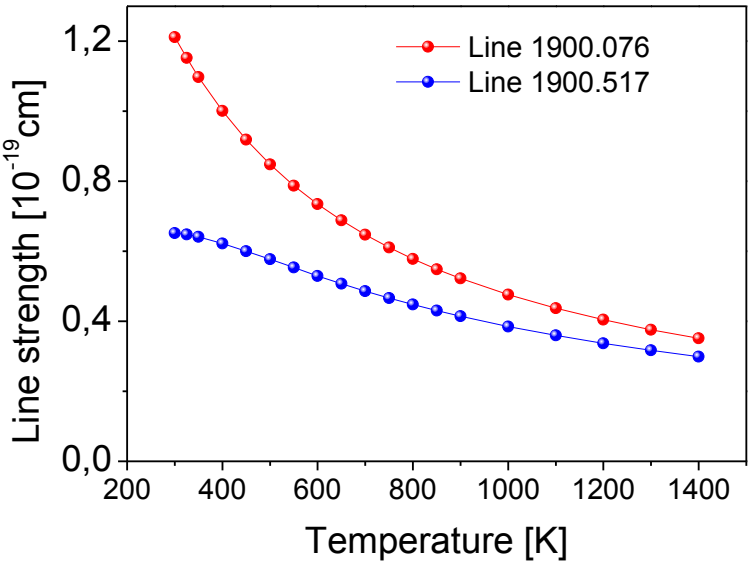

Figure 3.15: Line intensities decrease with rising temperature.

3.5.4 FWHM temperature dependency

Absorption features measured previously result from convolved spectra between the spectral profile of the laser, the absorption profiles of target molecules, and the spectral response of the detectors. Even with a spectrally narrow laser, measured lines would have not been Dirac. They are broadened by different mechanisms:

- **Natural broadening** is the intrinsic uncertainty (in wavelength) of a monochromatic source emitting at central wavelength λ_0. It results from the Heisenberg's uncertainty principle:

$$\Delta E \Delta t \geq \hbar \tag{3.29}$$

Last equation means that the lowest broadening is obtained at equality:

$$\begin{aligned} \Delta(hc\tilde{\nu})\Delta t &= \hbar \\ \Rightarrow \Delta\tilde{\nu} &= \frac{1}{2\pi c \Delta t} \end{aligned} \tag{3.30}$$

It follows that the line is actually broadened by the finite lifetime Δt of the radiating excited level [*Hutchinson*, 2005]. Since the excited level's population decays exponentially in time, the corresponding spectral line shape is a Lorentzian profile. In general, natural broadening is the smallest of the involved broadening mechanisms in plasma spectroscopy [*Griem*, 2005].
For a transition between an upper state with energy E_u and a lower state with energy E_l, the transition frequency is defined by:

$$\nu_{ul} = \frac{E_u - E_l}{h} \tag{3.31}$$

Differentiating the latter expression yields the uncertainty in the transition frequency:

$$\Delta\nu_{lu} = \Delta\nu_{ul} = \frac{\Delta E_u + \Delta E_l}{h} \tag{3.32}$$

Then applying Heisenberg uncertainty principle successively to the upper and lower states of lifetimes Δt_u and Δt_l leads to:

$$\Delta E_{u,l} \Delta t_{u,l} \sim \hbar \tag{3.33}$$

Combining equations 3.32 and 3.33 results in [*Penner*, 1959]

$$\Delta\nu_{ul} = \frac{1}{2\pi}\left(\frac{1}{\Delta t_u} + \frac{1}{\Delta t_l}\right) = \frac{1}{2\pi}(A_u + A_l) \tag{3.34}$$

A_u and A_l are the reciprocal lifetimes (or more conveniently, Einstein coefficients for spontaneous emission) of the upper and lower states. As a result, the uncertainty in the transition frequency is proportional to the sum of the upper and lower states Einstein coefficients for spontaneous emission. In terms of wavenumbers expression 3.34 is equivalent to:

$$\Delta\tilde{\nu}_{ul} = \frac{1}{2\pi c}(A_u + A_l) \tag{3.35}$$

The HITRAN database rather reports transitions Einstein coefficients for spontaneous emission of rotational line components instead of upper and lower states Einstein coefficients. An average value over all the sub-states must be therefore calculated [*Gamache*, 1992; *Šimečková*, 2006]:

$$A_{u\to l} = \frac{1}{d_u}\sum_{j,i} A_{uj\to li} \tag{3.36}$$

where d_u is the degeneracy (2J+1) of the upper state. Table 3.4 summarises Einstein spontaneous coefficients for both transitions sub-states.

Table 3.4: Einstein coefficients of rotational components of selected lines.

Line transition [cm^{-1}]	**A$_i$ [s^{-1}]**
1900.070578	5.851
1900.070593	5.955
1900.070596	5.837
1900.072052	1.210E-01
1900.072147	1.059E-01
1900.073620	5.401E-04
1900.077163	5.403E-04
1900.079250	1.059E-01
1900.079550	1.210E-01
1900.081594	5.958
1900.081628	5.836
1900.081636	5.851

Line transition [cm^{-1}]	A_i [s^{-1}]
1900.516490	5.213E-04
1900.516783	1.022E-01
1900.516903	1.168E-01
1900.517093	5.750
1900.517185	5.213E-04
1900.517196	5.643
1900.517276	5.631
1900.517453	1.022E-01
1900.517688	1.168E-01
1900.517870	5.750
1900.517956	5.643
1900.518033	5.631

The resulting FWHM is about 1.18 x 10^{-11} cm^{-1} at 1900.076 cm^{-1} and 1.13 x 10^{-11} cm^{-1} at 1900.517 cm^{-1}. We will see that these values are negligible with respect to the other forms of broadening.

- **Doppler broadening** results from the Doppler shift due to absorbing particles motion:

$$\frac{\Delta\tilde{\nu}}{\tilde{\nu}_0} = \frac{v}{c} \tag{3.37}$$

where v is the particle velocity along the line of sight and c the speed of light. A Maxwellian velocity distribution leads to a Gaussian line shape with a FWHM of:

$$\Delta\tilde{\nu} = 2\sqrt{\ln 2}\left(\frac{2k_BT}{mc^2}\right)^{1/2}\tilde{\nu}_0 \tag{3.38}$$

Doppler broadening is therefore dependent on the absorbing particle's temperature T and mass m. Assuming LTE, the absorbing particle temperature and the gas temperature are equal, so that equation 3.38 can be turned into:

$$\Delta\tilde{\nu}_{Doppler} = 7.162 \times 10^{-7}\tilde{\nu}_0\sqrt{\frac{T}{M}} \tag{3.39}$$

where T is the gas temperature and M, the molar mass (in g/mole) of the absorbing species. The FWHM of Doppler broadened NO lines as a function of gas temperature is presented in figure 3.16.

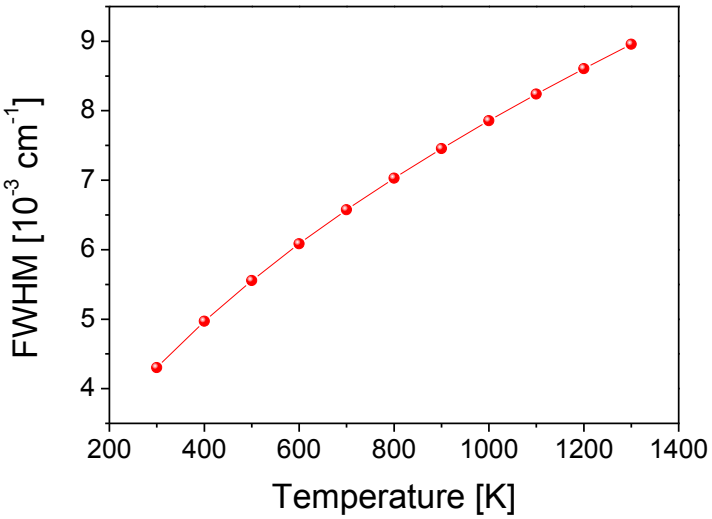

Figure 3.16: Evolution with respect to temperature of the FWHM of a NO Doppler-broadened line. Doppler FWHM is about 4.33 x 10^{-3} cm^{-1} at room temperature and around 9 x 10^{-3} cm^{-1} at 1300 K.

- **Pressure broadening** also named collisional broadening: it results from the influence of neighboring particles upon the absorbing species. It can be described by the "impact approach" (Lorentz's approach): collisions interrupt the wave train of radiating particles. Then, as for the natural broadening, reducing the lifetime of the absorber results in a broadened Lorentzian spectral line shape. The pressure broadened line HWHM for a gas at pressure P (in atm), temperature T (in K) and partial pressure P_s (in atm) in air, is given by [*Rothman et al.*, 1998]:

$$\Delta\tilde{\nu} = \left(\frac{T_{ref}}{T}\right)^{n}\left(\Delta\tilde{\nu}_{air}(P - P_s) + \Delta\tilde{\nu}_{self}P_s\right) \qquad (3.40)$$

where T_{ref} = 296 K, n is the coefficient of temperature dependence of the air-broadened halfwidth. $\Delta\nu_{air}$ is the air-broadened HWHM (cm^{-1}/atm) at 296 K and at atmospheric pressure and $\Delta\nu_{self}$ is the air-broadened HWHM (cm^{-1}/atm) at 296 K and at atmospheric pressure . Both parameters can be found in the HITRAN and HITEMP databases.

One can observe that this broadening is the summation of two broadening mechanisms, namely: **Van der Waals mechanism,** which is inducted by different

particles than the absorbing ones (it is the first term of the summation in brackets) and **resonant mechanism**, which corresponds to collisions of absorbing particles with like particles. Both the Van der Waals and resonant mechanisms depend on gas pressure, temperature, absorbing particles mole fraction and radiating transition. Since we are dealing with low nitric oxide mole fractions, in air at atmospheric pressure, the NO partial pressure that appears in equation 3.40 is negligible and we can write at $P = 1$ atm:

$$\Delta\tilde{\nu} = \left(\frac{T_{ref}}{T}\right)^{n} \Delta\tilde{\nu}_{air} \tag{3.41}$$

The HITRAN database reports a HWHM (at 296 K and atmospheric pressure) of 0.0559 cm^{-1} (i.e. a FWHM of 0.1118 cm^{-1}) and a temperature-dependence exponent n of 0.69 for the line at 1900.076 cm^{-1} and respectively 0.059 cm^{-1} (i.e. a FWHM of 0.118 cm^{-1}) and 0.67 for the transition at 1900.517 cm^{-1} (see table 3.5). Table 3.5 below summarizes the broadening parameters of both lines.

Table 3.5: Pressure broadening parameters of the two lines considered in this work.

Transition [cm^{-1}]	**HWHM [cm^{-1}]**	**Temperature exponent**
Line at 1900.076	0.0559	0.69
Line at 1900.517	0.059	0.67

Equation 3.41 can hence be computed to yield theoretical pressure broadened FWHMs as a function of the gas temperature. The results are displayed in figure 3.17. The collisional broadening of the lines decreases with increasing gas temperature.

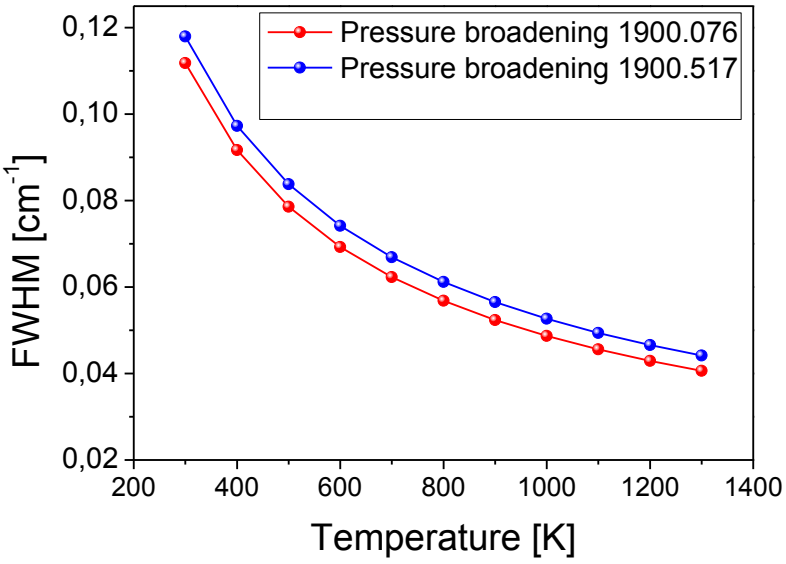

Figure 3.17: Temperature dependence of the theoretical pressure broadening of both lines. Lines narrow with increasing temperature.

At atmospheric pressure, the wings of adjacent transitions may overlap, and this is the case for the two lines at 1900.076 and 1900.517 cm^{-1}, as shown in figure 3.18. We therefore adopt the strategy of fitting the measurements with a sum of two Lorentzians as shown in figure 3.19. Absorbance simulations were performed at different temperatures as depicted in figure 3.20. Comparison between global fitting results and separate fits for both lines are presented in figure 3.21. If the overlapping is neglected, the maximum error is less than 7 % for both features as shown in figure 3.22.

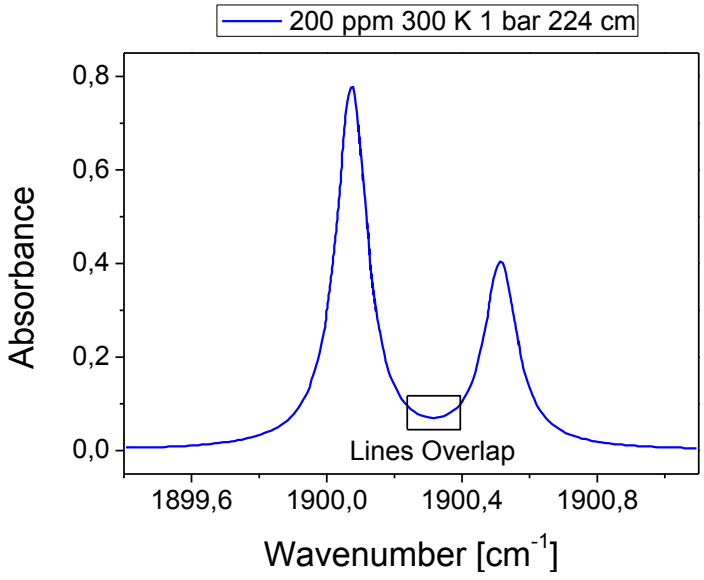

Figure 3.18: Transitions overlap at atmospheric pressure.

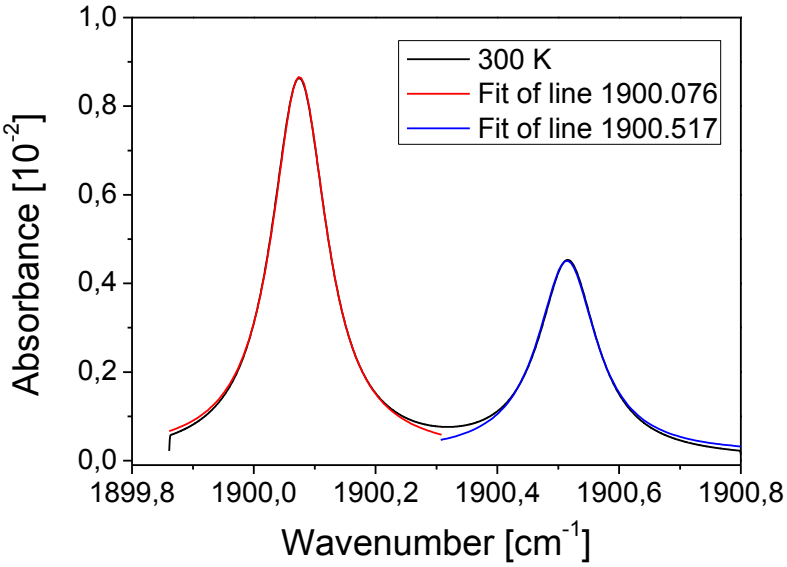

Figure 3.19: Fitting strategy at atmospheric pressure. 200 ppm of NO at 300 K and 5 cm absorption length.

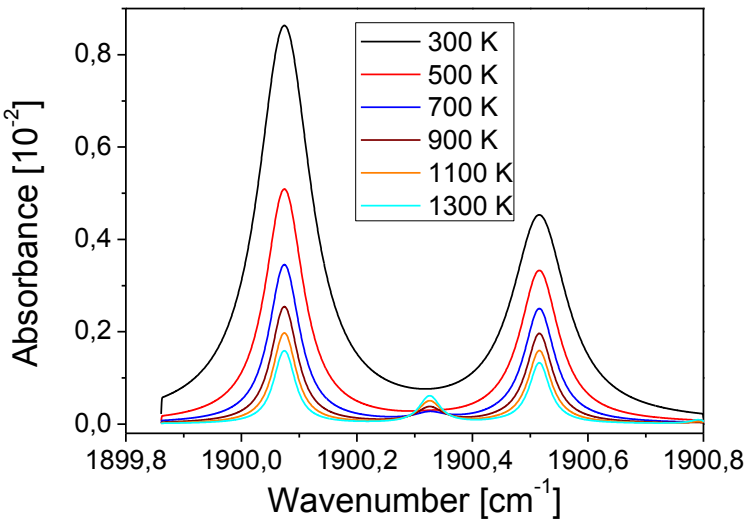

Figure 3.20: Absorbance lines profiles at different temperatures. The fitting strategy is applied to each of the curves. The FWHM is extracted from the global Lorentz fits.

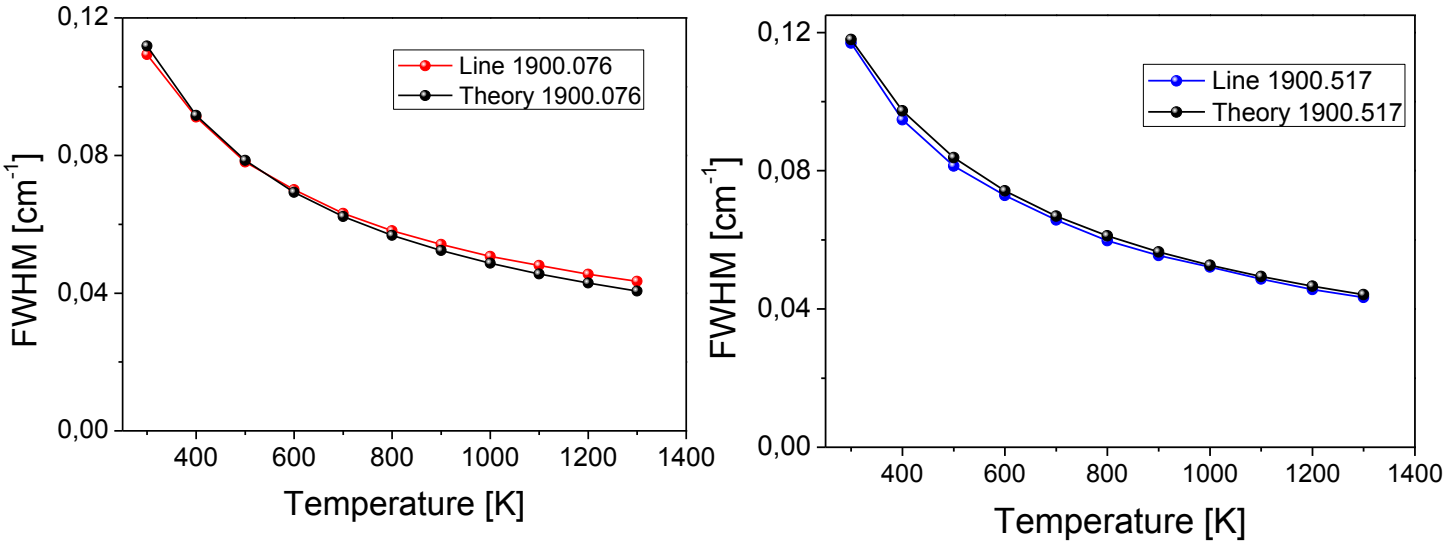

Figure 3.21: Comparison between individual and global fits.

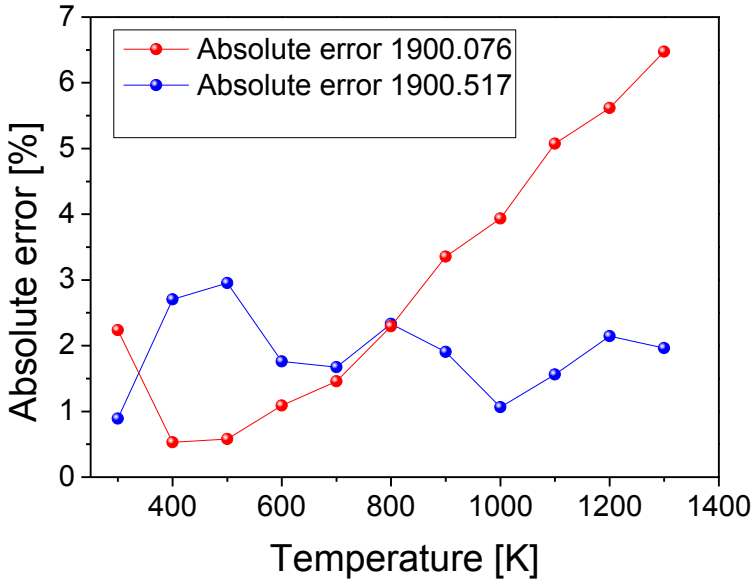

Figure 3.22: Error induced by neglecting line overlap.

- **Instrumental broadening**: wavelength dispersion by optics, laser spectral profile and detector spectral resolution widen the measured absorbing species line profiles. The resulting instrumental function can be approximated by a Gaussian profile in our case.

In most situations, lasers exhibit Gaussian profiles. An ideal laser will have a narrow FWHM, many times smaller than the typical FWHM of target molecules. Instrumental broadening was determined to be about 6 x 10^{-3} cm^{-1}.

- **Stark broadening**: It arises from the influence of the electric field of nearby charged particles (electrons and ions) [*Griem*, 2005]. This electric field displaces the energy levels of absorbing molecules by altering their potential energy. The line is broadened with a Lorentzian profile and is also shifted from line center (Stark shift). Stark broadening is a linear effect or hydrogen (i.e. the resulting FWHM is proportional to the electric field) and quadratic (hence much smaller) for other atoms [*Hutchinson*, 2005]. For the purpose of our work, Stark broadening is negligible for our post-NRP discharge and post-combustion configurations since the electron density is negligible. However absorptions profiles measured directly in the discharge are affected by the high-electron density ~ 10^{15} cm^{-3} attained during the pulse [*Kaddouri*, 2011; *Rusterholtz*, 2012]. To our knowledge, there is no Stark broadening data for the NO lines used here, for the purpose of NO measurements in the discharge. Therefore, we neglected Stark broadening in our analyses. Thus the main source for broadening was assumed to be collisional broadening.

The different types of broadening widths are summarized in figure 3.23. For the investigated temperature range, collisional broadening clearly dominates, even at the highest temperatures investigated (at 1300 K it is still four times greater than Doppler broadening).

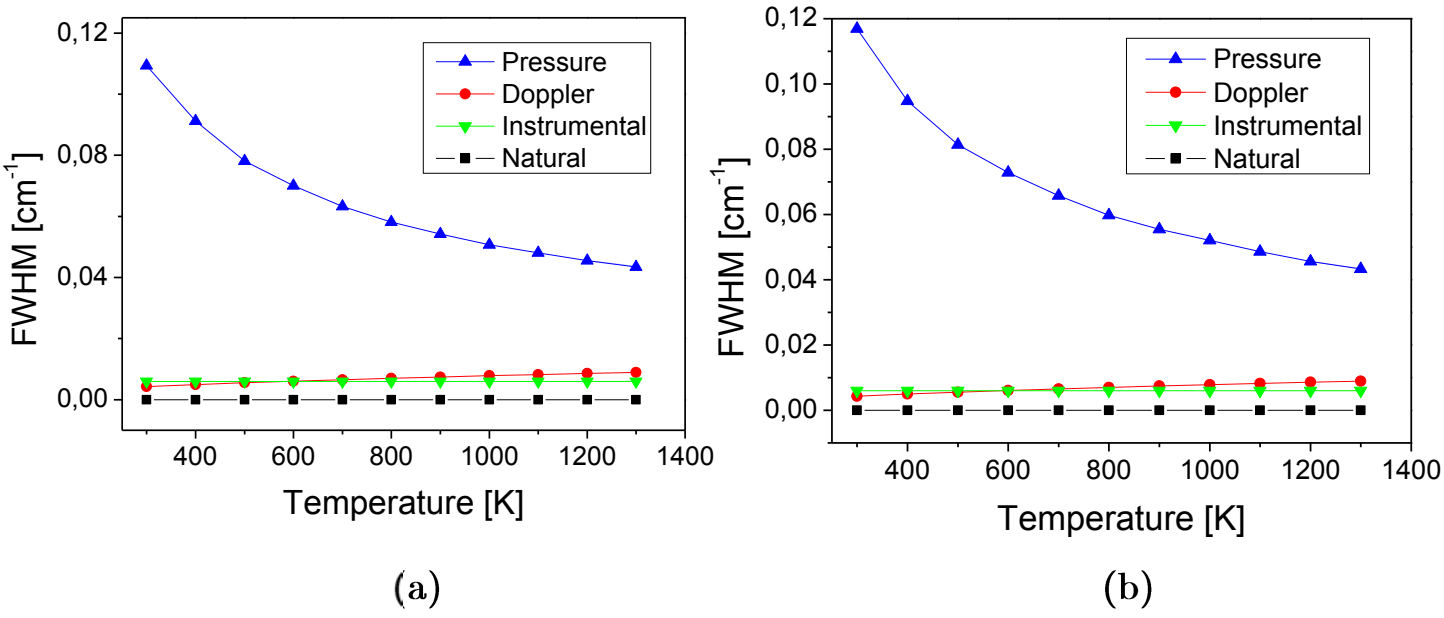

Figure 3.23: Comparisons of broadening widths as a function of the gas temperature. **(a)** line at 1900.076 cm^{-1} **(b)** line at 1900.517 cm^{-1}. The broadening of both lines is dominated by collisional broadening.

3.6 Temperature determination in the NRP discharge

Now that we are able to quantify the evolution of both lines in terms of strength and FWHM as a function of the gas temperature, this can serve up to the determination of gas temperature for the case of a non-uniform but axisymmetric environment. This will be possible by applying Abel inverse methods.

3.6.1 Lines intensities ratio

Equation 3.19 applied to both selected transitions yields:

$$\frac{\int_\nu k_r^1(\nu)d\nu}{\int_\nu k_r^2(\nu)d\nu} = \frac{S_1(T_r)N}{S_2(T_r)N} = \frac{S_1(T_r)}{S_2(T_r)} \tag{3.42}$$

Here S_1 and S_2 are respectively the line strengths of lines at 1900.076 and 1900.517 cm^{-1}. T_r is the radial distribution of temperature.

Equation 3.42 states that the ratio of the spectrally integrated radial absorption coefficients for both lines is equal to the ratio of the lines strengths. Assuming LTE, the ratio of line strengths can be analytically derived from equation 3.26. Here using the previously obtained intermediate results $S_1(T)$ and $S_2(T)$ of section 3.5.3, the ratio is computed. Figure 3.24 (left) depicts the outcome. The ratio of lines intensities decreases by 40 % from room temperature to 1400 K. The inverse transform is displayed on the right side of figure 3.24. The gas temperature is determined as a function of the ratio of the spectrally integrated absorption coefficients of both lines. The higher the ratio, the lower the gas temperature. Besides, an error of 40 % in the measurement of the ratio leads to a factor 4.7 error on the gas temperature determination. Note that the spectrally integrated radial absorption coefficients for each transition are calculated using equation 3.18 and the measured spectrally integrated lateral absorbances.

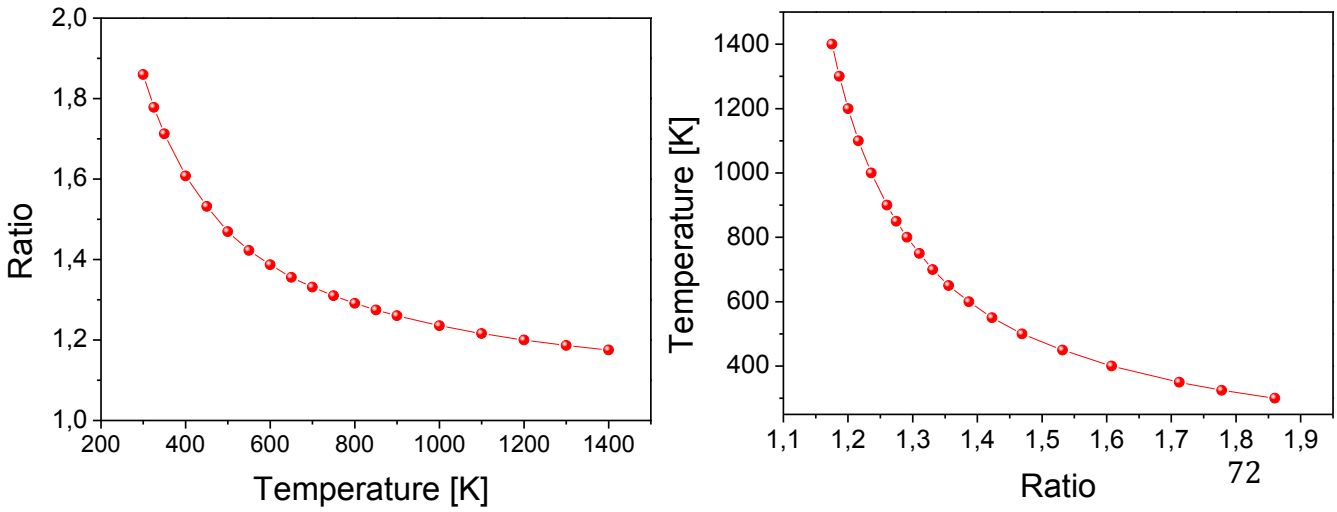

Figure 3.24: Ratio of lines intensities as a function of gas temperature. Gas temperature determination by the ratio of spectrally integrated absorption coefficients.

3.6.2 Collisional broadening

The previous method of gas temperature determination relies on the LTE assumption. Another method is to use collisional broadening. Collisional broadening is the dominant broadening mechanism of NO absorption profiles up to 1400 K as suggested by figure 3.23. Hence measuring the FWHM of spectrally resolved radial absorption coefficients (from equation 3.16) yields the gas temperature as illustrated by figure 3.25. In addition to not requiring the LTE assumption, another advantage of this second method is that it can be applied separately to both transitions. Figure 3.25 is the inverted form of the temperature-dependent collisional-FWHM of line 1900.517 cm^{-1} in figure 3.23-right. When the gas temperature increases from room temperature up to 1300 K, the FWHM of the line at 1900.517 cm^{-1} decreases from 0.12 cm^{-1} to about 0.04 cm^{-1}.

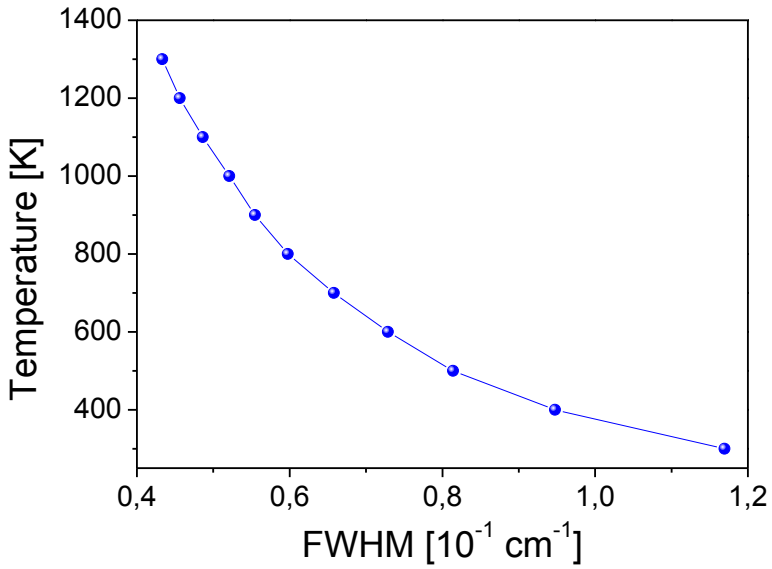

Figure 3.25: Line at 1900.517 cm^{-1}. Gas temperature as a function of the FWHM of spectrally resolved absorption lineshapes.

To compare the two methods, from figures 3.24-right and 3.25, it is clear that for the same ranges of absolute error bars (in percentage) on the measurements of lines FWHM and ratio, respectively, we expect that method 2 would provide more accurate results than method 1. However, as will be shown in chapter 5, the error bars on the determination of the radial line intensity ratio are much smaller than the

ones on the determination of the FWHM of the radial absorption lineshapes. This will affect the accuracy of temperature determination (see results in chapter 5).

3.7 Conclusions

In this chapter, we have detailed the theoretical tools required to treat experimental results. In section 3.2 we have explained the method of determination of the energy deposited by the discharge into the gas. We have explained the procedure of synchronization between voltage and current signals as well as the procedure for displacement current subtraction. Thereafter, we have presented in section 3.3 the principle of Mid-IR laser absorption in uniform environments (such as post-NRP discharge and post-NRP assisted combustion). The derivation of absorption coefficients and absolute species densities from measured quantities was outlined. In section 3.4 we presented the principle of laser absorption in axisymmetric environment (such as NRP discharge) using the Abel inversion. We showed how to simultaneously perform spectrally resolved Abel inversion and spectrally integrated Abel inversion. In section 3.5, we first selected high line strength and overlapping-free transitions, which will be probed in our experiments. Then we discussed the intensities and FWHM of the selected lines. The dependence of these line properties on the temperature were finally used atter properties of the lines with respect to temperature are used in section 3.6 to derive two methods for gas temperature determination in NRP discharges.

References

[1] Bracewell, R. (1999). *The Fourier Transform and its Applications, third ed. McGraw-Hill, New York*, 244.

[2] Celestin, S. (2008). *Study of the streamer dynamics in air at atmospheric pressure* (Doctoral dissertation, PhD thesis, Ecole Centrale Paris, France).

[3] Cremers, C. J., & Birkebak, R. C. (1966). Application of the Abel integral equation to spectrographic data. *Applied optics*, *5*(6), 1057-1064.

[4] Fischer, J., Gamache, R. R., Goldman, A., Rothman, L. S., & Perrin, A. (2003). Total internal partition sums for molecular species in the 2000 edition of the HITRAN database. *Journal of Quantitative Spectroscopy and Radiative Transfer*, *82*(1), 401-412.

[5] Gamache, R. R., & Rothman, L. S. (1992). Extension of the HITRAN database to non-LTE applications. *Journal of Quantitative Spectroscopy and Radiative Transfer*, *48*(5), 519-525.

[6] Griem, H. R. (2005). Principles of plasma spectroscopy. *Proceedings of the Physical Society*, *1*.

[7] Herzberg, G. (1950). Molecular spectra and molecular structure. Vol. 1: Spectra of diatomic molecules. *New York: Van Nostrand Reinhold, 1950, 2nd ed.*, *1*.

[8] Hutchinson, I. H. (2005). *Principles of plasma diagnostics*. Cambridge university press.

[9] Kaddouri, F. (2011). *Développement de diagnostics avancés pour l'étude de la cinétique ultrarapide de production d'oxygène par décharge nanoseconde dans l'air à pression atmosphérique* (Doctoral dissertation, Ecole Centrale Paris).

[10] Montgomery Smith, L., Keefer, D. R., & Sudharsanan, S. I. (1988). Abel inversion using transform techniques. *Journal of Quantitative Spectroscopy and Radiative Transfer*, *39*(5), 367-373.

[11] Pai, D. Z. (2008). Nanosecond repetitively pulsed plasmas in preheated air at atmospheric pressure. *PhD Report, Ecole Centrale Paris, France*.

[12] Pai, D. Z., Stancu, G. D., Lacoste, D. A., & Laux, C. O. (2009). Nanosecond repetitively pulsed discharges in air at atmospheric pressure—the glow regime. *Plasma Sources Science and Technology*, *18*(4), 045030.

[13] Penner, S. S. (1959). *Quantitative molecular spectroscopy and gas emissivities* (Vol. 12). Reading, Mass.: Addison-Wesley.

[14] Pretzler, G. (1991). A new method for numerical Abel-inversion. *Zeitschrift für Naturforschung. A, A Journal of physical sciences*, *46*(7), 639-641.

[15] Rothman, L. S., Rinsland, C. P., Goldman, A., Massie, S. T., Edwards, D. P., Flaud, J. M., ... & Varanasi, P. (1998). The HITRAN molecular spectroscopic database and HAWKS (HITRAN Atmospheric Workstation): 1996 edition. *Journal of Quantitative Spectroscopy and Radiative Transfer*, *60*(5), 665-710.

[16] Rothman, L. S., Jacquemart, D., Barbe, A., Chris Benner, D., Birk, M., Brown, L. R., ... & Wagner, G. (2005). The< i> HITRAN</i> 2004 molecular spectroscopic

database. *Journal of Quantitative Spectroscopy and Radiative Transfer*, *96*(2), 139-204.

[17] Rothman, L. S., Gordon, I. E., Barber, R. J., Dothe, H., Gamache, R. R., Goldman, A., ... & Tennyson, J. (2010). HITEMP, the high-temperature molecular spectroscopic database. *Journal of Quantitative Spectroscopy and Radiative Transfer*, *111*(15), 2139-2150.

[18] Rusterholtz, D. (2012). *Nanosecond repetitively pulsed discharges in atmospheric pressure air* (Doctoral dissertation, Ecole Centrale Paris).

[19] Šimečková, M., Jacquemart, D., Rothman, L. S., Gamache, R. R., & Goldman, A. (2006). Einstein A-coefficients and statistical weights for molecular absorption transitions in the HITRAN database. *Journal of Quantitative Spectroscopy and Radiative Transfer*, *98*(1), 130-155.

[20] Stancu, G. D., Röpcke, J., & Davies, P. B. (2005). Line strengths and transition dipole moment of the v2 fundamental band of the methyl radical. *The Journal of chemical physics*, *122*(1), 014306.

[21] Stancu, G. D., Simeni, M. S., & Laux, C. O. Study of nitric oxide and carbon monoxide production in plasma assisted com-bustion by Quantum Cascade Laser Absorption Spectroscopy. *21st ISPC*, Cairns, August 4-9, (2013) AUSTRALIA.

Chapter 4

Experimental setup: QCLAS, NRP

4.1 Introduction

This chapter sketches the different experimental set-ups implemented or developed during this thesis. We begin in section 4.2 with the presentation of the NRP plasma discharge generation system. Section 4.3 describes two high-temperature facilities, namely the burner used for the NRP discharge-assisted premixed combustion experiments and the air preheater system. Then section 4.4 details the electrical measurements tools. Finally section 4.5 provides information about the different QCLAS diagnostic strategies. The setup for spatially resolved NO density measurements in the NRP discharge, for the purpose of discharge analysis and the setup for multipass absorption, for the purpose of plasma-assisted combustion are presented.

4.2 NRP discharge

The plasma is generated by NRP discharges in the spark regime operating in open air or in confined combustion environment. Spark and other NRP discharges regimes in air at atmospheric pressure have been described in detail by *Pai et al* [*Pai*, 2008; *Pai et al.*, 2010-a, 2010-b]. NRP discharges were generated by applying nanosecond high-voltage pulses between two electrodes in a vertical pin-to-pin configuration. In the following subsections we will parse plasma generation systems employed for discharge characterization on the one hand and for post-discharge and plasma-assisted combustion characterizations on the other hand.

4.2.1 Electrodes assembly

Two electrode configurations were used. The first configuration, shown in figure 4.1 is mainly dedicated to post-discharge characterization: NO density measurements in plasma-assisted combustion and in pure air post-NRP discharge. NRP discharges were produced between a refractory steel anode and a small aluminium tip located at the top of the cylinder acting as the cathode. This cylinder is a bluff body placed at the exit of the burner and held by a thin (2-mm diameter) refractory steel electrode electrically connected to the pulse generator. NRP discharges are produced in the recirculation region of the flame, downstream of the bluff-body, as was done in

previous plasma-assisted combustion studies in our laboratory [*Galley*, 2006; *Pilla*, 2008]. Each electrode is mounted on three-axis micrometric translation stages allowing separate displacements of the cathode and the anode. The bluff-body cathode and the pin anode are aligned with the axis of the flow coming out of the 16-mm inner diameter tube through which the gas is injected. The inter-electrode gap distance can be adjusted from 1 to 5 mm. Note that for this configuration, the pin height at the top of bluff body can be adjusted from 1 to 5 mm, in order to change the position of the discharge above the bluff body.

The second configuration, presented in figure 4.2 uses anode and cathode both made of the refractory steel usually employed for gas boilers. The bluff body is removed. As for the previous configuration, the electrodes can be translated in orthogonal directions in the horizontal plane and another z-translation stage allows us to adjust inter-electrode gap distance. The gap distance is fixed at 2 mm. This configuration is used for spatially resolved measurements of NO density and gas temperature in the NRP discharge in pure air.

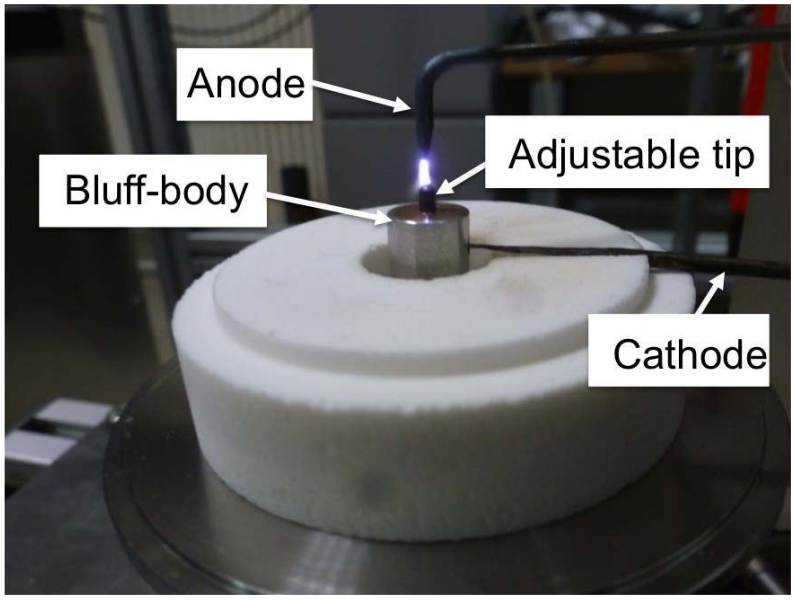

Figure 4.1: Discharge assembly with the bluff-body and the two electrodes. Bluff body tip is 5-mm long with a diameter of 2 mm. This configuration is mainly dedicated to combustion applications.

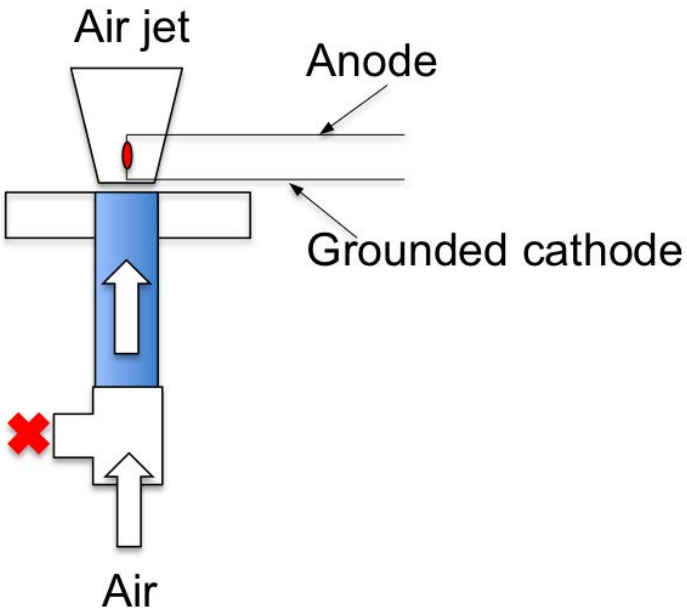

Figure 4.2: Schematic of discharge configuration for spatially resolved gas temperature and NO density in the discharge. Here the red cross shows the unemployed methane injection system.

4.2.2 High-voltage pulse generation

High-voltage nanosecond pulses were produced using three different types of pulse generators, manufactured by FID Technology[1]. They rely on the principle of the Drift Step Recovery Diode [*Prokhorenko et al.*, 2000].

The first pulse generator (PG1) is a FID Technology FPG 10-30NM10 that provides pulses with rise/fall times about 5 ns (time required to rise/fall from 10 % to 90 % of maximum amplitude), 10 ns duration (pulse width at 90 % of maximum amplitude), pulse amplitude ranging from 0 to 12 kV into an open circuit and from 1 to 30 kHz pulse repetition frequency. PG1 is used only for measurements in the post-NRP discharge in air and in combustion.
The second pulse generator (PG2) is a FID Technology FPG 20-30MKS50. It can be used on two separate channels that each delivers pulses of variable duration. The first channel provides pulses of duration 10-35 ns (width at 90% of maximum amplitude) and the second channel pulses of 2-4 ns. Both channels release pulse amplitude up to 20 kV into an open circuit for frequencies ranging from 1 Hz to 30 kHz. PG2 is used for spatially resolved measurements in the discharge in addition to post-NRP discharge measurements in pure air.

[1] http://www.fidtechnology.com/

The third pulse generator (PG3) is a FID Technology FPG 30-100MC4K. It can provide higher pulse voltage amplitude and frequency (up to 100 kHz) than both previous pulse generators. It consists of four output channels designed to produce positive and negative voltage pulses with maximum amplitude of ± 7.5 kV into 75 Ohm each. The combined output is 30 kV into 300 Ohm. PG3 is used for the optimization of NO released by NRP discharges in plasma-assisted combustion. Main features of the three pulse generators are presented in table 4.1.

Table 4.1: Main features of pulse generators.

Pulser	**PG 1**	**PG 2**		**PG 3**
Type	FPG 10-30NM10	FPG 20-30MKS50 **Channel 1**	**Channel 2**	FPG 30-100MC4K
Output impedance [Ω]	150	100	100	300
Voltage amplitude into an open circuit [kV]	0-12	0-20	0-20	0-30
Pulse width at 90% [ns]	10	10-35	2-4	9-10
Rise time [ns]	5	15	5	3-4
Frequency [kHz]	1-30			1-100

4.3 High-temperature facilities

Using NRP spark discharge to stabilize premixed propane/air flames, *Pilla et al.*, [2006] demonstrated a significantly extension of flame stability and lean extinction limit. In this section, the experimental setup used for studies of the effects of NRP spark discharges on premixed methane-air flames is presented. Then a second high-temperature facility, dedicated to experiments in pure preheated air, is introduced.

4.3.1 Methane-Air combustion at atmospheric pressure

For combustion and plasma-assisted combustion, the mini-PAC burner developed in [*Pilla*, 2008] was used. We use this burner for premixed methane/air combustion at atmospheric pressure. A supply of dry air at 6 bars and methane at 5 bars feeds the

burner. The methane flow rate is measured using a Bronkhorst Hi-Tech (model El-Flow) flowmeter, which supplies up to 0.42 $Nm^3.h^{-1}$. For air, a Bronkhorst Hi-Tech (model El-flow) flowmeter supplies up to 6 $Nm^3.h^{-1}$. The gases are premixed in a mixing cross (tube filled with glass pellets). Subsequently, the gas mixture is convected through a 30-cm long and 16-mm inner diameter tube toward the exit. The flame is stabilized by a bluff-body made of a 1-cm diameter aluminium cylinder. A 16-mm inner diameter refractory ceramic surrounding the exit of the burner thermally protects the metallic parts of the burner. An 8-cm diameter and 50-cm long steel confinement tube surrounds the flame in order to confine the species created by the plasma and/or the flame towards the exit of the tube. A schematic of the burner is presented in figure 4.3.

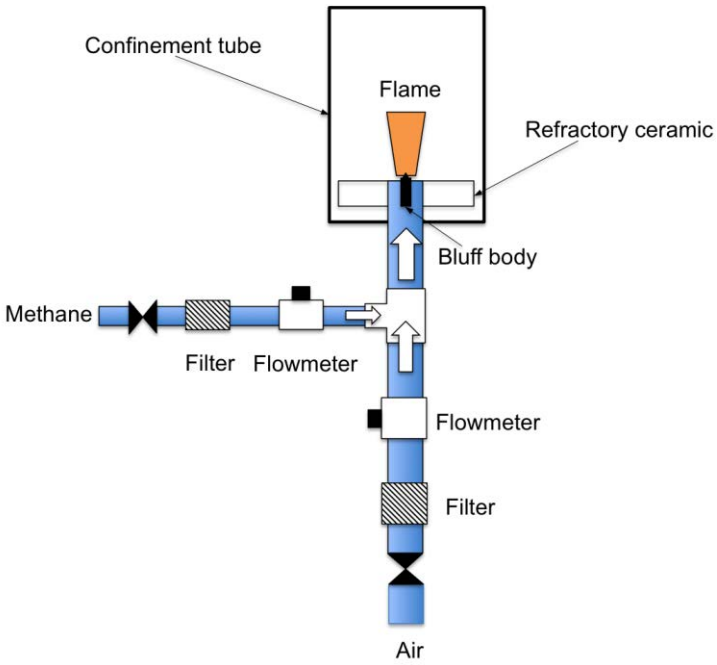

Figure 4.3: Schematic of the burner. Filters avoid that impurities wider than 5 µm affect the flow. The cross-section of the flow injection system at the exit is about 1.22 cm^2.

The combustion reaction of hydrocarbons C_nH_m in air is described by the global equation:

$$C_nH_m + \left(n + \frac{m}{4}\right)(O_2 + \beta_1 N_2 + \beta_2 Ar) \rightarrow nCO_2 + \frac{m}{2}H_2O + \left(n + \frac{m}{4}\right)(\beta_1 N_2 + \beta_2 Ar) \quad (4.1)$$

In air it is common to use $\beta_1 = 3.717$ and $\beta_2 = 0.047$ (1 % of Argon). Argon is neglected for our applications. As a result we use: $\beta_1 = 3.764$ and $\beta_2 = 0$ [*Darabiha et al.*, 2010]. For methane, the previous equation becomes:

$$CH_4 + 2(O_2 + \beta_1 N_2) \rightarrow CO_2 + 2H_2O + 2(\beta_1 N_2) \quad (4.2)$$

The lean flame extinction limit of a flame depends on the temperature and the pressure. Since we are working at atmospheric pressure, this parameter only depends on the temperature, which can be adjusted by varying the equivalence ratio. The equivalence ratio ϕ is defined as the ratio of the local mixture ratio by the stoichiometric mixture ratio. Local mixture ratio α corresponds to the ratio of the fuel's mass flow rate and oxidant's mass flow rate. The stoichiometric mixture ratio α_s is the mixture ratio at stoichiometry (i.e. at equivalence ratio 1).

$$\phi = \frac{\alpha}{\alpha_s} = \frac{m_{CH_4}/m_{air}}{(m_{CH_4}/m_{air})_s} \quad (4.3)$$

m_{CH4} and m_{air} are respectively the fuel and oxidant mass flow rates. We can then use the balanced combustion reaction equation to express mixture equivalence ratio as a function of the methane and air volumetric flow rates Q_{CH4} and Q_{air}:

$$\phi = 2\frac{\rho_{CH_4}}{\rho_{air}}\frac{(M_{O_2} + \beta_1 M_{N_2})}{M_{CH_4}}\frac{Q_{CH_4}}{Q_{air}} \quad (4.4)$$

ρ_{CH4} and ρ_{air} are volumetric mass densities of methane and air, respectively.
Numerically, we have:

$$\phi \approx 9.4\frac{Q_{CH_4}}{Q_{air}} \quad (4.5)$$

In our experiments we fixed the CH_4 volume flow rate at 0.40 m^3h^{-1} (which represents 95 % of the full scale of the CH_4 flowmeter) and we varied air volume flow rate from 3.5 up to 5.9 m^3h^{-1}, which represents 58 % to 98 % of the full scale. When $\phi < 1$, the flame is called as "lean" and $\phi > 1$ corresponds to a "rich" flame regime.

Using Particle Image Velocimetry (PIV) on the mini-PAC burner, *Pilla*, [2008] demonstrated that for a mixture volume flow rate between 3 and 15 m^3h^{-1}, there is a good agreement (10 % maximum difference) between the mean velocity measured by PIV near the bluff body and the velocity determined from the flow rate:

$$V = \frac{Q_{mixture}}{\frac{\pi}{4}(d_{ext}^2 - d_{int}^2)} \tag{4.6}$$

With d_{ext} and d_{int} been respectively the injection tube diameter (16 mm) and the bluff-body diameter (10 mm). $Q_{mixture}$ is the mixture volume flow rate.
The features of the injection system with and without combustion are presented in table 4.2.

Table 4.2: Specifics of the mixture injection. Equivalence ratio and flow velocity at exit. The methane flow rate is fixed at 0.40 m^3h^{-1}.

Air flow rate [m^3h^{-1}]	5.9	5.4	5.1	4.8	4.5	4.2	4.0	3.8	3.7	3.5
Equivalence ratio	0.65	0.70	0.75	0.80	0.85	0.90	0.95	1.00	1.05	1.1
Mixture velocity [m/s]	14.3	13.3	12.5	11.8	11.2	10.6	10.	9.5	9.3	8.9
Air velocity [m/s]	13.4	12.4	11.6	10.9	10.3	9.7	9.2	8.6	8.3	8

Figure 4.4 below depicts a lean methane-air flame at 0.9 equivalence ratio. Figure 4.4-right demonstrates that the flame is attached to the bluff-body.

Figure 4.4: Pictures of the methane-air flame without confinement tube at 0.9 equivalence ratio. The flame is attached to the bluff-body at the exit of the burner. Air flow rate is 4.2 m^3/h.

The lower heating value of the combustion of methane is about 50 MJ/kg [*Pittman and Pilcher*, 1972]. It represents the energy released by the complete combustion of 1 kg of methane in air. Hence the maximum flame power is released at stoichiometry and can be obtained by multiplying the methane heat of combustion by the methane volumetric mass density and by its flow rate (in m^3/s). As a result, at 20° C, we have $P \sim 50 \times 10^6 \times 0.668 \times 0.40/3600 \sim 3.71$ kW.

4.3.2 Air heater system

In addition to the previous air injection system, NRP discharges in a vertical pin-to-pin configuration can also be generated in a vertical preheated airflow thanks to an 8-kW Osram Sylvania Hot Air System. The system allows us to adjust the gas temperature between 300 and 1000 K. It basically consists in a 2.5-cm inner diameter metal tube including a ceramic heating coil and two internal thermocouples. The gas temperature in the system is controlled through an internal thermocouple, located 2.5 cm upstream of the heater outlet together with a regulation control loop. A picture of the device is provided in section 4.5.3 (figures 4.18 and 4.19).

4.4 Electrical diagnostics

The NRP discharges were also characterized by electrical diagnostics. Here we present the corresponding experimental setup. Voltage and current measurements are performed using high-frequency probes.

Voltage

The applied voltage is measured using a 100-MHz bandwidth Lecroy PPE20kV passive high-voltage probe with a 1000:1 attenuation factor. The probe clip was attached to the anode and connected in parallel with the discharge. When required, a Lecroy attenuator 10:1 is added to the voltage probe as a complement to the attenuation factor. Table 4.3 below summarizes the features of the voltage probe.

Table 4.3: Lecroy voltage probe features.

Model	System attenuation	Resistance [MΩ]	Capacitance [pF]	-3dB Bandwith [MHz]	Maximum voltage [kV]
PPE20kV	1000:1	100	3	100	20

Current

Electrical current is measured placing a Pearson Electronics 50-Ω Rogowski coil (Model 6585) current probe in the circuit connecting the pulse generator to the grounded cathode. It has a current-to-voltage ratio 1 A to 1 V, a 3 dB low frequency cutoff cf 400 Hz, a ± 3 dB high frequency cutoff at 250 MHz and a 1.5 ns rise time. Voltage and current signals are recorded using a 1-MΩ input impedance oscilloscope Lecroy, Wavepro 7100 A, 1 GHz sample frequency. Table 4.4 summarizes the characteristics of the current probe. Experimental setup for voltage and current measurements is shown in figure 4.5.

Table 4.4: Pearson coil features.

Model number	Sensitivity [V/A]	Maximum peak current [A]	Maximum I.t [A.s]	Output resistance [Ω]	Useable rise time [ns]	3 dB low frequency cutoff [Hz]	3 dB high frequency cutoff [MHz]
6585	1	500	0.002	50	1.5	400	250

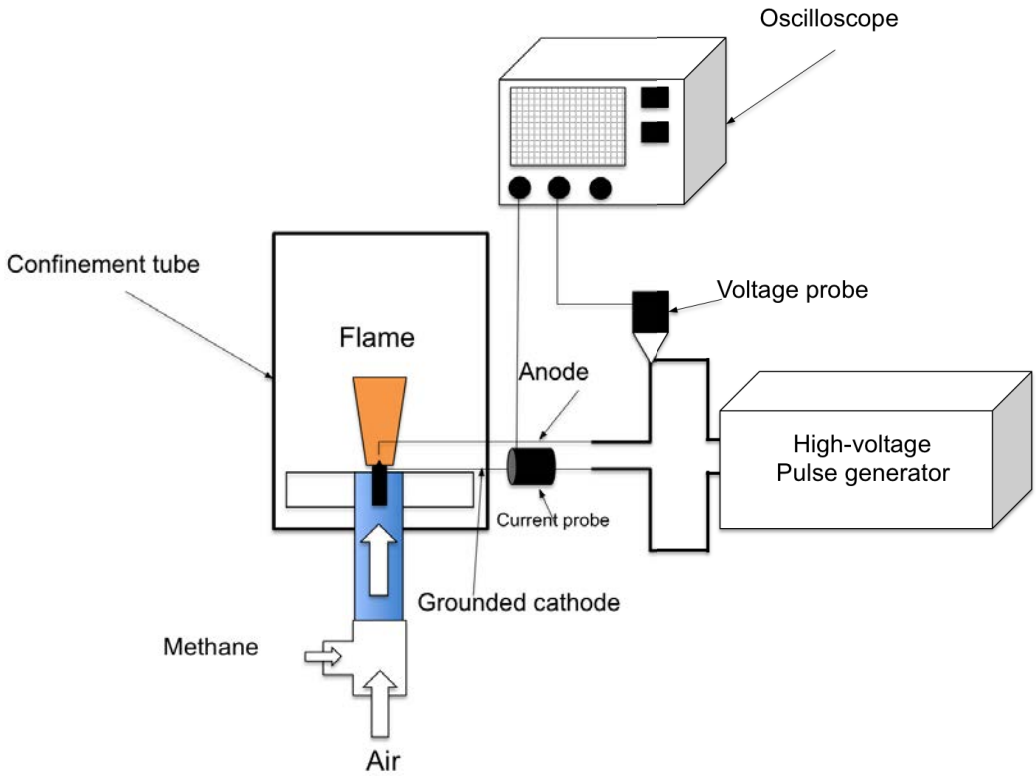

Figure 4.5: Schematic of the electrical measurements setup.

As shown by *Pai*, [2008], the bandwidth of the Pearson coil and of the high voltage probe was sufficient to accurately characterize the nanosecond pulses considered in this study.

4.5 QCLAS diagnostics

Nitric oxide ground-state detection in NRP spark discharges, post-discharges and plasma-assisted combustion was performed in this thesis using Mid-Infrared Quantum Cascade Laser Absorption Spectroscopy. In this section we present the operating principles of Quantum Cascade Lasers (QCLs), emphasizing on the advantages of the QCL system in comparison with Infrared Tunable Diode Lasers (IR-TDLs). Then experimental setups designed with the intent to characterize NRP discharge, post-discharge and post-NRP assisted combustion environments are discussed. Next, the wavelength calibration method for QCLAS is explained. Last, we discuss some artefacts, which may occur while performing QCLAS.

4.5.1 QCL principles and operation modes

Laser diodes operate via electrically injected electrons and holes in a semiconductor, which recombine to produce laser photons at a wavelength depending of the energy gap between the conduction and the valence bands. This can be modelled by a transition between two confined electronic states in quantum wells (figure 4.6-a). It is an interband transition as illustrated by the dispersion curve on figure 4.6-b. These transitions are only transparent in the low-energy side of their absorption spectrum and highly absorbing above the gap energy E_G (figure 4.6-c). Besides, TDLs operate at very low temperature (10 - 120 K). They hence require expensive and size consuming cryogenic cooling systems in order to release enough output power [*Welzel*, 2009].
QCLs rely instead on intersubband transitions in the conduction band [*Faist et al.*, 1994]. Consequently, in contrast to laser diodes, only electrons are involved. It is the reason why they are described as unipolar semiconductor lasers. The process of photon generation can be regarded as a transition between two confined electronic states in the same quantum well as shown in figure 4.6-d. The dispersion curve of figure 4.6-f shows that unlike laser diodes, the upper and lower levels exhibit now the same curvature ($K_{//}$ is the parallel wave-number). As a result, they feature an atomic-like density of states peaked at the transition energy E_{21} (figure 4.6-f) as explained by [*Hugi et al.*, 2010]. Furthermore, the laser wavelength can be adjusted by modifying the well and barrier thickness. Then, putting into cascade dissimilar active region emitting at different wavelengths, broadband emission can be achieved. The cascading principle is presented in figure 4.7. Recycling the electrons by tunneling them from one quantum well to another one permits high quantum

efficiency. It increases laser output power. Therefore QCLs exhibit four major features: they have a narrow linewidth, they can be tuned over a broadband region, they provide enough output power, and they operate at ambient temperature.
The laser used for our investigations is a pulsed distributed-feedback system from Alpes laser. It has a spectral width of about 6×10^{-3} cm^{-1} (FWHM). A Peltier module driven by a thermoelectric temperature control system from Thermocube enables the laser to operate from -30 to 45 °C. Varying the temperature in this range, the laser wavelength can be tuned from 1898 to 1910 cm^{-1}. A Q-MACS module provides input voltage to the QCL head. It also displays the average currents through the QCL and the thermoelectric element. Using a potentiometer, average voltage can be adjusted up to 12 V. At 12 V, the current rises up to 0.7 A for a maximum output power of 2.5 mW. The main laser features are summarized in table 4.5.

Table 4.5: Characteristics of the Alpes laser QCL for 50 ns pulses at 400 kHz repetition frequency.

Laser type	Pulsed Distributed-Feedback
Laser chip	Sb1770DN
Temperature range	-30 to +45 °C
Wavenumber range	1898 – 1910 cm^{-1}
Spectral width	0.006 cm^{-1}
Input voltage	0 – 12 V
Peak current	0 - 0.7 A
Average output power	0 - 2.5 mW

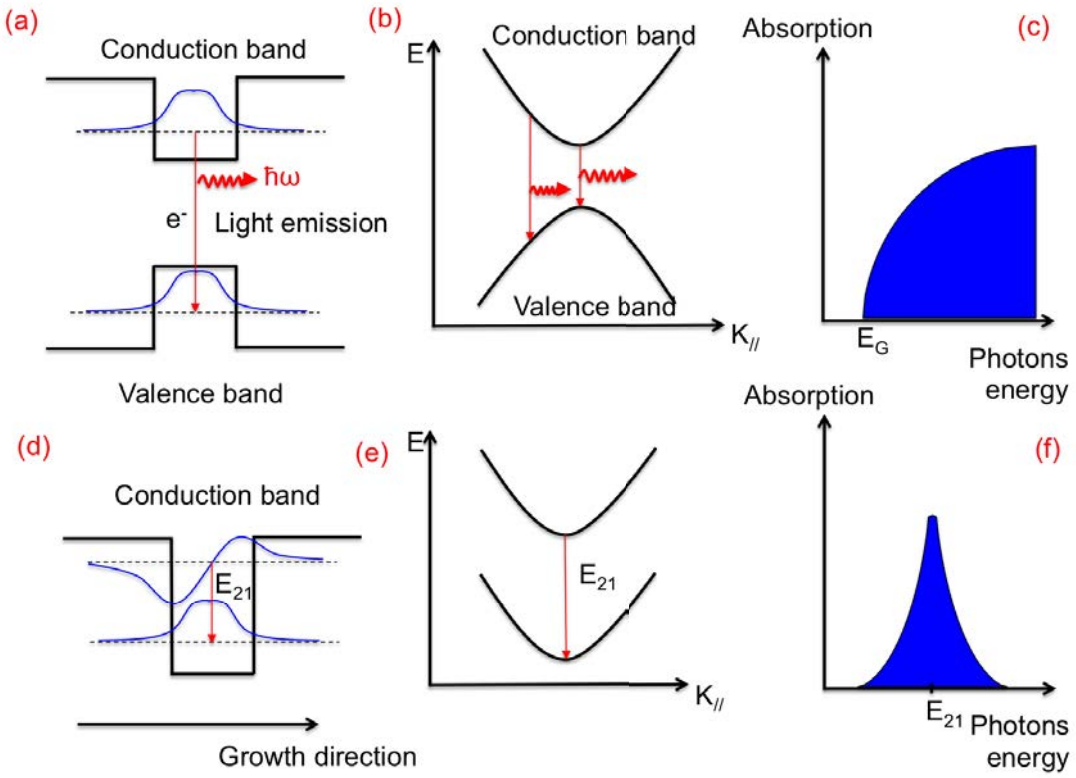

Figure 4.6: Compared features of interband and intersubband transitions in quantum wells. Figure adapted from [*Hugi et al.*, 2010].

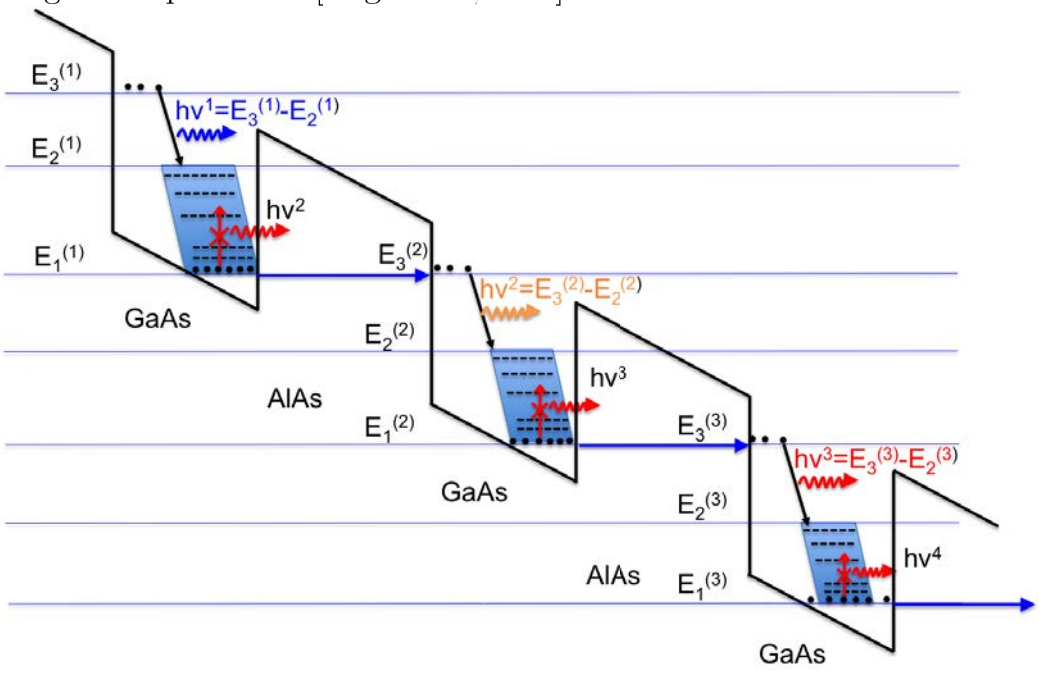

Figure 4.7: Cascading principle in a GaAs/AlAs QCL. Example with 3 quantum wells. Electrons tunnel from one quantum well to the next. The region of interest consists in three states. Lasing occurs between states 3 and 2 whereas electrons are injected via the lower level, which is aligned with the upper level of the next well. Figure adapted from [*Hugi et al.*, 2010].

Ramp generation system

The broad tuning range of QCLs is obtained by the modulation of their heat sink temperature with an external voltage applied to the Thermo-Electric Cooler (TEC) of the QCL. This can be done by several methods. In this thesis two methods are applied: inter-pulse and intra-pulse configurations.

The inter-pulse mode is the combination of a continuous current ramp with a train of short laser pulses. It creates a temperature modulation on the laser and therefore tunes the lasing frequency [*Namjou et al.*, 1998; *Kosterev et al.*, 2002]. Due to the ramp, each laser pulse corresponds to a new frequency. The laser chirp rate $d\nu/dt$ characterizes the speed of laser frequency change. It is an important parameter since it defines the spectral resolution (see appendix C). It depends on laser material properties and on the thermal behavior of the active laser region. Lower limits of QCLs reported in the literature are 3 - 5 x 10^{-3} cm^{-1}/ns (which corresponds to 90 - 150 MHz/ns in frequency unit).
All QCLAS measurements of the current work were performed using bursts of 1000 laser pulses of 10 ns duration and 200 kHz repetition frequency each (0.2 % duty cycle). In this configuration, the system provides a frequency sweep of the range of 0.4 cm^{-1} within 5 ms (see figure 4.8-left).

In the intra-pulse mode a single long laser pulse is used to record the entire spectrum [*McCulloch et al.*, 2003; *Beyer et al.*, 2003]. The tuning is still achieved by temperature change induced by the current flowing during the pulse. But because there is no more current ramp anymore, the frequency chirp rate cannot be directly controlled. It determines the frequency scan of the long laser pulse.
Thanks to the higher released laser intensity (figure 4.9-left) and faster spectrum scan (figure 4.8-right), this mode is convenient for time-resolved measurements and for the alignment of the system. For the latter purpose we used pulses of 100 ns duration and 100 kHz repetition frequency i.e. 1 % duty cycle (see figure 4.8-right).

Sample transmitted laser signals in both intra- and inter-pulse modes (without absorbing species in the optical path) are presented in figure 4.9. It is also remarkable that intra and inter pulse configurations can be intuited as two strategies designed to follow the constraint of the maximum (time-averaged) current capable of passing through the QCL without damage. Actually, for the same time elapsed, thousand "low" current pulses can match one high-current pulse, in terms of time averaged current intensity. More precisely, it is trade-off between laser peak current intensity and duty cycle. Moreover, all our measurements were carried out in the inter pulse mode to take advantage of its more suitable baseline in comparison with that of in

intra-pulse (figure 4.9). As a result, a small absorption signal can be directly visible by eyes in the inter pulse mode, which is not the case in the intra pulse mode.

Detailed setups for inter and intra pulse ramp generation systems are presented in figure 4.10. In the inter pulse mode we use a PC to record the spectra. The data acquisition card of a computer is used to trig detector measurements on the signal from a function generator contained in the Q-MACS supply.

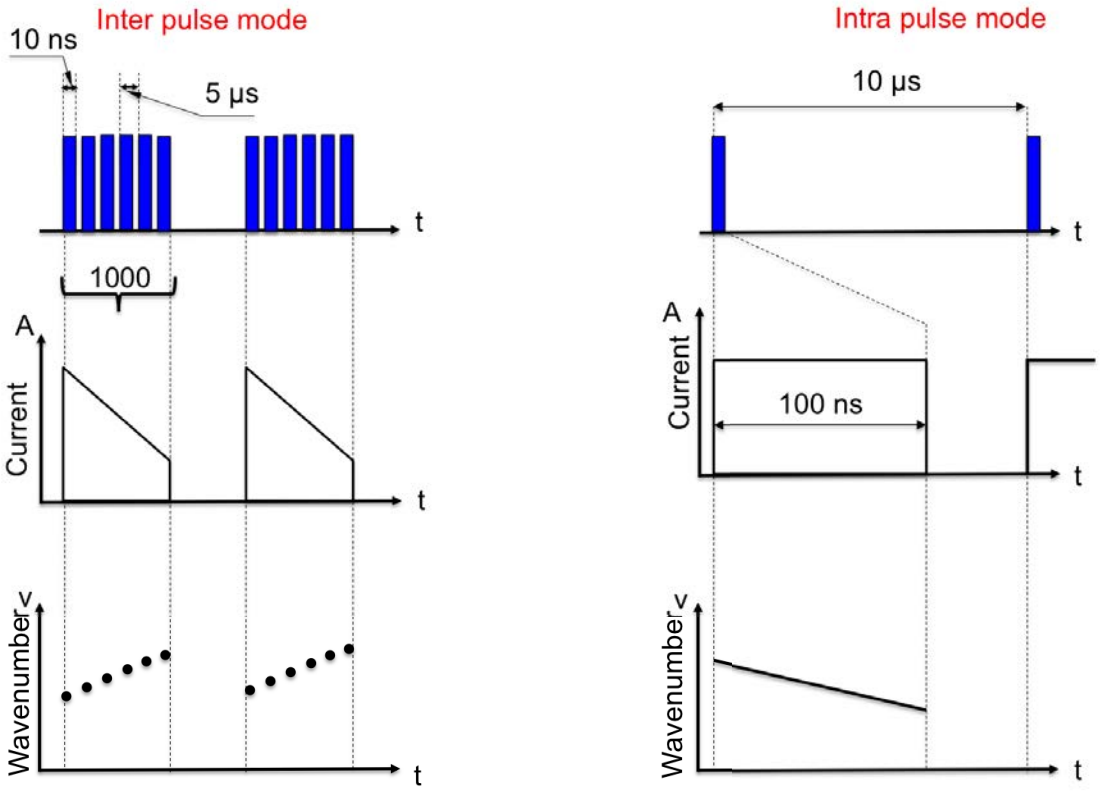

Figure 4.8: Principles of inter-pulse and intra-pulse laser tuning modes. A complete spectrum is recorded after about 5 ms using the inter-pulse mode while it takes 100 ns in intra-pulse mode.

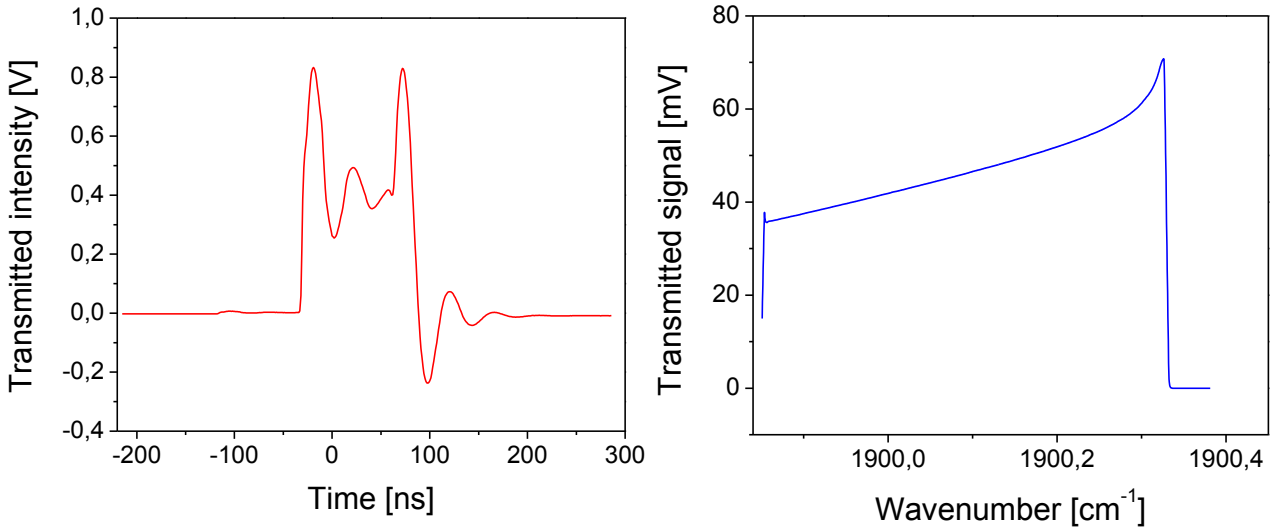

Figure 4.9: Samples laser signals in intra-pulse and inter-pulse configurations. The laser intensity is 10 to 20 times higher in the intra-pulse mode (left) but the baseline in the inter-pulse is more convenient for the detection of an absorption signal.

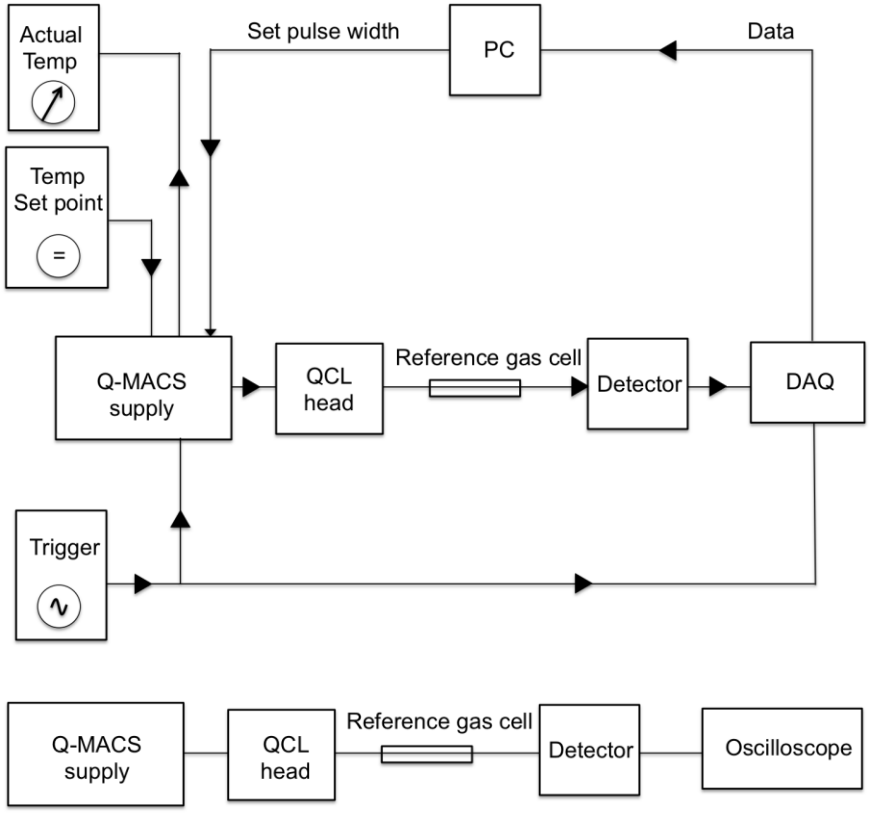

Figure 4.10: Inter-pulse (top) and intra-pulse (bottom) setups. In the inter-pulse mode measurement spectra are recorded using a PC while an oscilloscope is used in the intra- pulse mode. For both methods, the laser temperature is fixed via a control loop.

4.5.2 Platform for spatially resolved measurements (discharge analysis)

Figure 4.11 shows a schematic of the QCLAS (based on a Q-MACS system from Neoplas Control[2]) setup. Our laser system is similar to the device used by *Stancu et al.* [2007]. A thermoelectrically cooled (TEC) QCL (from Alpes Laser) operating at 5.2 µm was installed in a Q-MACS head. Apart from the laser chip, the Q-MACS head houses a temperature controller board, a pulse amplifier board and the thermo-electrical heat sink. The head is equipped with a 25.4-mm diameter Mid-IR transparent KBr window. The chip is placed precisely at the focal point of a 25.4-mm off-axis parabolic (OAP) mirror. The collimated beam is then split into two parts using an Edmund optics calcium fluoride (CaF_2) beam splitter. A 101.6-mm OAP mirror focuses the first part of the laser radiation on a TEC IR photovoltaic (TE-PVI) detector, optically immersed in high refractive index GaAs. This constitutes the reference channel. The second part of the beam is focused on the NRP discharge center via a 50.8-mm OAP mirror. The discharge is mounted on a 3-axis translation stage that we move for the purpose of spatially resolved measurements. The system in this configuration provides a magnification factor of 2. Laser chip size about 50 µm x 100 µm, which should result in a laser spot of about 100 µm x 200 µm in the center of the discharge. However, due to beam distortion when passing through optics, the measured beam size in the center of the discharge is about 250 µm x 300 µm. The laser spot size at discharge center was measured using a four-knife system (see figure 4.12 for more details). Note that the laser spot size is many times smaller than the spread of NO produced by the discharge, which can reach 5-mm distance from axis. After passing through the NRP discharge, the Mid-IR beam is collimated by another 50.8-mm OAP mirror. Finally, using a 25.4-mm OAP, the collimated beam is focused on a Room Temperature Mercury Cadmium Telluride (RT-MCT) IR detector from Daylight Solutions. This constitutes the measurement channel. The output signals from both detectors are synchronized and directed to the data-acquisition card installed in a PC. The characteristics of the optical system are summarized in table 4.6. The reflectance of the Thorlabs gold-coated mirrors is presented in figure 4.13.

[2] http://www.neoplas-control.de/

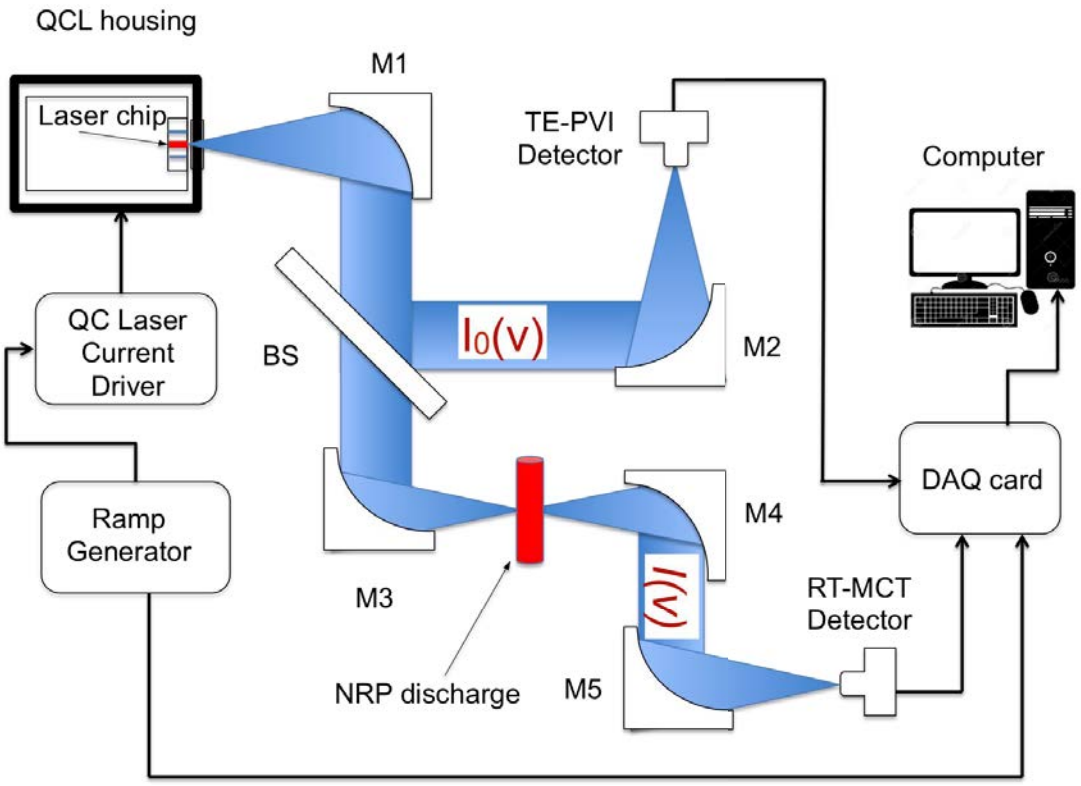

Figure 4.11: Spatially resolved QCLAS setup. The NRP discharge is mounted on a 3-axis translation stage.

Table 4.6: Optical system's properties.

	M1	BS	M2	M3	M4	M5
Provider	Thorlabs	Edmund optics	Thorlabs	Thorlabs	Thorlabs	Thorlabs
Type	90°-gold coated OAP	50/50 CaF_2	90°-gold coated OAP	90°-gold coated OAP	90°-gold coated OAP	90°-gold coated OAP
RFL	2.54	—	10.16	5.08	5.08	2.54
Size	2.54-diameter	2.54-diameter	2.54-diameter	2.54-diameter	2.54-diameter	2.54-diameter
Efficiency at 5 µm	>95% reflectivity		>95% reflectivity	>95% reflectivity	>95% reflectivity	>95% reflectivity

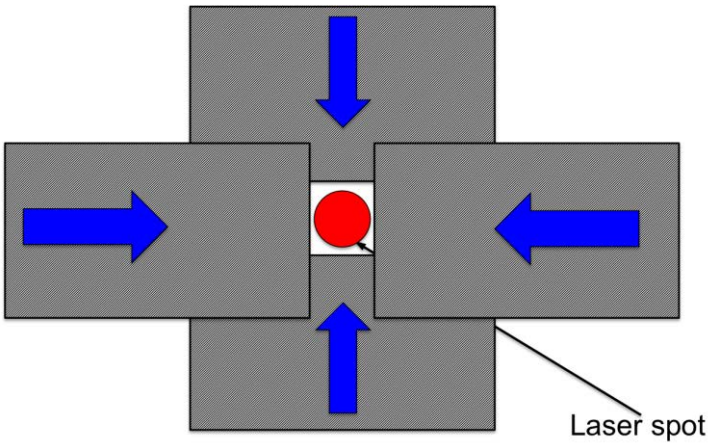

Figure 4.12: Measurement of IR-laser spot size at discharge center. Transmitted signal measured by the detector is the same with a 300 µm x 250 µm window defined by the four knives as without it.

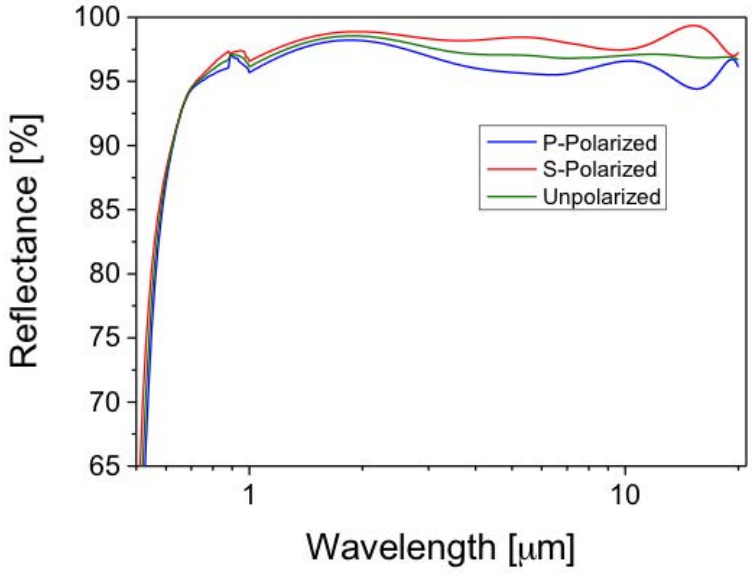

Figure 4.13: Reflectance at 45° angle of incidence of gold-coated mirrors from Thorlabs. Three types of polarization: parallel to the incidence plane (p-polarized), perpendicular to the incidence plane (s-polarized) and unpolarized.

4.5.3 Platform for multipass measurements

This experimental setup is based on that one used by *Stancu et al.* [2012] for carbon monoxide ground-state detection in post-NRP assisted flames. In order to increase the sensitivity, multipass cells can be used. Figure 4.14 presents schematics of the multipass absorption facility that was used for plasma-assisted combustion and post-discharge experiments. The reference channel is the same as that of the spatially resolved measurements. After the beam splitter, a 1500-mm focal length spherical

mirror focuses the transmitted laser radiation on the center of a 28-pass White cell. The cell was placed at the exit of the confinement tube from the gas injection system. The White cell consists of a first incoupling flange, which includes incoupling and outcoupling windows and a field mirror as well as second adjustment flange, which includes two objective mirrors, an observation window and adjusting spindles. The field and objectives mirrors are separated by 50 cm. The beam coming through the cell is directed horizontally in the center of a KBr coupling window and points perpendicular to the incoupling flange level. After this first pass the beam is reflected by the objective mirror in such a way that it strikes the field mirror as illustrated in figure 4.15-left. Then using the multiple passes number adjustment spindle, the number of passes through the cell can be modified. A reflection pattern on the field mirror for a 12-pass cell (28-pass is the maximum cell capability) is depicted on figure 4.15-right. The parallel-outcoupled beam exiting from the cell passes through the KBr outcoupling window and is then focused on the RT-MCT detector from Daylight Solutions using a 2.54-mm OAP mirror. Figure 4.16 details the components of the multiple pass cell. It presents a side view of the later while figure 4.17 displays a photograph of the set-up. The technical specifications of the White cell components are given in table 4.7. Details about the alignment of the QCL are provided in appendix D.

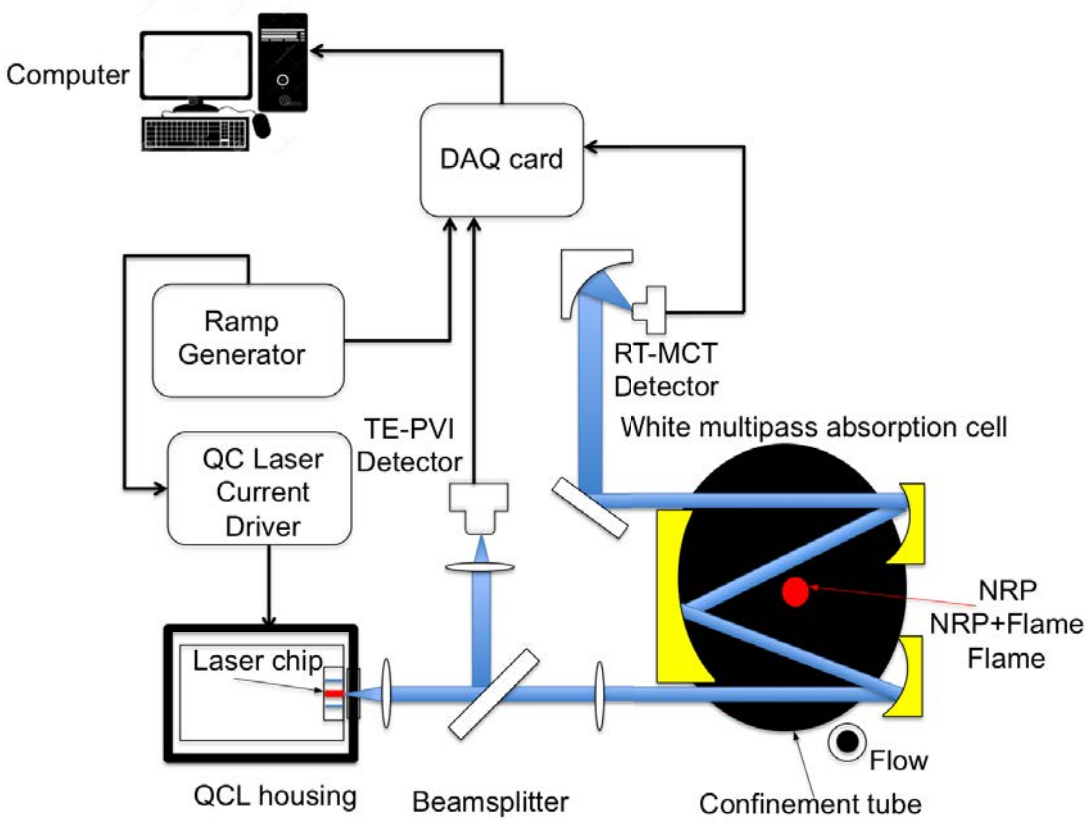

Figure 4.14: Multiple pass QCLAS setup. OAP mirrors have been replaced by lenses for clarity. The example is given is for a 4-pass White cell.

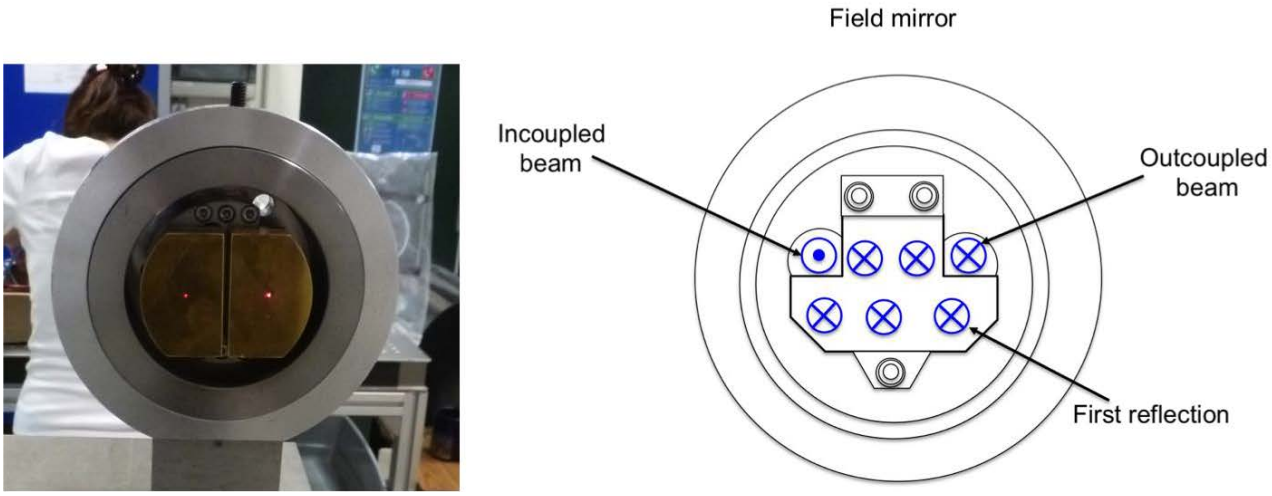

Figure 4.15: Front views of objective (left) and field (right) mirrors. Reflection patterns for a 12-pass system.

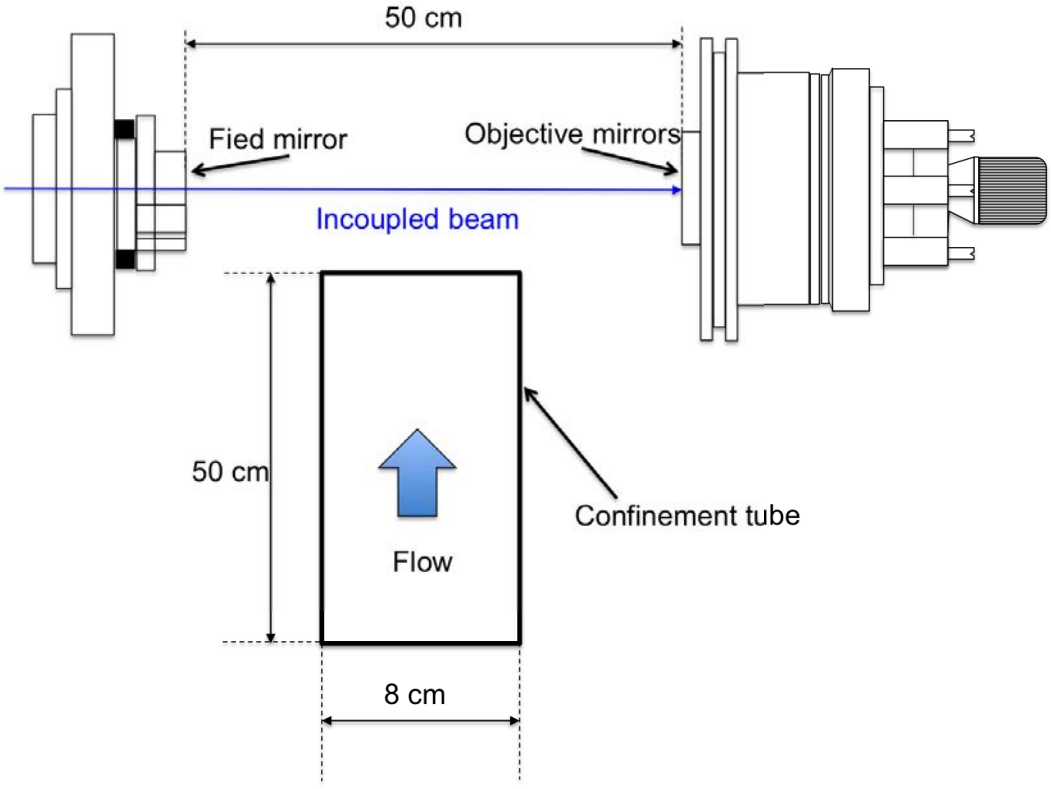

Figure 4.16: Side view of the multiple pass absorption cell with the confinement tube. Field and objective mirrors are 50-cm apart. The confinement tube is placed at the middle of the cell.

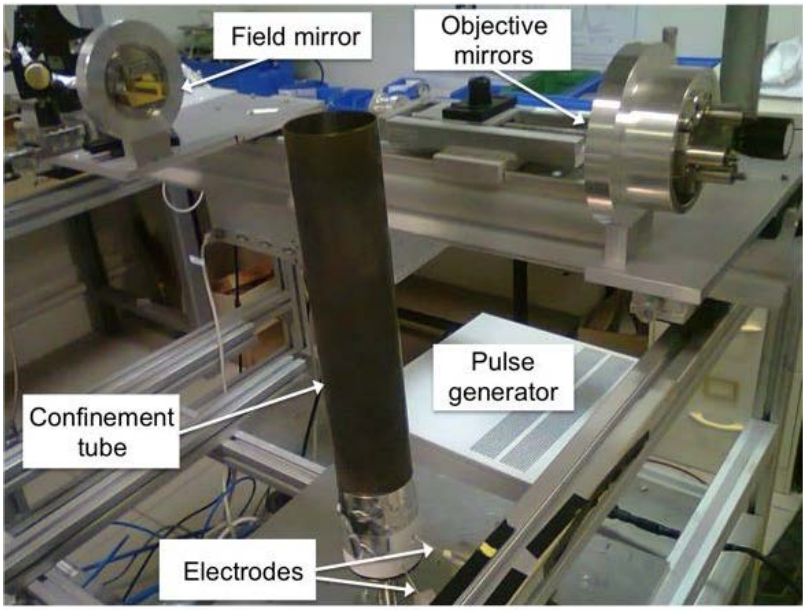

Figure 4.17: Side view of the multiple pass absorption cell with the discharge generation system and the confinement tube. NRP discharges are generated near the bottom of the confinement tube.

Table 4.7: Technical specifications for the multipass system.

Cell type	White
Flange size	DN 63
Distance between sealing surfaces of flanges	52 cm
Distance between mirrors	50 cm
Mirror's material	Gold-coated aluminium
Reflectivity (4 µm-7.5 µm)	0.96
Coupling windows	KBr
Observation window	Quartz

Multipass measurements in preheated air

In our kinetics studies, the NO density is measured in post-NRP discharges in preheated air, as a function of the gas temperature. To this aim, the foregoing facility was slightly modified: the air injection system was replaced by the one of the air preheater and the 50-cm long confinement tube at the top was replaced by a 25-cm tube in order to be able to reach high temperatures at the exit of the tube. The resulting setup is illustrated in figure 4.18 and a photograph is provided in figure 4.19.

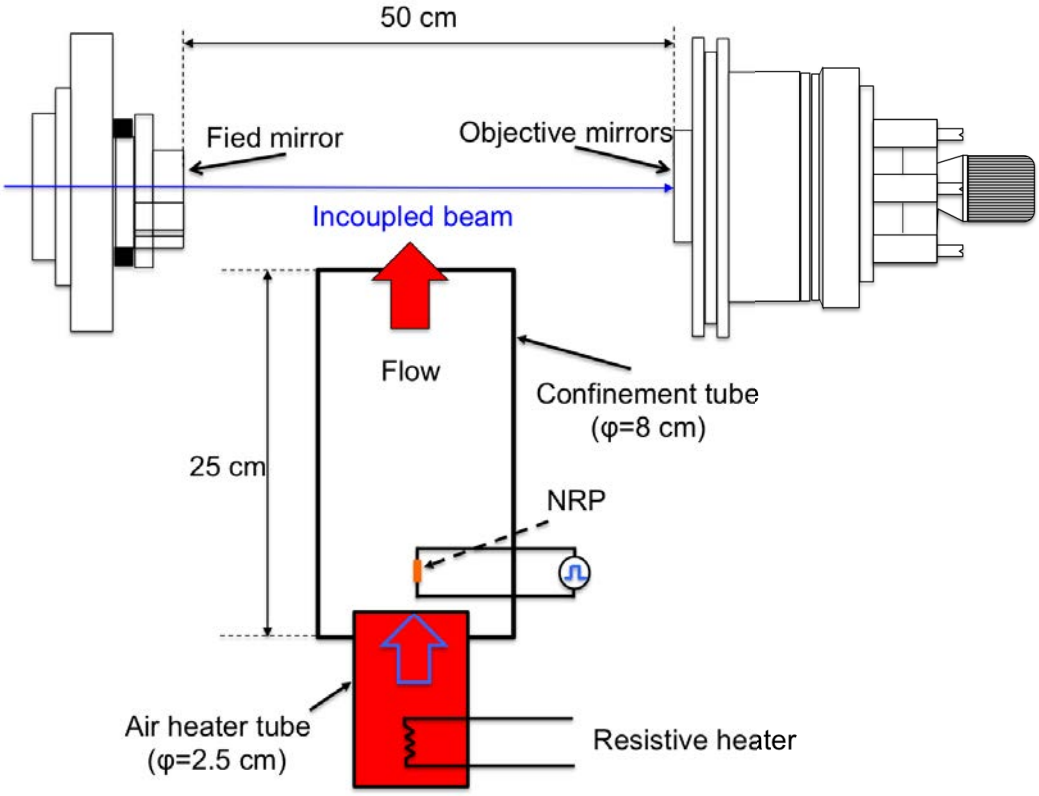

Figure 4.18: Multipass platform for NO measurements in post-NRP discharges in preheated air. The reduced tube height (25 cm instead of 50 cm) enables us to reduce thermal losses between the heating system and the exit of the confinement tube.

Figure 4.19: Photograph of the setup for measurements in preheated air.

Signal detection

The laser radiation on the reference and measurement channels are both acquired using MCT detectors.
For the reference measurement, we use a 600-MHz bandwidth Vigo System two-stage TEC photovoltaic element, which has a detectivity of up to 2 x 10^{10} cmHz$^{1/2}$W^{-1} at 5 µm. The photosensitive active area inside the detector is 1 x 1 mm^2 for a maximum solid angle field of view of 35°. The detector element is powered by a Q-MACS 5V/2A optimized supply.
A photoconductive RT-MCT detector from Daylight Solutions is used for the measurement channel. Its detectivity can reach 2.5 x 10^9 cmHz$^{1/2}$W^{-1} at 5 µm for a response time lower than 3 ns. The active area of the sensor is again 1 x 1 mm^2 for a maximum solid angle field of view of 78°. A +15 VDC, +5 VDC voltage supply is necessary to power the detector. The characteristics and performances of both detectors are summarized in tables 4.8 and 4.9.

The limitations of the laser and the detector for temporally and spectrally resolved measurements are discussed by *Welzel*, [2009] and presented in appendix C.

Table 4.8: Characteristics of the Vigo Photovoltaic MCT detector performances.

Detector type	PVI-2TE-5
Active area	1 x 1 mm^2
Field of view	35°
Supply voltage	5V/2A
Current responsivity ±20% (5 µm) [A/W]	1.9
Current Noise Density [pA/Hz$^{1/2}$]	8.8
Detectivity ±20% (5 µm) [cmHz$^{1/2}$/W]	2.2 x 10^{10}
Bandwidth	600 MHz

Table 4.9: Characteristics of the Daylight Solutions MCT detector.

Model	HPC-2TE-100
Detector material	HgCdTe
Spectral response	4-12 µm
Active area	1 x 1 mm^2
Field of view	78°
Supply voltage	+15 VDC, +5 VDC
Responsivity [V/W]	2.5
Detectivity [cm $Hz^{1/2}$/W]	2.5 x 10^9
Response time	3 ns

4.5.4 Wavelength calibration

In order to identify absorption lines and species, the system needs to be calibrated on the X-axis (wavelength calibration). Measurements in this work are conducted in the inter-pulse mode. In few ms, the laser generates a ramp over about 0.4 wavenumber. The displayed signal on the computer screen represents the transmitted signal in mV as a function of the pixel number.

The X-axis calibration consists in converting pixels (used to record spectra) into wavenumbers. This is done in two steps: a relative and an absolute calibration. For the relative calibration, we use a three-inches long, one-inch inner diameter single Germanium crystal (see figure 4.27) to convert distances in pixels into relative wavenumber (cm^{-1}). The single Ge crystal acts like a Fabry-Pérot interferometer (a Fabry-Pérot etalon precisely) when placed in the optical path of the QCL radiation. Up to 25 interference fringes are resolved over the operating window as depicted in figure 4.20. The distance between adjacent transmission peaks, which is called the free spectral range (FSR) is constant in the small spectral window of the QCL and is defined by (in wavelength units):

$$\Delta\lambda = \frac{\lambda_0^2}{2Ln(\lambda)cos(\alpha) + \lambda_0} \approx \frac{\lambda_0^2}{2Ln(\lambda)cos(\alpha)} \tag{4.7}$$

λ_0 is the laser central wavelength, L is the length of the etalon, $n(\lambda)$ is the wavelength- dependent Ge refractive index and α is the radiation incidence angle. At normal incidence it becomes:

$$\Delta\lambda \approx \frac{\lambda_0^2}{2Ln(\lambda)} \Rightarrow \Delta\tilde{\nu} \approx \frac{1}{2Ln(\lambda)} \tag{4.8}$$

The Ge refractive index variation with respect to the wavelength is plotted in figure 4.21 from [*Icenogle et al.*, 1976]. The evolution of the FSR with respect to the wavelength can then easily be deduced using equation 4.8. From figure 4.22, we have FSR ~ 0.0163 cm^{-1} at 5.2 µm.
As a result, 25 interference fringes represent about 0.0163 x 25 ~ 0.4 cm^{-1} ~ 3.4 x 0.12 cm^{-1}, where 0.12 cm^{-1} is the FWHM at room temperature and atmospheric pressure of the NO absorption feature at 1900.517 cm^{-1} (which is the widest of both absorption lines). Our system is therefore convenient for measurement at atmospheric pressure since we are able to record spectra on a spectral range three times greater than the FWHM of the lines at atmospheric pressure.

The calibrated spectrum is presented in figure 4.23. Now our measurement window is scaled in wavenumber. The X-axis wavenumbers are relative and must still be place on an absolute scale by finding the exact wavenumber of the peak's pixel at the center of the window.

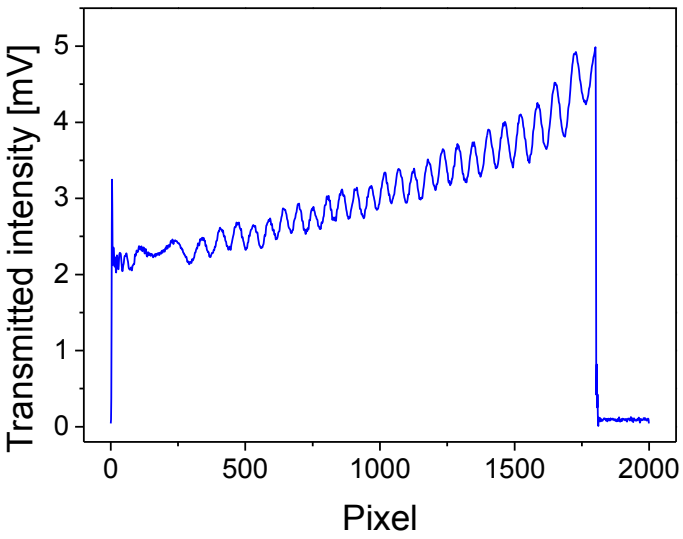

Figure 4.20: X-axis relative calibration. Germanium etalon fringes in pixels. The distance between the peaks of adjacent fringes is constant in the QCL spectral range and corresponds to the etalon free spectral range (FSR).

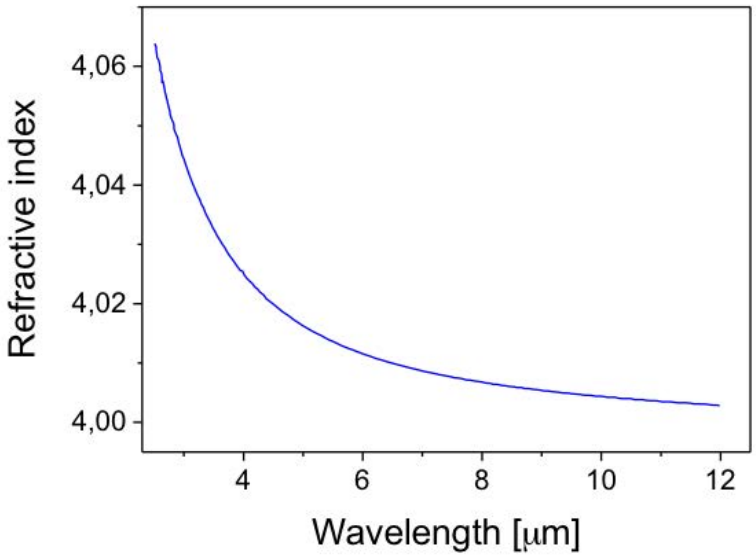

Figure 4.21: Germanium etalon refractive index as a function of the wavelength.

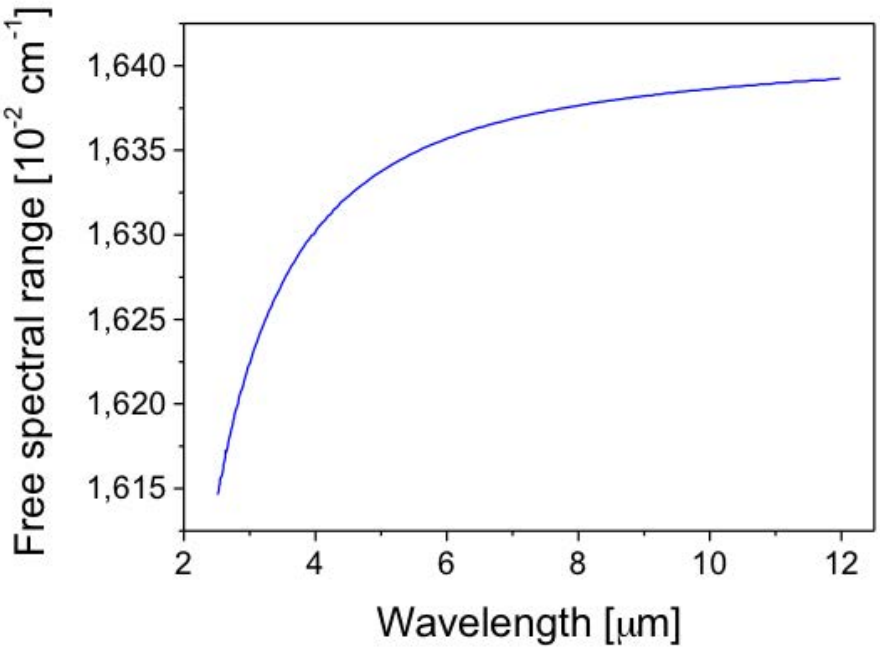

Figure 4.22: Germanium etalon free spectral range as a function of the wavelength. At 5.2 µm, FSR ~ 0.0163 cm^{-1}.

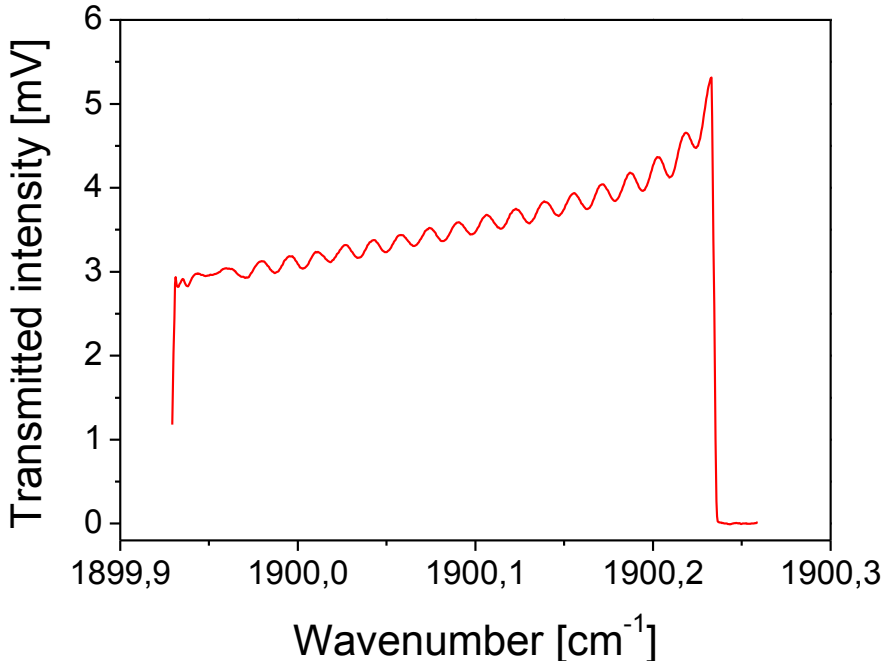

Figure 4.23: X-axis relative calibration. Germanium etalon fringes in wavenumber.

For the purpose of X-axis absolute calibration, we used a 5-cm long low-pressure cell filled with NO at room temperature and 2 mbar, in combination with Q-MACS software simulations. Figure 4.24 shows NO lines that we can probe by tuning the laser central wavelength (by changing the laser temperature). Four pairs of absorbing features can be observed. Each pair can be distinguished from the other ones by the distance between both lines constituting the pair. So a precise experimental measurement of the distance between two NO adjacent lines will result in an absolute calibration of the spectrum. However, the smallest target distance is 0.441 cm^{-1} (as outlined in figure 4.24), which is greater than the maximum spectral range (0.4 cm^{-1}) we can cover on the same window. To overcome this, we use at the same time NO lines from the low-pressure cell and water lines from the methane-air combustion. Figure 4.25 depicts a simulated transmittance spectrum of ambient NO, hot NO and hot water. It appears that water lines between NO lines can be used for distance measurements. Both NO lines are not visible simultaneously on the window but each of them is visible simultaneously with the water line. Figure 4.26 shows an experimental recording of the distance between each NO line and the water line at the middle. The results: 0.203 and 0.238 cm^{-1} are consistent with simulations for the pair (1900.076; 1900.517 cm^{-1}). As a result, to complete the calibration process we just need to tune the laser wavelength so that the high NO absorption feature (at low pressure) is located at the center of the window (pixel 900). Then for the relative calibration process, we set this pixel at 1900.076 cm^{-1}.

Finally, figure 4.27 shows a photograph of the QCL platform with the alignment and wavelength calibration tools.

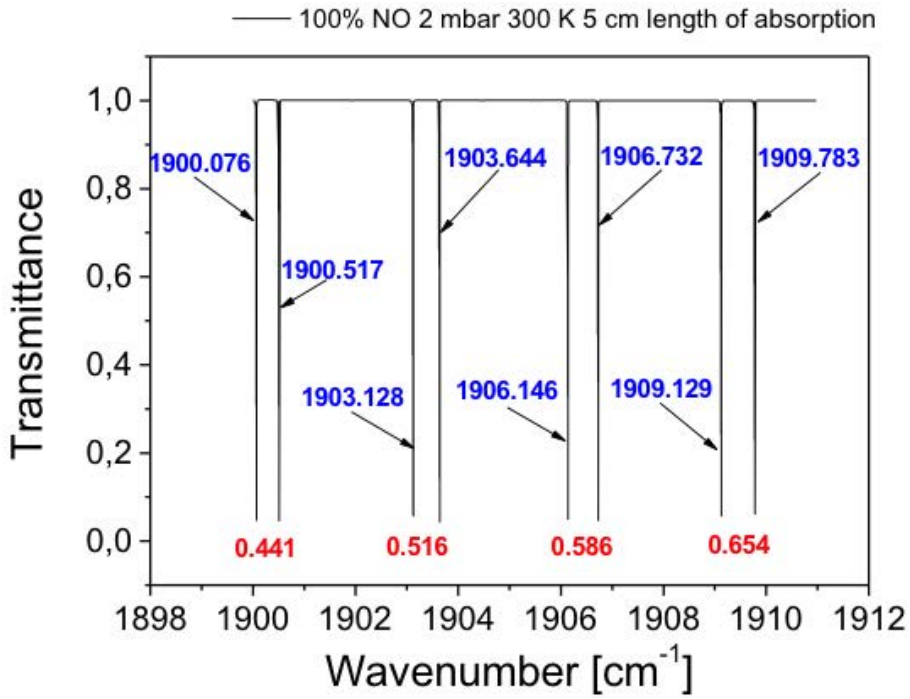

Figure 4.24: X-axis absolute calibration. Q-MACS simulation using HITRAN database: four pairs of NO lines are available over the laser spectral range.

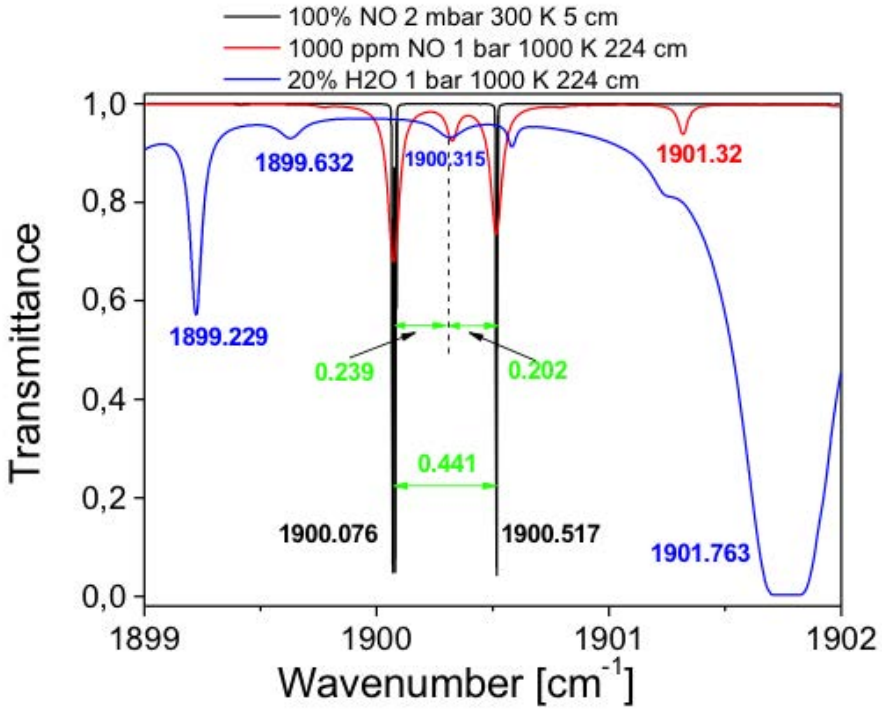

Figure 4.25: X-axis absolute calibration validation. Q-MACS simulation using HITRAN database: NO lines and hot water lines.

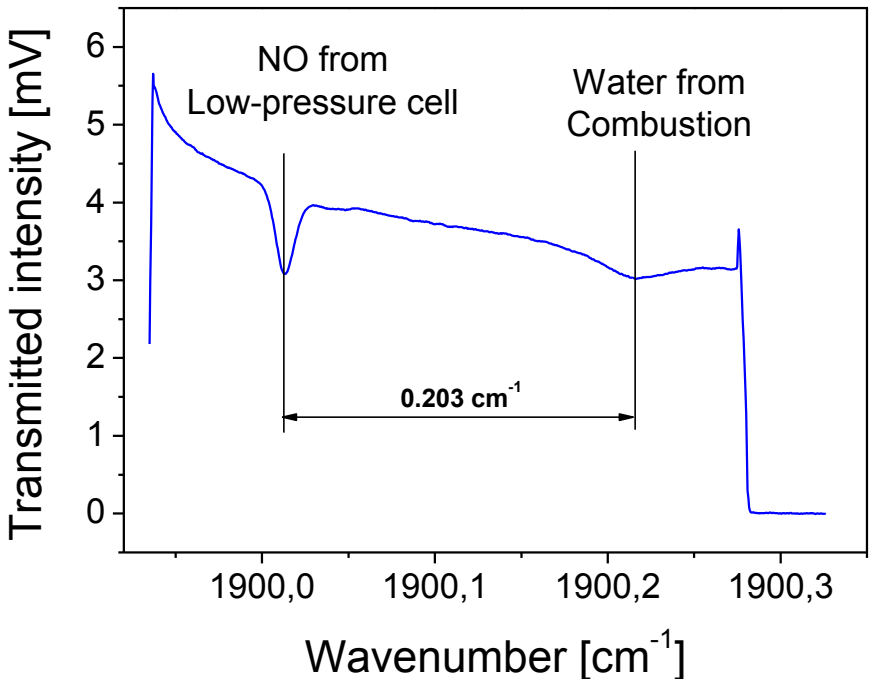

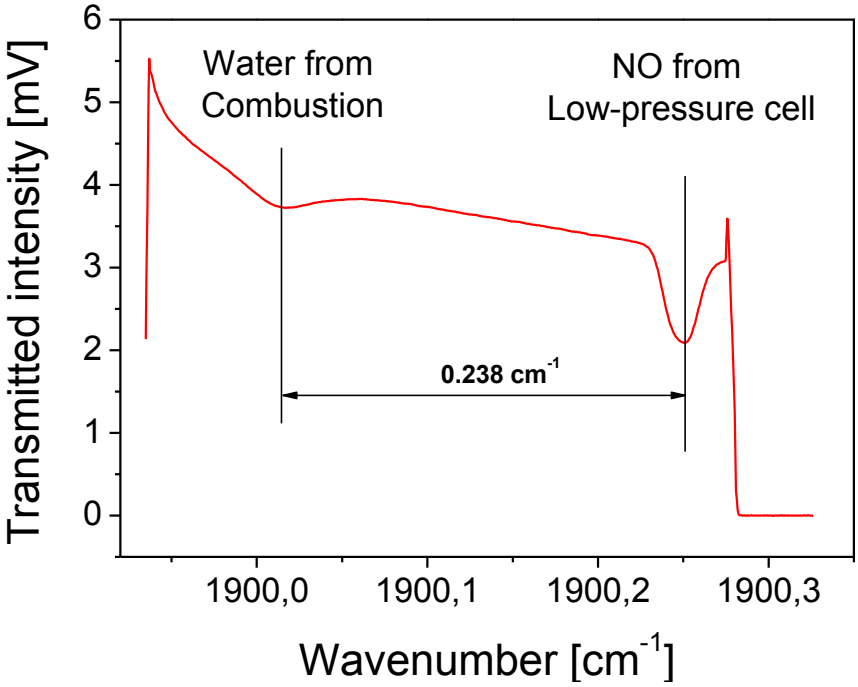

Figure 4.26: X-axis absolute calibration. Experimental measurements of spectral distance between absorption features in the NO cell and in combustion environment.

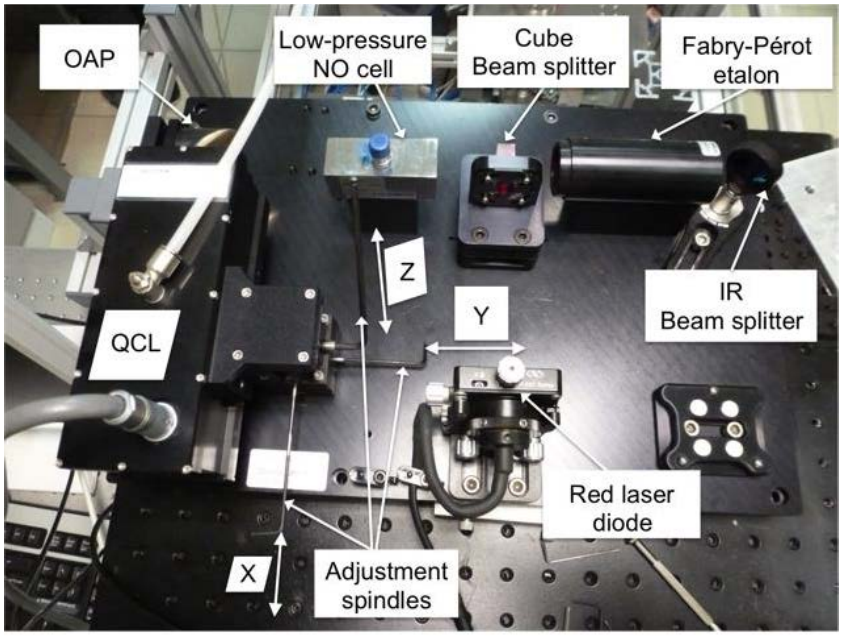

Figure 4.27: Photograph of the laser platform with the etalon, low-pressure cell and adjustment spindles.

4.5.5 QCL absorption artefacts

Equation 3.13 shows that the density of molecules is proportional to the area under the absorbance spectrum. Nevertheless this is true only if non-linear effects such as detector saturation, power saturation, laser broadening, multimode and rapid passage do not affect the recorded line shapes. The occurrence of each of these phenomena needs to be treated before the spectral data is converted into density or temperature. In the following, we will discuss these aspects in our measurements.

Detectors saturation

Photodetectors respond to incoming photons by creating electrons in their circuits. These electrons generate a current and thus a voltage. The quantum efficiency of such devices is defined as the ratio of the number of charge carriers generated in the circuit to the number of photons collected on the detector active area. At a fixed wavelength, the ideal detector exhibits a constant quantum efficiency over a large incoming photons power range. It has a linear behavior over this power range. Above a critical value the detector saturates i.e. the number of charge carriers generated remains constant even if the number of incoming photons increases. Figure 4.28 presents the laser signals measured using Daylight and QMACS detectors as a function of the wavenumber. No saturation is observable over the investigated laser input voltage range as the signals increase with laser input power. In figure 4.29, the mean transmitted signals as a function of the laser input voltage are shown to be linear using two detectors and two spectral regions. The linear behavior of laser intensity with the applied voltage is achieved when the laser is far from its threshold.

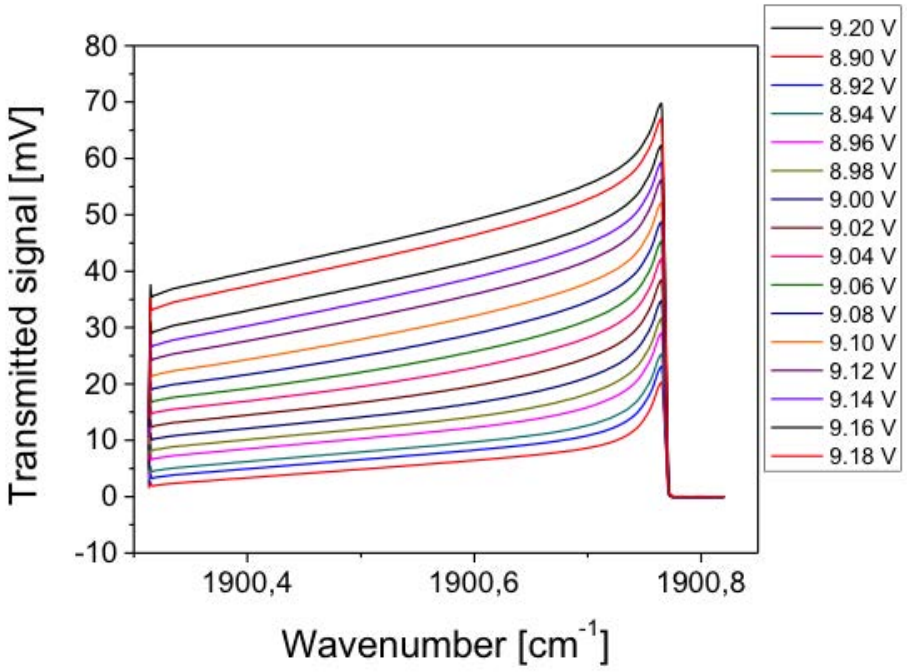

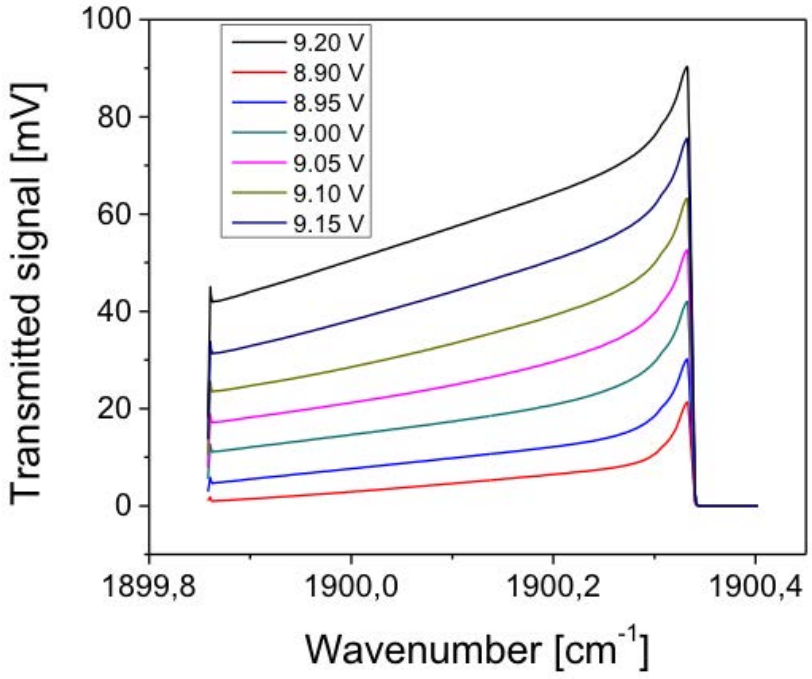

Figure 4.28: Detectors inter pulse response at different laser input intensities. Top graph: Daylight detector and line at 1900.517 cm^{-1}, Bottom graph: Q-MACS detector and line at 1900.076 cm^{-1}.

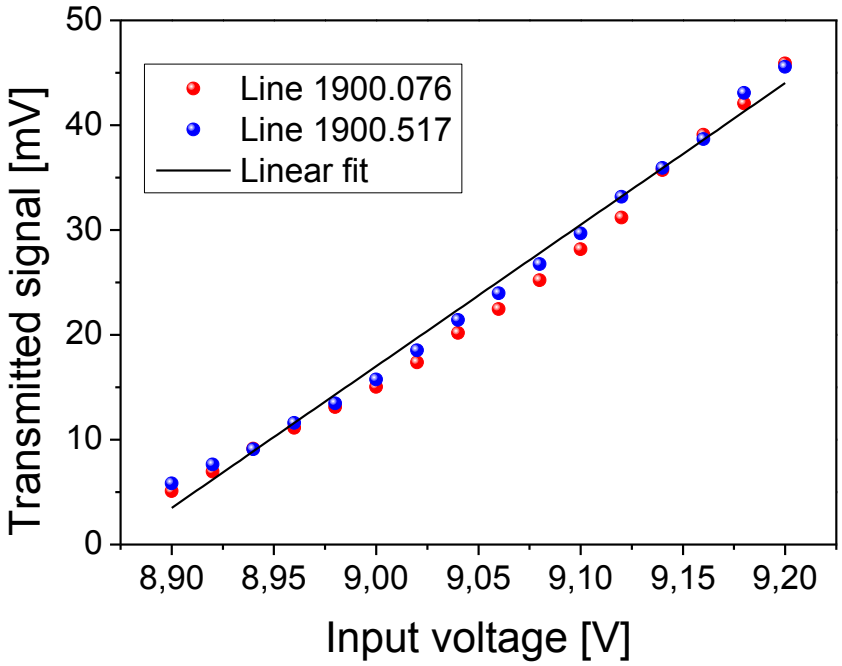

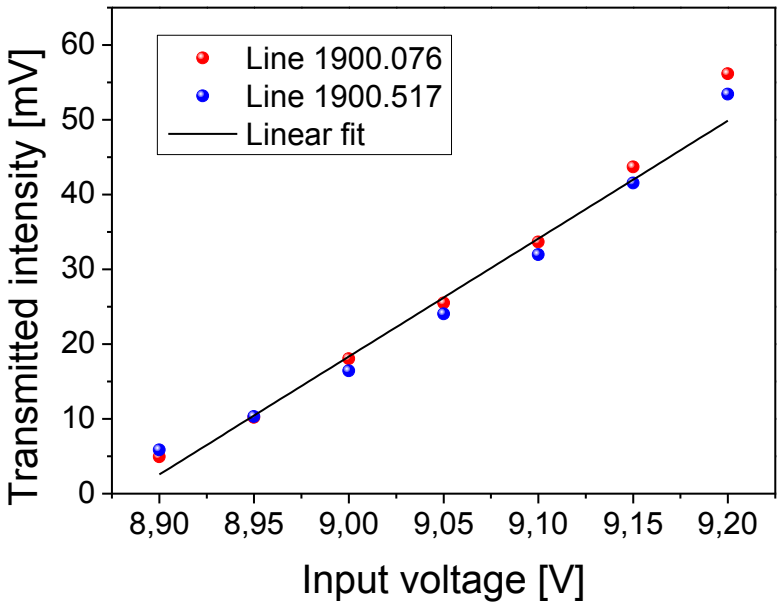

Figure 4.29: Linearity domain of the detectors. Top graph: Daylight detector, Bottom graph: Q-MACS detector.

Power saturation

When an atom or a molecule absorbs a photon, it excites bound electrons, which jump from a lower energy level to an upper one. The depopulation rate of the lower level is proportional to the product of the Einstein absorption coefficient by the spectral energy density of the incoming radiation field. The higher the incoming photon flux, the faster the lower level will be depopulated. If the incoming photons energy increases above a certain value, the depopulation process of the lower level can become faster than the repopulation ones. This will lead to a population inversion, as most of the particles will be in the upper level. As a result, the measured absorption signal will decrease: it is the power saturation. The latter can be derived from the atomic two-level system model illustrated in figure 4.30. When a laser field interacts with a sample of stationary atoms with only two energy levels, it involves four types of transition processes [*Stancu*, 2013]:

- **Stimulated absorption** whose event probability per unit time is $P_{12}(\nu) = B_{12}\,\rho(\nu)$, where B_{12} is the Einstein absorption coefficient and $\rho(\nu)$ the spectral energy density.

- **Stimulated emission** in which the atom starts in the excited level and emits a photon in coherence with those of the laser (same direction, frequency and polarization) and then ends up in the ground state. Its probability per unit of

time is $P_{21}(\nu) = B_{21}\ \rho(\nu)$. Here B_{21} is the Einstein coefficient for stimulated emission.

- **Spontaneous emission** (or fluorescence), for which the photon is spontaneously emitted in an arbitrary direction unrelated to the laser photons. The probability per unit time of the spontaneous process is equal to the Einstein coefficient for spontaneous emission A_{21}.

- **Non-radiative relaxations** (Collisional pumping and quenching loss) in which an atom in the ground state/excited state undergoes an excitation/a desexcitation due to collisions with others particles. The rate of pumping per unit of time is R_{12} and that of the quenching loss is R_{21}.

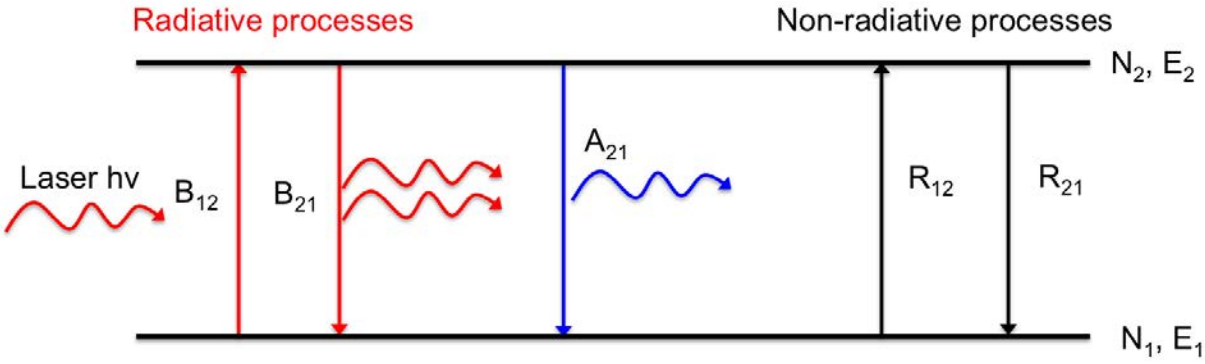

Figure 4.30: Schematic diagram of atomic two-level system model.

The statistical weights of levels 1 and 2 are g_1 and g_2. The temporal evolution of the populations N_1 and N_2 can be derived from equation:

$$\frac{dN_1}{dt} = -P_{12}N_1 - R_{12}N_1 + P_{21}N_2 + A_{21}N_2 + R_{21}N_2 = -\frac{dN_2}{dt} \tag{4.9}$$

If statistical weights g_1 and g_2 are equal, then $P_{12} = P_{21} = P$. Moreover considering the total population $N = N_1 + N_2$ and stationary conditions, it comes:

$$N_1 = N\frac{P + R_{21} + A_{21}}{2P + R_{12} + R_{21} + A_{21}} \tag{4.10}$$

If the laser is intense i.e. $P >> (A_{21}, R_{21}, R_{12})$, it results that $N_1 = N_2 = N/2$. In this configuration, accordingly to equation 2.14, the absorption coefficient approaches zero.
We can quantify the power saturation by comparing absorption probability per unit of time with the spontaneous emission probability per unit of time and quenching loss

rate R_{21}. The averaged Einstein spontaneous emission coefficient for the line at 1900.076 cm^{-1} is about 2.23 s^{-1} (see section 3.5.3).
At room temperature and atmospheric pressure, the FWHM of the line at 1900.076 cm^{-1} is about 0.112 cm^{-1}. As a result, the corresponding collision frequency $\lambda_{col} \sim 2\pi$ x FWHM = 2.1 x 10^{10} s^{-1}. For a Doppler dominated profile (at low pressure) and at room temperature, the FWHM of the foregoing line is 4.3 x 10^{-3} cm^{-1} and hence the collision frequency is about 8.2 x 10^{8} s^{-1}. To conclude, the quenching rate R_{21} ranges between 10^{8} and 10^{10} s^{-1} from low pressure (1 mbar) to atmospheric pressure.

Consider now the pumping rate:

$$P(\nu) = \frac{I}{h\nu} S(T) f(\nu) \tag{4.11}$$

where I is the power of the laser beam per unit of surface. $S(T)$ is the line intensity at a specified temperature T and $f(v)$ is the normalized line spectral shape. Since the maximum laser output average power is about 2.5 mW with a 0.2 % duty cycle and the diameter of the laser beam in the reference gas cell region is about 1 inch, the resulting maximum power per unit of surface is about 250 mW/cm^2. At 300 K for line at 1900.076 cm^{-1}, S(T) ~ 1.22 x 10^{-19} cm. At the center of the transition, we have $f(v_0) \sim 1/\Delta v_D \sim$ 231 cm in the case of a Doppler profile (at low pressure for instance) and $f(v_0) = 2/(\pi \Delta v_L) \sim 8$ cm in the case of a Lorentzian profile (at atmospheric pressure). Finally at 1900.076 cm^{-1}, $h\nu \sim 3.8$ x 10^{-20} J. As a result $P(v_0) \sim 3.75$ s^{-1} in the case of a a Lorentzian profile and $P(v_0) \sim 150$ s^{-1} in the case of a Gaussian Doppler profile. We hence have $A_{21} < P << R_{21}$. Power saturation is negligible even for the maximum laser output power.

The practical approach consists in measuring a known NO density with different laser intensities. Figure 4.31 shows an example of a transmitted signal for a 1 mbar NO cell, which corresponds to a 2.45 x 10^{16} cm^{-3} density. Figure 4.32 shows that both lines experience saturation when tuning the laser intensity from 8.90 to 9.20 V input voltage as the measured NO density decreases when the input voltage increases above 9 V. Within the error bars, a flat regime is observed between 8.90 and 8.95 V, which is the expected trend for a non-saturated regime. However, the measured densities are underestimated by 30 and 35 % respectively because the laser broadening was not considered. At low pressure, the Doppler FWHM is comparable with the laser FWHM of our system. Therefore the integrated absorption coefficient is underestimated [*Yalin and Zare,* 2002]. The decay of the density for higher laser input voltage is most certainly affected by laser multimode [*Paiella et al.*, 2000; *Gordon et al.*, 2008] and not by power saturation.

Multimode phenomena in QCLs were evidenced by *Paiella et al.* [2000] using a FTIR spectrometer. They found that above a critical pumping current value, QCLs could switch from a single mode operation to a multimode one. The latter exhibited a broadband spectrum besides an additional component to the laser "main frequency". This resulted therefore in an underestimation when using the probed line to get absolute densities.

In the case of atmospheric pressure measurements and for a laser input voltage below 9 V, no corrective factors are needed. This is because the laser width is much smaller than the collisional broadening width and the multimode effect is negligible.

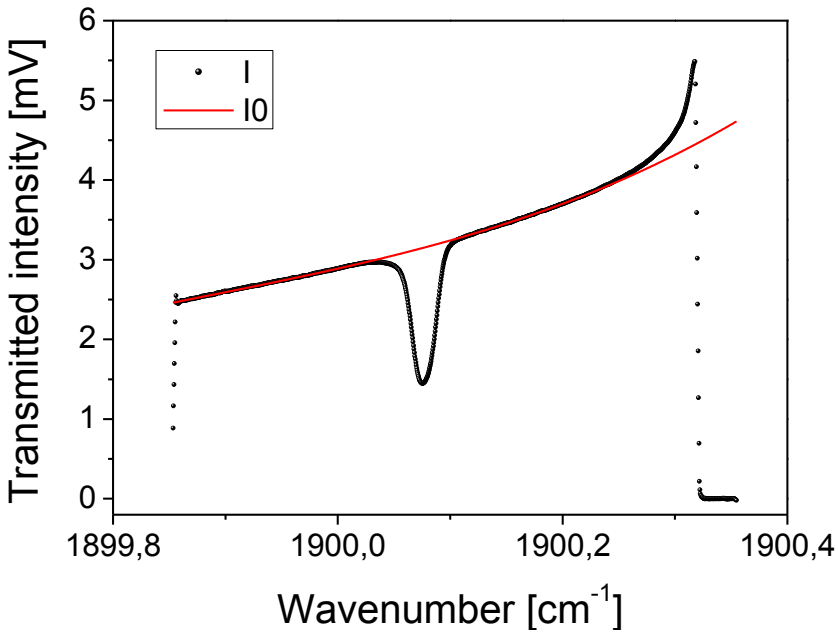

Figure 4.31: Sample measurement in the low-pressure cell. Measurement and third order polynomial reconstruction of the baseline (I_0).

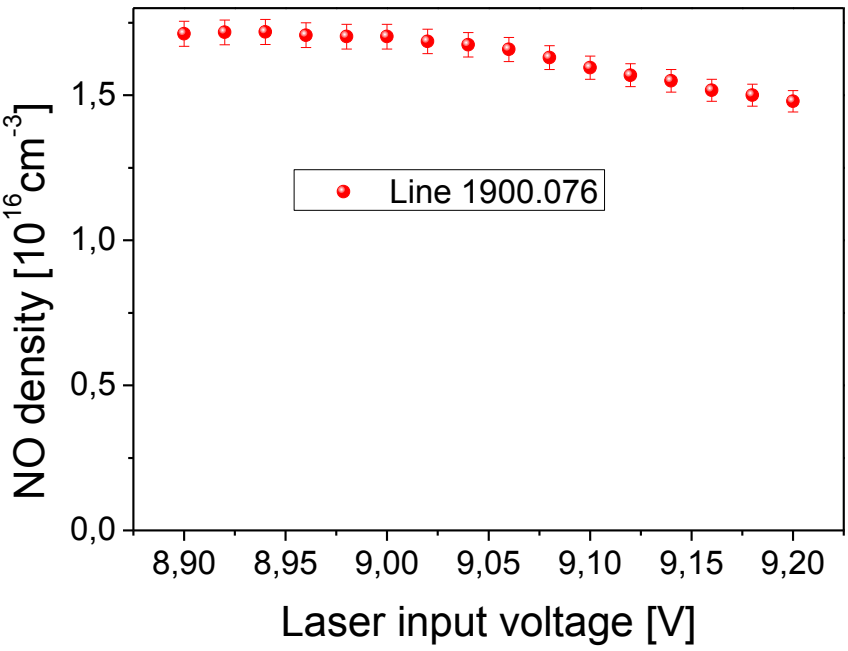

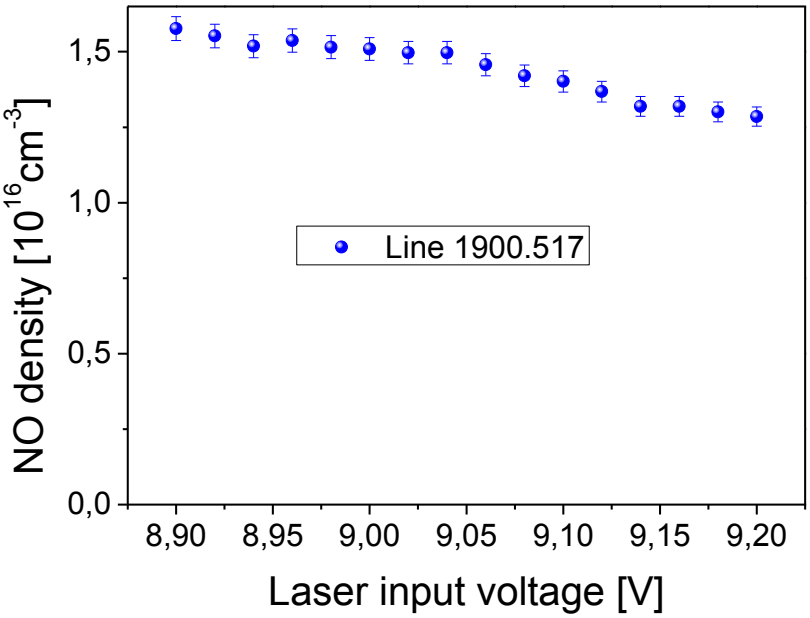

Figure 4.32: Power saturation verification. NO density measurements for both absorption lines as a function of laser intensity. The expected NO density at 1 mbar is 2.45 x 10^{16} cm^{-3}.

Rapid passage effect

This effect occurs when a rapidly swept radiation passes through a molecular resonance on a timescale much shorter than the collisional relaxation time

[*McCulloch et al.*, 2006; *Van Helden et al.*, 2009]. Since QCLs rapidly tune their emitted frequency to lower frequencies, the rapid "frequency down chirp" (typically 20-200 MHz/ns) can lead to rapid passage effects at low pressure. The higher the current intensity used to tune the QCL is increased, the higher the chirp rate is increased and the more rapid passage effects will appear. For instance, at 1 mbar and homogeneous NO sample exhibits Doppler absorption features with Doppler-limited FWHM about 0.0043 cm^{-1}, which is equivalent to about 120 MHz (considering that 1 cm^{-1} = 30 GHz). Under these conditions, the interaction between the QCL radiation and sample molecules ranges between 0.6 ns (120/200) and 6 ns (120/20), which is less than the characteristic "de-phasing" time 1/FWHM (~ 8 ns). An example of a non-linearity caused by the rapid passage effect on 1 mbar NO sample is presented in figure 4.33. A "wiggle" artefact is located at the low-wavenumber part of the absorbance spectrum.
Nevertheless, due to fast collisional relaxation time at atmospheric pressure (~ 300 ps), the rapid passage effect does not affect absorption features at atmospheric pressure even when increasing the current flowing through the QCL.
Rapid passage can be modelled applying Maxwell-Bloch equations to a two levels system [*Duxbury et al.*, 2005, *McCulloch et al.*, 2006].

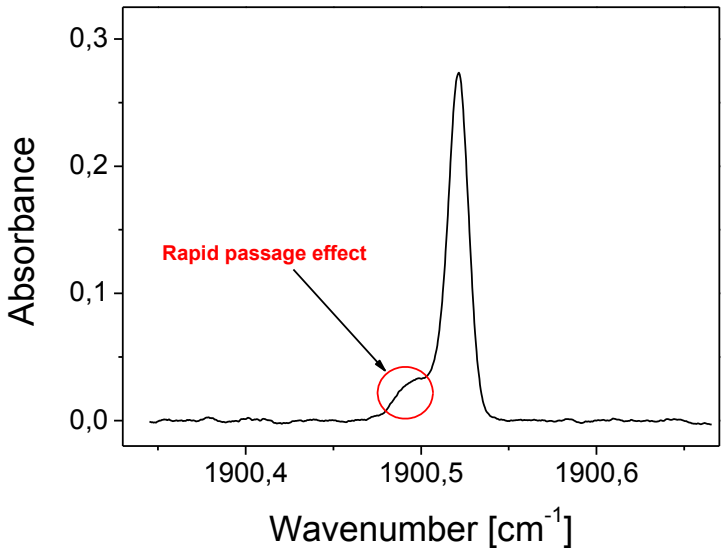

Figure 4.33: Sample absorbance measurement at 1 mbar showing the artefact caused by rapid passage effect.

4.6 Conclusions

In this chapter, we have presented the different experimental setups used in the present Phd thesis. In section 4.2, we have studied the NRP discharge, focusing on the electrode assemblies and on characteristics of the different pulse generator

systems. Then, high-temperature facilities, namely the combustion burner and the air preheater systems were described in section 4.3. In Section 4.4 we discussed the performances of both voltage and current probes used for the purpose of NRP discharge energy measurements. Finally, in section 4.5, we first outlined the QCL operating principles. Then, we described the different QCLAS experimental platforms developed. Third, we explained the wavelength calibration method in order to identify absorption lines and species. Fourth, we investigated the effects of artefacts phenomena on absolute density measurements. We have showed that over the investigated power range, our detectors were not subjected to saturation. Moreover, we have demonstrated that absorption lines at atmospheric pressure do not suffer from rapid passage and power saturation effects. Nevertheless, we experimentally found that absorption features could suffer from saturation effects arising from laser multimode. The latter effect was quantified in order to derive non-saturated profiles and hence absolute densities.

References

[1] Beyer, T., Braun, M., & Lambrecht, A. (2003). Fast gas spectroscopy using pulsed quantum cascade lasers. *Journal of applied physics*, *93*(6), 3158-3160.

[2] Darabiha, N. Esposito, E. Lacas F. Veynante, D. (2010). Combustion course of Ecole Centrale Paris.

[3] Duxbury, G., Langford, N., McCulloch, M. T., & Wright, S. (2005). Quantum cascade semiconductor infrared and far-infrared lasers: from trace gas sensing to non-linear optics. *Chemical Society Reviews*, *34*(11), 921-934.

[4] Faist, J., Capasso, F., Sivco, D. L., Sirtori, C., Hutchinson, A. L., & Cho, A. Y. (1994). Quantum cascade laser. *Science*, *264*(5158), 553-556.

[5] Galley, D. (2006). *Etude de la stabilisation de flammes turbulentes prévaporisées prémélangées pauvres* (Doctoral dissertation, Châtenay-Malabry, Ecole Centrale de Paris).

[6] Gordon, A., Wang, C. Y., Diehl, L., Kärtner, F. X., Belyanin, A., Bour, D., ... & Capasso, F. (2008). Multimode regimes in quantum cascade lasers: From coherent instabilities to spatial hole burning. *Physical Review A*, *77*(5), 053804.

[7] Hugi, A., Maulini, R., & Faist, J. (2010). External cavity quantum cascade laser. *Semiconductor Science and Technology*, *25*(8), 083001.

[8] Icenogle, H. W., Platt, B. C., & Wolfe, W. L. (1976). Refractive indexes and temperature coefficients of germanium and silicon. *Applied optics*, *15*(10), 2348-2351.

[9] Kosterev, A. A., Tittel, F. K., Gmachl, C., Capasso, F., Sivco, D. L., Baillargeon, J. N., ... & Cho, A. Y. (2000). Trace-gas detection in ambient air with a thermoelectrically cooled, pulsed quantum-cascade distributed feedback laser. *Applied Optics*, *39*(36), 6866-6872.

[10] McCulloch, M. T., Normand, E. L., Langford, N., Duxbury, G., & Newnham, D. A. (2003). Highly sensitive detection of trace gases using the time-resolved frequency downchirp from pulsed quantum-cascade lasers. *JOSA B*, *20*(8), 1761-1768.

[11] McCulloch, M. T., Duxbury, G., & Langford, N. (2006). Observation of saturation and rapid passage signals in the 10.25 micron spectrum of ethylene using a frequency chirped quantum cascade laser. *Molecular Physics*, *104*(16-17), 2767-2779.

[12] Namjou, K., Cai, S., Whittaker, E. A., Faist, J., Gmachl, C., Capasso, F., ... & Cho, A. Y. (1998). Sensitive absorption spectroscopy with a room-temperature distributed-feedback quantum-cascade laser. *Optics letters*, *23*(3) , 219-221.

[13] Pai, D. (2008). *Etude des plasmas générés par impulsions électriques nanosecondes répétitives dans l'air préchauffé à pression atmosphérique* (Doctoral dissertation, Châtenay-Malabry, Ecole Centrale de Paris).

[14] Pai, D. Z., Stancu, G. D., Lacoste, D. A., & Laux, C. O. (2009). Nanosecond repetitively pulsed discharges in air at atmospheric pressure—the glow regime. *Plasma Sources Science and Technology*, *18*(4), 045030.

[15] Pai, D. Z., Lacoste, D. A., & Laux, C. O. (2010). Nanosecond repetitively pulsed discharges in air at atmospheric pressure—the spark regime. *Plasma Sources Science and Technology*, *19*(6), 065015.

[16] Pai, D. Z., Lacoste, D. A., & Laux, C. O. (2010). Transitions between corona, glow, and spark regimes of nanosecond repetitively pulsed discharges in air at atmospheric pressure. *Journal of Applied Physics*, *107*(9), 093303.

[17] Paiella, R., Capasso, F., Gmachl, C., Sivco, D. L., Baillargeon, J. N., Hutchinson, A. L., ... & Liu, H. C. (2000). Self-mode-locking of quantum cascade lasers with giant ultrafast optical nonlinearities. *Science*, *290*(5497), 1739-1742.

[18] Pilla, G. (2008). *Etude expérimentale de la stabilisation de flammes propane-air de prémélange par décharges nanosecondes impulsionnelles répétitives* (Doctoral dissertation, Châtenay-Malabry, Ecole Centrale de Paris).

[19] Pittam, D. A., & Pilcher, G. (1972). Measurements of heats of combustion by flame calorimetry. Part 8.—Methane, ethane, propane, n-butane and 2-methylpropane. *Journal of the Chemical Society, Faraday Transactions 1: Physical Chemistry in Condensed Phases*, *68*, 2224-2229.

[20] Prokhorenko, V., & Boryssenko, A. (2000, April). Drift step recovery diode transmitter for high-power GPR design. In *8th International Conference on Ground Penetrating Radar* (pp. 277-281). International Society for Optics and Photonics.

[21] Stancu, G. D., Lang, N., Röpcke, J., Reinicke, M., Steinbach, A., & Wege, S. (2007). In situ monitoring of silicon plasma etching using a quantum cascade laser arrangement. *Chemical Vapor Deposition*, *13*(6-7), 351-360.

[22] Stancu, G., Lacoste, D., & Laux, C. (2012). Investigations of carbon monoxide emission in methane flames stabilized by nanosecond pulsed discharges using Mid-IR QCLAS. *Proceedings of the 21th ESCAMPIG*, 272-273.

[23] Stancu, G.D. (2013). Lectures notes. Plasma instrumentation, diagnostics and analysis. Master Optique, Matière, Plasma, Paris.

[24] Van Helden, J. H., Peverall, R., Ritchie, G. A. D., & Walker, R. J. (2009). Rapid passage effects in nitrous oxide induced by a chirped external cavity quantum cascade laser. *Applied Physics Letters*, *94*(5), 051116-051116.

[25] Welzel, S. (2009). *New Enhanced Sensitivity Infrared Laser Spectroscopy Techniques Applied to Reactive Plasmas and Trace Gas Detection* (Doctoral dissertation, Greifswald).

[26] Yalin, A. P., & Zare, R. N. (2002). Effect of laser lineshape on the quantitative analysis of cavity ring-down signals. *LASER PHYSICS-LAWRENCE-*, *12*(8), 1065-1072.

Chapter 5

Spatially resolved measurements of NO temperature and density in air NRP discharge

5.1 Introduction

In this chapter we present results from the 300-µm spatially resolved gas temperature and NO absolute density measurements in the NRP discharge. To the best of our knowledge, these results constitute the first reported radial gas temperature and species densities measurements, performed by QCLAS. This study is important because it allows the characterization of the NRP discharges in term of the effective length of absorption of NO and in term of the transport of species released by the discharge. This study gives also temperature and density results, which are useful for the understanding of NRP discharges kinetics.
The chapter is organized as follows. We first give in section 5.2, the experimental conditions of the studied case. The studied case is characterized in terms of voltage, current and energy deposited by the discharge in the gas. Section 5.3 presents the results of the lateral absorbance measurements for the two absorption features (1900.076 and 1900.517 cm^{-1}). Then, we apply the two methods exposed in section 3.6 to determine the gas temperature profile. More specifically, in section 5.4 we determine the gas temperature using the ratio of two absorption lines (assuming Boltzmann distribution). In section 5.5, the gas temperature is determined as well using the collisional width line shape. Then in section 5.6, the results of section 5.4 and 5.5 are discussed, compared each other and compared with literature results obtained in similar configurations. Finally, in section 5.7, the NO densities are inferred from the lateral absorbance measurements and from the gas temperature profiles. Both methods are compared.

5.2 Experimental conditions

All the measurements of this chapter are carried out with electrodes in a pin-to-pin vertical configuration (without bluff-body) separated by a 2-mm gap distance. The discharge operates in a vertical bottom-up airflow at ambient temperature with a 1.7 m/s typical velocity at the exit of the 16-mm tube, part of the injection system.
For these experiments, pulse generator PG2 on its second channel was employed. It furnishes a discharge pulse voltage about 3 kV, which results in a discharge current about 20 A. Energy deposited by the discharge is calculated with the method detailed

section 3.1. We find that about 0.5 mJ are given by the NRP discharge to the gas during the pulse. The recorded voltage signal is displayed in figure 5.1.

The NO diagnostic arrangement employed here is that shown in figure 4.11, in section 4.5.2. For a better signal to noise ratio, the measurements were averaged over 100 s each.

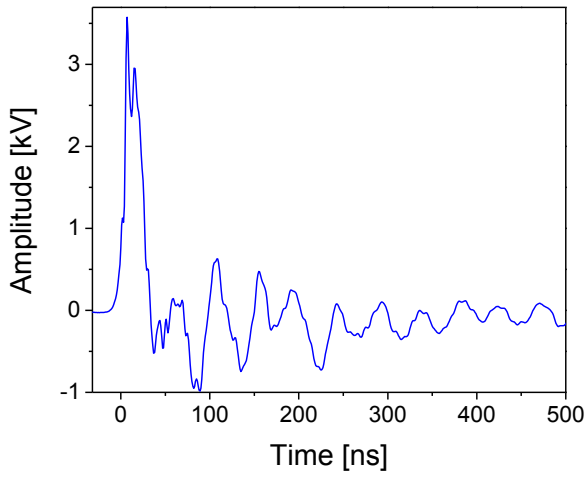

Figure 5.1: Studied case voltage signal.

5.3 Lateral absorbance measurements

Sample lateral absorbance measurements for both **lines 1 and 2** (at 1900.076 and 1900.517 cm^{-1} respectively) are shown in figure 5.2. For each line, measurements are displayed for two locations; at discharge center and at 4 or 5 mm distance from the axis. For each location, the measurement is well fitted by a Lorentzian profile as shown in figure 5.2. We notice that the lateral absorbance at discharge center is much bigger than the lateral absorbance recorded out of axis. This result will be discussed later.

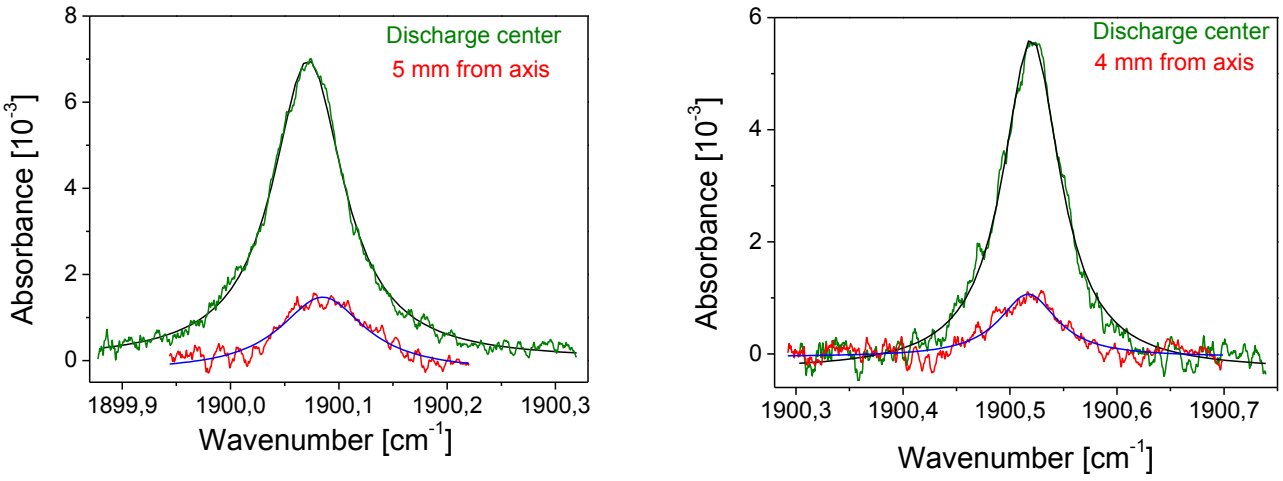

Figure 5.2: Sample lateral absorbance measurements for lines 1 (left) and 2 (right). Line of sight integrated lines are well fitted by Lorentzian profiles.

Full raw lateral data for line 1 are showed in figure 5.3. Observed trends of figure 5.2 are confirmed since first, the peak absorbance decreases with off-axis distance and second, the spread of NO produced by the NRP discharge in this configuration can reach up to 5-mm distance from axis (see figure 5.5). The Lorentzian fits of the absorbance profiles for each location are presented in figure 5.4 and figure 5.5 gives a 3D reconstruction of these lateral absorbance profiles.

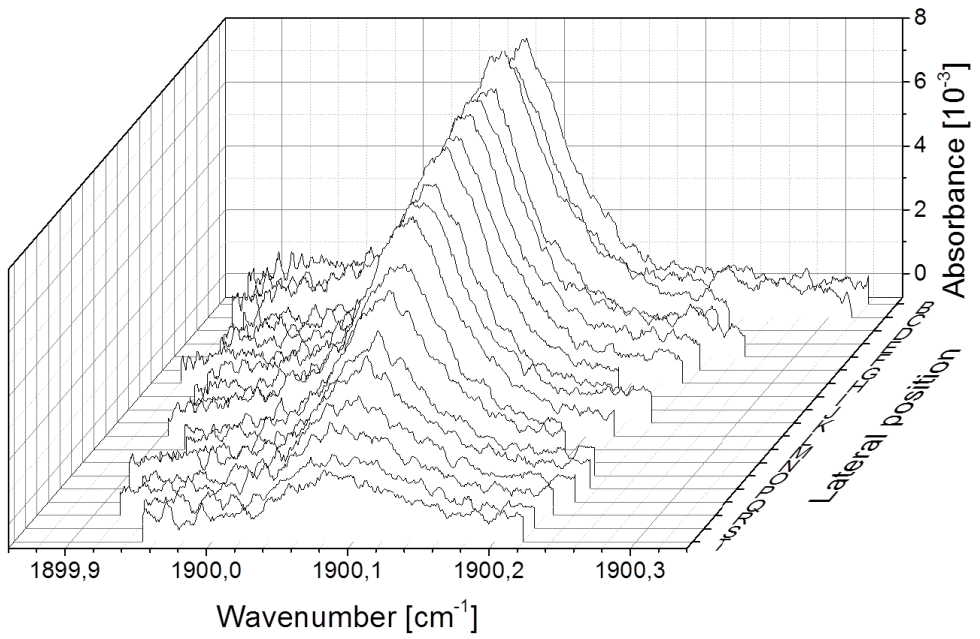

Figure 5.3: Complete line 1 raw lateral absorbance profiles.

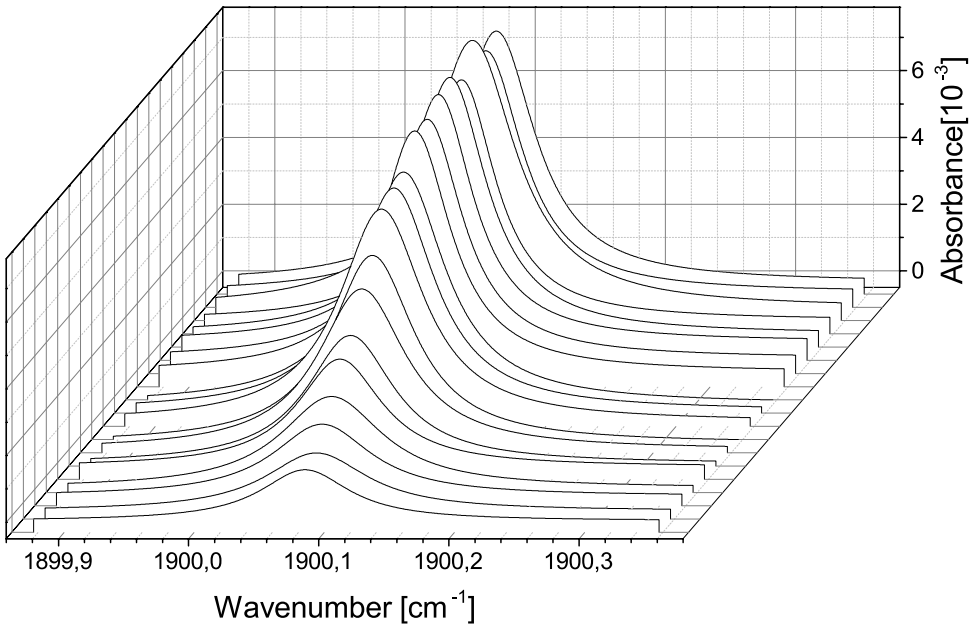

Figure 5.4: Complete Lorentzian fits of line 1 lateral absorbance profiles.

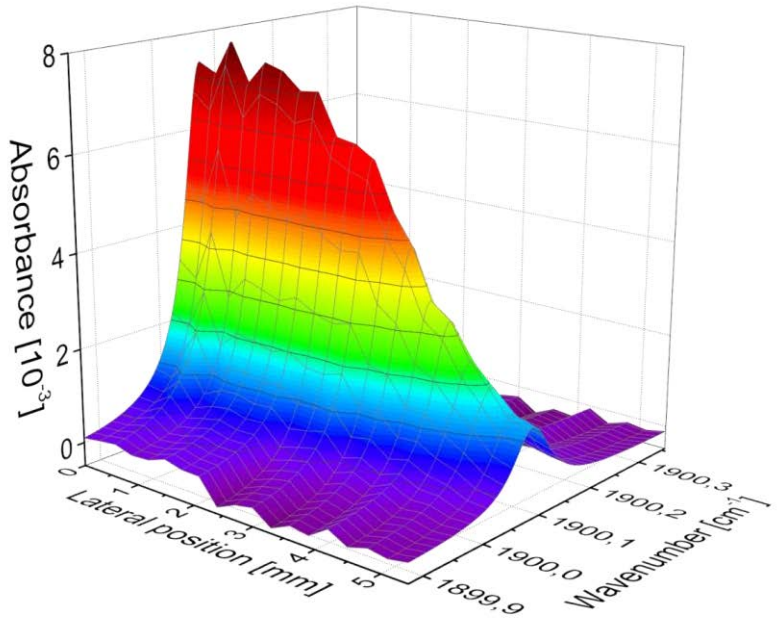

Figure 5.5: 3D map representation of Lorentzian fits of line 1 lateral absorbance profiles.

The same procedure is applied for line 2. The raw lateral measurements are depicted in figure 5.6. The Lorentzian fits of the raw profiles are given in figure 5.7. Figure 5.8 illustrates a 3D map representation of line 2 lateral absorbance profiles. Here again we observe that NO spreads far from discharge center and absorbance decreases as well with off-axis distance.

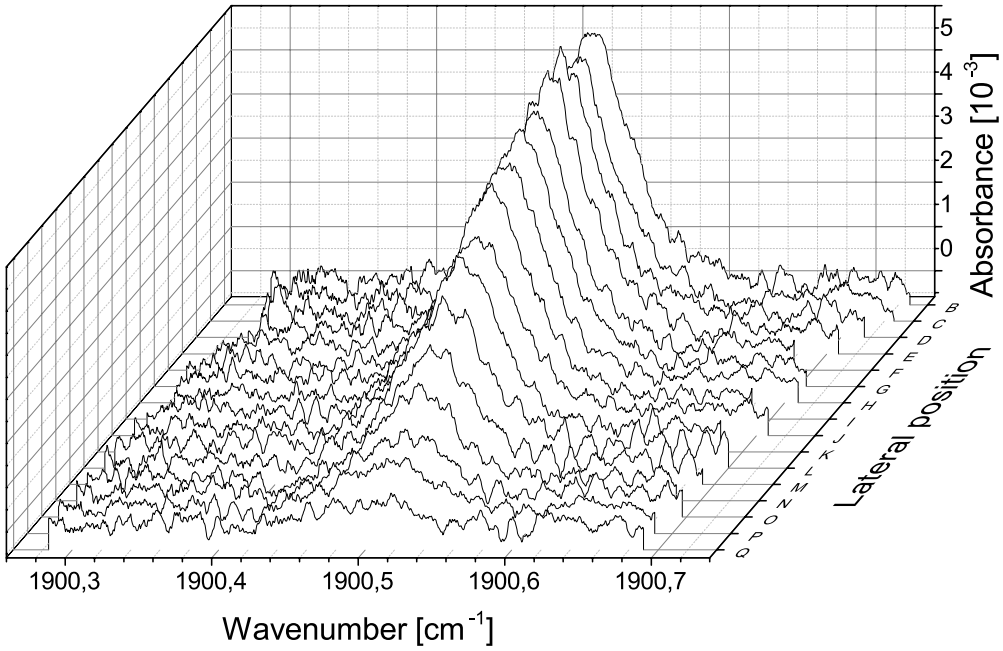

Figure 5.6: Complete line 2 raw lateral absorbance profiles.

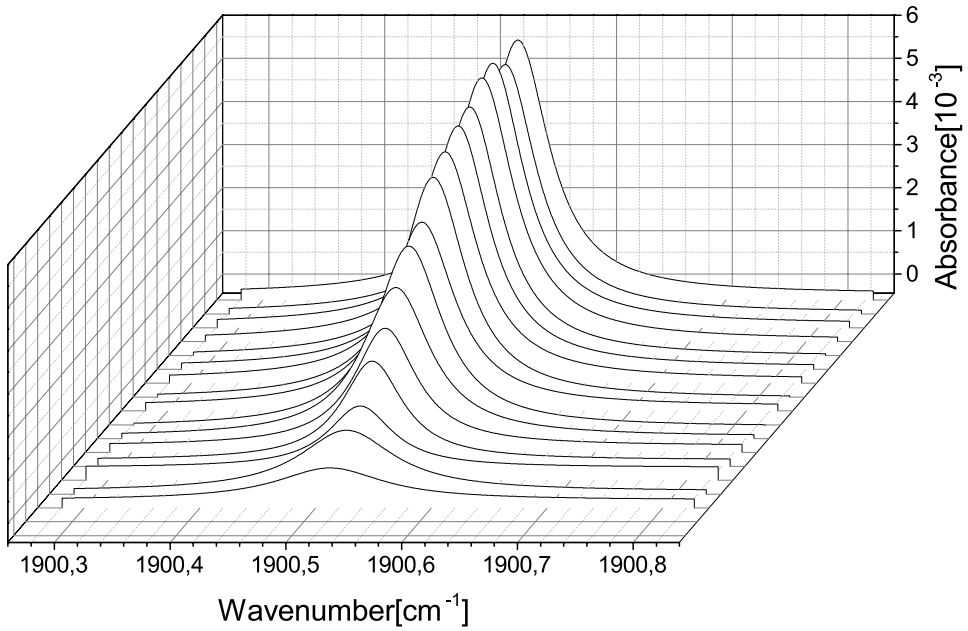

Figure 5.7: Complete Lorentzian fits of line 2 lateral absorbance profiles.

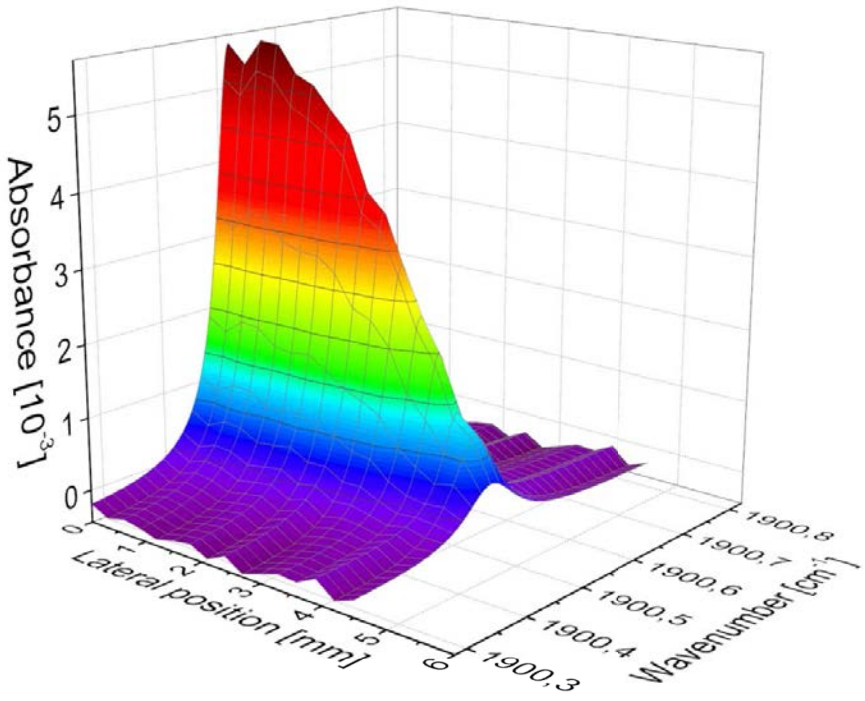

Figure 5.8: 3D map representation of Lorentzian fits of line 2 lateral absorbance profiles.

The large spread of NO in the radial direction is unexpected since the bottom-up airflow velocity at injection exit is about 1.7 m/s and the NO diffusion coefficient in air at atmospheric pressure is about 1.60 cm^2/s at 1000 K [*Yos*, 1963] and about 0.18 cm^2/s at 300 K [*Massman*, 1998]. This means that during the gas residence time between the electrodes, which is about 1 ms (2×10^{-3} /1.7), the expected diffusion length is at most about $(1.6 \times 10^{-4} \times 1 \times 10^{-3})^{0.5} = 0.4$ mm. This value is one order of magnitude lower than the 5-mm expansion measured. Hence the NO particles should be carried away by the vertical flow. However surprisingly, our results show an important spreading in the radial direction. Therefore, only the recirculation behind the electrodes can explain such results. Besides that, we assume here that there is no NO creation mechanism during the convection time.
The lateral absorbance profiles are surprisingly found to have Lorentzian shapes. Following the axisymmetry of NO temperature and density, we expect the local absorption coefficients to be Lorentzian and constant over rings of radius r (see figure 3.8 of section 3.4). Because the absorbance spectrum is obtained from a line-of-sight integrated lateral measurement, this summation result in a complex profile. The differences in density and temperature result in local Lorentzian profiles that can have different peak amplitude and width. The resulting profiles are therefore expected to be more complex than simple Lorentzian. However, in our case, the lateral profiles were well fitted by Lorentzian shapes.

Another key aspect of this measurement was the reproducibility. Prior to our measurements, the stability of the optical arrangement and of the NRP discharge was checked over duration of several hours. Firstly, for the optical stability, we carried out measurements far from the discharge center, where there is no absorption and then we verified that the ratio between the baselines recorded by reference and measurements detectors is constant up to 4 hours duration. Secondly, for the stability of the NRP discharge, using the strongest absorption line, we measured NO absorption spectra at discharge center and we verified that the (spectrally) integrated absorbance remains constant (the variation is less than 2 %) up to 3 hours duration.

5.4 Gas temperature determination using ratio of two absorption lines (Boltzmann distribution)

In this section, the spatially resolved gas temperature is determined using the method explained in section 3.6.1. As reminder, for both absorption features, we first need to calculate the (spectrally) integrated absorbance at each lateral location. Then second, the obtained profiles need to be Abel-inverted to yield the (spectrally) integrated absorption coefficients. The temperature is inferred from the ratio of lines 1 and 2 integrated absorption coefficients. This method relies on the Boltzmann distribution over the rotational structure of NO. This is justified in our case by the fast collisional relaxation time at atmospheric pressure ~ 1/FWHM. For a temperature ranging between 300 and 1400 K, NO profiles (line 2 for instance) FWHM vary from 5 x 10^{-2} cm^{-1} up to 0.12 cm^{-1}, which correspond to a relaxation time between 300 and 700 ps (1 cm^{-1} = 30 GHz). Few collisions are therefore required to reach equilibrium. In addition, the energy distance between rotational levels is small compared to translational energy, and therefore, heavy particle collision mechanism leads to equilibrium.

The area under each Lorentzian fit of absorbance curve is calculated. The results for both lines are displayed in figure 5.9. We can see that the integrated absorbance decreases with the off-axis distance for both lines. This decrease is not an obvious result. Actually, the line-of-sight-integrated, (spectrally) integrated absorbance measurements are affected by the absolute NO density but also by the temperature (via the line strength) as illustrated in equation 3.19. At discharge center (radially speaking) we expect a high-NO density and a high gas temperature. High NO density increases the integrated absorbance but high-temperature decreases the integrated absorbance (this is due to the line strength decrease with the rising temperature). The opposite trend is expected far from discharge axis (radially speaking): a low NO density will decrease the integrated absorbance while decreasing the temperature will increase the integrated absorbance. The plots in figure 5.9 result from both effects i.e. NO density and gas temperature effects.

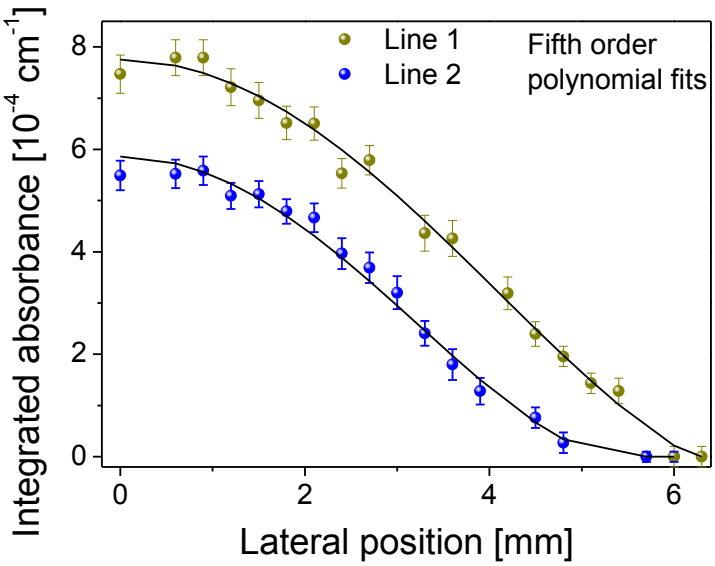

Figure 5.9: (Spectrally) integrated lateral absorbance profiles. Profiles are well fitted by fifth order polynomial functions.

Note that for these measurements the baseline measurement has a larger uncertainty. Because NRP discharges heat the gas, the index of refraction changes and hence the measured transmitted intensity (it is the so-called beam steering) changes. A convenient baseline measurement should include the effects of beam steering without any absorption feature. Consequently, error bars in figure 5.9 account for errors linked to the baseline change and to the variation of the NRP discharge from one shot to shot. Saturation effects have also been taken into account as explained in section 4.5.5.

Prior to Abel inversion, both integrated absorbance profiles of figure 5.9 are fitted by analytical functions. A good agreement is obtained using least-squares fifth order polynomial functions, as displayed in figure 5.9. Abel inversion is performed then on the polynomial fits. The outcome is given in figure 5.10. Following the previous discussion, as a result of a compromise between the integrated absorption coefficients decrease with the distance to discharge center and the line strength increase with this distance. In figure 5.10, the integrated absorption coefficient at discharge center is about 1.1 x 10^{-4} cm^{-2} for line 1 and about 8 x 10^{-5} cm^{-2} for line 2. Error bars are calculated using a code developed by [*Laux*, 1993]. It enables the computation of the uncertainty propagation through the Abel inversion process.

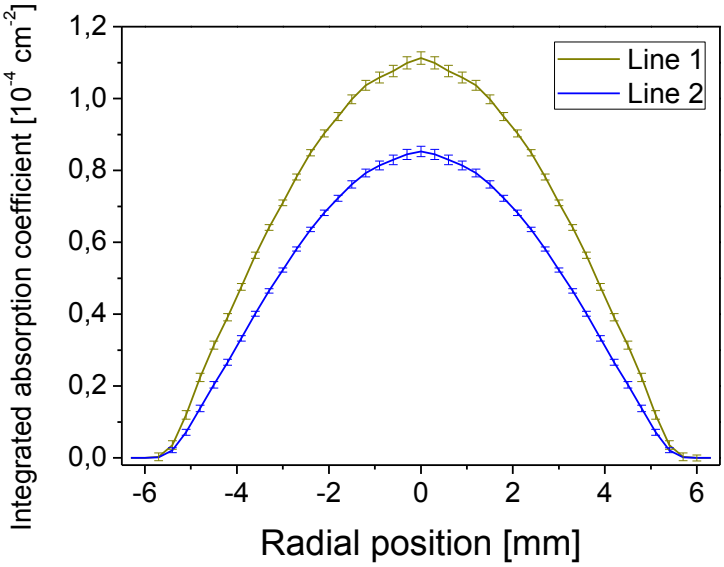

Figure 5.10: Integrated absorption coefficients obtained by Abel inverting the profiles of figure 5.9.

The ratio of lines 1 and 2 integrated absorption coefficients is calculated for each radial position. The result is shown in figure 5.11 (left). The ratio increases from a value of 1.3 at discharge center up to about 1.7 at 5 mm off-axis. The gas temperature as a function of the ratio of the integrated absorption coefficients (or line strengths) was presented in section 3.6.1, figure 3.24-right and is re-plotted in figure 5.11-right. The resulting temperature profile is plotted in figure 5.12.

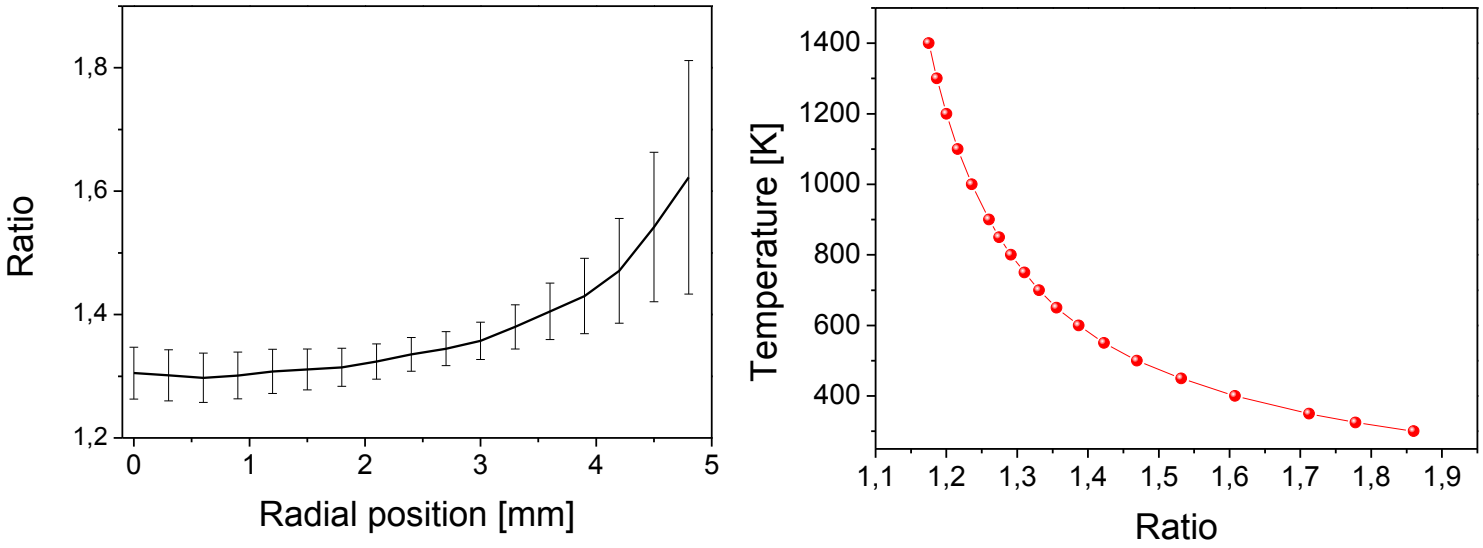

Figure 5.11: Ratio of the integrated absorption coefficients (left) and theoretical evolution of the gas temperature as a function of this ratio (right).

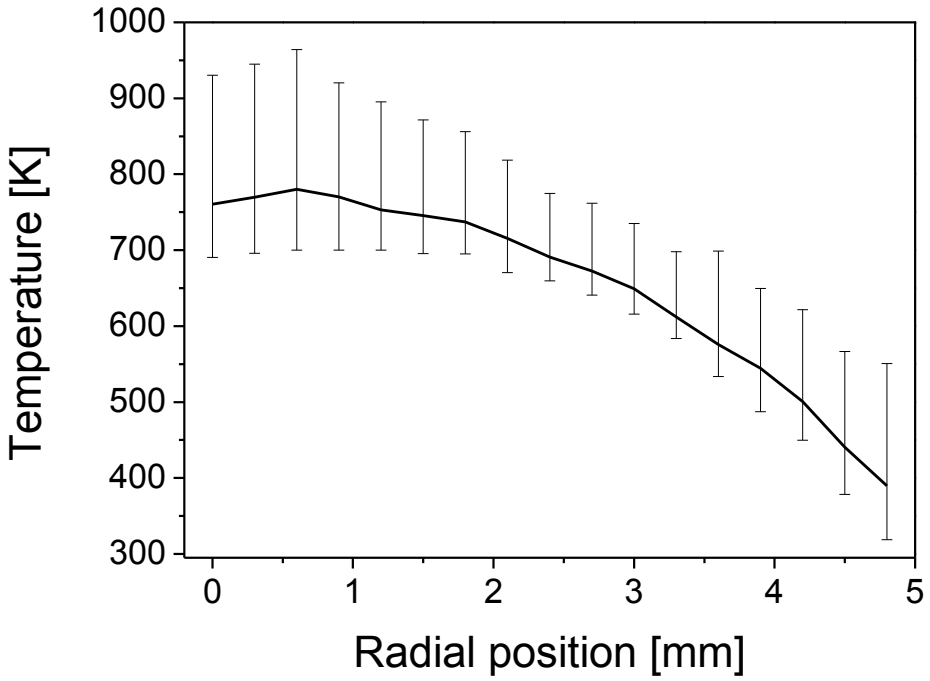

Figure 5.12: Radial gas temperature profile determined from the ratio of the two lines (method 1).

Figure 5.12 illustrates that the gas temperature is at maximum in the center (at about 800 K) and decreases down to room temperature at 5-mm off-axis distance. The heat diffusion from NRP discharge center to its vicinity is expected.

5.5 Gas temperature determination using collisional linewidth

In this section, we present the results from the second method used for the determination of the gas temperature. Unlike the previous method, this one only requires one absorption line. To obtain the gas temperature, we will first apply the Abel inversion to the lateral absorbance spectra. This provides the spectral absorption coefficient at each radial position. Then secondly, the FWHM of each of the absorption lines is used to determine the gas temperature.
The Lorentzian fits of the lateral absorbance measurements for line 2 represented in figure 5.6 are presented in figure 5.13 as a 2D contour color map.

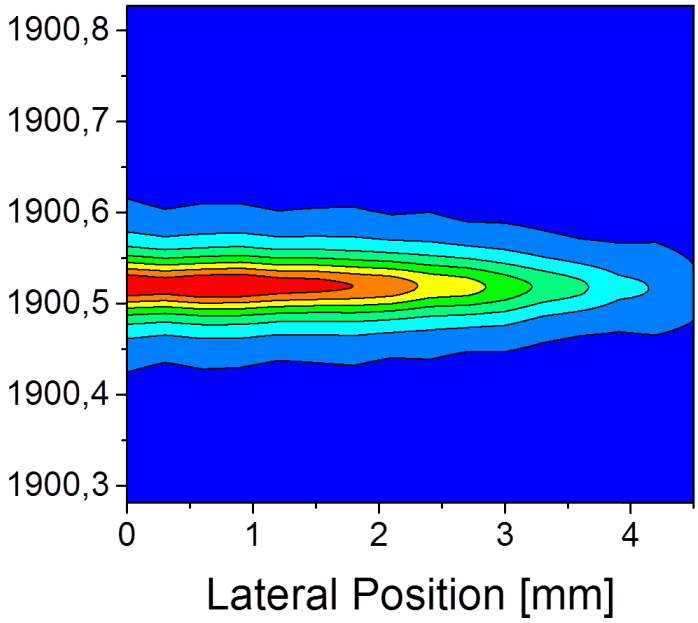

Figure 5.13: 2D contour colour map from Lorentzian fits of the lateral measurements for line centered at 1900. 517 cm^{-1}.

In order to perform the Abel inversion, we first selected the lateral absorbance distribution at a given wavenumber (see figure 5.14). Then, each spatial distribution at a particular wavenumber was Abel-inverted using fifth-order polynomial fits to yield the 3D map representation of the absorption coefficient. This is shown in figure 5.15. The absorption coefficient decreases with the radial distance with a peak value of 8 x 10^{-4} cm^{-1} at the center of the discharge.
Note that this method is more sensitive to the quality of input data than the method using Boltzmann distribution. We choose to apply the second method only on the line 2 because better quality data were measured.

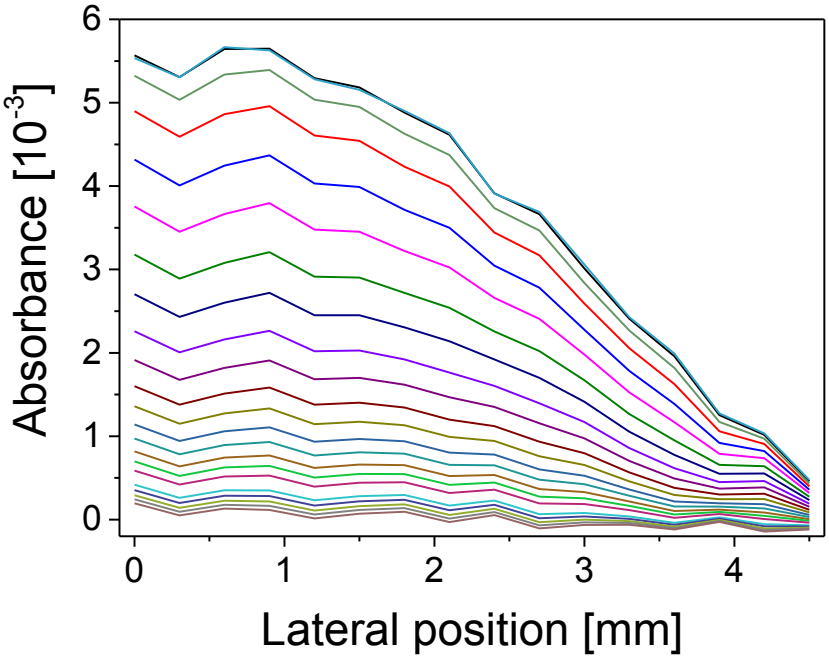

Figure 5.14: Lateral absorbance measurements for line 2 and at different wavenumber. From top to bottom, wavenumber goes from line center to the sides in steps of 5 x 10^{-3} cm^{-1}.

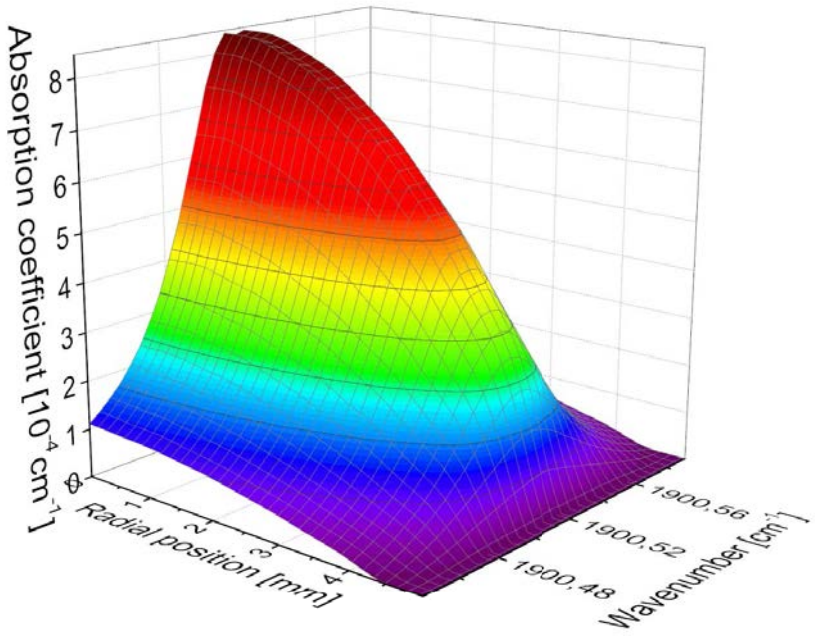

Figure 5.15: 3D reconstitution of the spectral absorption coefficient for line 2.

Our spatial resolution was limited by the laser waist, which was about 300-µm. The spectral absorption coefficients with radial step of 300 µm are shown in figure 5.16.

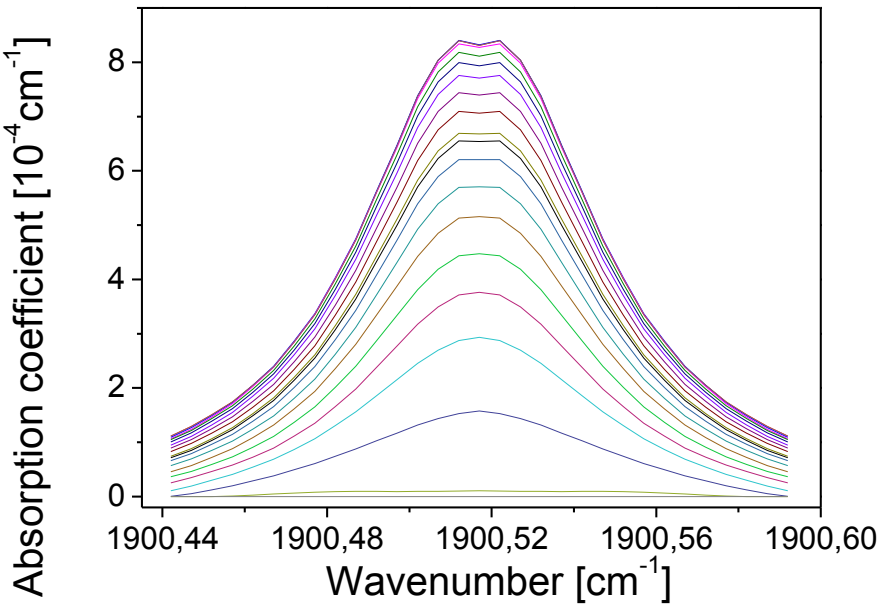

Figure 5.16: Spectral absorption coefficient as a function of the radial position, in steps of 300 µm.

Subsequently, each profile is fitted by a Lorentzian line shape (see figure 5.17 for instance) and the FWHM of the Lorentzian fits are recorded. The agreement with Lorentzian fits improves with the distance from discharge axis. The radial profile of the FWHM is given in figure 5.18-left. It shows a constant FWHM around 7 x 10^{-2} cm^{-1} up to a 4 mm radial distance from discharge center then it increases up to 0.11 cm^{-1} at 4.8 mm distance from axis. This value is close to the FWHM of line 2 at 300 K (0.118 cm^{-1}).

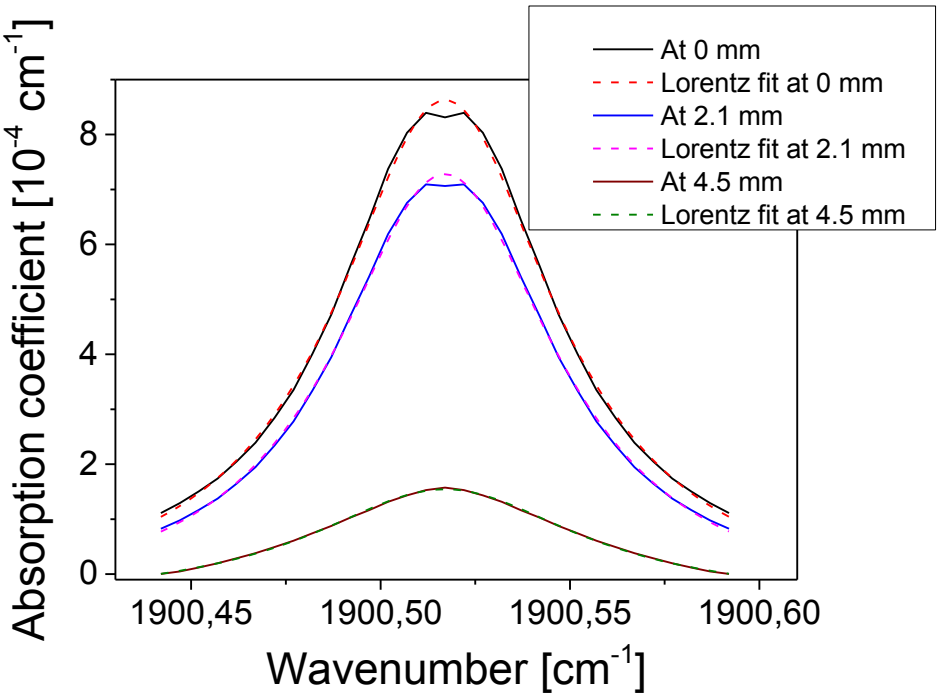

Figure 5.17: Lorentzian fits of obtained spectral absorption coefficient at various radii.

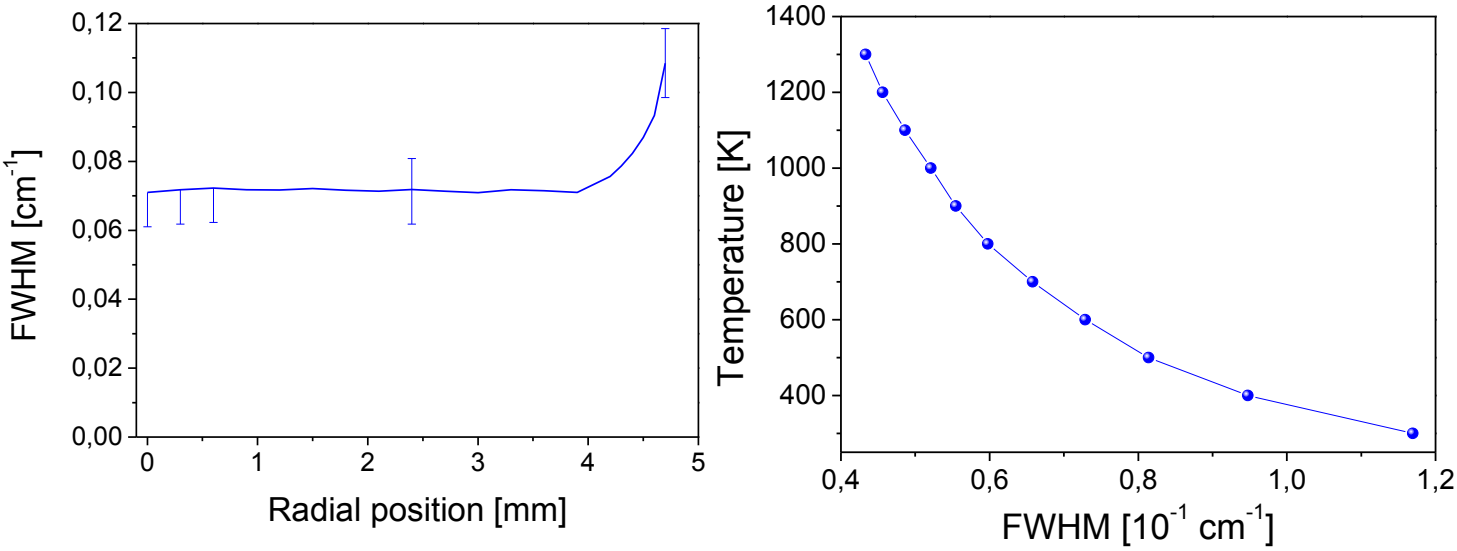

Figure 5.18: FWHM as a function of the radial position (left). Theoretical gas temperature as a function of the FWHM of line 2.

From the theoretical dependency of the temperature with respect to the FWHM of line 2 (presented figure 5.18-right), we deduced the gas temperature profile represented in figure 5.19. The radial temperature profiles for both methods are presented there. As expected, the flat feature of the FWHM from figure 5.18 is found also for the gas temperature profile using method 2. Up to 4-mm distance, the gas

temperature is constant at 600 K and then decays to room temperature at distance of 4.8 mm.

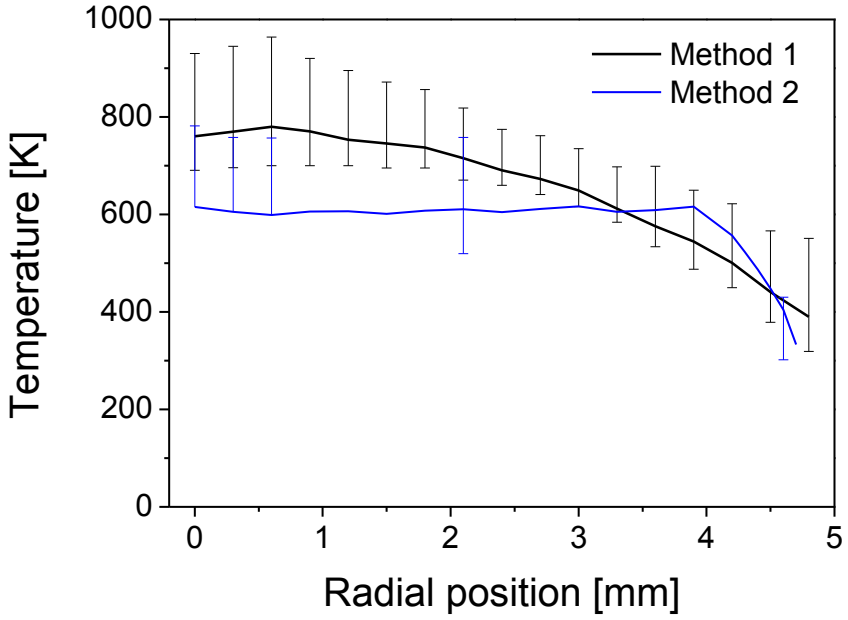

Figure 5.19: Methods 1 and 2 radial gas temperature profiles.

The temperature profiles from both methods are in agreement within the error bars. But since the expected decrease of the temperature from the discharge center to off-axis is better reproduced by method 1, the corresponding temperature profile was chosen as more reliable.

5.6 Discussions on the gas temperature

The gas temperature at discharge center is found to be about 800 K. This temperature is a space-averaged result over 300 µm and a time-averaged result over 100 s. These features should be taken into consideration when comparing our results with those from literature.

We compared our results with those from *Xu et al.* [2011]. These authors measured the gas temperature by carrying out time-resolved Schlieren imaging of the NRP discharge. They hence recorded the propagation of the shock-wave following the spark breakdown. The time-resolved gas temperature behind the shock-front was inferred from the determined shock-wave velocity using Rankine-Hugoniot relations. This result is a space-averaged measurement of the gas temperature over the size of the heated gas channel, which is initially about few hundreds of microns. Their results hence exhibit comparable spatial resolution with ours.

NRP discharges were generated applying voltage pulses of 6.3 kV amplitude between electrodes in a pin-to-pin configuration separated by a 2-mm gap distance. The pulse duration, repetition frequency, energy deposited per pulse and air flow temperature were respectively about 10 ns, 10 kHz, 0.5 mJ and 300 K. Under these conditions, authors found a maximum gas temperature about 620 K (see case 2 of figure 5.20). Notice this experiment is very close to ours. We have a similar energy deposited per pulse (0.5 mJ/pulse) as a result of the doubled pulse duration, for the same 2-mm gap distance. However, our pulse repetition frequency (30 kHz) is three-folds greater. This could explain our higher mean gas temperature (about 200 K higher).

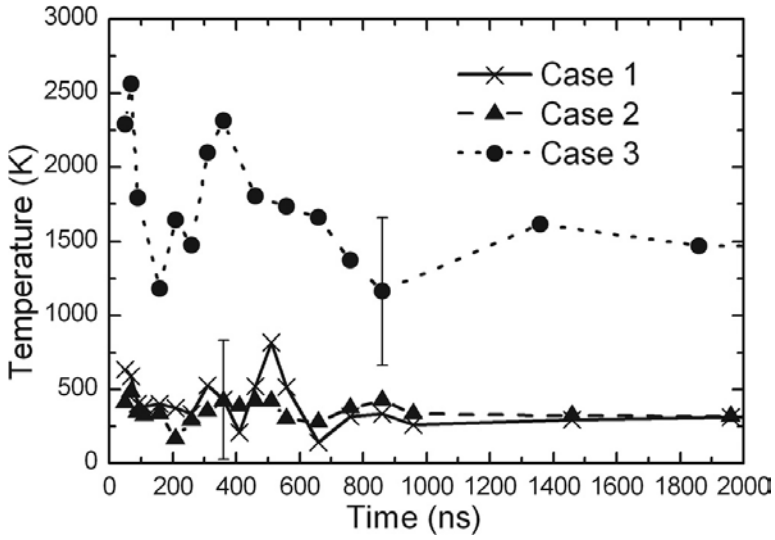

Figure 5.20: Temporal evolution of the gas temperature based on Rankine-Hugoniot relations. See "case 2" for comparison. Figure taken from [*Xu et al.*, 2011].

In the literature, the gas temperature measurements in NRP discharges operating in ambient air flows are commonly performed by OES, recording the emission of the second positive system of nitrogen [*Pancheshnyi et al.*, 2006; *Lo et al.*, 2014]. Even though for these references, NRP discharges operated in quite different conditions than ours, we can compare the advantages/inconveniences of gas temperature determination by OES and QCLAS.

OES can provide better resolved (space and time) results (up to 50 µm and few ns, respectively) than QCLAS measurements. However, QCLAS measures the temperature from a rotational-vibrational transition of NO in its ground state, which is more likely to be equal to the gas temperature than the rotational temperature of electronic excited N_2(B, C) levels. Besides, due to the short lifetimes of N_2(B, C) states (few ns), the gas temperature during the inter-pulse period cannot be accessed by OES. QCLAS is therefore a solution for temperature measurements in the discharge and post-discharge. *Lo et al.* [2014] proposed another solution. They complemented their gas temperature measurements during the inter-pulse period

using Spontaneous Raman Spectroscopy (SRS). However, this methods needs besides the laser system, a Raman spectrometer and it is more intrusive because of using high power lasers.

5.7 Absolute NO densities

We have applied successively methods 1 and 2 to determine the gas temperature. From method 1, in addition to the gas temperature we derived also the radial profiles of the integrated absorption coefficients. The latter together with the gas temperature profile lead to the determination of the NO absolute densities (see equation 3.19 of section 3.4.2). Line strength correction due to the temperature changes was considered.
From method 2, we inferred the radial distribution of the gas temperature and the spectral absorption coefficients. In order to obtain NO absolute densities, we used equation 3.19, we considered line 2 changes with respect to the temperature and then secondly we calculated the area under the spectral absorption coefficients at each radial position.

The calculated line strengths radial distribution of line 2 based on the temperature profiles of figure 5.19 are presented in figure 5.21. As a result of the lower temperature obtained with method 2, the line strengths are higher than those inferred from method 1. At discharge center, the line strength from method 2 is 1.4 times greater than the line strength from method 1.
The line 2 integrated absorption coefficients using both methods are depicted in figure 5.22. Up to 4.5-mm off-axis distance, the results from method 2 are larger than those from method 1 by 5 – 25 %. At discharge center, the integrated absorption coefficient from method 2 is about 1.25 times larger than that of method 1.

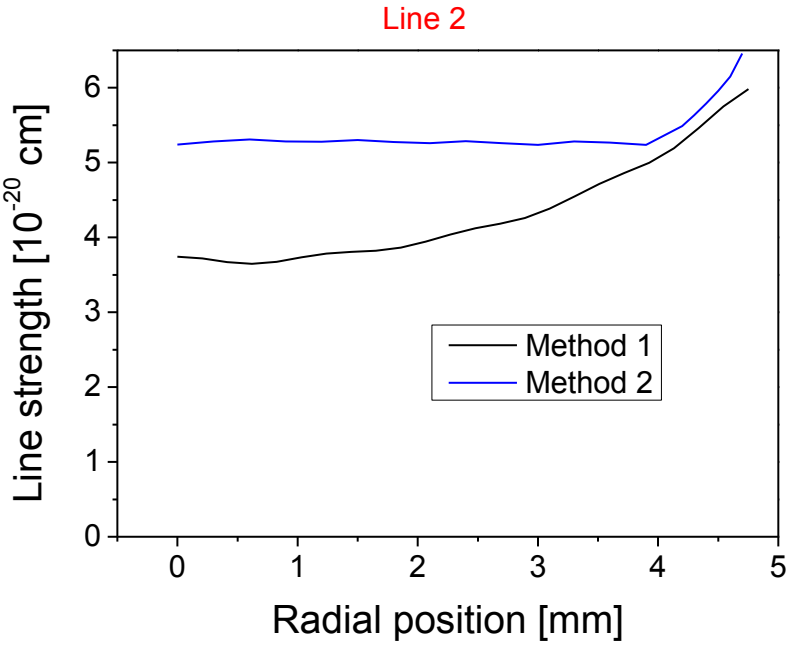

Figure 5.21: Radial line strengths of line 2 at 1900.517 cm^{-1} resulting from the radial temperature profiles determined with the two methods.

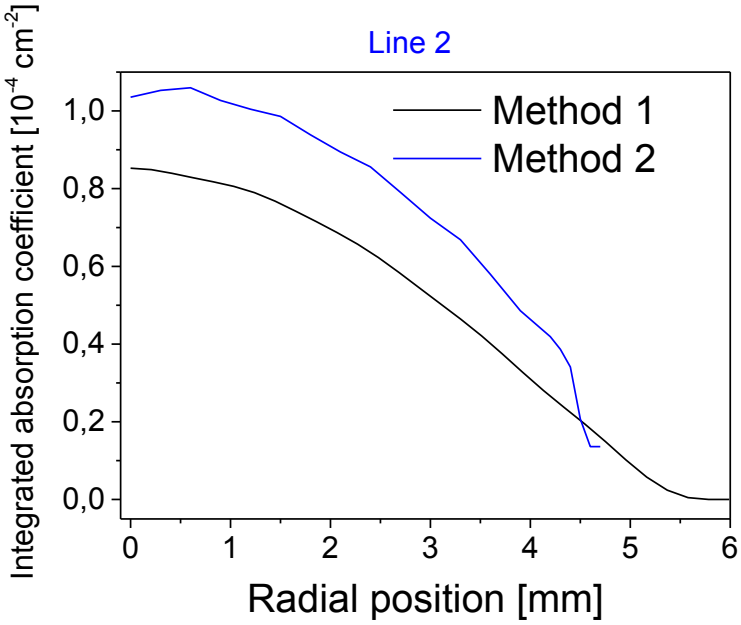

Figure 5.22: Radial profiles of the integrated absorption coefficients of the line at 1900.517 cm^{-1} resulting of the radial temperature profiles obtained by the two methods.

Using the results presented in figures 5.21 and 5.22, we deduce the radial density profiles presented in figure 5.23. For both methods the NO density decreases with the radius and the results are in good agreement. For method 1, the absolute NO density

at discharge center is found to be around 2.25 x 10^{15} cm^{-3} and decays to 1.5 x 10^{14} cm^{-3} at 5-mm off-axis.

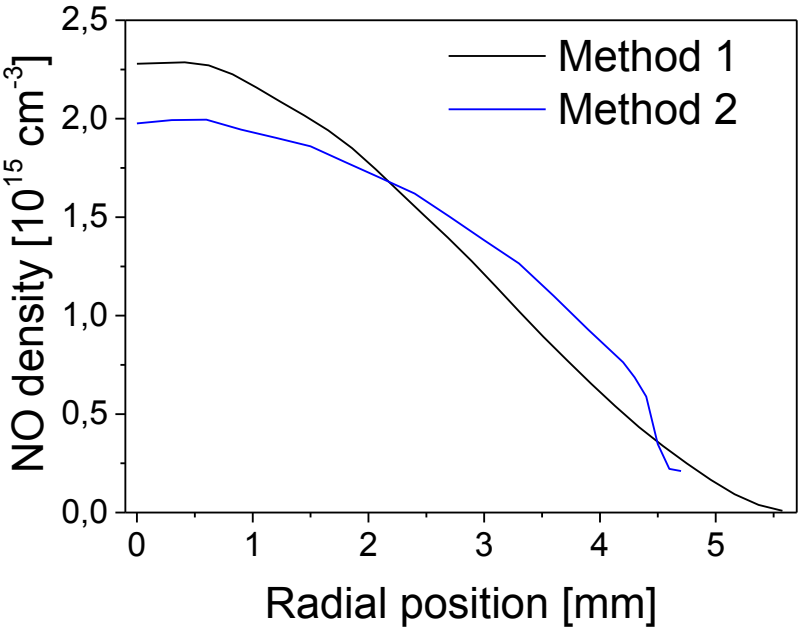

Figure 5.23: Radial profiles of absolute NO density profiles for methods 1 and 2.

At discharge center, the NO density obtained with method 1 is about 10 % greater than that from method 2, which is consistent with results of line strengths and integrated absorption coefficients shown in figures 5.19 and 5.20 (1.4/1.25~1.13).

Thus, NO is radially spread over about 1 cm with a HWHM of about 3 to 3.5 mm.

An analysis of the contribution of different radial regions in and around the NRP discharge, to the total lateral absorbance measurements is presented in appendix E. This analysis demonstrates the important contribution of the discharge center to the light-of-sight integrated absorbance measurements and explains the Lorentzian features of the measured lateral spectra.

5.8 Conclusions

In this chapter, the results from lateral absorbance measurements for two absorption lines were presented. We found that NO spreads radially up to 5-mm distance from the discharge center. This could not be attributed to diffusion effects. The large radial distribution of NO (much larger than the NRP discharge width, which is below 500 µm [*Stancu et al.*, 2010; *Rusterholtz et al.*, 2013]) was attributed to the existence of a flow recirculation zone at electrodes vicinity and the long lifetime of NO. We applied two methods for radial temperature determination. The temperatures and

densities were obtained from 100 s time-averaged measurements. Method 1, which is based on the ratio of the integrated absorption coefficients provided more reliable results. The average gas temperature at discharge center is found about 800 K whereas method 2 predicts a mean gas temperature at discharge center about 600 K. Both temperature radial profiles decrease with off-axis distance and reach near room temperature at radius of 5-mm. Following radial temperature determination, the NO densities are inferred using both methods and assuming no NO creation mechanism during its convection. Results exhibit a good agreement. The maximum NO density is about 2.3 x 10^{15} cm^{-3} and 2 x 10^{15} cm^{-3} for methods 1 and 2, respectively. The NO density profile exhibits a HWHM of about 3 to 3.5 mm.

References

[1] Laux, C. O. (1993). Optical diagnostics and radiative emission of air plasmas. (Doctoral dissertation, Stanford University).

[2] Lo, A., Cessou, A., Boubert, P., & Vervisch, P. (2014). Space and time analysis of the nanosecond scale discharges in atmospheric pressure air: I. Gas temperature and vibrational distribution function of N2 and O2. *Journal of Physics D: Applied Physics*, *47*(11), 115201.

[3] Massman, W. J. (1998). A review of the molecular diffusivities of H 2 O, CO 2, CH 4, CO, O 3, SO 2, NH 3, N 2 O, NO, and NO 2 in air, O 2 and N 2 near STP. *Atmospheric Environment*, *32*(6), 1111-1127.

[4] Pancheshnyi, S. V., Lacoste, D. A., Bourdon, A., & Laux, C. O. (2006). Ignition of propane–air mixtures by a repetitively pulsed nanosecond discharge. *Plasma Science, IEEE Transactions on*, *34*(6), 2478-2487.

[5] Rusterholtz, D. L., Lacoste, D. A., Stancu, G. D., Pai, D. Z., & Laux, C. O. (2013). Ultrafast heating and oxygen dissociation in atmospheric pressure air by nanosecond repetitively pulsed discharges. *Journal of Physics D: Applied Physics*, *46*(46), 464010.

[6] Stancu, G. D., Kaddouri, F., Lacoste, D. A., & Laux, C. O. (2010). Atmospheric pressure plasma diagnostics by OES, CRDS and TALIF. *Journal of Physics D: Applied Physics*, *43*(12), 124002.

[7] Xu, D. A., Lacoste, D. A., Rusterholtz, D. L., Elias, P. Q., Stancu, G. D., & Laux, C. O. (2011). Experimental study of the hydrodynamic expansion following a

nanosecond repetitively pulsed discharge in air. *Applied Physics Letters*, *99*(12), 121502.

[8] Yos, J. M. (1963). *Transport properties of nitrogen, hydrogen, oxygen, and air to 30,000 K* (No. TM-63-7). AVCO CORP WILMINGTON MA RESEARCH AND ADVANCED DEVELOPMENT DIV.

Chapter 6

Characterization of NRP post-discharge: NO density as a function of discharges parameters

6.1 Introduction

In this chapter we study the NRP post-discharge. In particular, the NO production as a function of the discharge parameters, namely the applied pulse voltage amplitude, pulse repetition frequency, gap distance and flow rate. The goal is to investigate how to optimize NO production for the different types of applications considered in this thesis.
Section 6.2 presents a parametric study of NO production in the post-NRP discharge operating in a flow of ambient air. Then section 6.3 is dedicated to the analysis of NO density evolution with respect to the incoming gas flow temperature. Section 6.4 presents another parametric survey, but this time with the NRP discharges operating in a 1000-K preheated airflow. In section 6.5, the results from chapter 5 and 6 are analyzed to determine the dominant mechanisms of NO formation and loss in NRP discharges. All the measurements of this chapter are performed using only the strongest transition, namely line 1. Note that for all the measurements of this chapter, we will use the following nomenclature: U, f, d, E, v, z and T respectively for the applied pulse voltage, the pulse repetition frequency, the gap distance, the energy deposited per pulse, the air flow velocity, the height at which the measurement is performed and the temperature of the injected air. Finally we note that all the measurements in this chapter are averaged over 10-second duration.

6.2 Characterization of NRP post-discharge at 300 K

In this section we present NO density measurements in the NRP post-discharge as a function of the discharge parameters. For this purpose we use the setup for multipass measurements (28 passes), which is depicted in figure 4.14. This configuration is simpler than the one of chapter 5 since here we are in a uniform environment (we do not have to perform Abel inversion). Besides, unlike the measurements of chapter 5, the gas temperature in the post-discharge region with the discharge turned on remains at ambient temperature (this was proven using a thermocouple). In this case, we have also a lower electromagnetic noise due to the confinement of the NRP discharge by the 50-cm long steel tube. Note that in this section we use PG1 to

generate NRP discharges between a bluff-body pin and a refractory steel electrode as shown in figure 4.1.

6.2.1 Influence of high voltage amplitude

We study the impact of the variation of the discharge-applied voltage amplitude on the density of NO produced by NRP discharges. For each voltage amplitude between 5.5 and 9.5 kV, we recorded the transmitted intensity $I(v)$ together with the baseline $I_0(v)$ and then secondly we deduced the absorbance spectra as illustrated in figure 6.1. The absorbance at the center of the line increases with the increase of the discharge voltage. Note that apart from the pulse voltage amplitude, all the other parameters were kept constant i.e. the repetition frequency, the gap distance and the flow velocity were fixed at 30 kHz, 4 mm and 8.6 m/s, respectively.

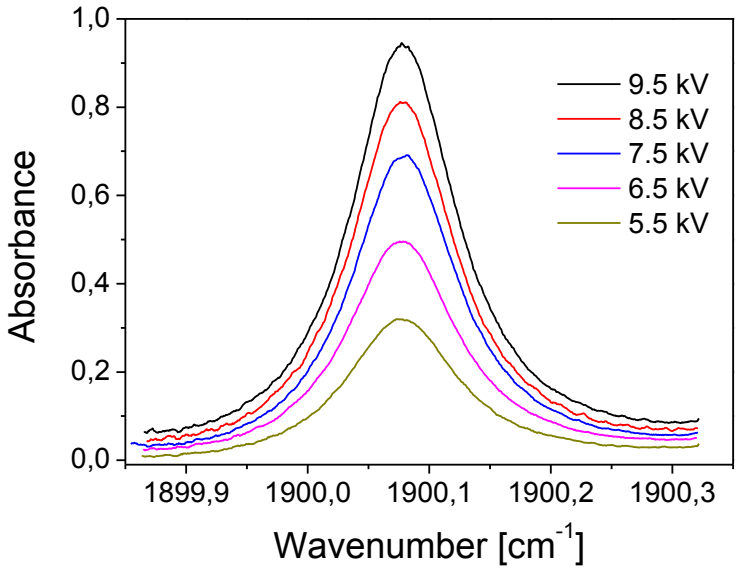

Figure 6.1: Absorbance spectra at different pulse voltage amplitudes between 5.5 and 9.5 kV. The peak absorbance increases with the increase of pulse voltage amplitude.

To deduce absolute NO densities from the absorbance spectra we used the expression 3.13 of section 3.4, corresponding to uniform environments. The line strength to be considered is consequently the line strength of line 1 at 300 K, which is 1.22 x 10^{-19} cm. For the 28-pass configuration at the exit of the 8-cm diameter tube, the length of absorption is estimated to be about 216 cm. Due to our limited spectral window (about 0.4 cm^{-1}) in comparison with the large wings of the absorption features at atmospheric pressure, we use three strategies of integration.
The first method of integration consists in integrating the spectra over the available spectral window. We expect an underestimation of the area and therefore of the

determined density using this method since the contribution of wings is not taken into account.

The second method consists in fitting each absorbance spectrum by a Lorentzian profile, setting the offset of wings to 0 at "infinity". This method should provide reliable results since the wings are now taken into account. But this method suffers from the overlap of the second absorption feature (centered at 1900.517 cm^{-1}) at the high-wavenumber side of the spectrum. For instance figure 6.2 illustrates the second method fitting strategy and shows the difference between the recorded spectrum and the Lorentzian fit in the "high-wavenumber" region.

The third method, which gives the best accuracy, employs the Q-MACS simulation tool. It uses as inputs, the gas pressure and temperature (in the region where the measurement is performed), the absorption length, the mole fraction, line spectroscopic parameters and the laser instrumental function. The tool computes transmitted spectra using the HITRAN database over a given spectral range. In practice, after setting all input parameters, the NO mole fraction is adjusted to get the best fit of the measured transmitted spectrum. An illustration of the implementation of this method is given in figure 6.3, for a measurement at 7.5 kV voltage amplitude. The best match is found for a simulated spectrum with 135 ppm of NO and an absorption length about 216.3 cm.

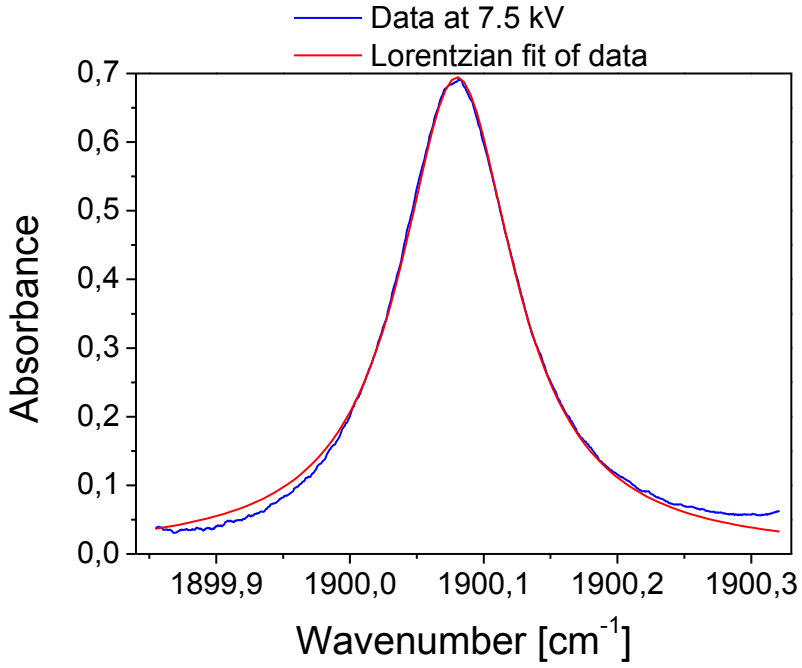

Figure 6.2: Recorded absorbance spectrum at 7.5 kV and corresponding Lorentzian fit for the purpose of area calculation. The fit fails at the wing on the high-wavenumber side.

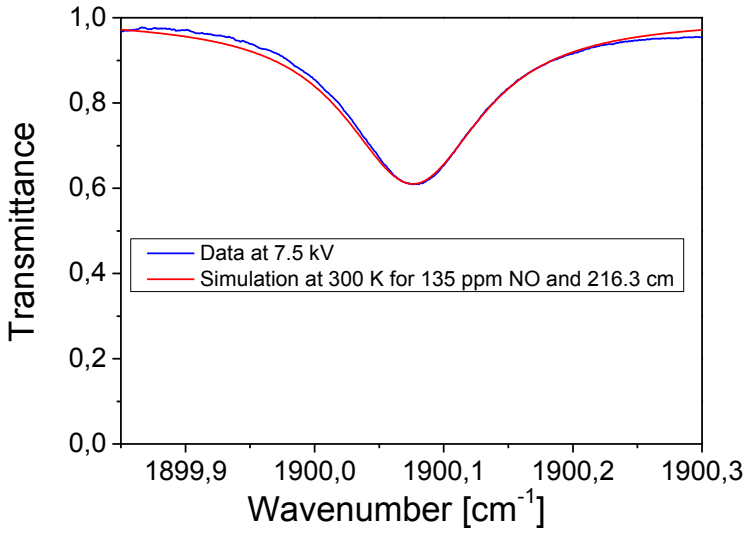

Figure 6.3: Recorded transmittance spectrum at 7.5 kV and best fit provided by the Q-macs tool using the HITRAN database.

The three methods are compared in figure 6.4. All three predict an increase in NO density with increasing applied voltage amplitude. As expected, method 1 underestimates the NO density over the investigated range of applied voltages. This underestimation can reach up to 67 % of the NO density as shown for instance at 5.5 kV. For this and for the following investigations, we choose method 3 in order to obtain the NO density. Results from method 3 are displayed in figure 6.5.

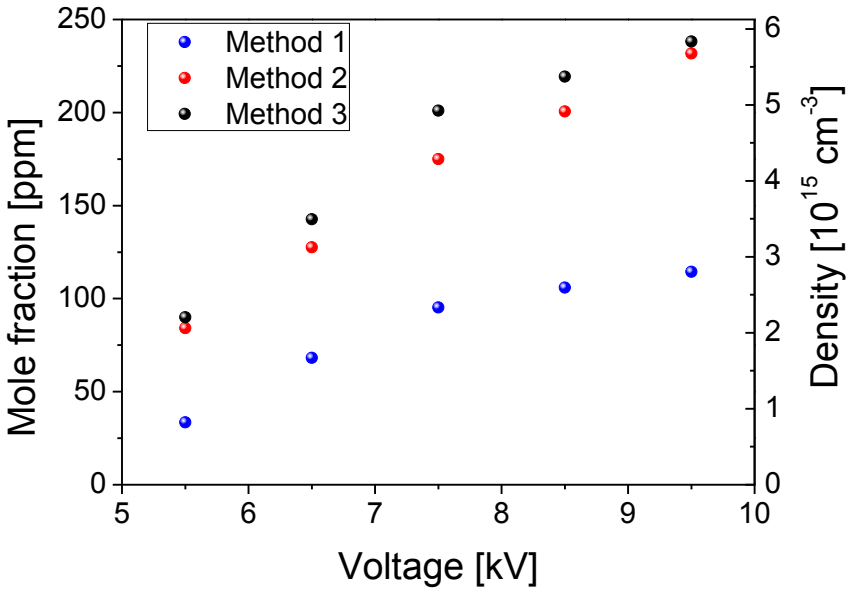

Figure 6.4: Comparison of the three methods for NO density determination. Method 1 systematically underestimates the NO density while methods 2 and 3 give close results.

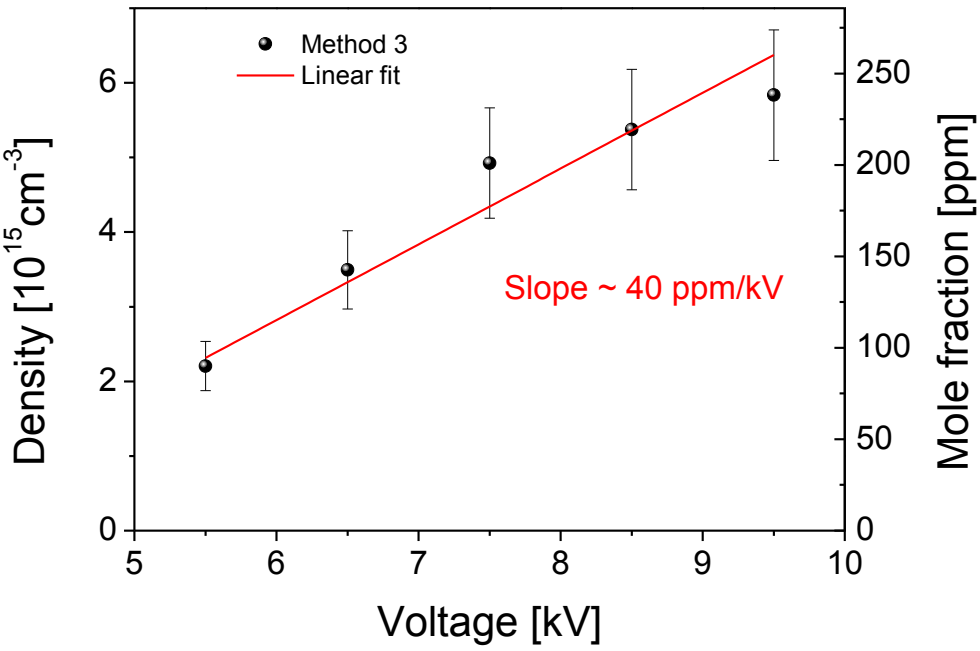

Figure 6.5: NO density/mole fraction as a function of the applied voltage amplitude. The NO mole fraction increases with voltage amplitude with a slope of about 40 ppm/kV. Conditions: $f = 30$ kHz, $d = 4$ mm, $v = 8.63$ m/s, $z = 50$ cm, $T = 300$ K.

From 5.5 to 9.5 kV, the NO density increases by a factor 3, from about 2 x 10^{15} cm^{-3} to 6 x 10^{15} cm^{-3}. This corresponds to an increase of NO mole fraction from about 80 to 250 ppm. A linear fit yields an increase with a characteristic slope of about 40 ppm/kV. The error bars account mainly for the quality of the confinement of the NRP discharge located at the base of the tube and not of the absorption measurements. In a less careful confinement configuration, air particles outside the tube are entrained by the flow inside the tube leading to a lower density at the tube exit.

6.2.2 Influence of pulse repetition frequency

Here we repeat the procedure implemented in the previous section to investigate the influence of the repetition frequency on the amount of NO produced in the NRP post-discharge. The pulse voltage amplitude, gap distance and air flow velocity are kept constant at 9.5 kV, 4 mm and 8.63 m/s, respectively. Figure 6.6 presents the NO density as a function of the pulse repetition frequency. From this figure we learn that the NO density increases linearly with the pulse repetition frequency. More precisely, from about 6.5 to 30 kHz repetition frequencies, NO increases from 1.5 x 10^{15} to 5.5 x 10^{15} cm^{-3}, i.e. more than a factor 3.5. This corresponds to a mole fraction increase from about 60 to 225 ppm. This time, assuming a linear behavior of the

increase of NO mole fraction with respect to repetition frequency, we obtain a rate of 7 ppm/kHz.

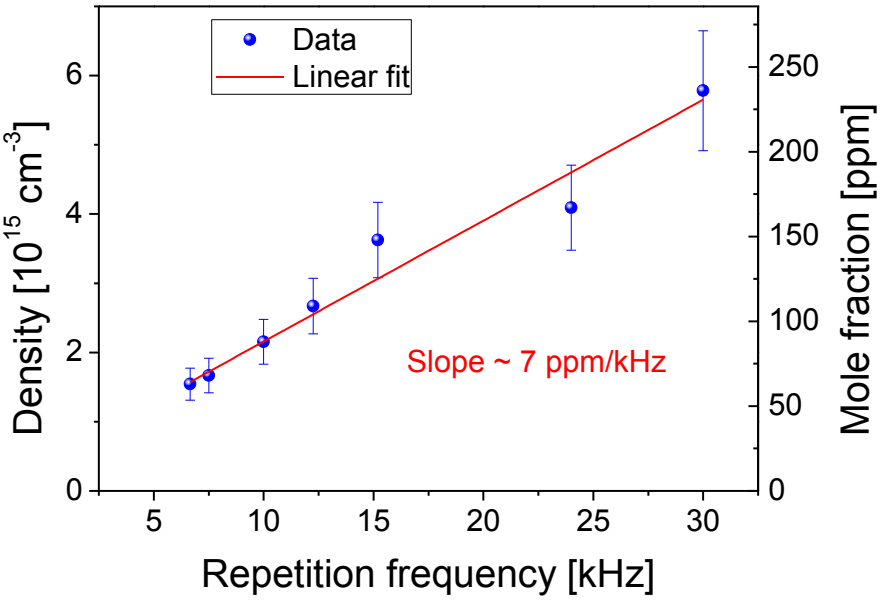

Figure 6.6: NO density/mole fraction as a function of repetition frequency. The NO mole fraction increases with the pulse repetition frequency with a slope of about 7 ppm/kHz. Conditions: $U = 9.5$ kV, $d = 4$ mm, $E = 6$ mJ, $v = 8.63$ m/s, $z = 50$ cm, $T = 300$ K.

6.2.3 Influence of gap distance

We investigate here the influence of the inter-electrode gap distance on the NO density. The pulse voltage amplitude, repetition frequency and air flow velocity were kept constant at 5.3 kV, 30 kHz and 8.63 m/s, respectively. Figure 6.7 shows that the NO density raises with increasing gap distance. From 1 to 5 mm, the NO density increases by a factor 2.5, from 1 x 10^{15} to 2.5 x 10^{15} cm^{-3}. In mole fraction, this corresponds to changes of about 40 ppm to 110 ppm.

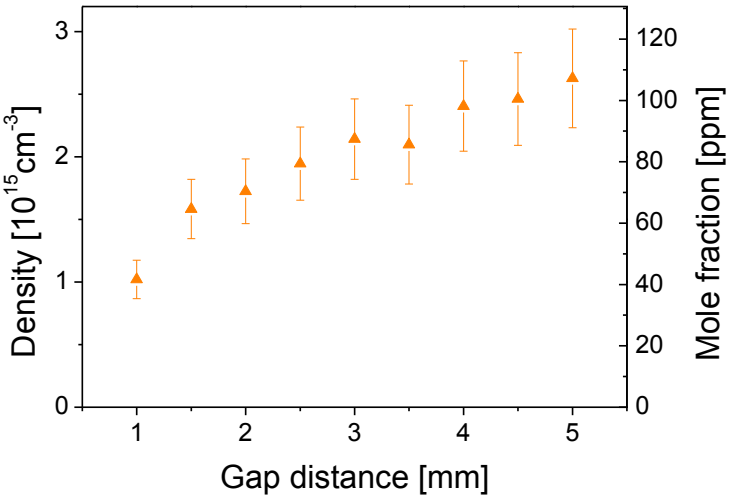

Figure 6.7: NO density/mole fraction as a function of the gap distance. The NO mole fraction increases with gap distance. Conditions: $U = 5.3$ kV, $f = 30$ kHz, $v = 8.63$ m/s, $z = 50$ cm, $T = 300$ K.

6.2.4 Influence of flow rate

Figure 6.8 illustrates NO density variation with respect to the incoming flow rate. Increasing of the airflow rate from zero to 6 m^3/h leads to a factor 4 decrease of the NO density, i.e. from about 4 x 10^{15} cm^{-3} down to 1 x 10^{15} cm^{-3}.

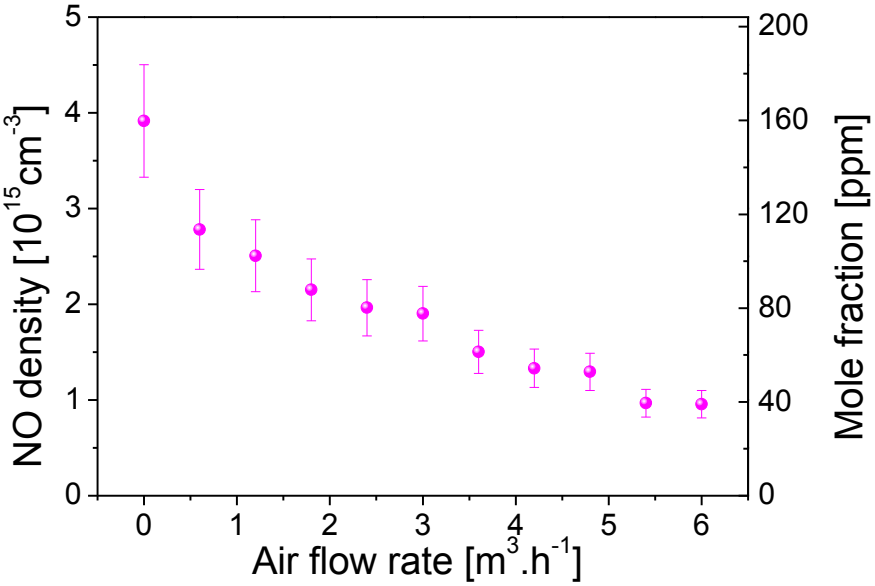

Figure 6.8: NO density/Mole fraction as a function of the air flow rate. The NO mole fraction decreases with increasing flow rate. Conditions: $U = 5.3$ kV, $f = 30$ kHz, $d = 4$ mm, $z = 50$ cm, $T = 300$ K.

NO density measurements with respect to the airflow rate can be converted to production rates as described by *Pipa et al.* [2008]. At steady state, the NO production rate X (in cm^3/s) is expressed as:

$$X = \frac{n_{NO}}{n}\Phi \tag{6.1}$$

where n_{NO} and n are the density of NO and the total density of the gas, respectively. At 300 K, the total density n is about 2.45 x 10^{19} cm^{-3}. Φ is the airflow rate in cm^3/s. The production rate is plotted in figure 6.9. From 0 to 6 m^3/h flow rate, the NO production rate increases to about 2 x 10^{18} molecule/s. This NO production rate is comparable with that of *Pipa et al.* [2008], which showed a maximum NO production of about 2.2 x 10^{18} molecule/s for their atmospheric pressure RF plasma jet.

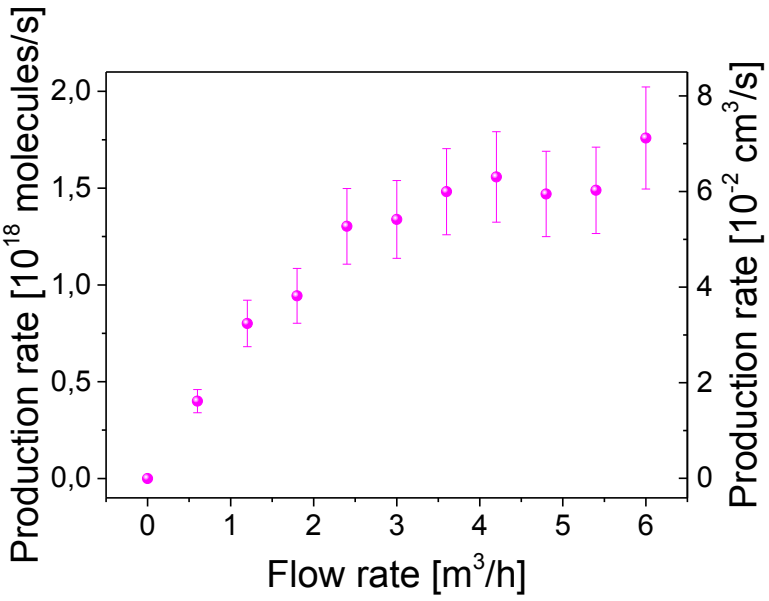

Figure 6.9: NO production rate as a function of the air flow rate. NO production rate increases with increasing flow rate. Conditions: $U = 5.3$ kV, $f = 30$ kHz, $d = 4$ mm, $z = 50$ cm, $T = 300$ K.

6.2.5 Two-key parameters

The above results can be summarized as follows. The NO density increases with increasing:

- Applied voltage amplitude
- Pulse repetition frequency
- Inter-electrode gap distance

In contrast, the NO density decreases with increasing

- Air flow rate

However the production rate increases with increasing air flow rate.
Based on these results, we can extract two relevant parameters accounting for the influences of all the previously listed discharge parameters.
The first one is df/v, a dimensionless parameter combining the repetition frequency, the inter-electrode gap distance and the air flow velocity (which is proportional to the airflow rate). This parameter is equal to the number of pulses seen by the gas in the gap.
The second key parameter is the amplitude of the applied pulse voltage.

Figure 6.10 summarizes the results from previous sections using both key parameters. Using the different experimental conditions, we converted the NO mole fractions as a function of repetition frequency, gap distance and air flow rate (each conducted at fixed pulse voltage amplitude) into NO mole fractions as a function of the dimensionless parameter (number of pulses seen by the gas). We can see from figure 6.10 that at fixed pulse voltage amplitude, the NO density in the post-discharge is driven by the number of discharge pulses seen by the gas between the electrodes. Second, at fixed number of discharge pulses seen by the gas, the NO density increases with the applied voltage.

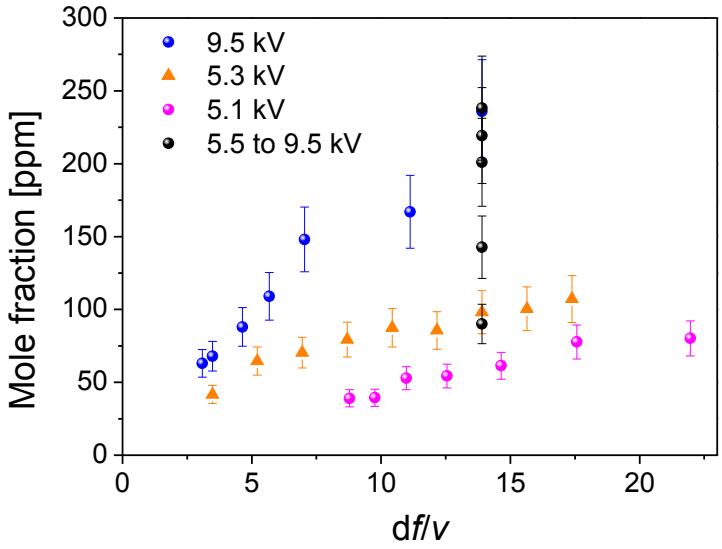

Figure 6.10: NO mole fraction as a function of the dimensionless parameter. At fixed pulse voltage amplitude, the NO mole fraction increases with the number of discharge pulses seen by the gas. In the same time, at fixed number of pulses, the NO mole fraction increases with the applied voltage.

6.2.6 Comparison with the NO density produced in other types of discharges

We compare here the production of NO by NRP discharges with that of other types of discharges. First, the typical 10^{15} cm^{-3} NO density measured in our NRP post-discharge is similar to that of coaxial microwave and radio frequency atmospheric pressure plasma jets [*Van Gessel et al.*, 2013a; *Van Gessel et al.*, 2013b]. These jets operated in helium and argon respectively with small air admixtures (up to 6 %). Plasma power could reach about 50 W in the case of the microwave plasma jet whereas it was less than 10 W in the RF case. Moreover, the maximum NO density found in our study (6 x 10^{15} cm^{-3} ~ 250 ppm) is about twice higher than that obtained in the latter references. However, our density is one order of magnitude lower than the density measured by [*Kühn et al.*, 2009] in an atmospheric high-frequency plasma source operating in N_2/O_2 mixtures (with up to 60 % of O_2).

6.3 Effects of the gas flow temperature on NO production

In this section, we analyze the influence of the air flow temperature on the production of NO in the post-discharge. For this purpose, we first present the experimental conditions, which are quite similar to those of chapter 5. Then using the air preheater system, we conduct NO density measurements in NRP post-discharges operating in air flows at temperature ranging from 300 to 1000 K. This enables us also to compare for the same experimental conditions, measurements in the discharge and measurements in the post-discharge (here, about 25 cm downstream of the electrodes) and to draw conclusions regarding the creation and loss mechanisms in the post-discharge.

6.3.1 Experimental conditions

All measurements presented in this section are performed with electrodes in a vertical pin-to-pin configuration, at 1 cm above the exit of the air preheater (see figure 4.18). As mentioned above, the experimental conditions are similar to those of the spatially resolved measurements. We use the second channel of pulse generator PG2, which provides pulses of about 3 kV amplitude at 30 kHz repetition frequency to generate NRP discharges in a 2-mm gap. The only difference is that a preheater is added in the air injection system. However the flow velocity is kept at the same value: 1.7 m/s. It should also be noted that in this section we use a 20-pass QCLAS system.

6.3.2 NO density as a function of the gas temperature

Prior to measuring the NO density, we measured the gas temperature in the gap using a thermocouple of type K (+/- 2 K accuracy), with the discharge turned off (and without the confinement tube). We found that the gas temperature in the gap

region is very close (within a few K) to the temperature set by the air-heating device. Afterward, inserting the 25-cm long and 8-cm inner diameter confinement tube, for each set gas temperature we performed measurements of the gas temperature at the tube exit with both the discharge turned off and on, in order to determine the gas temperature increase resulting from the application of the NRP discharge. Measuring the gas temperature with the discharge turned on is important because the line strength changes with the gas temperature. The gas temperature measurements are presented in figure 6.11. The green curve corresponds to the set gas temperature. The black curve is the temperature measured with the thermocouple at the exit of the tube with the discharge turned off. As expected, the black curve is always lower than the green curve because of thermal losses between the exit of the heating system and the exit of the confinement tube, where the measurements are performed.

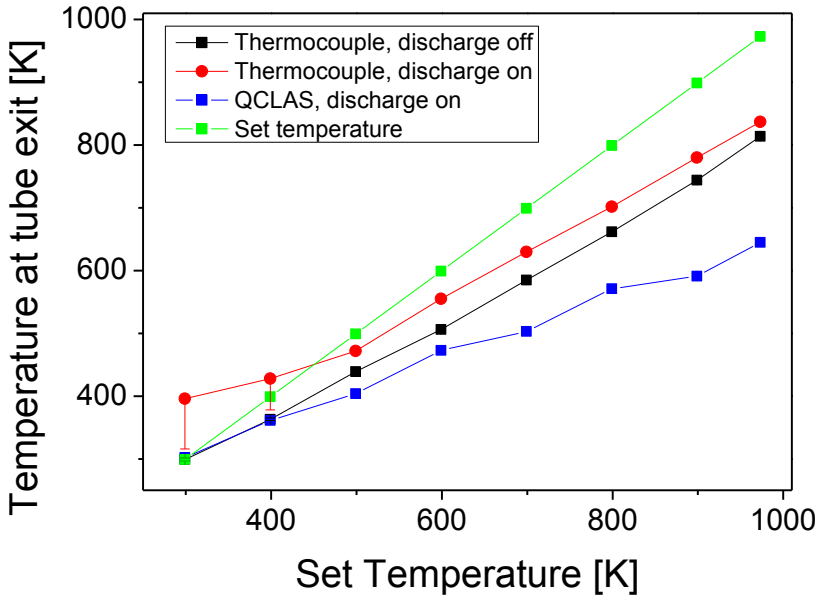

Figure 6.11: Measured gas temperatures at the exit of the confinement tube as a function of the set gas temperature. Four curves are displayed: the set temperature (green), the temperature measured with the thermocouple with the discharge turned off (black), the temperature measured with the thermocouple with the discharge turned on (red) and the temperature deduced from the measured spectral widths (blue). Conditions: $U = 3$ kV, $f = 30$ kHz, $d = 2$ mm, $v = 1.7$ m/s, $z = 25$ cm.

The measured temperature in the post-discharge with the discharge turned on (red curve) is systematically higher than the gas temperature with the discharge turned off (black curve). The difference is about 50 K for most points, except for the first two points where the measured temperature is about 100 K higher. We suspect that these differences may be due to electromagnetic noise on the thermocouple. We should also mention that the thermocouple measurements were taken at the center of

the exit of the confinement tube. These measurements should be higher than the QCLAS measurements, which are averaged over the diameter of the tube. The spatially averaged gas temperatures measured with QCLAS at the exit of the tube are displayed in figure 6.11 (blue curve). These temperatures are obtained from the FWHM of the absorbance spectra for each set temperature using the known dependence of the FWHM of line 1 on the gas temperature. The temperatures measured with QCLAS are lower by about 100-200 K than the thermocouple measurements, but nevertheless they show the same increasing trend and about the same slope.

The measured absorbance spectra are shown in figure 6.12. As expected, the absorbance profiles narrow with increasing temperature due to the decrease of the collisional frequency. The peak absorbance decreases with the temperature due to the temperature dependence of the line strength.

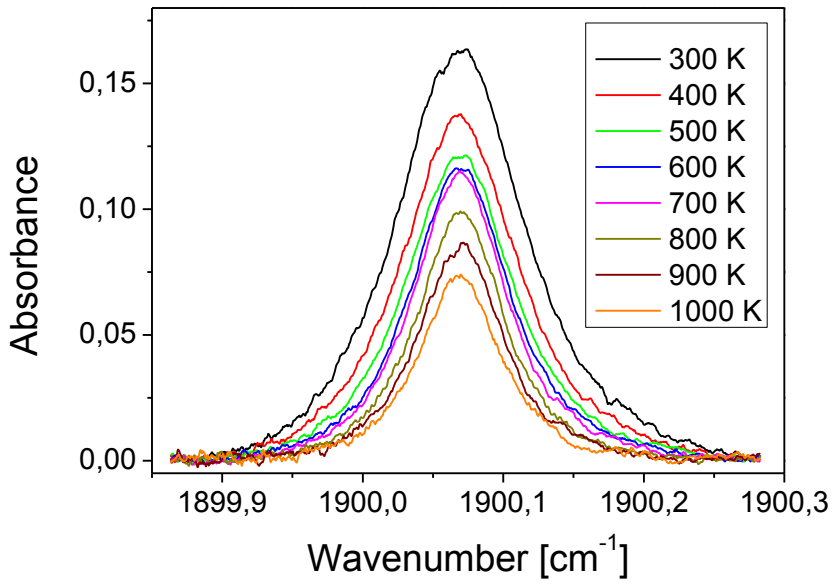

Figure 6.12: Absorbance spectra at different set gas temperatures. Conditions: $U = 3$ kV, $f = 30$ kHz, $d = 2$ mm, $v = 1.7$ m/s, $z = 25$ cm.

From figure 6.11 we deduce the line strength of line 1 based on temperatures measured at the exit of the tube. Figure 6.13 displays the line strengths inferred respectively from the temperatures measured with the thermocouple and those deduced from the collisional broadening. Because the temperatures measured with the thermocouple are higher than the temperatures determined by the spectral widths, they lead to about 17 % lower line intensities. Absorbance spectra combined with line strengths (the length of absorption was estimated to be about 150 cm for the 20-pass configuration) enable us to determine the NO absolute densities. The results are

shown in figure 6.14. Both temperature measurement methods give consistent results. The NO density decreases from about 1.6 x 10^{15} cm^{-3} at 300 K incoming airflow temperature down to about 7 x 10^{14} cm^{-3} at 1000 K.
Note that since the temperature measurements obtained with the thermocouple appear to give good estimates of the NO density, we will only use this simpler method for the measurements in high-temperature environments presented next.

We can also plot the results of figure 6.14 (NO vs temperature) in terms of NO mole fraction vs temperature. The results are shown in figure 6.15. Unlike to results of section 6.2 (relative to other discharge parameters), here the NO mole fraction is approximately independent of the temperature of the incoming air, with an averaged value about 70 ppm (and about 110 ppm if we base the results on the temperatures measured by QCLAS). This result suggests that increasing the gas temperature from 300 to 1000 K does not have any effect on the NO production. This result may appear surprising because the reactions forming NO, whether involving electron-impact reactions should depend on the gas temperature (either directly or through the parameter E/N where E is the electric field and N the gas density). One possible explanation may be that the gas temperature in the discharge region is nearly independent of the incoming flow temperature. This could be the case if the heating locally induced by the discharge in the inter-electrode region produced a much higher temperature than that of the incoming flow. Further work is required to better understand this result.

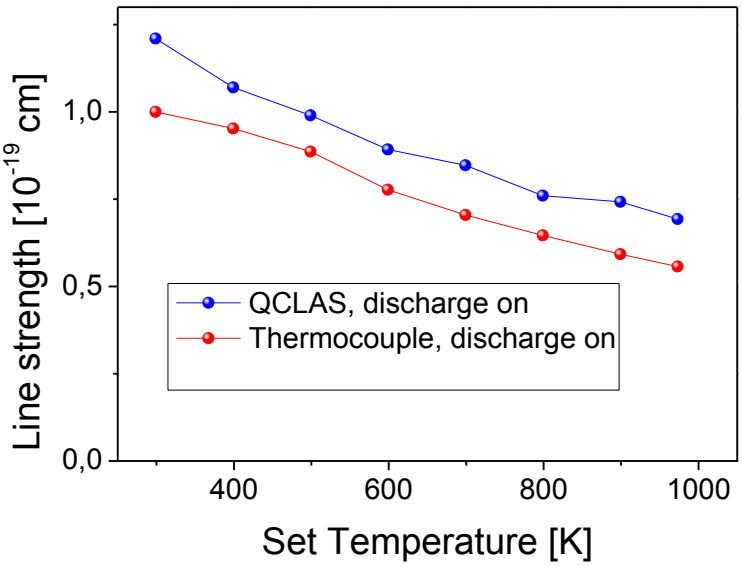

Figure 6.13: Line 1 intensity as a function of the set gas temperature. Two cases: using the temperatures measured with the thermocouple and with the collisional spectral width. Conditions: U = 3 kV, f = 30 kHz, d = 2 mm, v = 1.7 m/s, z = 25 cm.

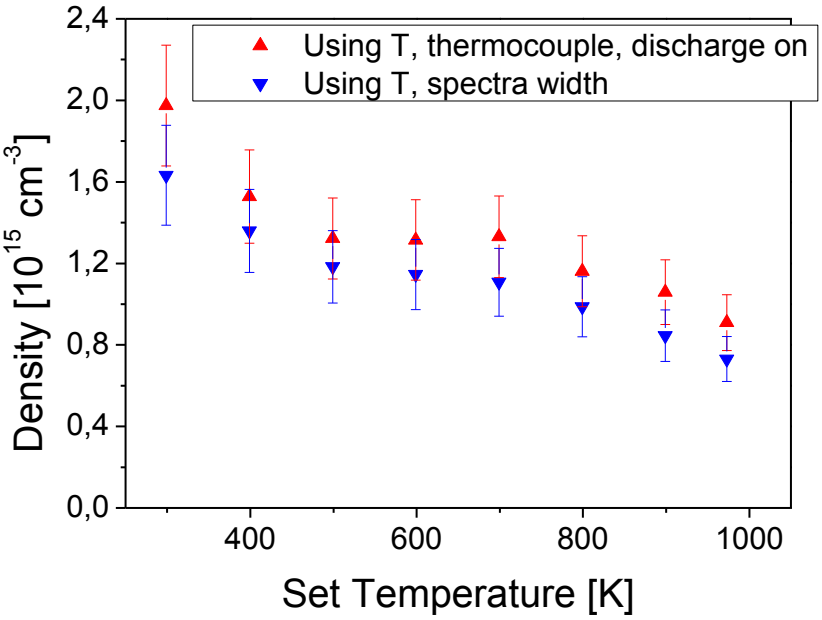

Figure 6.14: NO density as a function of the gas temperature. The NO density decreases with increasing gas temperature. Conditions: $U = 3$ kV, $f = 30$ kHz, $d = 2$ mm, $v = 1.7$ m/s, $z = 25$ cm.

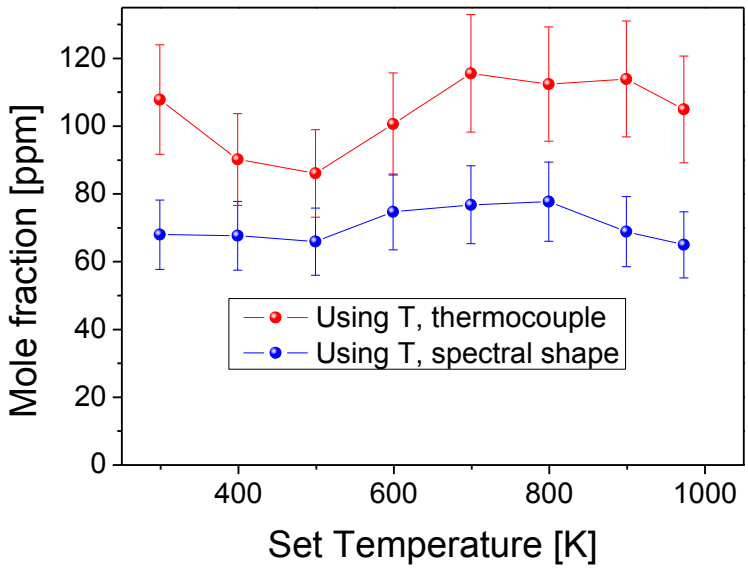

Figure 6.15: NO mole fraction as a function of the gas temperature. The NO mole fraction remains constant with increasing gas temperature. Conditions: $U = 3$ kV, $f = 30$ kHz, $d = 2$ mm, $v = 1.7$ m/s, $z = 25$ cm.

6.3.3 Post-discharge NO species flux

We now can compare, measurements in the discharge and measurements in the post-discharge, for the same conditions at 300 K. From figure 6.14, we know that the NO density in the post discharge at 300 K is about 1.6 (0.24) x 10^{15} cm^{-3}. This value has to be compared with the value of 2.25 x 10^{15} cm^{-3} found in chapter 5. For the purpose of comparison, the radial profile of the NO density in the discharge is given again in figure 6.16.

If we assume that the kinetics effects are negligible for NO leaving the discharge region until arriving at the post-discharge (25 cm downstream), then the flow rate of NO particles created in the small discharge volume is conserved up to the exit of the confinement tube, across the tube cross-section. Note that NO particles lifetime can reach hours in air at room temperature. This is many times larger than the convection time required for NO particles to travel from the discharge to the exit, i.e. about 25cm/1.7m/s ~ 0.15 s. Conservation of the flow rate of NO particles implies (assuming the velocity to be uniform and constant in the tube from the discharge region to the tube exit):

$$\int_{s_1} n_1(r)v_1(r)ds = \int_{s_2} n_2(r)v_2(r)ds = n_2 s_2 v_2 \qquad (6.2)$$

where s_1 and s_2 represent the cross-section of the discharge area and of the tube exit, respectively. v_1 and v_2 are the corresponding flow velocities, respectively. $n_1(r)$ and $n_2(r)$ are radial density distributions in the discharge and in the post-discharge regions, respectively. In the post-discharge, the radial distribution is assumed constant. *Stancu et al.* [2013] used the same experimental configuration for CO density measurements at the exit of the tube and they found a uniform radial distribution of CO.

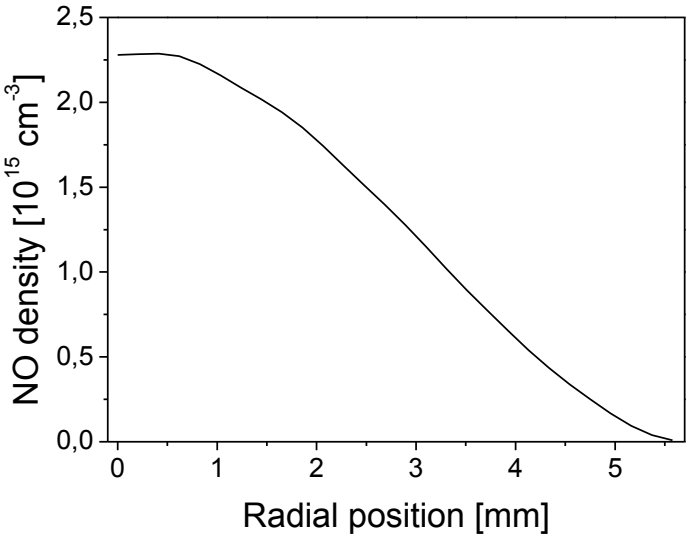

Figure 6.16: NO density radial distribution in the discharge. Conditions: $U = 3$ kV, $f = 30$ kHz, $d = 2$ mm, $v = 1.7$ m/s, $z = 0$ cm, $T = 300$ K.

The right-hand side member of equation 6.2 can be easily quantified. At the exit of the 4-cm radius, tube, the cross-section is 16 x π ~ 50.3 cm^2 while the corresponding NO density is equal to 1.6 x 10^{15} cm^{-3}. The cross-section of the flow in the discharge is about π x 6.4 x 10^{-1} ~ 2.01 cm^2. Assuming that v_1 ~1.7 m/s, v_2 ~ 1.7 x 2.01/50.3 ~6.8 x 10^{-2} m/s Hence, the right-hand side member is about 5.4 x 10^{17} molecule/s. Using the axisymmetry in the plane, the left-hand side of equation 6.2 can be developed as it follows:

$$\int_{s_1} n_1(r)v_1(r)ds = v_1 \int_{s_1} n_1(r)rdrd\theta = 2\pi v_1 \int_0^R n_1(r)rdr \tag{6.3}$$

where $R = 5.6$ mm.

Using equation 6.3 and the radial NO density distribution displayed in figure 6.16, the calculation of the left-hand side member of equation 6.2 results in about 1.4 x 10^{17} molecule/s. This is four times lower than the value in the post-discharge. In other words, the density measured in the post-discharge is about four times higher than what we would expect after NO particles had experienced dilution from the NRP discharge where they are produced up to the exit of the confinement tube where they are measured. This result suggests that a NO creation mechanism occurs in the post-discharge. The latter mechanism increases the NO density by a factor 4.

6.4 Characterization of the NRP post-discharge at 1000 K

In this section, we repeat part of the analysis carried out in section 6.2. This time, the NRP discharges operate in air flows at 1000 K and we perform measurements at the exit of the 25-cm long confinement tube. Similar to the measurements of section 6.3, we applied the QCLAS diagnostic using a 20-pass configuration. This section begins with the presentation of the experimental conditions. Then we investigate successively, the influences of the pulse voltage amplitude, the pulse repetition frequency and the air flow rate on the production of NO.

6.4.1 Experimental conditions

All the measurements performed in this section are carried out with the NRP discharges operating in an incoming flow at 1000 K. Using pulse generator PG2, NRP discharges are generated between two electrodes in a vertical pin-to-pin configuration

without the bluff body. The gap distance is fixed at 4 mm and the electrodes are located 1-cm above the exit of the air-heater.

6.4.2 Influence of pulse voltage amplitude

We carried out the NO density measurements at applied pulse voltage amplitude from 2 to 4.4 kV. Other NRP discharges parameters are fixed. The repetition frequency and the airflow rate are kept constant at 30 kHz and at 4.6 m^3/h (velocity about 2.6 m/s in the electrodes region), respectively. For each voltage amplitude value, we use a thermocouple to record the gas temperature when the discharge is turned on. The measured temperatures serve to correct the line strength changes for each measurement. The temperatures and corresponding line strengths are displayed in figure 6.17. From 2 to 4.4 kV, the gas temperature downstream rises by 50 K, from about 850 up to 900 K. Consequently, line 1 intensity decreases by less than 6 %, from about 5.5 x 10^{-20} cm to 5.2 x 10^{-20} cm. The inferred NO densities are shown in figure 6.18. The NO density increases with the increase of the voltage amplitude, in the same manner as in an airflow at 300 K. For our experimental conditions, figure 6.19 shows that the slope featured (12.5 ppm/kV) is about three times lower than that for the conditions at 300 K (i.e. 40 ppm/kV).

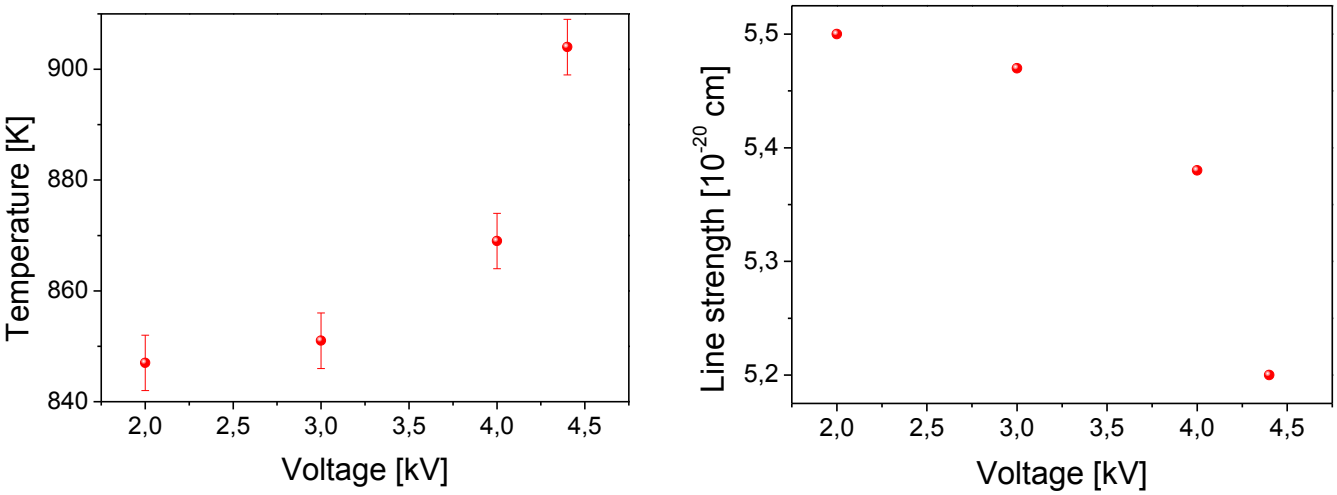

Figure 6.17: Gas temperature as a function of the pulse voltage amplitude (left). Line 1 intensity as a function of the voltage amplitude (right). The temperature increases by about 50 K leading to a 5 % decrease of the line strength. Conditions: f = 30 kHz, d = 4 mm, v = 2.6 m/s, z = 25 cm, T = 1000 K.

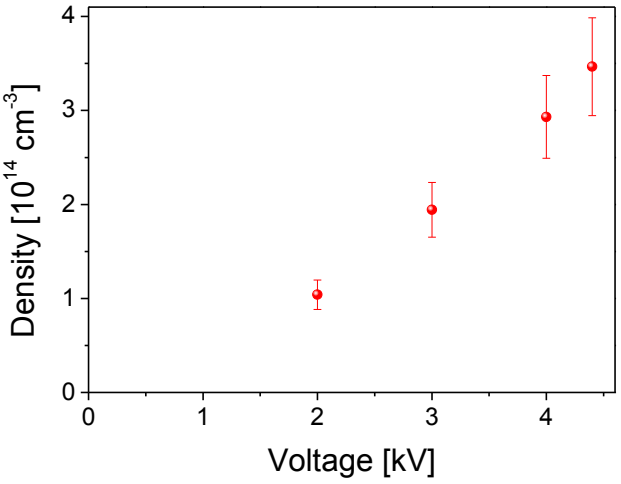

Figure 6.18: NO density as a function of the pulse voltage amplitude. The NO density increases by a factor about 3.5 from 2 to 4.4 kV. Conditions: $f = 30$ kHz, $d = 4$ mm, $v = 2.6$ m/s, $z = 25$ cm, $T = 1000$ K.

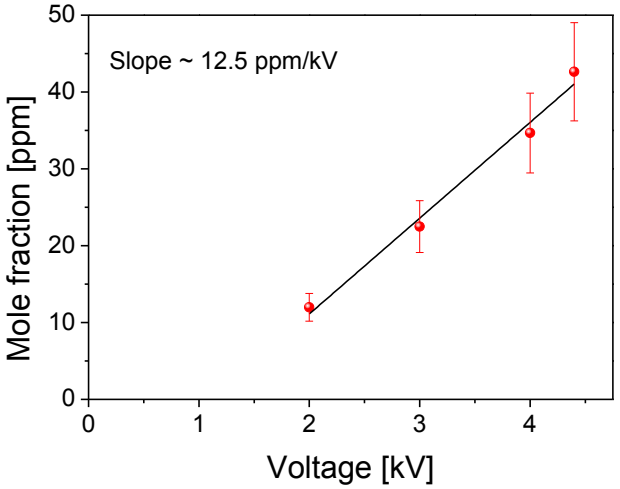

Figure 6.19: NO mole fraction as a function of the pulse voltage amplitude. The NO mole fraction increases with rising pulse voltage amplitude exhibiting a slope about 12.5 ppm/kV. Conditions: $f = 30$ kHz, $d = 4$ mm, $v = 2.6$ m/s, $z = 25$ cm, $T = 1000$ K.

6.4.3 Influence of pulse repetition frequency

Here, we repeated the analysis of the last subsection, exploring the influence of the repetition frequency. The voltage amplitude is kept constant at 5.7 kV. The gap distance and the flow velocity in the electrodes region are 4 mm and 2.6 m/s, respectively.

Figure 6.20 displays the NO density as a function of the pulse repetition frequency. As expected, the NO density increases (by a factor 3.5) with the increase of the repetition frequency from 10 to 30 kHz. Note that the first point of figure 6.20, which is the measurement data at 10 kHz, corresponds to the NRP "*reference case*" investigated by [*Kaddouri*, 2011; *Rusterholtz*, 2012]. The NO density in the reference case, measured in the post-discharge is hence about 2.5 x 10^{14} cm^{-3}. As depicted in figure 6.21, the NO mole fraction increases from about 30 to 80 ppm with increasing repetition frequency. The slope of the rise is about 2.6 ppm/kHz, which is also about three times lower than the slope determined for measurements in ambient air, i.e. 7 ppm/kHz.

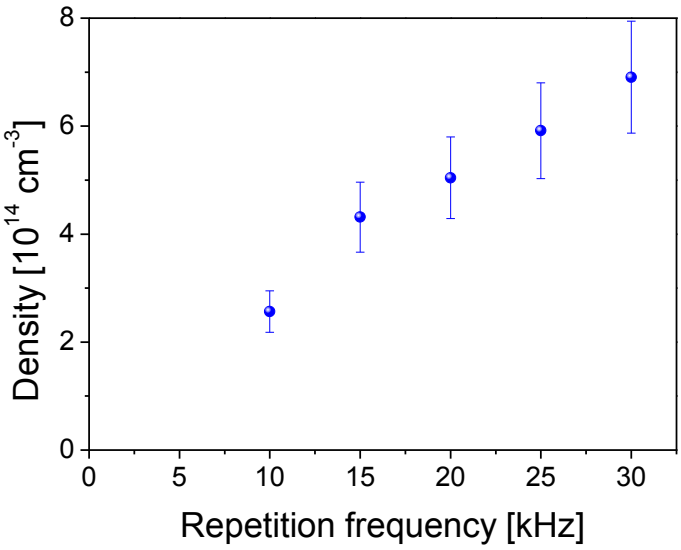

Figure 6.20: NO density evolution as a function of the voltage amplitude. The NO density increases by a factor about 3.5 from 2 to 4.4 kV. Conditions: U = 5.7 kV, d = 4 mm, v = 2.6 m/s, z = 25 cm, T = 1000 K.

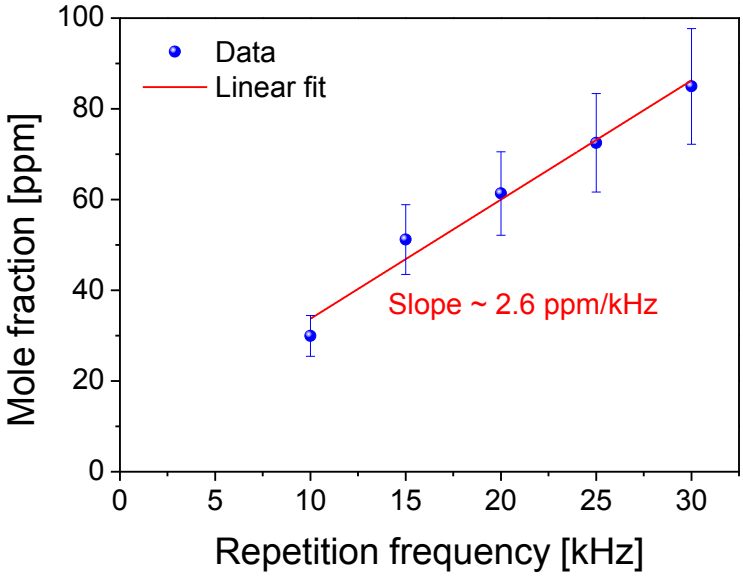

Figure 6.21: NO mole fraction as a function of the pulse repetition frequency. The NO mole fraction increases with increasing pulse repetition frequency exhibiting a slope about 2.6 ppm/kV. Conditions: $U = 5.7$ kV, $d = 4$ mm, $v = 2.6$ m/s, $z = 25$ cm, $T = 1000$ K.

6.4.4 Influence of flow rate

Finally, we investigated the influence of the air flow rate on the NO densities released by NRP discharges operating in a preheated airflow at 1000 K. Figure 6.22 presents the results of the gas temperature measurements using a thermocouple. The gas temperature at the tube exit increases with the increase of the air flow rate. This is because the flow has less time to cool down. In this way, the gas temperature augments by about 150 K when airflow rate is increased from 1.2 to 4.8 m^3/h. Consequently, the line intensity decreases by about 30 % from about 7.5 x 10^{-20} at 1.2 m^3/h down to 5.25 x 10^{-20} cm at 4.8 m^3/h.
The resulting NO density as a function of the air flow rate is shown in figure 6.23. We observe that the NO density decreases from about 1.5 x 10^{15} cm^{-3} to 2 x 10^{14} cm^{-3} with the increase of the airflow rate. The NO density in the NRP "*reference case*" corresponds to the interpolation at 4.6 m^3/h of the curve of figure 6.23. This yields about 2.5 x 10^{14} cm^{-3}, in a good agreement with the result of the previous subsection.

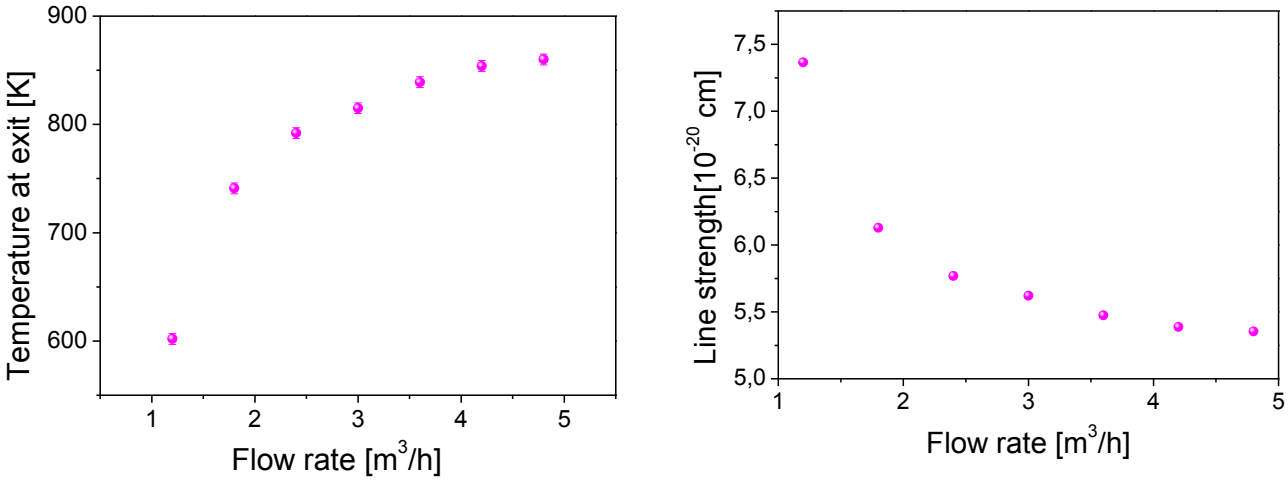

Figure 6.22: Gas temperature at tube exit measured with a thermocouple (left). Deduced line strength evolution with respect to airflow rate (right). The gas temperature increases by about 150 K between 1.2 and 4.8 m³/h. As a result, the intensity of line 1 falls by 30 % for the same range of air flow rates. Conditions: U = 5.7 kV, f = 10 kHz, d = 4 mm, z = 25 cm, T = 1000 K.

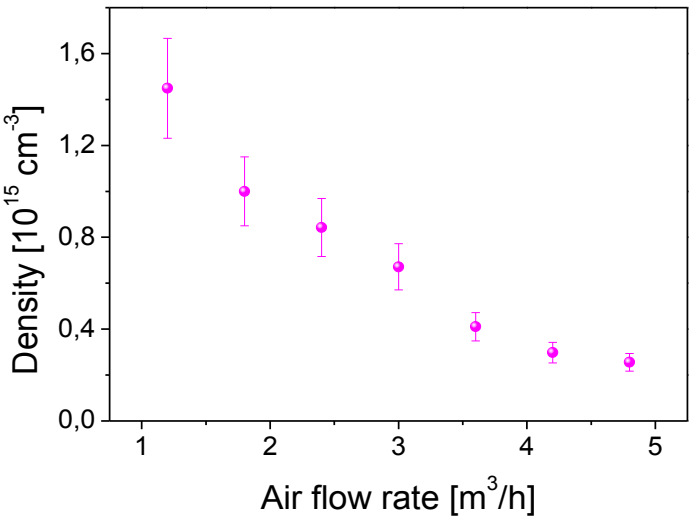

Figure 6.23: NO density evolution with respect to air flow rate. The NO density decreases by a factor 7 from 1.2 to 4.8 m³/h. Conditions: U = 5.7 kV, f = 10 kHz, d = 4 mm, z = 25 cm, T = 1000 K.

Similarly to section 6.2, we can use measurements with respect to the flow rate to deduce the NO production rate at 1000 K. The result is outlined in figure 6.24. In a 1000 K, air flow we find that the NO production rate ranges from 3 to 5.5 x 10^{17} molecule/s. The maximum value is hence about 3 times lower than that at 300 K (2 x 10^{18} molecule/s).

If we compare to the studies at 300 K, the main difference is that the production rate has a slight decay tendency at 1000 K while at room temperature the increase was evident.

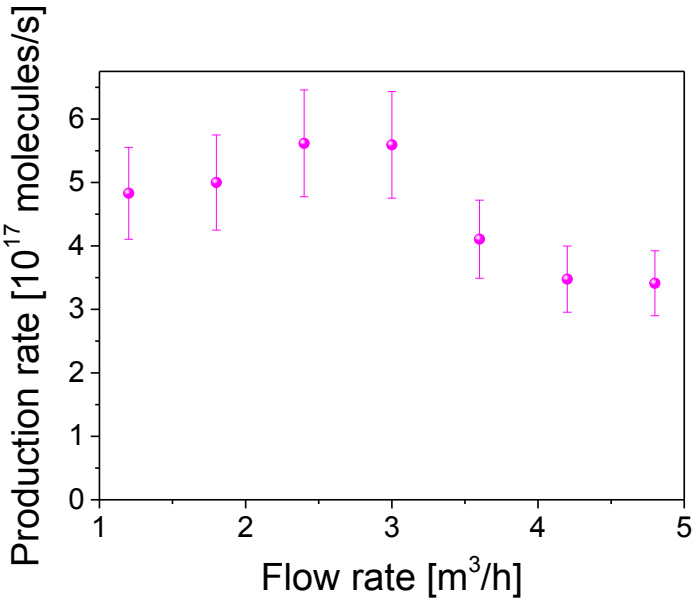

Figure 6.24: NO production rate as a function of the airflow rate. The NO production rate reaches about 6.5 x 10^{17} molecules/s. Conditions: $U = 5.7$ kV, $f = 10$ kHz, $d = 4$ mm, $z = 25$ cm, $T = 1000$ K.

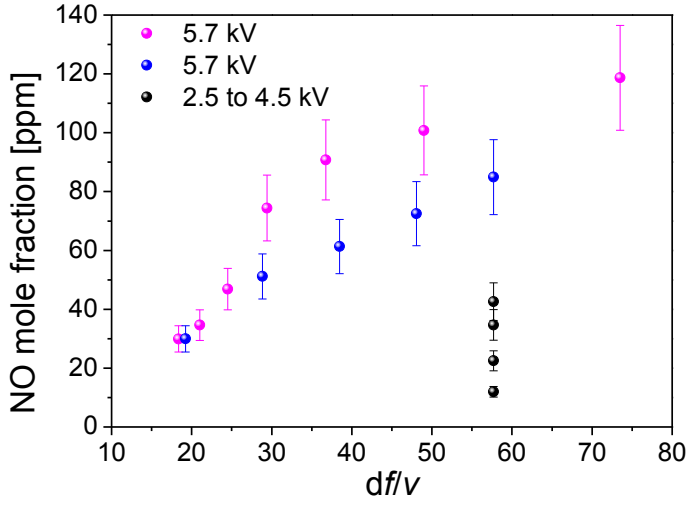

Figure 6.25: NO mole fraction as a function of the dimensionless parameter for various pulse voltage amplitudes. Conditions: $z = 25$ cm, $T = 1000$ K.

In order to check if the two keys parameters found in section 6.2 were also relevant in a 1000 K air flow, figure 6.25 shows the NO mole fraction (ensuing from studies with respect to pulse amplitude, pulse repetition frequency and air flow rate) as a

function of the dimensionless parameter. Similarly to what we obtained at 300 K, at constant voltage pulse amplitude, the NO mole fraction increases with the increase of the number of discharges seen by the gas in the gap. In addition, for the same number of discharges seen by the gap, the NO mole fraction rises with the increase of the applied pulse voltage amplitude.

6.5 NO dominant formation and destruction mechanisms in NRP discharges

In the foregoing sections of this chapter, we showed how the NO production was influenced by varying the NRP discharge parameters. The goal of this section is to understand the main production and losses pathways of NO in NRP discharges and post-discharge. In subsection 6.5.1, we present a literature review of the processes of NO creation and destruction. Then, in subsection 6.5.2, using data from the literature together with results of the studied "reference case", we calculate the temporal evolution of the NO production/loss rates for the various processes proposed in the literature. Finally from the reaction rates, we infer the NO absolute densities in section 6.5.3. The results of the experiments together with the estimated NO densities enable us to conclude on the main kinetics occurring in the discharge and in the post-discharge.

6.5.1 NO production and destruction processes: rate constants

In equilibrium systems with gas temperature above 1800 K, it is well known that the Zel'dovich thermal mechanism is the dominant route for NO formation [*Bowman*, 1992]:

$$N_2 + O \rightarrow NO + N \tag{6.4}$$

$$N + O_2 \rightarrow NO + O \tag{6.5}$$

In addition, the thermal mechanism can be extended to a third reaction in the presence of hydroxyl radicals:

$$N + OH \rightarrow NO + H \tag{6.6}$$

However, in non-equilibrium systems, the internal degree of freedom of gas molecules and radicals can be significantly excited and can overcome the activation energy barriers of reactions 6.5 and 6.6. This results in faster NO formation [*Kim et al.*, 2007; *Uddi*, 2008; *Burnette et al.*, 2014] and hence «enhanced» Zel'dovich reactions [*Burnette et al.*, 2014]. Several authors in the literature investigated the latter

«enhanced» reactions in order to find the dominant NO formation routes for different types of plasmas and at different pressures.

For instance, for low-pressure discharges, *Gordiets et al.* [1995] concluded that for their DC flowing air glow discharge at 2 Torr, the main NO production route is via the reaction $N_2(X\ ^1\Sigma,\ v > 12) + O \rightarrow NO + N$. A similar conclusion was drawn by *Guera et al.* [2001] for their RF discharge in an N_2/O_2 mixture at 3.3 Torr. They also mentioned that $N_2(A\ ^3\Sigma) + O \rightarrow NO + N(^2D)$ could contribute significantly to the production of NO. This reaction could even be dominant at lower pressure as claimed by *Benedictis et al.* [1997] following NO and $N_2(A,\ v)$ measurements by LIF in their 0.1 Torr 27 MHz RF discharge.

At high-pressure, *Zhao et al.* [2005], *Herron*, [2001] and *Penetrante et al.* [1997] suggested that the reaction $N(^2D) + O_2 \rightarrow NO + O$ is the principal path of NO production in a pulsed corona discharge at 217 kPa, a pulsed dielectric barrier discharge at atmospheric pressure and an electron beam plasma, respectively. *Uddi et al.* [2009] claimed that this reaction was the dominant mechanism in filamentary discharges.

More recently, comparing their kinetic model to measurements of O, N (by TALIF), NO (by LIF), N_2 ($X,\ v=0\text{-}4$) and gas temperature (both by picosecond CARS) [*Burnette et al.*, 2014] in a nanosecond pulse discharge at 100 Torr, *Shkurenkov et al.* [2014] suggested that NO is mainly produced by the enhanced Zel'dovich reactions:

$$N_2^* + O \rightarrow NO + N \qquad (6.7)$$

where $N_2^* = N_2(A\ ^3\Sigma_u^+,\ B\ ^3\Pi_g,\ W\ ^3\Delta_u,\ B'\ ^3\Sigma_u^-,\ a'\ ^1\Sigma_u^-,\ a\ ^1\Pi_g,\ w\ ^1\Delta_u,\ C\ ^3\Pi_u,\ E\ ^3\Sigma_g^+,\ a''\ ^1\Sigma_g^+)$.

Because NRP discharges in the spark regime efficiently excite of the electronic levels of nitrogen by electron impact (100 Td ≤ E/n ≤ 300 Td) and because the filamentary regime at atmospheric pressure provides an intense gas heating [Pai et al., 2010], the NO main formation routes will be a competition between Zel'dovich thermal mechanisms, reactions involving vibrationally and electronically excited levels of nitrogen, and reactions involving the excited metastable states of atomic nitrogen produced by filamentary discharges. The rate coefficients for all these reactions are presented in tables 6.1 to 6.4. Table 6.1 gives the rate coefficients of NO formation and loss by forward and reverse Zel'dovich reactions. The latter are taken from *Kossyi et al.* [1992] and *Capitelli et al.* [2000]. The rates of NO production by the quenching of excited nitrogen electronic levels with O atoms are taken from *Kossyi et al.* [1992] and *Shkurenkov et al.* [2014] and are displayed in table 6.2. Table 6.3 presents the rate constants of NO production by the quenching of excited nitrogen vibrational levels [*Gordiets et al.*, 1995]. Finally, *Kossyi et al.* [1992] also give the rate constants for NO creation by the quenching of metastable levels of nitrogen atoms

with O_2. The corresponding rate coefficients are summarised in table 6.4. Whenever available, the temperature domain is specified in the tables.

Table 6.1: Forward and reverse Zel'dovich rates (labelled R1-R6).

Processes	k (cm^3/s)	T (K)	Ref
R1: $N + O_2 \rightarrow NO + O$	1.1 x 10^{-14} T exp(-3150/T)	$300 \leq T \leq 3000$	*Kossyi et al.* [1992]
R2: $N + O_2 \leftarrow NO + O$	2.5 x 10^{-14} T exp(-19500/T)	$1000 \leq T \leq 3000$	*Capitteli et al.* [2000]
R3: $N_2 + O \rightarrow NO + N$	3 x 10^{-10} exp(-38370/T)	$2000 \leq T \leq 5000$	*Capitteli et al.* [2000]
R4: $N_2 + O \leftarrow NO + N$	1.8 x 10^{-11} $(T/300)^{0.5}$	$200 \leq T \leq 4000$	*Kossyi et al.*, [1992]
R5: $N + OH \rightarrow NO + H$	7.5 x 10^{-11}		*Capitteli et al.* [2000]
R6: $N + OH \leftarrow NO + H$	2.8 x 10^{-10} exp(-24500/T)		*Capitteli et al.* [2000]

Table 6.2: Rate constants of NO formation by the quenching of excited N_2 electronic levels with O and NO (labelled R7-R10).

Processes	k (cm^3/s)	T (K)	Ref
R7: $N_2(A) + O\ (^3P) \rightarrow NO + N(^2D)$	7 x 10^{-12}		*Kossyi et al.* [1992]
R8: $N_2(B, C) + O \rightarrow NO + N$	3 x 10^{-10}		*Shkurenkov et al.* [2014]
R9: $N_2(A) + NO \rightarrow NO + N_2$	7 x 10^{-11}		*Kossyi et al.* [1992]
R10: $N_2(B) + NO \rightarrow NO + N_2(A)$	2.4 x 10^{-10}		*Kossyi et al.* [1992]

Table 6.3: Rate constants of NO formation by the quenching of excited N_2 vibrational levels with O atoms (labelled R11).

Processes	k (cm^3/s)	T (K)	Ref
R11: $N_2(v > 12) + O \rightarrow NO + N$	10^{-11}		*Gordiets et al.* [1995]

Table 6.4: Rate constants of NO formation by the quenching of metastable levels of nitrogen atoms with O_2 (labelled R12-R14).

Processes	k (cm^3/s)	T (K)	Ref
R12: $N(^2D) + O_2 \rightarrow NO + O(^3P)$	$1.5 \times 10^{-12} (T/300)^{0.5}$		*Kossyi et al.* [1992]
R13: $N(^2D) + O_2 \rightarrow NO + O(^1D)$	$6 \times 10^{-12} (T/300)^{0.5}$		*Kossyi et al.* [1992]
R14: $N(^2P) + O_2 \rightarrow NO + O$	2.6×10^{-12}		*Kossyi et al.* [1992]

We did not discuss here NO formation via the Fenimore "prompt mechanism" [*Fenimore*, 1971], the nitrous oxide (N_2O) mechanism [*Malte and Pratt*, 1974] or NO from the fuel. This is because for gas temperatures above 1800 K, these reactions are dominated by the Zel'dovich mechanism. Furthermore, the prompt mechanism and NO from the fuel do not apply for NRP discharges in air because of the lack of carbon and hydrogen compounds on the one hand and of the lack of fuel containing nitrogen (see section 2.5.2 of chapter 2) on the other hand.
In addition, some authors also mention NO formation/loss through reactions including NO_2 and O_3 [*Zhao et al.*, 2005; *Van Gessel et al.*, 2013, *Van Gaens et al.*, 2014]. The rate coefficients of the corresponding reactions are reported in table 6.5.

Table 6.5: Rate constants of NO formation/loss via NO_2 and O_3 (labelled R15-R18).

Processes	k (cm^3/s or cm^6/s)	T (K)	Ref
R15: $NO_2 + O \rightarrow NO + O_2$	$6.5 \times 10^{-12} \exp(120/T)$	$200 \leq T \leq 300$	*Atkinson et al.* [1997]
R16: $NO_2 + M \leftarrow NO + O + M$	$1.01 \times 10^{-31} (T/300)^{-1.6} [N_2]$	$200 \leq T \leq 300$	*Atkinson et al.* [1997]
R17: $NO_2 + O_2 \leftarrow NO + O_3$	$1.8 \times 10^{-12} \exp(-1370/T)$	$195 \leq T \leq 300$	*Atkinson et al.* [1997]
R18: $2NO_2 \leftarrow NO + NO + O_2$	$3.3 \times 10^{-39} \exp(530/T)$	$270 \leq T \leq 600$	*Atkinson et al.* [1997]

Electron kinetics are important in plasma kinetics. But for the NO production, electrons appear to have an indirect influence via the formation of excited states of molecules and radicals. Regarding NO loss by electron impact, *McLarmon and Penetrante*, [1998] found that charged species (including electrons) do not contribute significantly to the NO conversion in their DBD plasma reactor.

Figure 6.26 displays the rate coefficients of forward and reverse Zel'dovich reactions as a function of the temperature. All rate constants R1 to R6 increase with the temperature. Over the investigated range of temperatures, reactions R5, R4 and R1 have the strongest rate coefficients. At 2000 K (gas temperature at peak current for NRP discharge in the "reference case" as will be shown in the next subsection), they are respectively about 7.5 x 10^{-11}, 3 x 10^{-11} and 4 x 10^{-12} cm^3/s. Other rates are at least 3 orders of magnitude lower.
The rate constants for NO formation and loss processes related to NO_2 and O_3 are presented in figure 6.27. Reaction R15 has the highest rate constant, with a value about 7 x 10^{-12} cm^3/s at 2000 K. Rate coefficients of the two other reactions are at least one order of magnitude lower.
Finally, figure 6.28, which shows the major rate constants for reactions R1 to R14 shows that overall, the largest rate coefficient for NO formation is the one of reaction R8 involving the quenching of N_2 B and C electronic levels with O atoms, k = 3 x 10^{-10} cm^3/s at 2000 K. Then come the rates of reactions R10 (k = 2.4 x 10^{-10} cm^3/s) and R5 (k = 7.5 x 10^{-11} cm^3/s). Otherwise, the NO loss rate constants are dominated by the rate of Zel'dovich R4 reaction involving the quenching of NO molecules with N atoms. Less important are the quenching of NO molecules with O_3 (R17) and then with O atoms in the three-body reaction (R16).

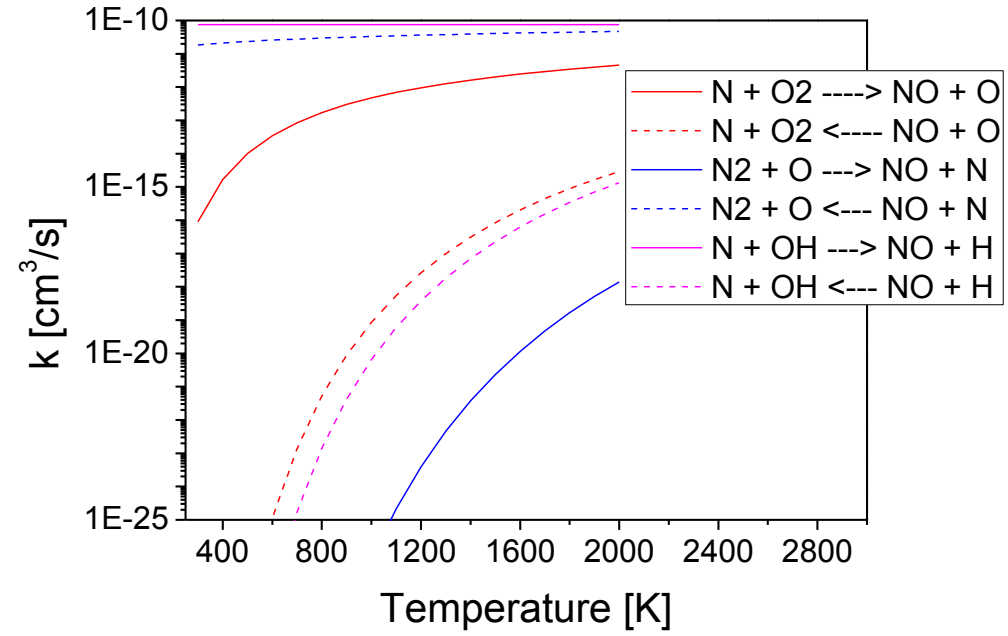

Figure 6.26: Forward and reverse Zel'dovich rate constants as a function of temperature. In the investigated temperature range, forward rate constants are dominated by the quenching of nitrogen atoms with the hydroxyl radical whereas reverse rates are dominated by the quenching of nitrogen atoms with NO molecules.

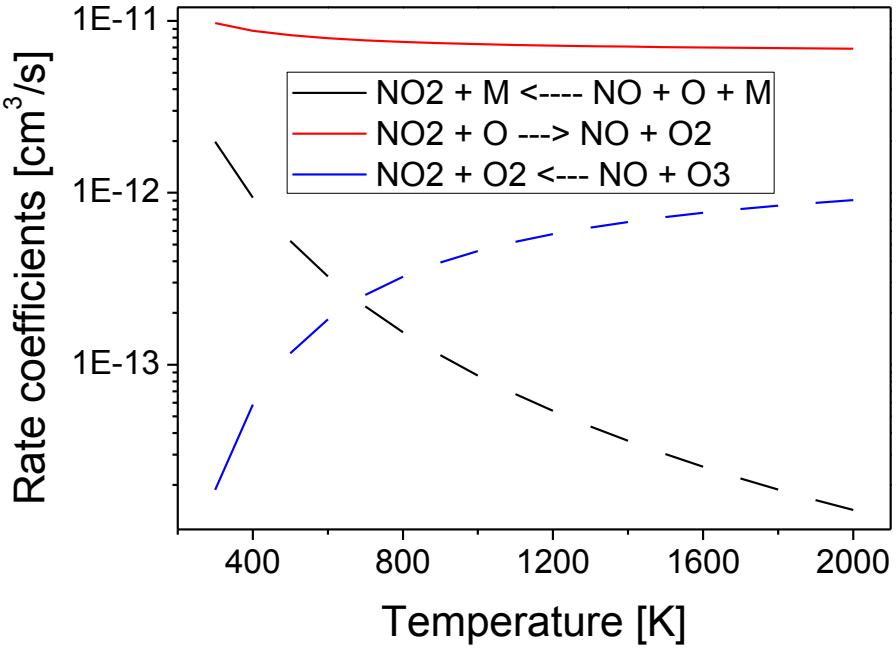

Figure 6.27: Rate constants for reactions R15 to R17. The formation rates are dominated by the reactions of NO_2 molecules with O atoms whereas reverse rates at 2000 K are dominated by the reactions of NO with ozone.

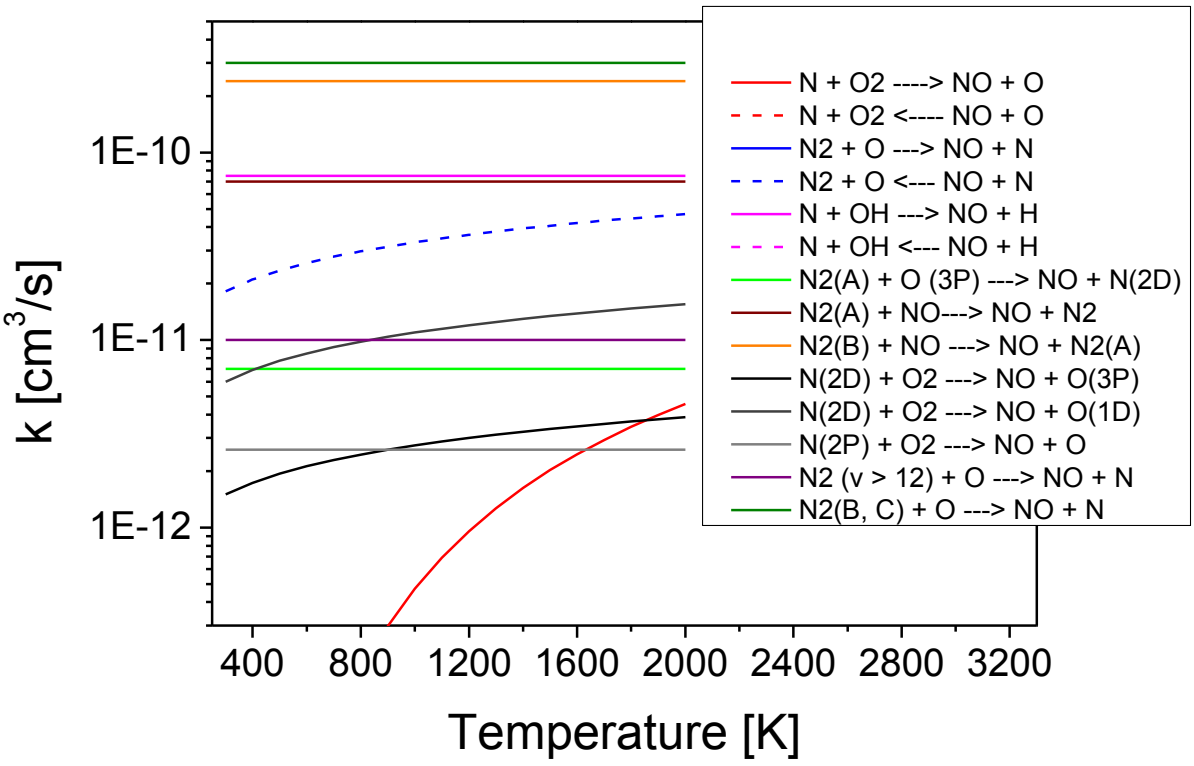

Figure 6.28: Zoomed view of the major rate constants as a function of temperature.

6.5.2 NO production/destruction rates: application to the reference case

Stancu et al. [2010] and *Rusterholtz et al.* [2013] measured the temporal evolution of N_2 (A, B, C), O densities, together with gas temperature and electrons density in the NRP "*reference case*" (U = 5.7 kV, f = 10 kHz, d = 4 mm, v = 2.6 m/s, T = 1000 K) - (see figure 6.29). We can therefore use these data to deduce the rates of production/loss of NO by previously quoted processes and then the NO density produced/lost by the same processes. To estimate the production/loss rates and densities, we considered here that reactions R1 to R18 are uncoupled. As a result, for instance, the NO production rate (in cm^{-3}/s) from reaction R1 can be written as:

$$\frac{d[NO]}{dt} = k_{R1}[N][O_2] \tag{6.8}$$

where k_{R1} is the temperature-dependant reaction rate coefficient of reaction R1 and [NO], [N], and [O_2] are the time-resolved densities of NO, N and O_2 species, respectively.

Unfortunately, we do not have N atoms density. We considered here a constant 10^{15} cm^{-3} N density during the pulse (and until 40 ns). This value was chosen two orders of magnitude lower than the O density (10^{17} - 10^{18} cm^{-3}) because of the higher energy required to dissociate N_2 molecules (9.8 eV) in comparison with the 5.15 eV required for the dissociation of O_2 [*Kerr and Stocker*, 1993].
Reverse processes leading to NO loss require the NO density as input to quantify NO loss rate. Here again, because we do not have time-resolved NO density measurements in the reference case (and in the discharge), we considered a constant 10^{15} cm^{-3} NO density during the pulse (this being the typical average density measured by QCLAS).

With these assumptions, the temporal evolutions of the NO production rates by the quenching of excited electronic states of N_2 with O atoms are calculated and presented in figure 6.30. The production rate from $N_2(B)$ state varies between 2 x 10^{22} and 3 x 10^{24} cm^{-3}/s and has an 8.8 x 10^{23} cm^{-3}/s time-averaged value. The production rate from $N_2(C)$ rather ranges between 2.1 x 10^{20} and 2.7 x 10^{23} cm^{-3}/s. It also corresponds to a mean production rate of 5.2 x 10^{22} cm^{-3}/s. The production rate from $N_2(A)$ varies between 6 x 10^{20} and 2.3 x 10^{21} cm^{-3}/s and has an average value around 1.5 x 10^{21} cm^{-3}/s. Reactions R9 and R10 were not considered because each of them yield to same NO production and loss rates.

The NO production and loss rates by Zel'dovich reactions are shown in figure 6.31. Production is dominated by the quenching of N atoms with O_2 molecules. The corresponding rate ranges between 2 - 6.4 x 10^{22} cm^{-3}/s with a mean value of 4.2 x 10^{22} cm^{-3}/s. Note that we did not consider reactions R5 and R6 since they only apply in combustion environments. The production rates from reactions involving nitrogen excited electronic states and from the Zel'dovich reactions are combined in figure 6.32.

Figure 6.33 displays the NO loss rates leading to NO_2 formation. The related loss rates range respectively between 3x 10^{18} and 7.7 x 10^{18} cm^{-3}/s for the three-body reaction of NO with O atoms and a third body (reaction R16) and between 3.3 x 10^{9} and 1 x 10^{10} cm^{-3}/s for reaction of NO with O_2.
The NO production and loss rates are summarized in table 6.6.
Finally, since we do not have yet time resolved density measurements of N, $N_2(v > 12)$, $N(^2D)$, $N(^2P)$, NO_2 and O_3 species, for the intent of comparison, we show some NO production/loss rates in table 6.7. The rates from table 6.7 are calculated at the time corresponding to the peak conduction current of figure 6.29 (about 10 ns). The gas temperature in these conditions is about 2000K.

From table 6.7 we learn that at peak discharge current, the NO production rate by the quenching of $N_2(B)$ with O atoms is about 10^{24} cm^{-3}/s. Consequently, for the reaction of N atoms with O_2 molecules to give a comparable rate, the density of N would have to be on the order of 3 x 10^{17} cm^{-3}, and the reaction of N atoms with OH radicals would require N density of about 2 x 10^{19} cm^{-3}. Continuing the same type of analysis, we will need for $N_2(v > 12)$, $N(^2D)$, $N(^2P)$, and NO_2 densities of about 2.5 x 10^{17} cm^{-3}, 10^{17} cm^{-3}, 5 x 10^{17} cm^{-3} and 5 x 10^{17} cm^{-3} respectively.
These densities, of the order of 10^{17} cm^{-3} or higher, are very unlikely given that they would all be higher or comparable to the measured O density. Thus, we expect that all above processes are negligible compared to the quenching of $N_2(B)$ with O atoms in term of NO production rate. Similarly, a $N_2(v > 12)$ density about 2.5 x 10^{17} cm^{-3} seems not probable since this would represent about 10 % of the N_2 density at 2000 K (0.8 x 2.45 x 10^{19} x 300/2000 ~ 3 x 10^{18} cm^{-3}).

Regarding the loss processes, the NO loss rate by its quenching with O atoms is about 10^{18} cm^{-3}/s. NO loss via its quenching with N atoms requires a N density about 2.5 x 10^{13} cm^{-3} to be comparable with the former process and loss through its reaction with ozone requires an O_3 density of about 1.4 x 10^{15} cm^{-3}. Because we expect the N density to be in the range of 10^{15} cm^{-3}, the loss by quenching with N is expected to be important. The loss by quenching with ozone is expected to be negligible because of the low ozone content expected in high temperature environments above 1000 K [*Benson and Axworthy,* 1957; *Michael*, 1971; *Center and Kung*, 1975]. In these studies, the rate constant of ozone decomposition was shown to increase with the gas temperature following the two steps mechanism:

$$O_3 + M \rightarrow O_2 + O + M \tag{6.9}$$

$$O_3 + O \rightarrow O_2 + O_2 \tag{6.10}$$

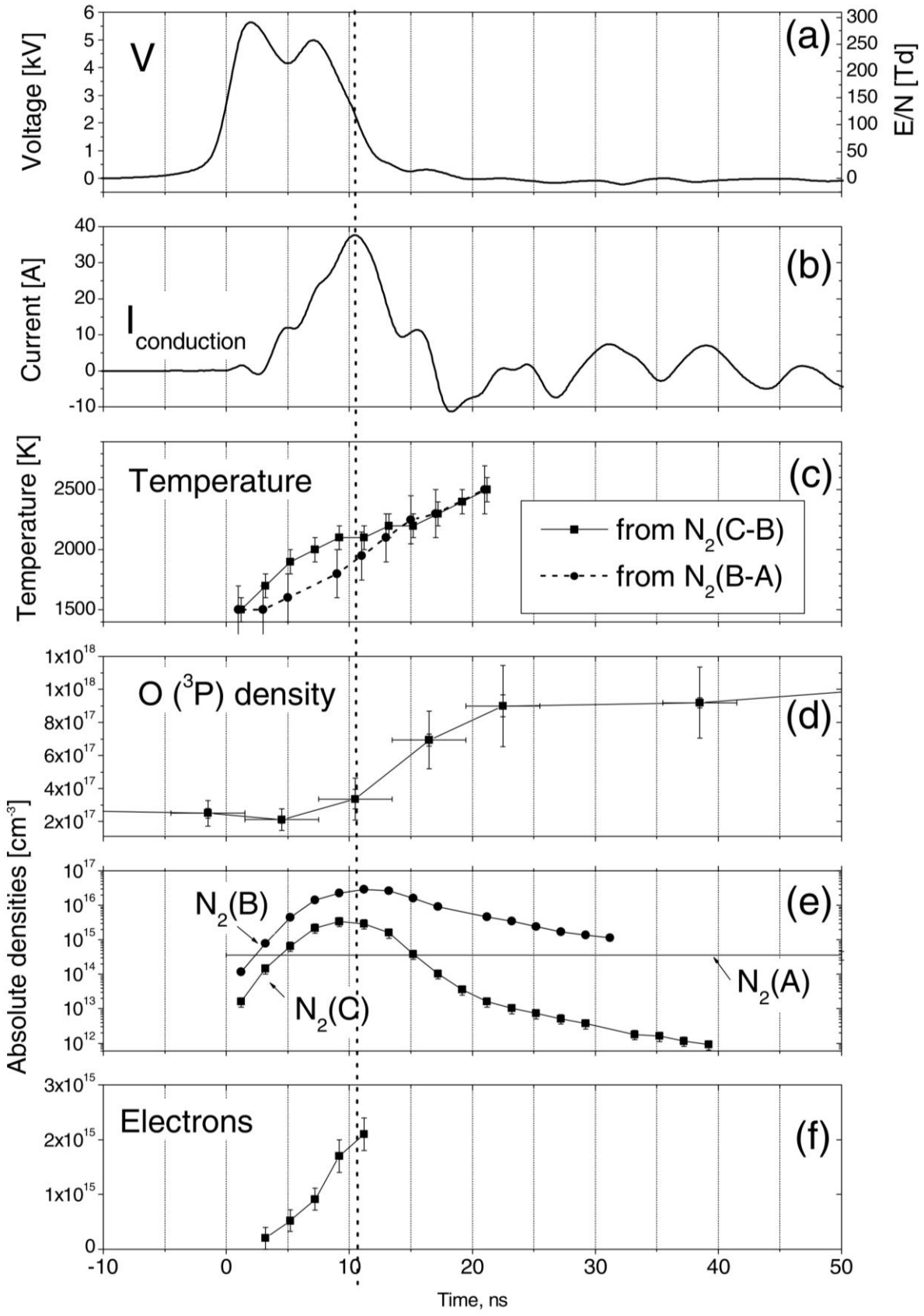

Figure 6.29: Synchronized measurements of voltage, current, temperature, O, N_2(A, B, C) and electron densities from *Rusterholtz et al.*, [2013].

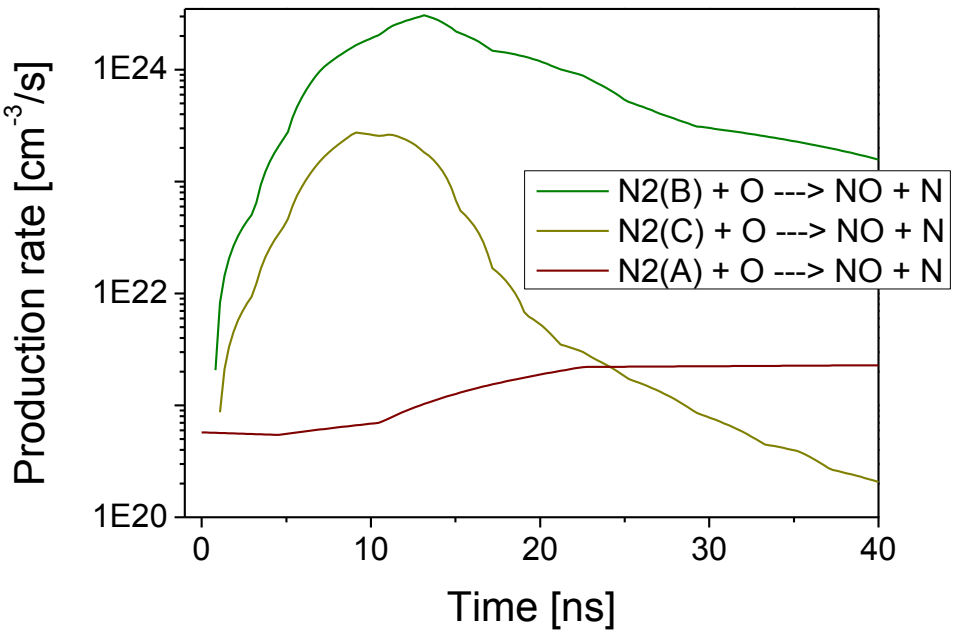

Figure 6.30: Time evolution of the NO production rates by quenching of atomic oxygen with nitrogen excited electronic states.

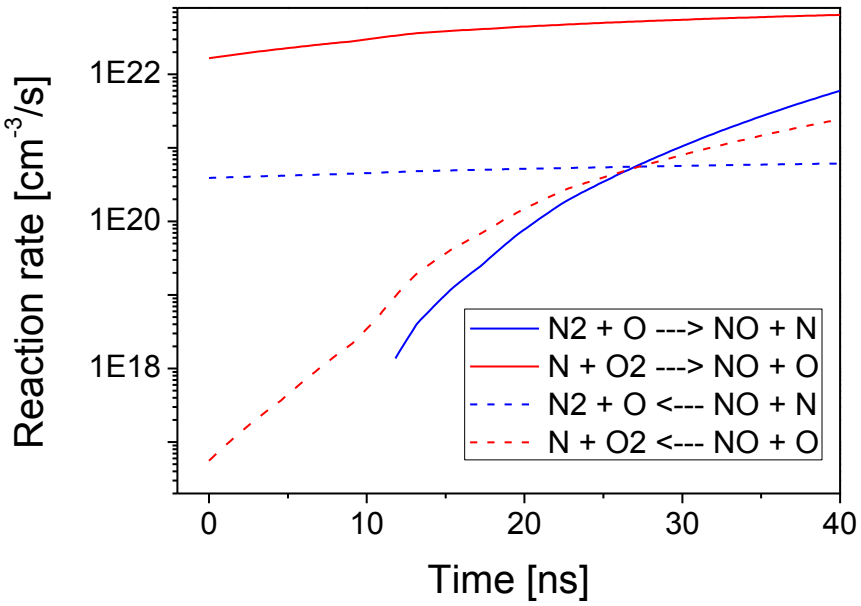

Figure 6.31: Time evolution of the NO production and loss rates rate by Zel'dovich mechanism (in environments without OH radicals).

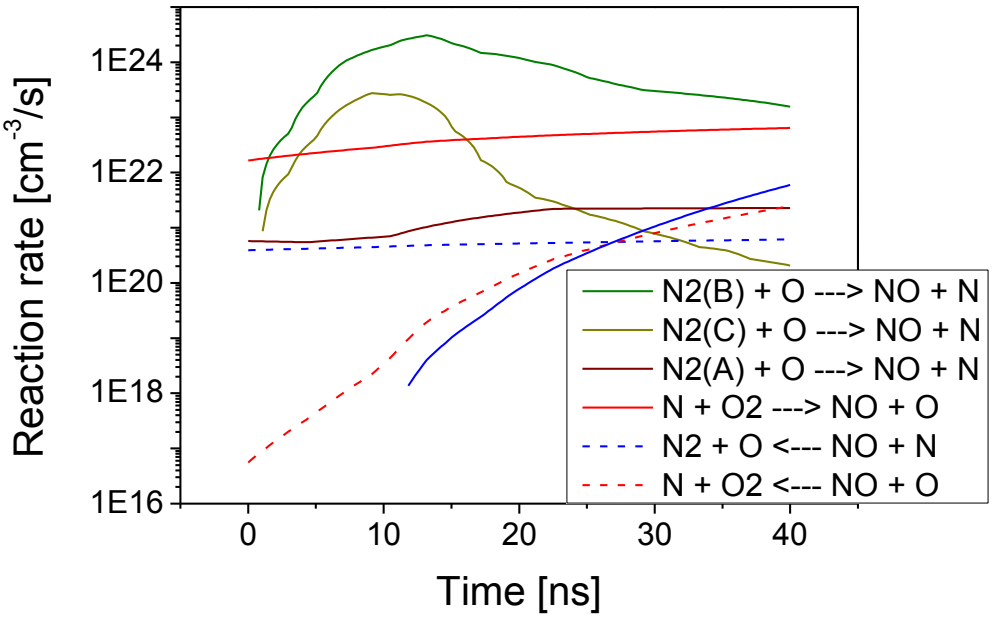

Figure 6.32: Time evolution of the NO production and loss rates.

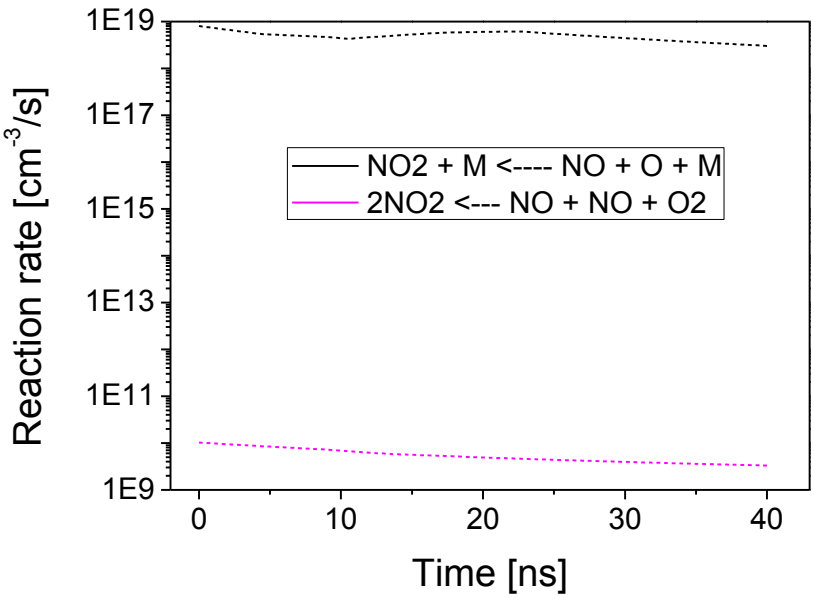

Figure 6.33: Time evolution of the NO loss rates leading to the formation of NO_2.

Table 6.6: NO production and destruction rates. Ranges and average values.

Processes	NO Production/loss rate (cm^{-3}/s)	Average Production/loss rate (cm^{-3}/s)
$N + O_2 \rightarrow NO + O$	2 - 6.4 x 10^{22}	4.2 x 10^{22}
$N + O_2 \leftarrow NO + O$	5.6 x 10^{16} -2.4 x 10^{21}	5 x 10^{20}
$N_2 + O \rightarrow NO + N$	1.4 x 10^{18} – 5.7 x 10^{21}	1.1 x 10^{21}
$N_2 + O \leftarrow NO + N$	3.9-6 x 10^{20}	5 x 10^{20}
$N_2(A) + O\ (^3P) \rightarrow NO + N(^2D)$	6 x 10^{20} - 2.3 x 10^{21}	1.5 x 10^{21}
$N_2(B) + O \rightarrow NO + N$	2 x 10^{22} - 3 x 10^{24}	8.8 x 10^{23}
$N_2(C) + O \rightarrow NO + N$	2.1 x 10^{20} - 2.7 x 10^{23}	5.2 x 10^{22}
$NO_2 + M \leftarrow NO + O + M$	3-7.7 x 10^{18}	5 x 10^{18}
$2NO_2 \leftarrow NO + NO + O_2$	3.3 x 10^{9} – 1 x 10^{10}	5.6 x 10^{9}

Table 6.7: NO production and loss rates at peak conduction current.

Processes	NO Production/loss rate (cm^{-3}/s)
$N + O_2 \rightarrow NO + O$	3.4 x 10^{6} x [N]
$N + O_2 \leftarrow NO + O$	1.2 x 10^{18}
$N_2 + O \rightarrow NO + N$	2.4 x 10^{18}
$N_2 + O \leftarrow NO + N$	4.5 x 10^{4} x [N]
$N_2(A) + O\ (^3P) \rightarrow NO + N(^2D)$	5.6 x 10^{20}
$N_2(B, C) + O \rightarrow NO + N$	1.2 x 10^{24}
$N_2(A) + NO \rightarrow NO + N_2$	1.4 x 10^{19}
$N_2(B) + NO \rightarrow NO + N_2(A)$	4.8 x 10^{21}
$N_2\,(v > 12) + O \rightarrow NO + N$	4 x 10^{6} x [N_2 (v > 12)]
$N(^2D) + O_2 \rightarrow NO + O(^3P)$	3 x 10^{6} x [$N(^2D)$]
$N(^2D) + O_2 \rightarrow NO + O(^1D)$	1.1 x 10^{7} x [$N(^2D)$]
$N(^2P) + O_2 \rightarrow NO + O$	2 x 10^{6} x [$N(^2P)$]
$NO_2 + O \rightarrow NO + O_2$	1.8 x 10^{6} x [NO_2]
$NO_2 + M \leftarrow NO + O + M$	4.6 x 10^{18}
$NO_2 + O_2 \leftarrow NO + O_3$	8.6 x 10^{2} x [O_3]
$2NO_2 \leftarrow NO + NO + O_2$	7 x 10^{9}

6.5.3 NO densities in the reference case

The temporal evolution of the NO densities can be deduced by integrating the rate equations. The temporal evolution of the NO densities created by N_2 (A, B, C) is displayed in figure 6.34. After 40 ns, the NO density produced by the quenching of N_2(B) state with O atoms is about one order of magnitude larger than that due to N_2(C) state and about three orders of magnitude greater than NO from N_2(A) state.
Figure 6.35 shows the temporal evolution of NO densities created or lost by reactions involving the quenching excited electronic nitrogen levels with O atoms together with the Zel'dovich reactions. The NO density lost by transformation into NO_2 is displayed in figure 6.36.
Figure 6.35 and 6.36 suggest that the NO density produced by NRP discharge in the "reference case" is on the order of 10^{16} cm^{-3} and mainly results (by about 90 %) from the quenching of O atoms with molecules in the N_2(B) state. The averaged NO density over 40 ns is about 2 x 10^{16} cm^{-3}. Table 6.7 gives the ranges and average values of the NO densities produced/lost by all other reactions. The dominant formation reactions of the average column are sketched in the histogram in figure 6.37. This enables us to conclude that for our NRP discharge reference case, NO is primary formed via reactions R8 (with N_2(B) and N_2(C)) and R1. Moreover, NO is mainly lost by its quenching with N atoms (R4) and O atoms (R2).
Of course we should consider that the calculated absolute NO density has large uncertainty because of the assumptions of the model. Nevertheless, the main reactions identified here are in good agreement with the latest literature results (see for instance [*Popov*, 2015]).

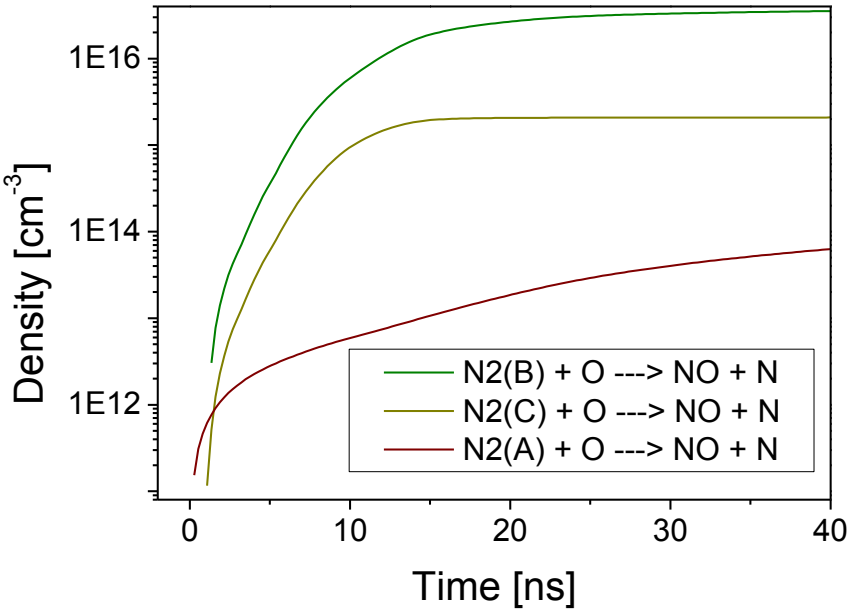

Figure 6.34: Time evolution of the NO densities due to quenching of atomic oxygen with nitrogen excited electronic states.

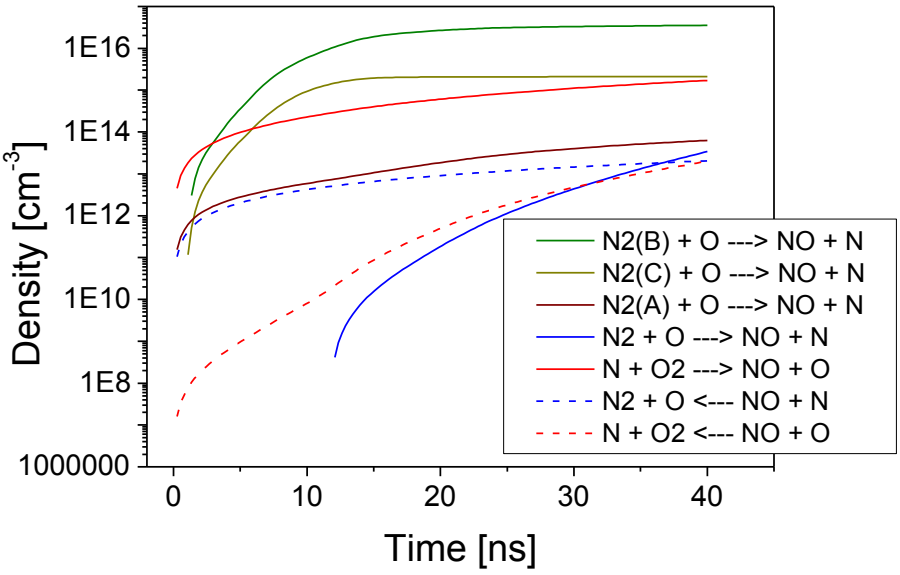

Figure 6.35: Time evolution of the NO densities due to different processes.

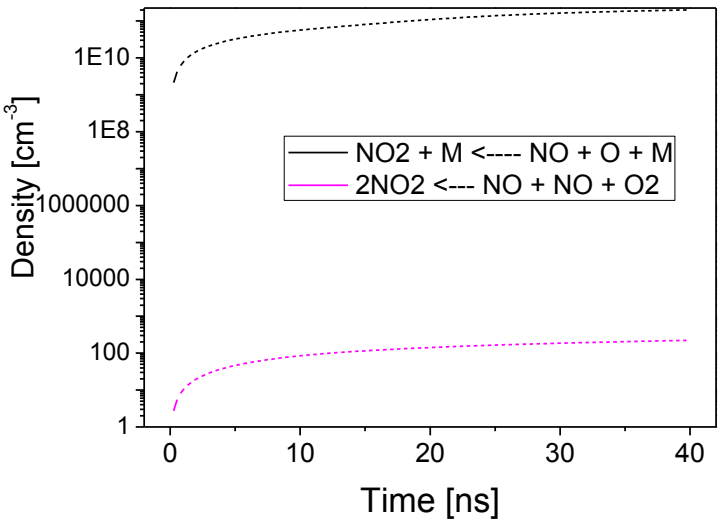

Figure 6.36: Time evolution of the NO losses due to NO_2 formation.

Table 6.7: NO densities created/lost. Ranges and averaged values.

Processes	NO density Production/loss (cm^{-3})	Average density Production/loss (cm^{-3})
$N + O2 \rightarrow NO + O$	4.5×10^{12} - 1.7×10^{15}	1×10^{14}
$N + O2 \leftarrow NO + O$	1.6×10^{7} - 2×10^{13}	3.3×10^{12}
$N_2 + O \rightarrow NO + N$	4.1×10^{8} – 3.2×10^{13}	5.6×10^{12}
$N_2 + O \leftarrow NO + N$	1×10^{11} – 1.8×10^{13}	9.5×10^{12}
$N_2(A) + O\ (^3P) \rightarrow NO + N(^2D)$	1.5×10^{11} - 6×10^{13}	2.4×10^{13}
$N_2(B) + O \rightarrow NO + N$	3×10^{12} - 3.5×10^{16}	2×10^{16}
$N_2(C) + O \rightarrow NO + N$	1.2×10^{11} - 2×10^{15}	1.5×10^{15}
$NO_2 + M \leftarrow NO + O + M$	2.1×10^{9} - 2×10^{11}	1.1×10^{11}

This modeling result is also supported by the experimental fact that the NO mole fraction is found independent of the gas temperature (see section 6.3) whereas Zel'dovich and NO_2 related processes are strongly temperature-dependent. This is consistent with the fact that the quenching reactions are, to a good approximation, temperature independent.

Using the estimated NO density released by the NRP discharges in the reference case ($\sim 4 \times 10^{16}$ cm^{-3}), we can compare with the measurement obtained in section 6.4. We recall that the NO density produced by NRP discharges in the reference case but measured 25 cm downstream of the discharge was about 2.5×10^{14} cm^{-3}.

Assuming that the retrieved NO density in the reference case is uniform over the 400 µm discharge diameter, we have a number of NO particles per unit of time about $4 \times 10^{16} \times \pi \times (2 \times 10^{-2})^2 \times 260 \sim 1.3 \times 10^{16}$ molecule/s. However, applying the same calculation in the post-discharge area results in $2.5 \times 10^{14} \times 16 \times \pi \times 260 \times 2.01/50.3 \sim 1.3 \times 10^{17}$ molecule/s. This value is about ten times greater than that in the discharge. This result suggests as well as in section 6.4 that there is a NO creation mechanism happening in the NRP post-discharge. The process responsible of such a kinetic must involve long-lived species. From reactions R1 to R18 illustrated tables 6.1 to 6.5, only equations R12, R13 and R14 are plausible candidates since they involve $N(^2D)$ and $N(^2P)$ metastables, which have radiative lifetime about 26 h and 12 s, respectively [*Alagia et al.*, 1999, *Lin et al.*, 1971] and O_2.

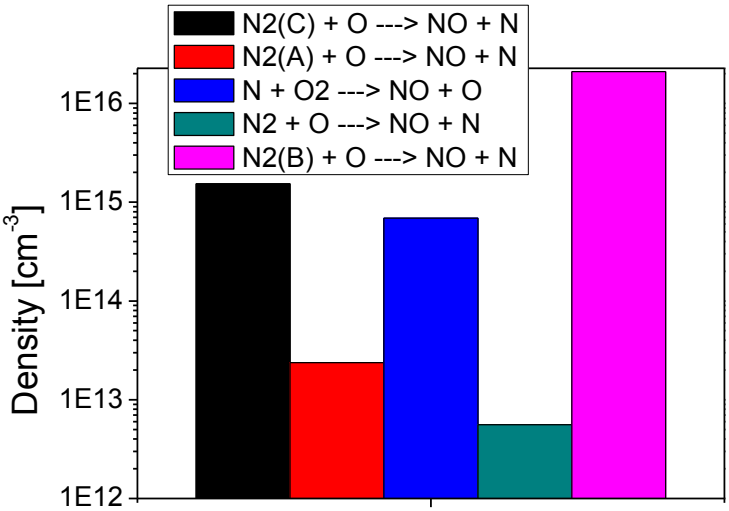

Figure 6.37: Histogram of the time-averaged NO densities created by various processes.

Finally, the NO density in the NRP post-discharge was measured as a function of the distance from the discharge to the region where the measurement is performed. This was possible thanks to 5-cm height slotted tube pieces. The result is shown in figure 6.38. We see that the NO density increases by a factor 4 if measurements are performed at 20 cm and 50 cm in the post-discharge downstream. This can be explained by post-discharge kinetics since between these positions speed and section are constant.

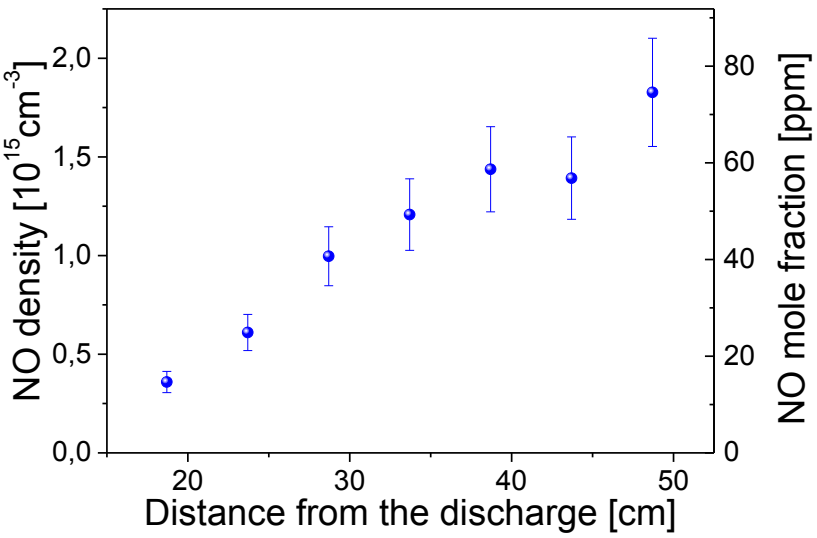

Figure 6.38: NO density as a function of the vertical distance to the discharge. The NO density increases with the increase of the distance to the discharge. At 30 cm, the NO density increases by a factor 4. Conditions: $U = 6.5$ kV, $f = 30$ kHz, $d = 1$ mm, $v = 8.63$ m/s, $T = 300$ K.

6.6 Conclusions

In this chapter, for NRP discharges operating in both ambient and 1000 K preheated air flows, we have studied the influence of various discharges parameters namely, the applied pulse voltage amplitude, pulse repetition frequency, gap distance and airflow rate. We have demonstrated that the NO density depends only on two parameters: the pulse voltage amplitude and the number of pulse seen by the gas in the gap between electrodes. The second parameter is proportional to the gap distance and repetition frequency, and inversely proportional to the air flow rate. At 1000 K, the measured NO density in the post-discharge, in the reference case (U = 5.7 kV, f = 10 kHz, d = 4 mm, v = 2.6 m/s) is found to be about 2.5 x 10^{14} cm^{-3}.

Then, investigating the influence of the incoming gas flow temperature, we found that the NO density in the NRP post-discharges decreases with the increase of the temperature because the total gas density decreases with the rise of the temperature. Consequently, the NO mole fraction was constant with the increase of the temperature. For the same conditions, we have compared NO measurements in the discharge (chapter 5) and in the post-discharge. We observed that the NO density in the post-discharge was four times greater than the expected diluted value. This proves that NO creation mechanisms occur in the NRP post-discharges.

To understand NO creation mechanisms in our discharge, we reviewed NO main creation/loss pathways for various types of discharges and at different pressures. Rate constants for the various routes were analyzed as a function of the temperature. Afterwards, benefiting of the previous work achieved on NRP discharges in the reference case, we used the synchronized time resolved measurements of O atoms, N_2 (A, B, C) densities together with the gas temperature to derive NO production/ loss rates as a function of time. Integrating the latter rates over time yielded the NO densities created/lost. After 40 ns, we calculated a total NO density about 4 x 10^{16} cm^{-3}. Up to 90 % of the NO released was found to come from the reaction: $N_2(B) + O \rightarrow NO + N$ while NO is found to be lost by reactions $NO + N \rightarrow N_2 + O$ and $NO + O \rightarrow N + O_2$. Comparison of the value predicted by kinetic estimates with the value measured in the post-discharge supports the idea of a NO creation process occurring in the post-discharge. This result is confirmed at the end of the chapter by experimental results showing the increase in NO density with respect to the vertical distance to the location where NRP are generated. After kinetic analysis, we suggest that NO creation in the post-NRP discharges involves reactions of types: $N(^2D, ^2P) + O_2 \rightarrow NO + O$.

References

[1] Alagia, M., Balucani, N., Cartechini, L., Casavecchia, P., Volpi, G. G., Pederson, L. A., ... & Rabitz, H. (1999). Exploring the reaction dynamics of nitrogen atoms: a combined crossed beam and theoretical study of N (2D)+ D2→ ND+ D. *The Journal of chemical physics*, *110*(18), 8857-8860.

[2] Atkinson, R., Baulch, D. L., Cox, R. A., Hampson Jr, R. F., Kerr, J. A., Rossi, M. J., & Troe, J. (1997). Evaluated kinetic and photochemical data for atmospheric chemistry: supplement VI. IUPAC subcommittee on gas kinetic data evaluation for atmospheric chemistry. *Journal of Physical and Chemical Reference Data*, *26*(6), 1329-1499.

[3] Benson, S. W., & Axworthy Jr, A. E. (1957). Mechanism of the gas phase, thermal decomposition of ozone. *The Journal of Chemical Physics*, *26*(6), 1718-1726.

[4] Bowman, C. T. (1992). Control of combustion-generated nitrogen oxide emissions: technology driven by regulation. In *Symposium (International) on Combustion* (Vol. 24, No. 1, pp. 859-878). Elsevier.

[5] Burnette, D., Montello, A., Adamovich, I. V., & Lempert, W. R. (2014). Nitric oxide kinetics in the afterglow of a diffuse plasma filament. *Plasma Sources Science and Technology*, *23*(4), 045007.

[6] Center, R. E., & Kung, R. T. V. (1975). Shock Tube Study of the Thermal Decomposition of O3 from 1000 to 3000 K. *The Journal of Chemical Physics*, *62*(3), 802-807.

[7] DeBenedictis, S., & Dilecce, G. (1997). Rate constants for deactivation of N-2 (A) v= 2-7 by O, O-2, and NO. *Journal of Chemical Physics*, *107*(16), 6219-6229.

[8] Fenimore, C. P. (1971, December). Formation of nitric oxide in premixed hydrocarbon flames. In *Symposium (International) on Combustion* (Vol. 13, No. 1, pp. 373-380). Elsevier.

[9] Ferreira, C. M., Gordiets, B. F., Osipov, A. I., Capitelli, M. (2000). *Plasma kinetics in atmospheric gases* (Vol. 99). Berlin: Springer.

[10] Gordiets, B. F., Ferreira, C. M., Guerra, V. L., Loureiro, J. M., Nahorny, J., Pagnon, D., ... & Vialle, M. (1995). Kinetic model of a low-pressure N 2-O 2 flowing glow discharge. *Plasma Science, IEEE Transactions on*, *23*(4), 750-768.

[11] Guerra, V., Sa, P. A., & Loureiro, J. (2001). Role played by the N2 (A3Σu+) metastable in stationary N2 and N2-O2 discharges. *Journal of Physics D: Applied Physics*, *34*(12), 1745.

[12] Herron, J. T. (2001). Modeling studies of the formation and destruction of NO in pulsed barrier discharges in nitrogen and air. *Plasma Chemistry and Plasma Processing*, *21*(4), 581-609.

[13] Kerr, J. A., & Stocker, D. W. (1993). Strengths of chemical bonds. *Handbook of chemistry and physics*, *78*.

[14] Kim, W., Do, H., Mungal, M. G., & Cappelli, M. A. (2007). Investigation of NO production and flame structure in plasma enhanced premixed combustion. *Proceedings of the Combustion Institute*, *31*(2), 3319-3326.

[15] Kossyi, I. A., Kostinsky, A. Y., Matveyev, A. A., & Silakov, V. P. (1992). Kinetic scheme of the non-equilibrium discharge in nitrogen-oxygen mixtures. *Plasma Sources Science and Technology*, *1*(3), 207.

[16] Kühn, S., Bibinov, N., Gesche, R., & Awakowicz, P. (2010). Non-thermal atmospheric pressure HF plasma source: generation of nitric oxide and ozone for bio-medical applications. *Plasma Sources Science and Technology*, *19*(1), 015013.

[17] Lin, C. L., & Kaufman, F. (1971). Reactions of metastable nitrogen atoms. *The Journal of Chemical Physics*, *55*(8), 3760-3770.

[18] Malte, P. C., & Pratt, D. T. (1974). The role of energy-releasing kinetics in NOx formation: fuel-lean, jet-stirred CO-air combustion. *Combustion Science and Technology*, *9*(5-6), 221-231.

[19] McLarnon, C. R., & Penetrante, B. M. (1998). *Effect of gas composition on the NOx conversion chemistry in a plasma* (No. 982433). SAE Technical Paper.

[20] Michael, J. V. (1971). Thermal decomposition of ozone. *The Journal of Chemical Physics*, *54*(10), 4455-4459.

[21] Pai, D. Z., Lacoste, D. A., & Laux, C. O. (2010). Nanosecond repetitively pulsed discharges in air at atmospheric pressure—the spark regime. *Plasma Sources Science and Technology*, *19*(6), 065015.

[22] Penetrante, B. M., Bardsley, J. N., & Hsiao, M. C. (1997). Kinetic analysis of non-thermal plasmas used for pollution control. *Japanese journal of applied physics*, *36*(7S), 5007.

[23] Pipa, A. V., Bindemann, T., Foest, R., Kindel, E., & Weltmann, K. D. (2008). Absolute production rate measurements of nitric oxide by an atmospheric pressure plasma jet (APPJ). *Journal of Physics D: Applied Physics*, *41*(19), 194011.

[24] Popov, N. A. Active particles production by pulsed nanosecond discharge in ambient air. Quenching of electronically excited states of nitrogen by O2 molecules and O (3P) atoms. In *53nd AIAA Aerospace Sciences Meeting (5-9 January, 2015, Kissimmee, Florida). AIAA-2015 (23p).*

[25] Rusterholtz, D. L., Lacoste, D. A., Stancu, G. D., Pai, D. Z., & Laux, C. O. (2013). Ultrafast heating and oxygen dissociation in atmospheric pressure air by nanosecond repetitively pulsed discharges. *Journal of Physics D: Applied Physics*, *46*(46), 464010.

[26] Shkurenkov, I., Burnette, D., Lempert, W. R., & Adamovich, I. V. (2014). Kinetics of excited states and radicals in a nanosecond pulse discharge and afterglow in nitrogen and air. *Plasma Sources Science and Technology*, *23*(6), 065003.

[27] Stancu, G. D., Kaddouri, F., Lacoste, D. A., & Laux, C. O. (2010). Atmospheric pressure plasma diagnostics by OES, CRDS and TALIF. *Journal of Physics D: Applied Physics*, *43*(12), 124002.

[28] Stancu, G. D., Simeni, M. S., & Laux, C. O. Study of nitric oxide and carbon monoxide production in plasma assisted com-bustion by Quantum Cascade Laser Absorption Spectroscopy. *21st ISPC*, Cairns, August 4-9, (2013) AUSTRALIA.

[29] Uddi, M. (2008). *Non-equilibrium kinetic studies of repetitively pulsed nanosecond discharge plasma assisted combustion* (Doctoral dissertation, The Ohio State University).

[30] Uddi, M., Jiang, N., Adamovich, I. V., & Lempert, W. R. (2009). Nitric oxide density measurements in air and air/fuel nanosecond pulse discharges by laser induced fluorescence. *Journal of Physics D: Applied Physics*, *42*(7), 075205.

[31] Van Gaens, W., Bruggeman, P. J., & Bogaerts, A. (2014). Numerical analysis of the NO and O generation mechanism in a needle-type plasma jet. *New Journal of Physics*, *16*(6), 063054.

[32] Van Gessel, A. F. H., Hrycak, B., Jasiński, M., Mizeraczyk, J., Van der Mullen, J. J. A. M., & Bruggeman, P. J. (2013). Temperature and NO density measurements by LIF and OES on an atmospheric pressure plasma jet. *Journal of Physics D: Applied Physics*, *46*(9), 095201.

[33] Van Gessel, A. F. H., Alards, K. M. J., & Bruggeman, P. J. (2013). NO production in an RF plasma jet at atmospheric pressure. *Journal of Physics D: Applied Physics*, *46*(26), 265202.

[34] Zhao, G. B., Garikipati, S. V. B., Hu, X., Argyle, M. D., & Radosz, M. (2005). Effect of oxygen on nonthermal plasma reactions of nitrogen oxides in nitrogen. *AIChE journal*, *51*(6), 1800-1812.

Chapter 7

NRP discharge optimizations for plasma-assisted combustion

7.1 Introduction

Here, we first present the experimental conditions for optimization studies (section 7.2). Then, we use the results on NRP characterization given in chapters 5 and 6 to investigate how to meet the requirements of the combustion application field, namely, low NO emissions. More precisely, in section 7.3, starting from an experimental configuration in ambient air, we implemented two different strategies to reduce the amount of NO released by NRP discharges. Based on these NO optimization results, three discharge configurations were employed to stabilize a lean methane/air flame (section 7.4). We carry out the NO density measurements with and without discharges. For each of the three cases, we compare the NO densities measured in air, in plasma-assisted flames and in regular flames.

7.2 Experimental conditions

In the entire chapter, NRP discharges were generated in a vertical pin-to-pin configuration between a bluff-body tip acting as the cathode and a pin as the anode. The discharge pulses are generated using PG1 and PG3 (the latter for frequencies higher than 30 kHz). The QCLAS measurements are performed at the outlet of the 50-cm high confinement tube. The measurements were performed in a 28-pass configuration, or a 20-pass configuration. The CH_4/air flame is attached at the cathode for all combustion experiments and all measurements are performed in the post-discharge, i.e. in the burned gases.

7.3 Optimization of the NO amount released in air

In figure 7.1, we recall the result of chapter 6 (for NRP discharges in ambient flows), which shows that at fixed pulse voltage amplitude, the NO density decreases with the number of pulses seen by the gas and that at fixed number of pulses seen by the gas, the NO density decreases with the applied voltage amplitude. This will guide our approach for NO mole fractions reduction in this chapter.
We start from a baseline configuration (case 1 of table 7.1) with an applied voltage amplitude of about 5.3 kV at 30-kHz pulse repetition frequency, and with an inter-

electrode gap of 4 mm, we implemented two strategies to reduce NO densities. As shown in table 7.1, we either keep the same number of pulses seen by the gas in the gap and decrease the voltage amplitude (case 2 of table 7.1) or we decrease both the pulse voltage amplitude and the number of pulses seen by the gap (case 3).
In case 2, we keep constant the dimensionless parameter $d\ f\ /v$ (number of pulses seen by the gas). Since all configurations will be investigated as functions of the flow rate, we modify only the numerator ($d\ f$) of the dimensionless parameter. In the baseline case, the value of this numerator is 4 x 30 = 120 m/s. In addition, we keep the same reduced electric field (E/N) in order to keep the same rate of electron-impact excitation by the NRP discharge. Since we divided the pulse voltage amplitude by a factor of 2 (from 5.3 to 2.7 kV), the gap distance was also reduced by a factor of 2 (from 4 to 2 mm). Finally, in order to have the same number of discharge pulses as in the baseline case, we multiply the pulse repetition frequency by a factor 2. The characteristics of this case are then: 2.7-kV voltage amplitude, 60-kHz repetition frequency and 2-mm gap distance.
For case 3, starting from the baseline configuration, we decrease both the gap distance and the pulse voltage amplitude without keeping constant neither the reduced electric field nor the number of discharge pulses seen by the gap. We have: 4.2-kV pulse amplitude, 30-kHz repetition frequency and 1-mm gap distance.

Table 7.1 summarizes the experimental conditions for the three selected configurations. Note that The E/N values mentioned here correspond to the reduced field at the maximum of the voltage amplitude and do not account for the heating by the previous pulses. They are hence calculated for a gas temperature of 300 K. The number of pulses seen by the gas are estimated for a flow velocity about 8.6 m/s, which corresponds to the air flow velocity at the “fictitious ER =1” (see next paragraph).

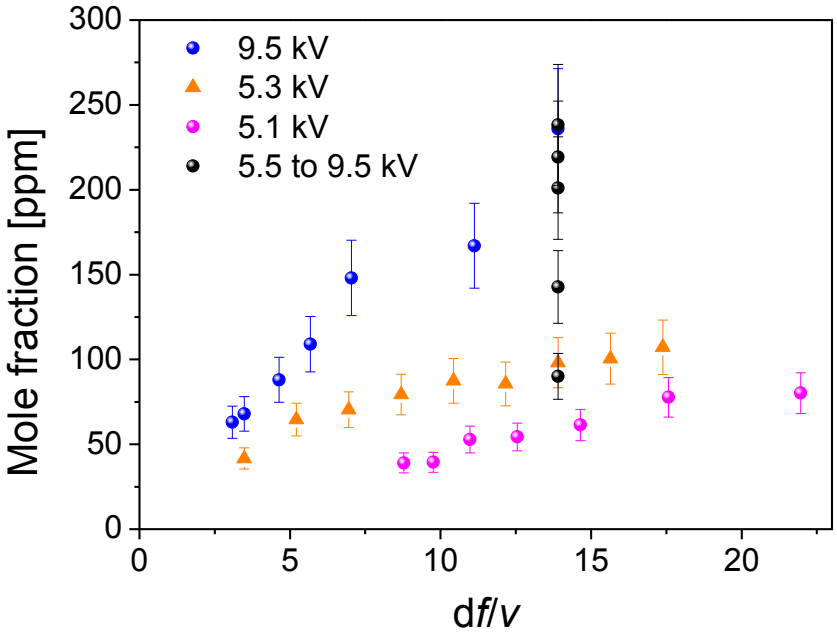

Figure 7.1: NO mole fraction as a function of the number of pulses seen by the gap. Conditions: $z = 50$ cm, $T = 300$ K.

Table 7.1: Three experimental conditions.

	d [mm]	f [kHz]	V [kV]	E/N [Td]	$d\,f$ [m/s]	*#pulses seen*
Case 1	4	30	5.3	54	120	14
Case 2	2	60	2.7	54	120	14
Case 3	1	30	4.2	171	30	3.5

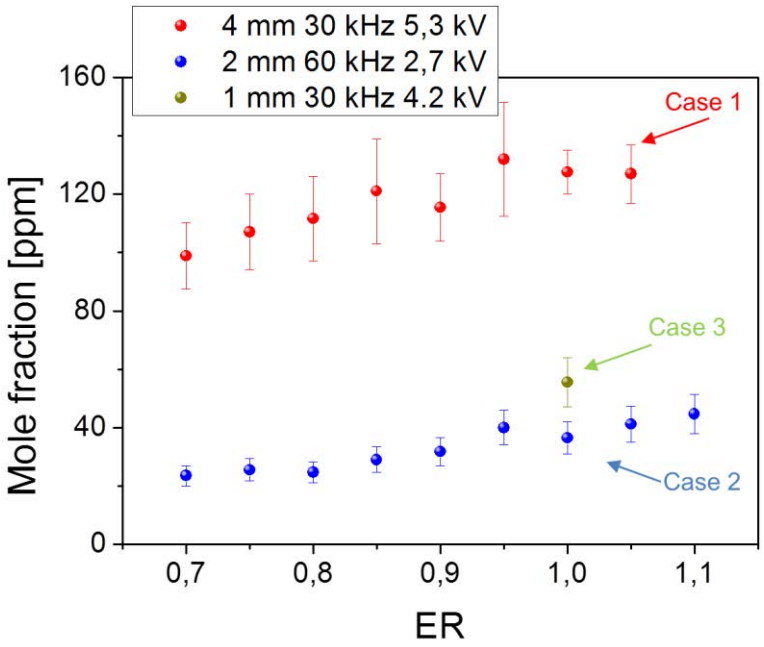

Figure 7.2: NO density/mole fraction as a function of the air flow rate. Conditions: z = 50 cm, T =300 K.

The NO mole fractions in air, for the three cases, are compared in figure 7.2. The NO densities are plotted as a function of the air flow rate. "ER" is the corresponding "equivalent ratio" of the mixture considering a fictitious addition of 0.40 m^3/h of methane. As expected, over the investigated range of air flow rates, figure 7.2 demonstrated that cases 2 and 3 release less NO than the baseline case 1. Essentially, the NO densities in case 2 are about three to four times lower than those of the baseline configuration whereas results from cases 2 and 3 are very close.

7.4 Compared densities measurements of NO densities in air, plasma-assisted combustion and combustion

Above we demonstrated that it is possible to reduce by a factor 3 the NO densities released by NRP discharges in air. This was achieved either by decreasing the electric field (keeping the same number of pulses seen by the gas and the same ratio E/N) or by reducing both the number of pulses seen by the gas and the pulse voltage amplitude. We also conducted experiments in methane/air flame without the confinement tube, and we observed that it was possible to achieve flame stabilization for cases 2 and 3 down to equivalence ratios 0.80 (vs. down to 0.75 in case 1). We now seek to determine the NO densities in the plasma-assisted flames for all three cases.

A particular challenging issue for the QCLAS diagnostic is the presence of large amounts of water at the tube outlet. In this section, we will first explain (subsection 7.4.1) how to disentangle NO and H_2O absorption signals in combustion environments. Then in section 7.4.2, we present the results of the three cases operating in combustion. Part of the results of this section were presented in [*Stancu et al.*, 2013-a; *Stancu et al.*, 2013-b].

7.4.1 Feasibility of NO detection in a combustion environment

NO detection in combustion environment is challenging because the probed NO line overlaps with H_2O lines as shown in the simulations presented in figure 3.10 (section 3.5.1). Due to the high gas temperature, the NO density is also expected to be lower than in air. Moreover, even though the multipass cell increases the NO detection sensitivity, it also increases the water background, which challenges the selectivity. Furthermore, the laser beam experiences beam steering while passing through the high-temperature exhaust of the confinement tube. Consequently, it is very difficult to have a proper measurement of the baseline signal, which should account for the water background absorption and beam steering effects but without accounting for NO absorption.

To perform absolute NO density measurements in combustion and plasma-assisted combustion using QCLAS, we developed a method for the treatment of experimental spectra. Figure 7.3 displays atmospheric pressure HITEMP simulations of the transmittance spectra of 20 % of water at 1180 K (typical temperature at ER 1.0 as will be shown later) and of 20 % of water at 1180 K with the addition of 100 ppm of NO. The length of absorption is 216 cm (simulating the 28-pass configuration). From the simulated spectra combining NO and water contributions, we see that it is possible to detect the 100 ppm NO mole fraction for these configurations. The calculated absorbance spectrum corresponding to the transmittance spectrum of figure 7.3 is displayed in figure 7.4. The absorption feature centered at the NO transition does not appear symmetric because of the water background. Besides, the wings of the absorption line do not decrease down to 0 as expected. Nevertheless, the absorbance at the center of the line clearly emerges from the water background. Using the constraint to have a symmetric NO line centered at 1900.076 cm^{-1}, we can build a synthetic baseline using polynomial functions. The result is shown in figure 7.5 (blue curve) together with the simulation of a pure 100 ppm NO absorbance spectrum at 1180 K (red curve). It appears that due to the error in the estimation of the baseline, the shapes of blue and red curves are slightly different. However, calculating the area of both displayed curves will yield close results, and using the peak absorbance the differences are even smaller. If the temperature is known, the FWHM of the expected NO Lorentzian profile is also known. The absorbance area under the Lorentzian curve can be determined as: Area = (π x amplitude x

FWHM)/2. The NO density was determined here from peak and integrated absorbances.

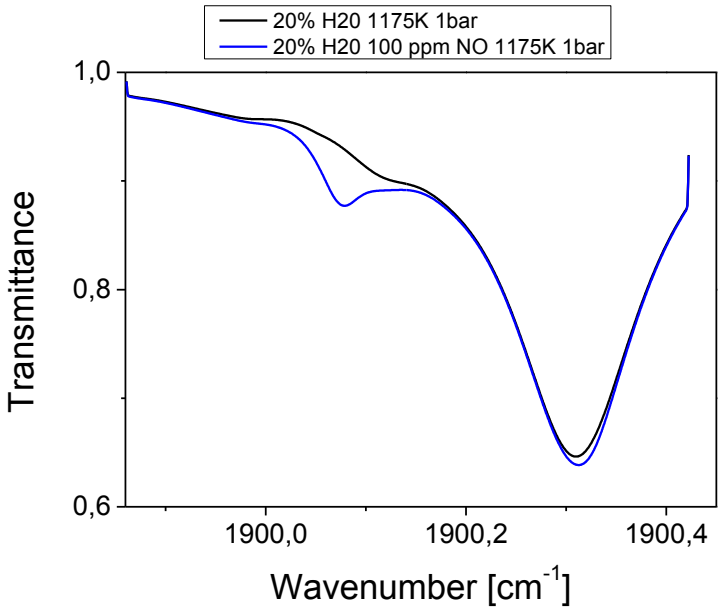

Figure 7.3: HITEMP simulation at atmospheric pressure and for a 216 cm length of absorption. Transmittance spectra of 100 ppm NO + 20 % water and of 20 % water.

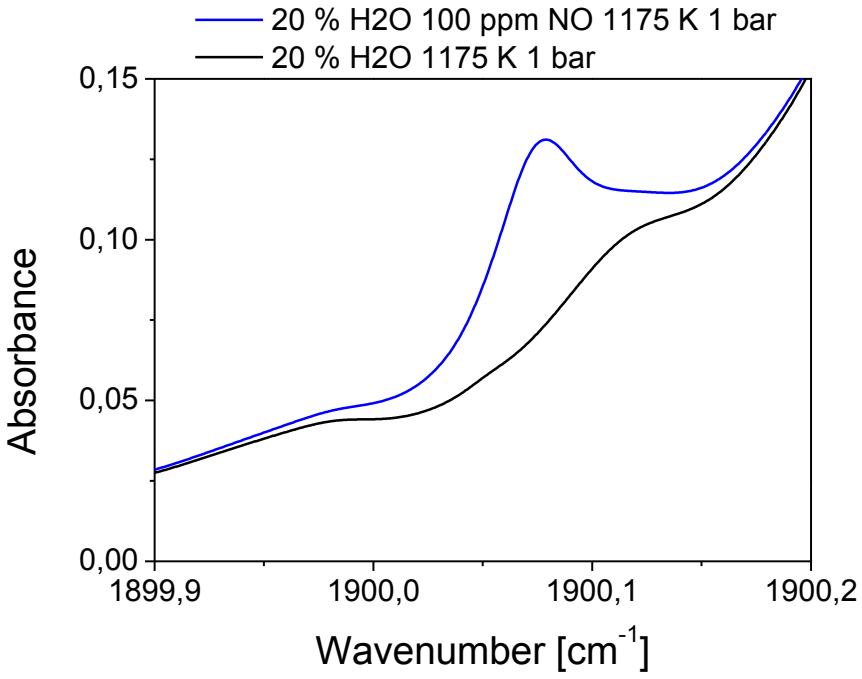

Figure 7.4: Calculated absorbance spectra from the transmittance spectra of figure 7.3. NO peak absorption at the center of the line is clearly distinguishable from the water background.

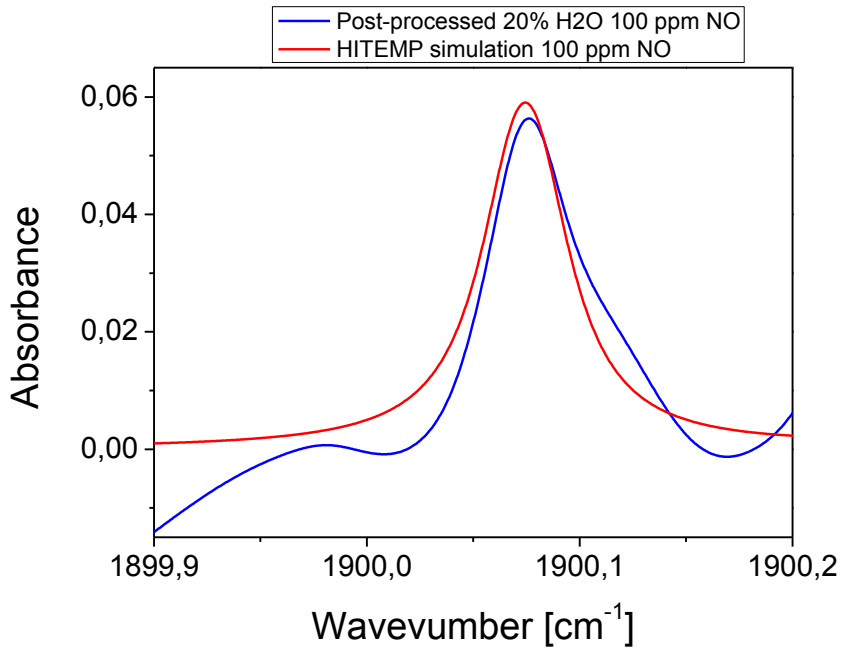

Figure 7.5: Theoretical 100 ppm NO absorbance spectrum (red) and post-processed 20 % water + 100 ppm NO absorbance spectrum.

For 100 ppm NO, the error introduced by this method is about 4 %. This error arises essentially from the error in the determination of the absorbance peak amplitude. When measurements were performed with lower NO mole fraction (10 ppm for instance), the NO absorbance peak is more hidden by the water background. This leads therefore to a bigger uncertainty on the measured densities.
Notice that the FWHM is determined by collisions and depends on the nature of the colliders. However, the N_2 mole fraction in the measurement region is at least about 70 %. Consequently, even if NO lines are broadened by CO_2, H_2O and CH_4 (in rich conditions), the recorded line FWHM is close to that in air.

7.4.2 NO densities in plasma-assisted combustion and in combustion

Case 1

A typical thermocouple gas temperature measurement at confinement tube outlet is illustrated in figure 7.6. As expected, the flame temperature rises from low ER up to the stoichiometry. Then, in the rich flame regime, the temperature decreases. This is a typical result observed for premixed flames. The flame temperature at the tube exit is about 1175 K and an addition of NRP discharges seems to increase the gas temperature by no more than 10 K. The correction of line strength changes in the case of a flame or a plasma-assisted flame is not necessary. This is because a 10 K temperature difference at 1175 K leads to only 2 % change of the line strength.

Figure 7.4 displays density results for the case 1. In the case of NRP discharges operating in pure in air (red curve), NO density is in the range of 2.4 x 10^{15} to 3.2 x 10^{15} cm^{-3}, which is about 16 to 20 times higher than NO density in the case of the plasma coupled with a flame (blue curve). In the latter case, NO density ranges from 1.22 x 10^{14} to 2 x 10^{14} cm^{-3}. Finally, for the case of the flame alone, NO density ranges from 8.75 x 10^{12} to 1.5 x 10^{14} cm^{-3} for equivalence ratios from 0.75 to 1.05. Note that at 0.70 equivalence ratio, NO in the flame case is below the detection limit of our system.

Figure 7.8 represents results from figure 7.7 in terms of mole fractions. This emphasizes the conclusion that NO from the discharge seems to be consumed by the flame. Actually, from the previous chapter we know that for the same conditions (voltage amplitude, repetition frequency, gap distance and flow rate), the NO mole fraction produced by NRP discharges is fairly constant with the gas temperature. However, this is not the case in figure 7.8 since the red and blue curves are different.

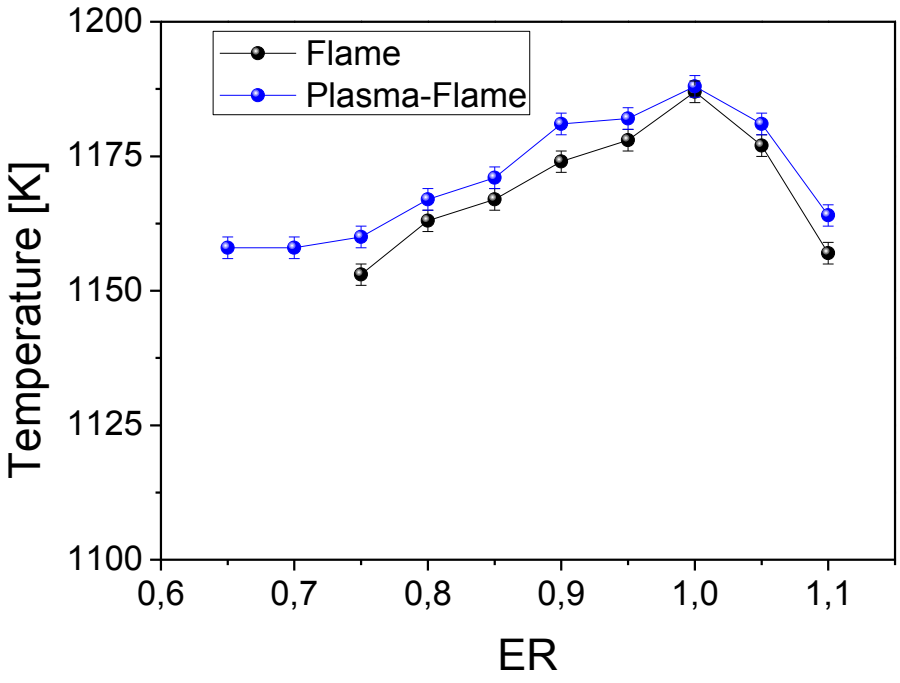

Figure 7.6: Gas temperature at tube exit as a function of flame equivalence ratio. Conditions: $z = 50$ cm, T =300 K.

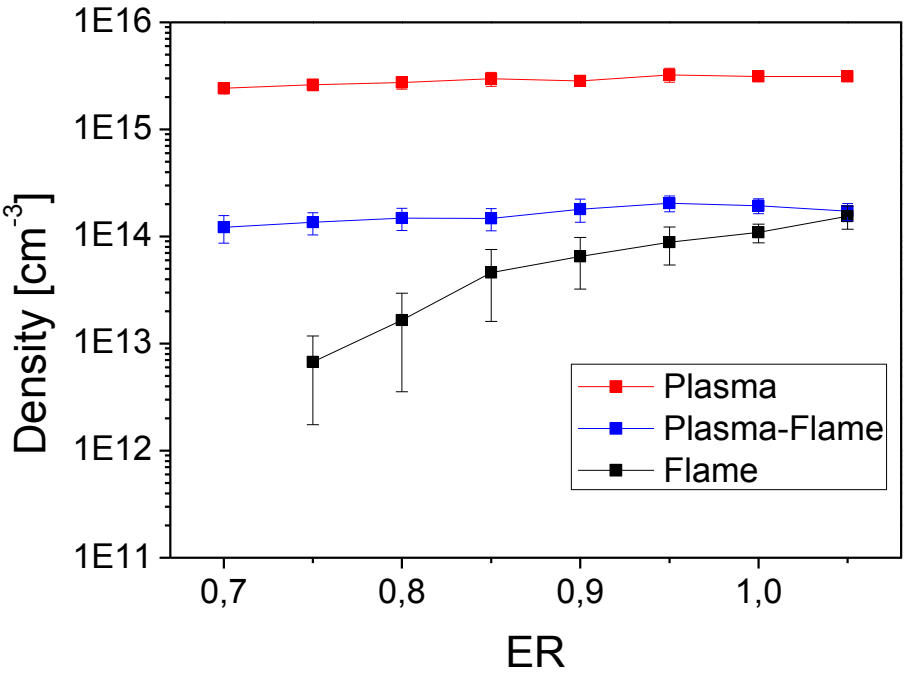

Figure 7.7: NO density as a function of flame equivalence ratio. Three configurations: plasma, plasma + flame and flame. Conditions: $U = 5.3$ kV, $f = 30$ kHz, $d = 4$ mm, $z = 50$ cm.

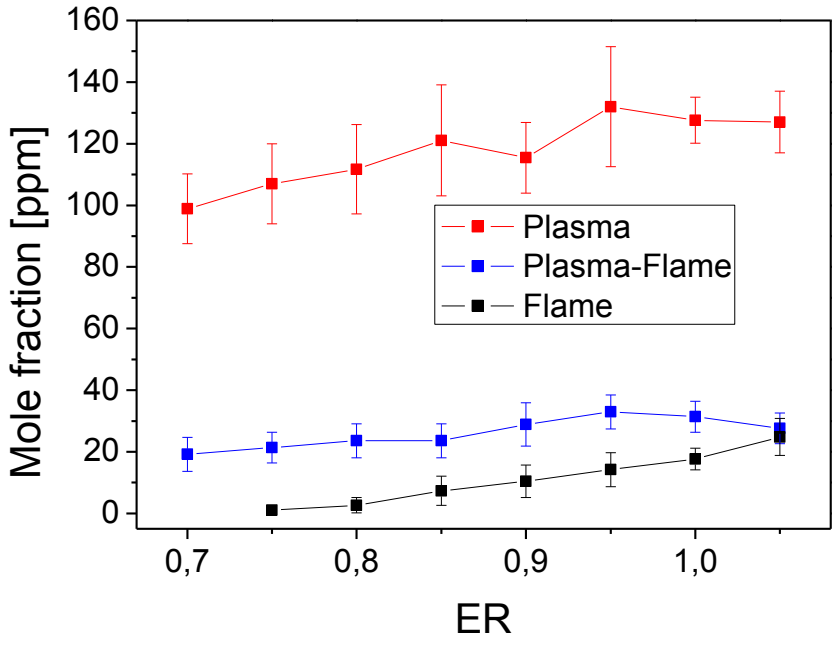

Figure 7.8: NO mole fraction as a function of flame equivalence ratio. Three cases: plasma, plasma + flame and flame. Conditions: $U = 5.3$ kV, $f = 30$ kHz, $d = 4$ mm, $z = 50$ cm.

Case 2

For case 2, absorbance spectra in plasma-assisted combustion are shown in figure 7.9. From equivalence ratio 0.7 up to 1.10, the peak absorbance varies from 8 x 10^{-3} to 1.2 x 10^{-2}. The densities inferred from figure 7.9 are presented in figure 7.10 (red curve) together with NO densities respectively released by the plasma operating in pure ambient air and by the flame alone. NO densities produced by NRP discharges in the optimized configuration 2 in ambient air are in the range of 6 x 10^{14} to 10^{15} cm^{-3}. In the case of plasma-assisted combustion, NO density is practically constant at 10^{14} cm^{-3}, which is lower than NO released by the discharge in air by a factor about 6 to 10. For equivalence ratios between 0.70 and 1.10, NO released in plasma-assisted combustion is comparable to the amount of the NO released by the flame alone at the stoichiometry (if error bars are considered). In case 2, the method proposed fails to reduce NO emissions levels below the level of stoichiometric flames (see figure 7.11).

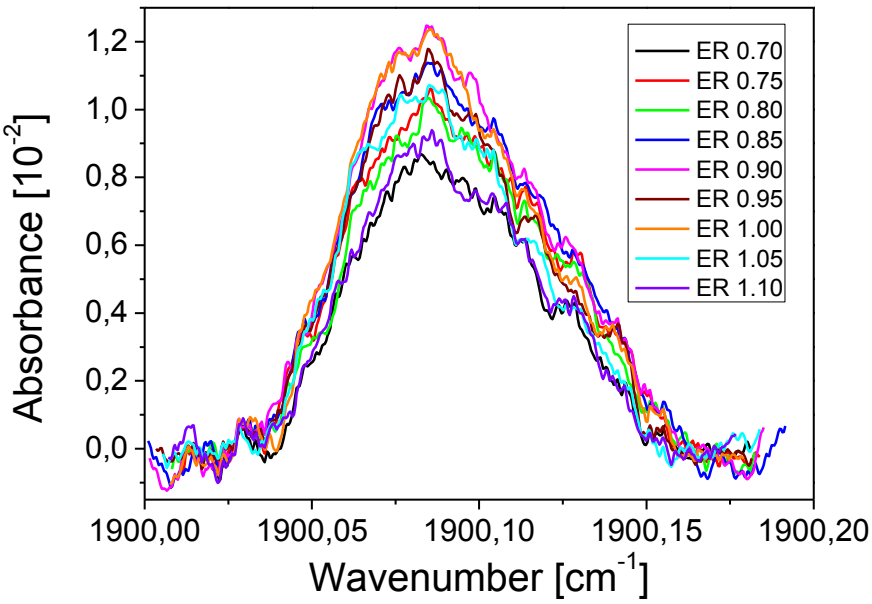

Figure 7.9: Case 2 absorbance spectra for ER from 0.70 to 1.10. Conditions: $U = 2.6$ kV, $f = 60$ kHz, $d = 2$ mm, $z = 50$ cm.

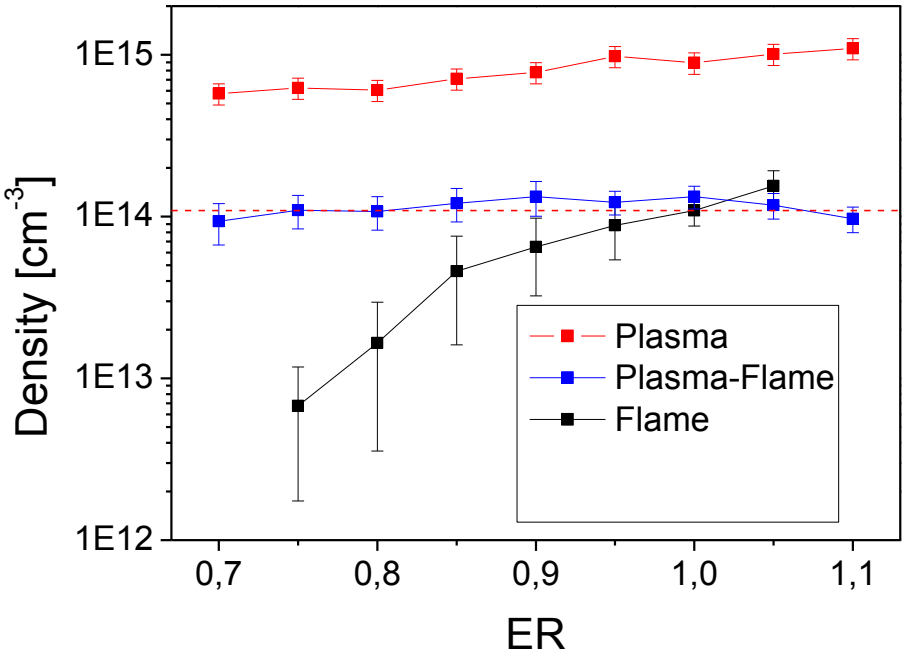

Figure 7.10: NO density as a function of flame equivalence ratio. Three configurations: plasma, plasma + flame and flame. Conditions: $U = 2.6$ kV, $f = 60$ kHz, $d = 2$ mm, $z = 50$ cm.

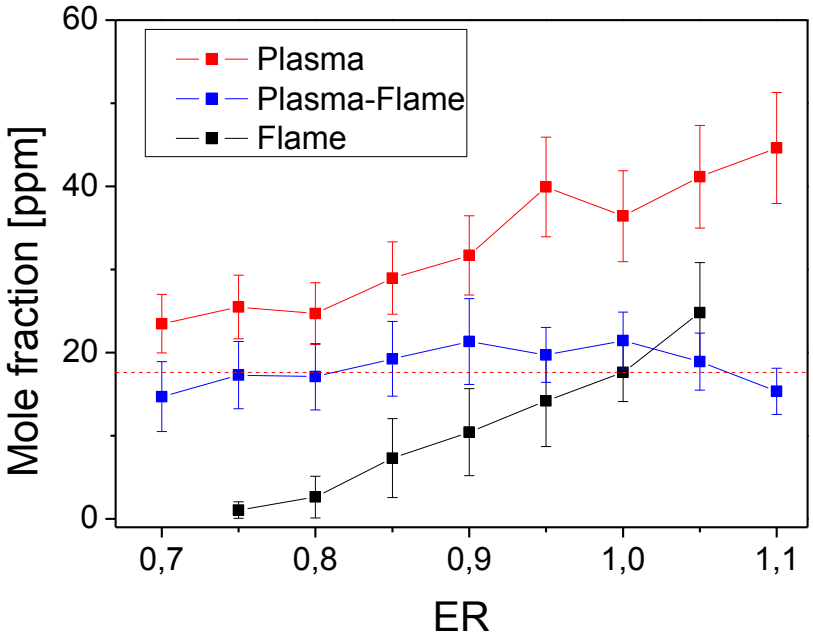

Figure 7.11: NO mole fraction as a function of flame equivalence ratio. Three configurations: plasma, plasma + flame and flame. Conditions: $U = 2.6$ kV, $f = 60$ kHz, $d = 2$ mm, $z = 50$ cm.

Case 3

For case 3, density and mole fractions results are respectively shown in figures 7.12 and 7.13. We see that NO released in plasma-assisted combustion is always higher than in flame alone. However the densities are comparable with those produced by the flame at stoichiometry.

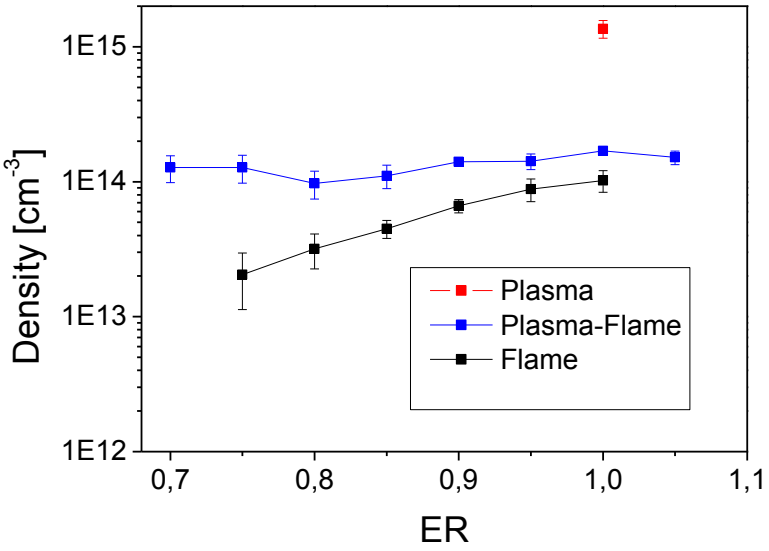

Figure 7.12: NO density as a function of flame equivalence ratio. Three configurations: plasma, plasma + flame and flame. Conditions: $U = 4.2$ kV, $f = 30$ kHz, $d = 1$ mm, $z = 50$ cm.

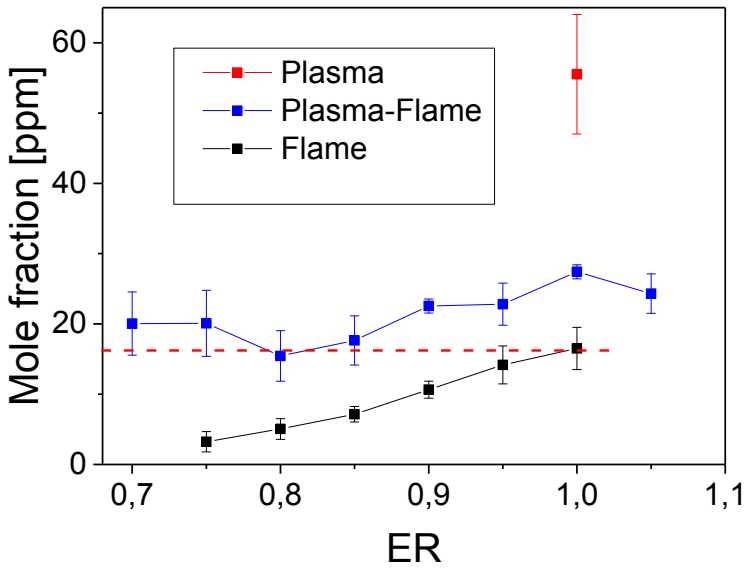

Figure 7.13: NO mole fraction as a function of flame equivalence ratio. Three configurations: plasma, plasma + flame and flame. Conditions: $U = 4.2$ kV, $f = 30$ kHz, $d = 1$ mm, $z = 50$ cm.

The combined results for the three cases are presented in figure 7.14.

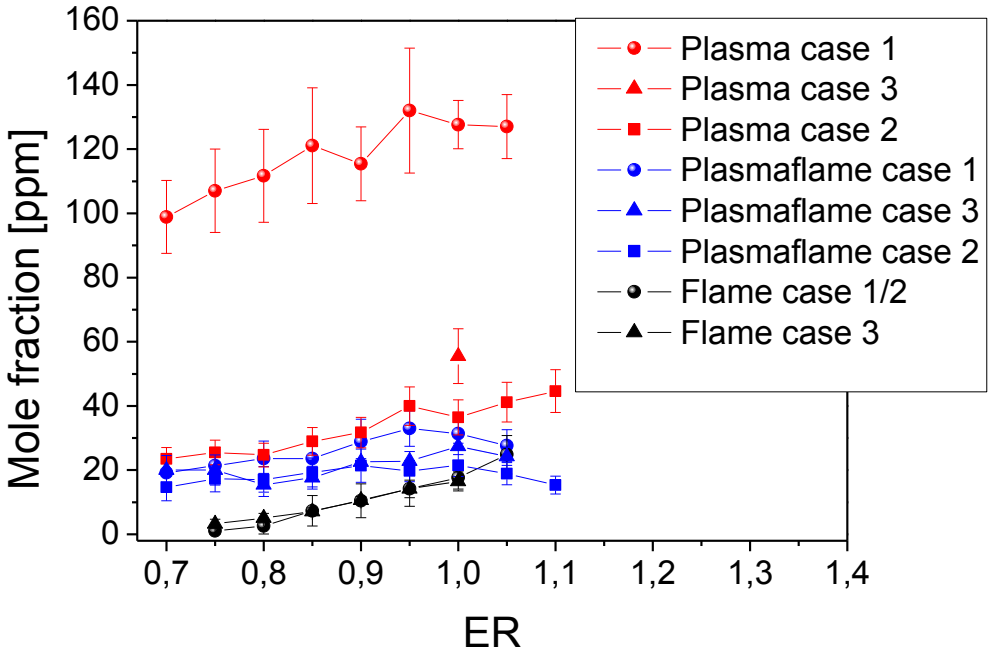

Figure 7.14: NO mole fraction as a function of flame equivalence ratio. Three experimental cases and three configurations each: plasma, plasma + flame and flame. Conditions: $z = 50$ cm.

7.4.3 Discussion

NO consumption by flame in plasma-assisted combustion was already observed by [*Kim et al.*, 2007; *Rao et al.*, 2009; *Kim et al.*, 2010]. *Kim et al.* [2007] evidenced the latter phenomenon by performing chemiluminescence NO mole fraction measurements in a NRP-assisted methane-air premixed mixture as a function of the equivalence ratio from 0 up to 0.55. Authors found a significant drop in the NO mole fraction just beyond the flame ignition limit (at ER 0.49). Besides, the "slight" variation (in comparison with the flame case) of NO mole fraction in NRP-assisted methane-air premixed combustion with respect to equivalence ratio was also reported by *Lacoste et al.* [2013]. In the latter reference, the NO mole fractions were measured with an *ex-situ* gas analyzer, which performed UV absorption spectroscopy for ER ranging between 0.57 and 0.67.

We expect that NO kinetics in NRP-enhanced flames result from a competition between the Zel'dovich thermal NO mechanism, the quenching reactions of electronically excited N_2 levels with O atoms and the fuel dissociation reactions. Table 7.2 recalls the rate coefficients of NO formation and loss by forward and reverse Zel'dovich reactions. The rate constants of NO formation by the quenching of

excited N_2 electronic levels are recalled in table 7.3. Finally, table 7.4 displays the reactions of CH_4 dissociation by electron impact [*Motlagh and Moore*, 1998] and by collision with electronically excited N_2 molecules [*Golde et al.*, 1989; *Piper*, 1992; *Albugues et al.*, 1974]. Whenever available, the temperature domain is specified in the tables.

Table 7.2: Forward and reverse Zel'dovich rates (labelled R1-R6).

Processes	k (cm^3/s)	T (K)	Ref
R1: $N + O_2 \rightarrow NO + O$	1.1×10^{-14} T exp(-3150/T)	$300 \leq T \leq 3000$	*Kossyi et al.* [1992]
R2: $N + O_2 \leftarrow NO + O$	2.5×10^{-14} T exp(-19500/T)	$1000 \leq T \leq 3000$	*Capitteli et al.* [2000]
R3: $N_2 + O \rightarrow NO + N$	3×10^{-10} exp(-38370/T)	$2000 \leq T \leq 5000$	*Capitteli et al.* [2000]
R4: $N_2 + O \leftarrow NO + N$	1.8×10^{-11} $(T/300)^{0.5}$	$200 \leq T \leq 4000$	*Kossyi et al.* [1992]
R5: $N + OH \rightarrow NO + H$	7.5×10^{-11}		*Capitelli et al.* [2000]
R6: $N + OH \leftarrow NO + H$	2.8×10^{-10} exp(-24500/T)		*Capitelli et al.* [2000]

Table 7.3: Rate constants of NO formation by the quenching of excited N_2 electronic levels with O (labelled R7-R8).

Processes	k (cm^3/s)	T (K)	Ref
R7: $N_2(A) + O\ (^3P) \rightarrow NO + N(^2D)$	7×10^{-12}		*Kossyi et al.* [1992]
R8: $N_2(B, C) + O \rightarrow NO + N$	3×10^{-10}		*Shkurenkov et al.* [2014]

Table 7.4: Fuel dissociation rate coefficients (labelled R9-R12).

Processes	Ref
R9: $CH_4 + e^- \rightarrow CH_3 + H + e^-$	*Motlagh and Moore* [1998]
R10: $N_2(A) + CH_4 \rightarrow N_2 + CH_3 + H$	*Golde et al.* [1989]
R11: $N_2(B) + CH_4 \rightarrow N_2 + CH_3 + H$	*Piper*, [1992]
R12: $N_2(C) + CH_4 \rightarrow N_2 + CH_3 + H$	*Albugues et al.* [1974]

Table 7.4 shows that in plasma-assisted combustion, CH_4 molecules depopulate N_2(A, B, C) states. This reaction is in competition with the dissociative quenching of O_2 by the N_2(A, B, C) states. It means that the production of atomic oxygen in plasma-assisted combustion is expected to be lower than for the discharge in air, as a result of lower N_2(A, B, C) densities in addition to its consumption by combustion. Then, according to reactions R7 and R8 of table 7.3, lower O and N_2(A, B, C) densities would lead to lower NO densities produced by these reactions. However, regarding Zel'dovich thermal mechanism, reaction R5 could also provide a significant contribution to the production of NO as suggested by [*Burnette*, 2014], thanks to its high-rate coefficient (7.5×10^{-11}) and to high-OH densities produced by methane/air flames (up to 10^{15} cm^{-3}) [*Desgroux and Cotterau*, 1991; *Versluis et al.*, 1997; *Mercier et al.*, 1999] and by NRP-assisted methane/air flames (up to 10^{16} cm^{-3}) [*Wu et al.*, 2011].
Regarding loss processes, we expect also a great impact of the quenching of NO by O and N atoms due to the high temperature environment.

7.5 Conclusions

In this chapter, three NRP configurations were used to reduce NO released in plasma-assisted lean methane/air combustions environments, while still stabilizing them. To this end, we first optimized NO released by NRP discharges running in ambient air, using the two key parameters found in chapter 6. We also provided a method to obtain NO under strong spectral overlapping with the hot water lines. The developed method relies on spectra simulations, on the accuracy of the detection of the NO absorption peak line and on the calculated FWHM. Afterward, in section 7.4, we implemented the three cases in combustion environments. In the three cases investigated here, comparing the NO mole fraction in air and in plasma-assisted combustion and combustion, we found that NO is consumed by combustion

processes. Nevertheless, the NO reduction by the flame is limited to the stoichiometric level. Even though the NO mole fractions in cases 2 and 3 are lower in the NRP discharge than that of the case 1 by a factor 3, the NO mole fractions of the three cases are nearly the same in plasma-assisted combustion.

References

[1] Albugues, F., Birot, A., Blanc, D., Brunet, H., Galy, J., Millet, P., & Teyssier, J. L. (1974). Destruction of the levels C3Πu ($v'= 0$, $v'= 1$) of nitrogen by O2, CO2, CH4, and H2O. *The Journal of Chemical Physics*, *61*(7), 2695-2699.

[2] Burnette, D. (2014). *Nitric oxide studies in low temperature plasma generated with a nanosecond pulse sphere gap electrical discharge* (Doctoral dissertation, The Ohio State University).

[3] Desgroux, P., & Cottereau, M. J. (1991). Local OH concentration measurement in atmospheric pressure flames by a laser-saturated fluorescence method: two-optical path laser-induced fluorescence. *Applied optics*, *30*(1), 90-97.

[4] Ferreira, C. M., Gordiets, B. F., Osipov, A. I., Capitelli, M. (2000). *Plasma kinetics in atmospheric gases* (Vol. 99). Berlin: Springer.

[5] Golde, M. F., Ho, G. H., Tao, W., & Thomas, J. M. (1989). Collisional deactivation of nitrogen (A3. SIGMA. u+, v= 0-6) by methane, carbon tetrafluoride, hydrogen, water, chlorotrifluoromethane, and chlorodifluoromethane. *The Journal of Physical Chemistry*, *93*(3), 1112-1118.

[6] Kim, W., Do, H., Mungal, M. G., & Cappelli, M. A. (2007). Investigation of NO production and flame structure in plasma enhanced premixed combustion. *Proceedings of the Combustion Institute*, *31*(2), 3319-3326.

[7] Kim, W., Mungal, M. G., & Cappelli, M. A. (2010). The role of in situ reforming in plasma enhanced ultra lean premixed methane/air flames. *Combustion and Flame*, *157*(2), 374-383.

[8] Kossyi, I. A., Kostinsky, A. Y., Matveyev, A. A., & Silakov, V. P. (1992). Kinetic scheme of the non-equilibrium discharge in nitrogen-oxygen mixtures. *Plasma Sources Science and Technology*, *1*(3), 207.

[9] Lacoste, D. A., Moeck, J. P., Paschereit, C. O., & Laux, C. O. (2013). Effect of plasma discharges on nitric oxide emissions in a premixed flame. *Journal of Propulsion and Power*, *29*(3), 748-751.

[10] Mercier, X., Therssen, E., Pauwels, J. F., & Desgroux, P. (1999). Cavity ring-down measurements of OH radical in atmospheric premixed and diffusion flames: A comparison with laser-induced fluorescence and direct laser absorption. *Chemical physics letters*, *299*(1), 75-83.

[11] Motlagh, S., & Moore, J. H. (1998). Cross sections for radicals from electron impact on methane and fluoroalkanes. *The Journal of chemical physics*, *109*(2), 432-438.

[12] Piper, L. G. (1992). Energy transfer studies on N2 (X 1Σ+ g, v) and N2 (B 3Πg). *The Journal of chemical physics*, *97*(1), 270-275.

[13] Rao, X., Matveev, I. B., & Lee, T. (2009). Nitric oxide formation in a premixed flame with high-level plasma energy coupling. *Plasma Science, IEEE Transactions on*, *37*(12), 2303-2313.

[14] Shkurenkov, I., Burnette, D., Lempert, W. R., & Adamovich, I. V. (2014). Kinetics of excited states and radicals in a nanosecond pulse discharge and afterglow in nitrogen and air. *Plasma Sources Science and Technology*, *23*(6), 065003.

[15] Stancu, G. D., M. Simeni Simeni, and C. O. Laux. Investigations by Mid-IR QCLAS of pollutant emissions in high temperature exhaust gases released from plasma-assisted combustion. *31st ICPIG*, Granada, July 14-19, (2013) SPAIN.

[16] Stancu, G. D., M. Simeni Simeni, and C. O. Laux. Study of nitric oxide and carbon monoxide production in plasma assisted combustion by Quantum Cascade Laser Absorption Spectroscopy. *21st ISPC*, Cairns, August 4-9, (2013) AUSTRALIA.

[17] Versluis, M., Georgiev, N., Martinsson, L., Aldén, M., & Kröll, S. (1997). 2-D absolute OH concentration profiles in atmospheric flames using planar LIF in a bi-directional laser beam configuration. *Applied Physics B: Lasers and Optics*, *65*(3), 411-417.

[18] Wu, L., Lane, J., Cernansky, N. P., Miller, D. L., Fridman, A. A., & Starikovskiy, A. Y. (2011). Plasma-assisted ignition below self-ignition threshold in methane, ethane, propane and butane-air mixtures. *Proceedings of the Combustion Institute*, *33*(2), 3219-3224.

Chapter 8

General conclusion

8.1 Contributions of this thesis

The aim of this work was to investigate the amount of nitric oxide released by NRP discharges in air at atmospheric pressure and in combustion. Nitric oxide is a key species involved in many physiological processes such as vasodilation, wound healing, killing bacteria or neurotransmission between nerve cells. However, NO contributes as well to the air pollution by providing the nitrogen dioxide responsible for the photochemical smog and for acid rains. Consequently our goal turned into:

- Developing a diagnostic capable of in-situ, non-intrusive, highly sensitive, highly spectrally resolved NO density measurements in harsh environments such as combustion and NRP discharges operating in open space.

- Optimizing the production of NO by the NRP discharges for biomedical and for combustion applications.

- Gaining a better understanding of NRP discharges kinetics by investigating the NO creation and loss routes.

To meet these three requirements, we established two new laser-based optical diagnostics:

- A multiple passes (28) Mid-Infrared Quantum Cascade Laser Absorption Spectroscopy (Mid-IR QCLAS) setup capable to detect NO-ground state particles (in the post-NRP discharges and post-combustion) at atmospheric pressure down to about 6 x 10^{12} cm^{-3} (which is about 0.25 ppm at ambient room temperature and about 1 ppm at 1200 K).

- A 300-µm spatially resolved Mid-IR QCLAS platform designed to perform NO densities measurements in the NRP discharge. This one-pass configuration was found able to detect NO absorbance down to about 5 x 10^{-4}.

In parallel with the new optical diagnostics, we applied various techniques to extract quantitative data from experiments:

- For the case of combustion, we developed a method to circumvent the overlap of NO and H_2O spectra in the Mid-IR spectral region. The result constitutes to the best of our knowledge the first detection of NO densities by MID-IR QCLAS above 1000 K.

- In the NRP discharges, we designed two methods to derive the radial gas temperature and NO densities profiles. The first method relies on the ratio of line intensities of two absorption features assuming local thermodynamic equilibrium. The second method is instead based on the evolution of the collisional width of the chosen absorption line with respect to the gas temperature. To this end, we applied two strategies for Abel inversion of absorbance spectra: spectrally integrated Abel inversion and spectrally resolved Abel inversion. To our knowledge, this was for the first time applied using QCLAS technique.

Regarding kinetics understanding, we used previously obtained experimental results in the NRP "*reference case*" and the literature rate constants for reactions of formation/loss of NO in air plasmas and estimate the dominant reactions responsible for NO creation/destruction in NRP discharges. Note that these previous work had provided the following NRP discharge parameters: species densities O, N_2 (A, B, C), gas temperature and electron density.

In the thesis, we studied NRP discharges generated in a vertical pin-to-pin configuration, in a bottom-up airflow. We chose to generate the discharge pulses either between two refractory steel electrodes usually employed for gas boilers or between a bluff-body and a refractory steel electrode. The first configuration is convenient for the analysis of the discharge itself whereas the second one is used because it is often employed in combustion applications.

Our findings are summarized as follows:

The NO density in the discharge operating in ambient air flow is found to be in the range of 2 x 10^{15} cm^{-3} at discharge center and decreases by a factor 15 from discharge center to 5-mm off- axis. This result is an average value over a duration of about 100 s. Besides, we observed a radial spread of the NO particles up to about 5-mm distance from axis. The spread of NO by diffusion could not explain such result since the NO diffusion length during the flow residence time between electrodes is at most one order of magnitude lower than the 5-mm expansion measured. So, only recirculation of the NO particles behind electrode tips could explain our results.

The time-averaged **gas temperature in the discharge** operating in ambient air flow is found to be about 800 K at discharge center and decreases as expected with the radial distance to the axis, down to room temperature, at about 5-mm off-axis.

The NO density in the post-NRP discharges in air (downstream the discharge) can be optimized using NRP discharges parameters. More precisely, the NO density (in the post-discharge) at 300 K increases with the applied voltage amplitude, pulse repetition frequency and gap distance, whereas it decreases when the air flowrate rises. In addition, the increases of the NO mole fraction with the pulse voltage amplitude and repetition frequency were found to be linear. The same trend was observed for NRP discharges operating in a 1000-K preheated air flow. We found that in both cases (ambient or preheated air flows), the NO produced in post-NRP discharges is only function of two parameters, namely the pulse voltage amplitude and the number of discharge pulses seen by the gas in the gap. The second parameter is proportional to the dimensionless parameter: $d\ f/v$. d being the gap distance, f the pulse repetition frequency and v the flow velocity. At a fixed pulse voltage amplitude, the NO density is only controlled by this dimensionless parameter and conversely, at a fixed number of pulses seen by the gap, the amount of NO in the post-discharge depends only on the applied voltage amplitude. We also derived the rate of NO production in the post-discharge. We evidenced maximum production rates of about 2×10^{18} molecule/s and 6×10^{17} molecule/s at 300 and 1000 K, respectively. Then, carrying out experiments as a function of the flow temperature (from 300 to 1000 K), we determined that the NO mole fraction was approximately independent of the gas flow temperature. Finally, from the parametric studies, we demonstrated that the NO densities in the post-NRP discharge can be varied from 40 to 250 ppm ($1 - 6 \times 10^{15}$ cm^{-3}). This meets the requirements for biomedical applications, which are in the range of 5 – 200 ppm.

A NO creation post-discharge kinetics may occur in the NRP discharges. We first demonstrated this assertion by comparing for the same conditions, density measurements in the discharge and in the post-discharge. In the post-discharge we found a density four times greater than the expected value. Afterwards, we found that the NO density increases with the vertical distance to the discharge. This supported the foregoing result. We suggest that if occurring, the NO creation in the post-discharge is related to the reactions: $N(^2D, ^2P) + O_2 \rightarrow NO + O$, which involve long-lived $N(^2D, ^2P)$ metastables.

90% of the NO creation in NRP discharges is estimated to result from the quenching of $N_2(B)$ electronically exited nitrogen states with O atoms. And **NO in the discharge is lost** mainly by quenching of NO molecules with nitrogen and oxygen atoms.

For combustion applications, we investigated three experimental cases in order to find a case in which NRP discharges can stabilize lean flames at equivalence ratio about 0.8, while releasing less NO than the stoichiometric flame alone. Starting from a baseline configuration in air, we studied two optimization cases in air. For each of these cases, while maintaining stabilization effects, the NO densities (or mole fraction) were about three times lower than that of the baseline case. Then, implementing the optimized cases in the combustion environment showed that the plasma-assisted combustion system operating between equivalence ratio 0.70 and 1.10 was able to release NO densities comparable to the amounts released by the stoichiometric flame. But we did not succeed to produce less NO than the stoichiometric flame alone. Another important point is the fact that the flame through its chemistry consumes the NO produced by NRP discharges. Actually, NO mole fractions in the cases of plasma-assisted combustion were found lower than NO mole fractions for plasma in pure air. We also noticed that the NO consumption rate of the flame diminishes when the NO density is produced in lower amounts by the NRP discharge in air. This means that minimizing at maximum NO released by NRP discharges in air leads to a reduction of NO consumption by the flame and, therefore is not efficient for NO further reduction.

NO creation in flames is indeed mainly due to the reactions of N atoms with O_2 molecules, following the Zel'dovich mechanism whereas NO decay arises primary from the quenching of NO with N atoms. NO creation/loss kinetics in plasma-assisted combustion are still uncertain. We suggest that its creation arises from the combined contributions of the thermal mechanism (with the addition of the reaction N + OH $\rightarrow$ NO + H) with the reactions: $N_2(B, C) + O \rightarrow NO + N$ and its loss arises from the reactions $NO + N \rightarrow N_2 + O$ and $NO + O \rightarrow N + O_2$.

8.2 Perspectives for future work

The Mid-IR QCLAS setups developed in this work have provided insights on the nitric oxide released by NRP discharges in air at atmospheric pressure and in combustion. Nevertheless, in the best case, these setups could only provide time resolution about 1 s and spatial resolution about 200-µm. Consequently, the time resolution should be improved up to about few nanoseconds, to follow NRP discharges characteristic times. NO kinetics could be clearly validated by synchronized ns-time resolved measurements with key species such as N_2^*, O... The spatial resolution needs to be improved to reach 50 µm, in order to provide a more accurate description of the discharge center knowing that discharge diameter is about 400 µm. The time-resolved radial-spread of NO in the discharge region can learn us about the discharge dynamics and its coupling with flow recirculation. Both

requirements can be achieved for instance by a time-resolved Mid-IR QCLAS diagnostic, working in the intra-pulse mode combined with a modified optical system arrangement, for a better spatial resolution.
Another possibility to meet these two goals would be to perform NO detection using the LIF method and to calibrate the LIF method by the current Mid-IR QCLAS. In this case, we combine the high temporal and spatial resolutions of LIF with the calibration-free advantage of the QCLAS.

Moreover, regarding the results obtained in the post-discharge, i.e. NO dependency on two parameters, a comparison with discharge is necessary. First, we need to carry out NO density measurements in the discharge as a function of the number of discharge pulses applied to the gap. Secondly we should investigate the influence of the pulse duration on the NO density measurements. Since an increase of the pulse duration leads to an increase of the number of pulses seen by the gap, we expect a rise in NO density following the increase of the pulse duration.

Regarding kinetic modeling, the time-resolved density measurements of key species such as N, N(^{2}D, ^{2}P) (in the discharge) and N, O, OH, H (in combustion and plasma-assisted combustion) have to be performed. N, O and H atoms density measurements can be performed using the TALIF method. Note that the time-resolved O densities have already been measured in the discharge, in the NRP "reference case".
N(^{2}D) atoms density in NRP discharges in air and in plasma-assisted combustion can be determined by VUV line absorption or electronic spin resonance absorption.
OH densities for their part can be measured using either LIF or UV absorption.

Finally, in addition to the measurements a detailed kinetic modeling of the NRP discharges should be performed. In our study, we assumed that NO creation and destruction processes were uncoupled, which is not the case. The coupling of the reviewed processes can be taken into account for instance, by inserting the latter processes in a simulation tool such as the Zero Dimension Plasma Kinetics solver (ZDPLASKIN). Discharge and combustion need to be coupled for a detailed understanding of the NRP-assisted combustion.

A Abel inversion code validation

Bracewell, [1999] calculated analytically Abel inverse transforms of most of usual functions. Some of the pairs (lateral and radial distributions) are presented table 1 below. These pairs will be used to validate results from the Matlab code provided online by Carsten Killer (see figure A.1).

Table A.1: Some of the usual functions Abel inverse transforms. $\Pi_a(x)$ is the rectangle function centered at a/2 and with a full-width a.

Conditions	g(x)	f(r)
$0 < x < a$	$\pi(a^2\text{-}x^2)/2$	$(a^2\text{-}x^2)^{1/2}\Pi_a(r)$
$0 < x < a$	a-x	$\text{acosh}(a/r)/\ \pi$
$0 < x < a$	$2\ (a^2\text{-}x^2)^{1/2}$	$\Pi_a(r)$
$0 < x < a$	π	$(a^2\text{-}x^2)^{-1/2}\Pi_a(r)$
$\sigma > 0$	$\sigma\pi^{1/2}e^{-x2/\sigma2}$	$e^{-r2/\sigma2}$

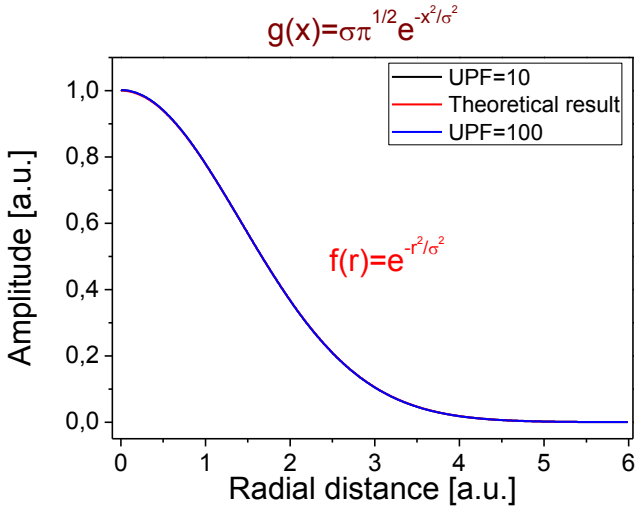

(a)

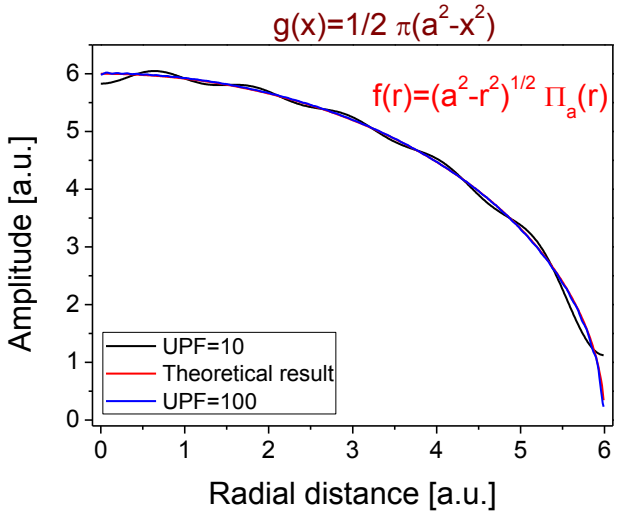

(b)

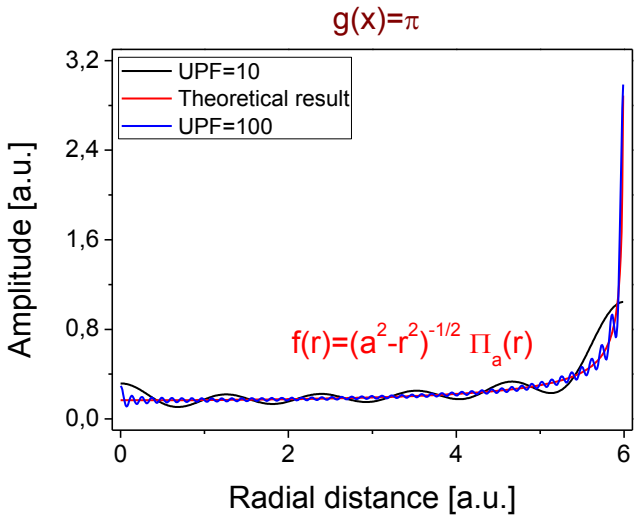

(c)

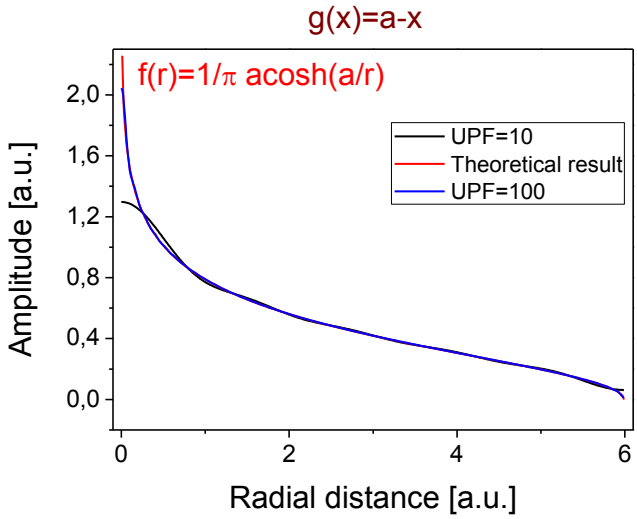

(d)

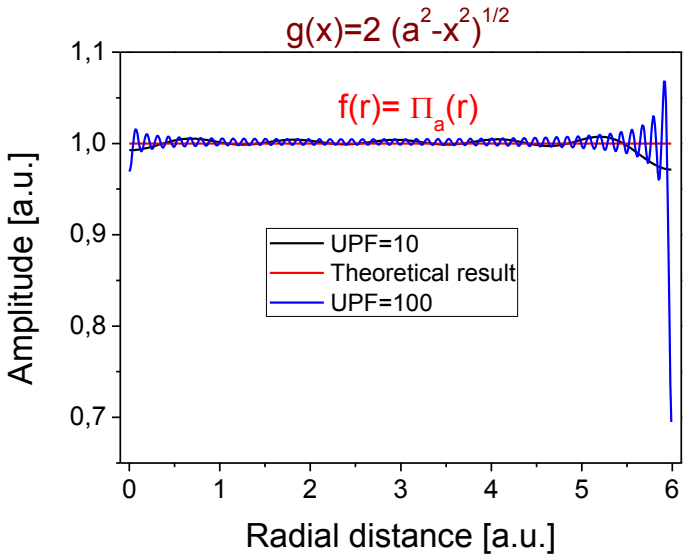

(e)

Figure A.1: Five validation test cases of the Matlab Abel inversion code. Here test values are: a = 6 and σ = 2.

Test cases results show that the applied method with UPF = 100 fit perfectly analytical solutions if the lateral function to be inverted is a continuously differentiable function (a C^1 function) of lateral position x. In this configuration inverted radial function is also a C^1 function (see test cases a, b and d). For test cases c and e where lateral distributions are not C^1, the outcome displays little oscillations around analytical solutions. Nevertheless, since our experimental data are fitted with

fifth order polynomial functions (which are C^1) prior to Abel inversion, the outcome will not suffer from such kind of oscillations.
The applied method with UPF = 10 works perfectly for Gaussian function (test case a). But for other C^1 functions, it exhibits a disagreement with analytical results at both ends of the compact support (test cases b and d). For non-C^1 functions (test cases c and e), amplitude of the foregoing oscillations around analytical solutions is increased. As a result, inversion method was applied with UPF = 100.

References

[1] Bracewell, R. (1999). *The Fourier Transform and its Applications, third ed. McGraw-Hill, New York*, 244. (p.264)

B Analytical calculations of the line strength

As both transitions considered here are in the ground state, $Q_{el} = 1$. The vibrational partition sum Q_{vib} is derived under the approximation of the quantum harmonic oscillator:

$$Q_{vib} = \sum g_{vib} e^{-\frac{\epsilon_{vib}}{kT}} = \sum_{\nu=0}^{\infty} e^{-\frac{\Theta_{vib}(\nu+\frac{1}{2})}{T}} = \frac{e^{-\frac{\Theta_{vib}}{2T}}}{1 - e^{-\frac{\Theta_{vib}}{T}}} \quad \text{(B.1)}$$

g_{vib}, the vibrational degeneracy factor is 1. k is Boltzmann constant, ε_{vib} and Θ_{vib} are respectively the vibrational energy and temperature. They are given respectively by:

$$\epsilon_{vib}(\nu) = \omega_e \left(\nu + \frac{1}{2}\right) \quad \text{(B.2)}$$

$$\Theta_{vib} = c_2 \omega_e \approx 1.44 \omega_e \quad \text{(B.3)}$$

with ω_e being the vibrational constant. For the NO ground state, ω_e = 1904.04 [*Gillette et al.*, 1939; Hüber *and Herzberg*, 1979].

The rotational partition sum is given by:

$$Q_{rot} = \frac{1}{\sigma} \sum_{rot} g_{rot} e^{-\frac{\epsilon_{rot}}{kT}} = \frac{1}{\sigma} \sum_{J=0}^{\infty} (2J+1) e^{-\frac{B_e J(J+1)}{kT}} \quad \text{(B.4)}$$

where J is the previously defined rotational quantum number, g_{rot} the rotational degeneracy factor (which is equal to 2J+1), σ is the symmetry number, which is equal to 2 for homonuclear molecules and 1 for heteronuclear ones. B_e the rotational constant expressed in cm^{-1} is 1.7 for NO ground state [*Gillette et al.*, 1939; *Hüber and Herzberg*, 1979]. ε_{rot}, the rotational energy of level of rotational quantum number J is defined as:

$$\epsilon_{rot} = B_e J(J+1) \quad \text{(B.5)}$$

when rotational energy levels are very close to one another, the summation of equation B.4 can be turned into an integral. Then using a variable substitution, equation B.4 yields:

$$Q_{rot} \approx \frac{T}{\sigma \Theta_{rot}} \tag{B.6}$$

where Θ_{rot} is the rotational temperature defined as:

$$\Theta_{rot} = c_2 B_e \approx 1.44 B_e \tag{B.7}$$

Putting together the vibrational and rotational partition sums gives the "classical" TIPS:

$$Q(T) \approx \frac{1}{\sigma} \frac{e^{-\frac{1.44\omega_e}{2T}}}{1 - e^{-\frac{1.44\omega_e}{T}}} \frac{T}{1.44 B_e} \tag{B.8}$$

Nonetheless, due to complications such as molecule hyperfine structure, lambda doubling, spin coupling and torsional motion, authors [*Gamache et al.*, 1990; *Goldman et al.*, 2003] reported modified TIPS. Particularly for NO, Goldman showed that when the TIPS was calculated upon rotational states, an additional product $\Pi(2I+1)$ accounting for the effects of nuclear spin states must be taken into account. I is the nuclear spin quantum number. Including lambda doubling and spin coupling leads to:

$$Q = \sum_{\Lambda=\pm 1} \sum_{\Omega=\frac{1}{2},\frac{3}{2}} (2I+1) Q^{Class} \tag{B.9}$$

Q^{Class} is the classical TIPS. For NO, 2I+1=3. Lambda doubling factor is 2 and the summation over the $\Pi_{1/2}$ and $\Pi_{3/2}$ states factor is taken into account adding a factor:

$$1 + e^{-\frac{1.44\delta E}{T}} \tag{B.10}$$

Where δE is the energy spacing between $\Pi_{1/2}$ and $\Pi_{3/2}$ states. From *Hüber and Herzberg* [1979] we have $\delta E \approx 119.9$ cm^{-1}. The resulting TIPS is therefore:

$$Q(T) = 6\left(1 + e^{-\frac{1.44\delta E}{T}}\right) Q^{Class} \tag{B.11}$$

At last the temperature dependence of the partition sum can be calculated and is displayed figure B.1.

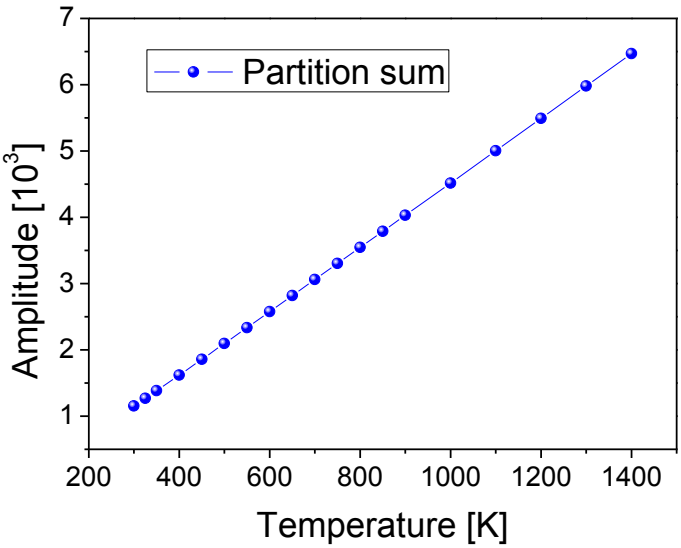

Figure B.1: NO internal partition sum as a function of temperature.

With these calculations, the value of the partition sum for NO at 300 K is about 1151.96, which is in good agreement with the value from JPL [*Pickett et al.*, 1996], 1159.58.

Now that the TIPS is known, the ratios of Boltzmann populations and of stimulated emission can easily be computed for each of lines components. The results for the first component of the strongest line are shown in figure B.2. Then summing the different contributions leads to the effective line strengths. Figure B.3 shows that both line intensities decrease with an increasing temperature. More precisely, the strongest line intensity decreases by a factor 2.5 between room temperature and 1000 K whereas the decreasing factor is 1.7 for the other absorption feature.

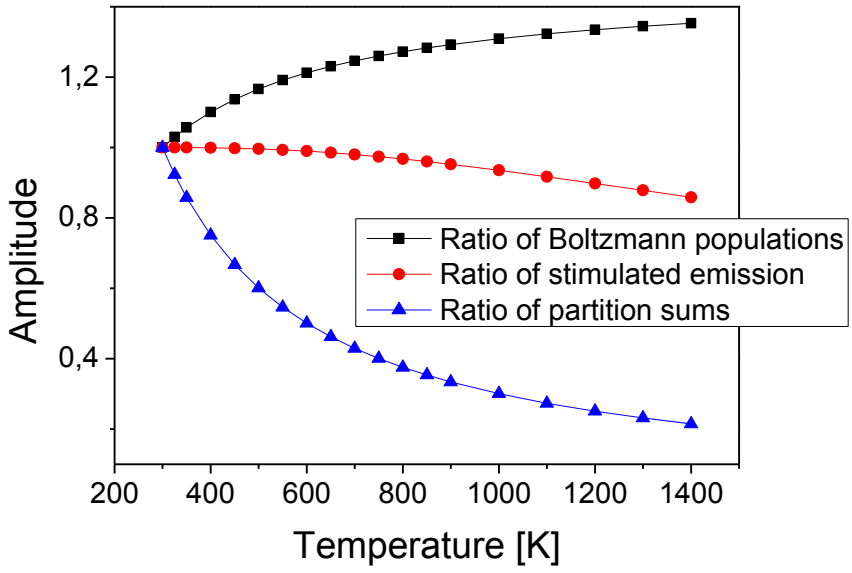

Figure B.2: Evolution with respect to the temperature of line strength different contributions for first component of line at 1900.076.

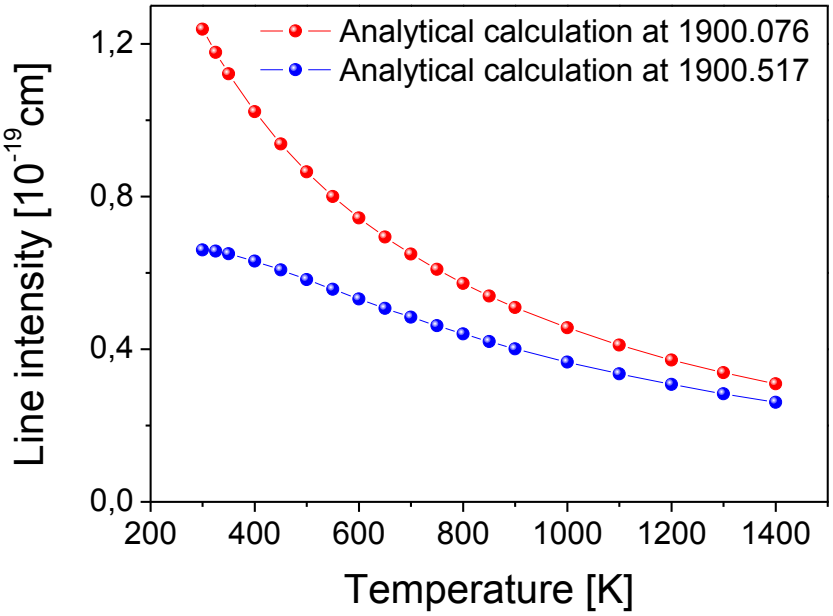

Figure B.3: Lines intensities decrease with the gas temperature.

A comparison with simulations is provided in figure B.4.

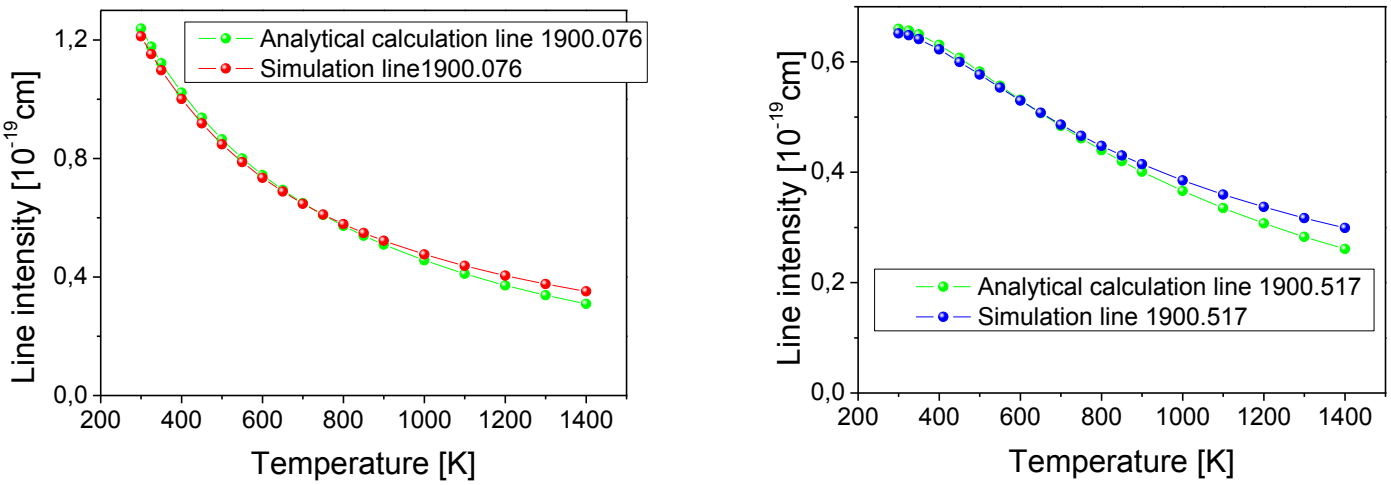

Figure B.4: Comparison between line strength analytical calculations and numerical simulations.

References

[1] Gamache, R. R., Hawkins, R. L., & Rothman, L. S. (1990). Total internal partition sums in the temperature range 70–3000 K: atmospheric linear molecules. *Journal of molecular spectroscopy*, *142*(2), 205-219.

[2] Gillette, R. H., & Eyster, E. H. (1939). The Fundamental Rotation-Vibration Band of Nitric Oxide. *Physical Review*, *56*(11), 1113.

[3] Goldman, A., Gamache, R. R., Perrin, A., Flaud, J. M., Rinsland, C. P., & Rothman, L. S. (2000). HITRAN partition functions and weighted transition-moments squared. *Journal of Quantitative Spectroscopy and Radiative Transfer*, *66*(5), 455-486.

[4] Hüber, K. P., & Herzberg, G. (1979). *Constants of diatomic molecules*. Springer US.

[5] Pickett, H. M., Poynter, R. L., Cohen, E. A., Delitsky, M. L., Pearson, J. C., & Muller, H. S. P. (1996). Submillimeter millimeter and microwave spectral line catalog. 1996 ed. *Caltech, Pasadena Calif. JPL Publication*, 80-23.

C Bandwidth of the detection system

Bandwith effects on resolution employing QCL an MCT detectors

Thanks to their atom-like spectral shape, QCLs display much narrower intrinsic line width compared to semiconductor lasers. Theoretical FWHM of QCL line is only limited by the modified Schawlow-Tones formula:

$$\Delta\nu = \frac{\pi h\nu(\Delta\nu_c)^2}{P_{out}} \tag{C.2}$$

Here P_{out} is the laser output power and $\Delta\nu_c$ is the laser cavity bandwidth (FWHM). This intrinsic line width is reported to be about 10^{-7} cm^{-1}. However the effective line width measured on a NO absorption feature at low pressure (1 mbar) and at room temperature (it is a case where the line width is limited by laser width) is about 10^{-2} cm^{-1} (see section 4.5.5). Hence, measurement is limited by the uncertainty principle between the laser equivalent bandwidth and the laser equivalent duration. It arises from the Fourier transforms theory [*Bracewell*, 1986]:

$$\Delta\nu\Delta t \geq C \tag{C.3}$$

$\Delta\nu$ is the laser equivalent bandwidth (here in frequency unit) and Δt is laser equivalent duration. C is a constant determined by the laser pulse shape. *McCulloch et al.*, [2003] reported a value of C = 0.886 for rectangular time window and C = 0.441 for a Gaussian one. For a single pulse of duration τ_p, the swept frequency (which is also the spectral resolution) is obtained multiplying pulse duration by the average frequency chirp:

$$\Delta\nu = \tau_p\left(\frac{d\nu}{dt}\right) \tag{C.4}$$

Applying the uncertainty principle in the most favorable case (i.e. the equality case of equation C.2) to the previously defined single pulse yields:

$$\Delta\nu = \left(C\frac{d\nu}{dt}\right)^{\frac{1}{2}} \tag{C.5}$$

For C = 1 (limiting case) and for a chirp rate of 150 MHz/ns (5 x 10^{-3} cm^{-1}/ns in wavenumber unit), laser spectral resolution is found to be around 387 MHz (1.3 x 10^{-2}

cm-[1]). This falls to 8.6 x 10^{-3} cm-[1] for a Gaussian pulse shape. Equation 2.23 points out reducing pulse duration will not improve spectral resolution as chirp rate will become the limiting parameter. Moreover form the uncertainty principle; it can even lead to worse resolution.

The previous uncertainty principle can also be applied to laser signal detectors. Hence, the spectral resolution of these Mid-IR spectrometers will be dependent on the laser chirp rate and its bandwidth. It is possible to show that the minimum bandwidth BW required to preserve a laser spectral resolution of $\Delta\nu$ defined by its chirp is:

$$BW = 0.7\left(\frac{1}{C}\frac{d\nu}{dt}\right)^{\frac{1}{2}} = 0.7\frac{\Delta\nu}{C} \tag{C.6}$$

Note that the detector rise time t_{rise} and bandwidth BW are linked by the equation:

$$t_{rise} = \frac{0.35}{BW} = \frac{C}{2\Delta\nu} \tag{C.7}$$

Consequently, to preserve a 6 x 10^{-3} cm^{-1} (180 MHz) spectral resolution requires a detection system response time lower than 2.8 ns. It corresponds to a required equivalent bandwidth about 126 MHz. The measurement detector from Daylight Solutions (with its 3 ns rise time) is hence convenient for the purpose of spectrally resolved measurements.

References

[1] Bracewell, R. N., & Bracewell, R. N. (1986). *The Fourier transform and its applications* (Vol. 31999). New York: McGraw-Hill.

[2] McCulloch, M. T., Normand, E. L., Langford, N., Duxbury, G., & Newnham, D. A. (2003). Highly sensitive detection of trace gases using the time-resolved frequency downchirp from pulsed quantum-cascade lasers. *JOSA B*, *20*(8), 1761-1768.

D Alignment of the QCL

The Mid-IR laser radiation at 5.2 µm is not visible with human eyes. Moreover, the typical laser viewing cards (fluorescence-based) don't work with IR radiation, as they require multiphoton processes. In addition, IR laser viewing cards require high-power laser beam. Furthermore, we need to maximize the signal to noise ratio to record full spectrally resolved absorption profiles. The alignment of the QCL radiation i.e. the control of the Mid-IR beam shape and position along its propagation from the QCL to MCT detectors is therefore a critical issue.
We can divide the alignment procedure into two parts: geometry alignment and Mid-IR signal maximization.

The geometry alignment consists on using a co-aligned red (visible) laser to the infrared one, in the "ray optics" approximation. In this approximation, when the laser wavelength is many times smaller than the size of objects with which it interacts (here 5.2 µm << 2.54 cm) we can consider that both red and IR radiations are affected the same manner when passing through the optics. This means that the red laser stands as a visible trace of the IR radiation in terms of beam position (but not in terms of beam size). But this is true only if both radiations are co-aligned. To achieve this co-alignment we use the principle of inverse return of light. Figure D.1 below shows the detailed principle of the alignment. The red radiation (parallel rays) from a laser diode is splitted in two parts by a removable cube beam splitter. A plane mirror adjoined to the cube reflects the transmitted part of the radiation. The reflected radiation is then splitted again by the cube. This results in a reflected beam going in the opposite direction than the first reflected beam through the cube. An OAP mirror focuses this parallel radiation on its focal point. The QCL is placed at this focal point in order to create a parallel beam after the OAP mirror. In this configuration the first reflected red radiation and the QCL radiation (without the cube) are roughly co-aligned. Then, using the red laser, the centers of optics before the multipass absorption cell are aligned to define the optical axis. The multipass absorption cell and the detector are then aligned as specified above (platform for multipass absorption measurements).

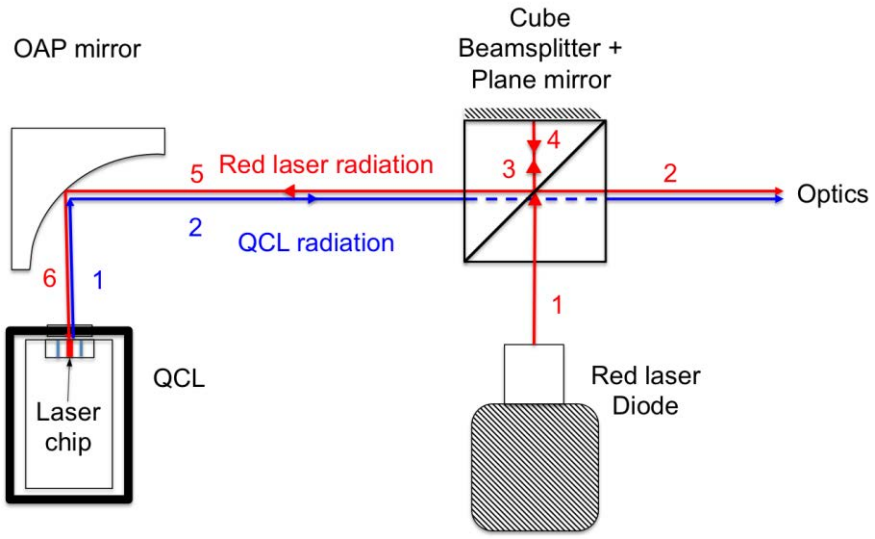

Figure D.1: Geometry alignment. Positioning of the QCL at the focal point of the OAP mirror.

Once the geometry alignment is completed, the laser beam divergence and position are supposed to be known everywhere in the setup. But we assumed here that the red and the Mid-IR radiation propagate the same way when passing through optics. This is not exactly true because of the difference of wavelength (632 nm and 5.2 µm), which leads to difference in terms of propagation (when using "wave optics" approximation instead of "ray optics" approximation) and also because of chromatic aberrations from optics, which can be wavelength dependent. As a result, the beam reflected on the OAP mirror could be not parallel and so for the outcoupling beam from the multipass absorption cell. In this case the focal point of the IR radiation on the MCT detector will differ from the one of the red radiation (which is the active area of the detector). To solve this and precisely align the setup, one solution is to run the system in the intra pulse mode (fast response time) and to maximize the signal recorded by MCT detector and displayed by a 100-MHz oscilloscope. For this purpose the QCL and MCT detectors are placed each on 3-axes translation stages. The maximization of the intra pulse signal is obtained by moving alternatively different adjustment spindles. Figure D.2 presents the QCL board with its 3 adjustment spindles together with the beam splitter cube.

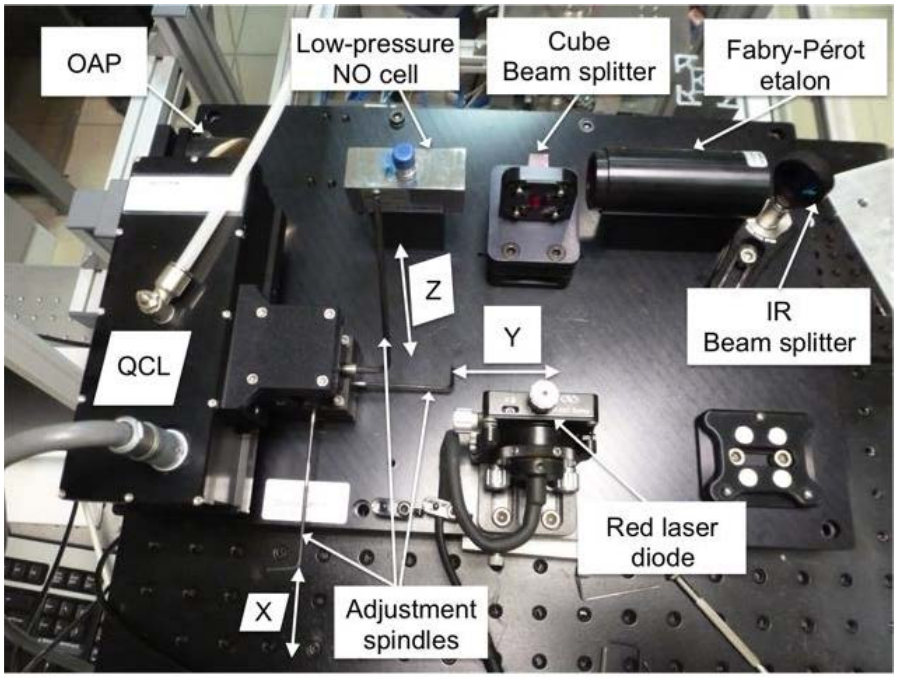

Figure D.2: Signal maximization. Positioning of the QCL at the focal point of the OAP mirror using precise adjustment spindles.

E Contribution of discharge center for spatially resolved measurements

One of our goals was to quantify the amount of NO released by one pulse of the NRP discharge. Due to its long lifetime, we expected NO accumulations around the discharge channel. However during the flow residence time between electrodes, the NO diffusion length is shorter than the width of the discharge for our experimental conditions (see discussions in chapter 5) and therefore the accumulation out of the discharge channel should be negligible. Our experimental investigations showed an accumulation of NO over 1 cm around the discharge axis, this being likely due to flow recirculation behind the electrodes. For our measurements, we want to quantify the part of NO density coming from the discharge itself and the part resulting from the accumulation.
Here we performed an analysis of the contribution of discharge center to the light-of-sight integrated lateral absorbance measurements. To this end, we use the radial temperature and NO density profiles resulting from method 1 and the forward Abel transform. The first step consists in calculating the spectral absorption coefficient at each radius and then integrating along chords to get the spectrally resolved lateral absorbance profiles. Finally, we examine the relative contribution of the various radii to the total lateral absorbance.

We start by calculating the spectral absorption coefficients of line 2 at each radial position using equation 3.11 and the measured temperature and density profiles from method 1. The obtained spectral absorption coefficient is illustrated in figure E.1.

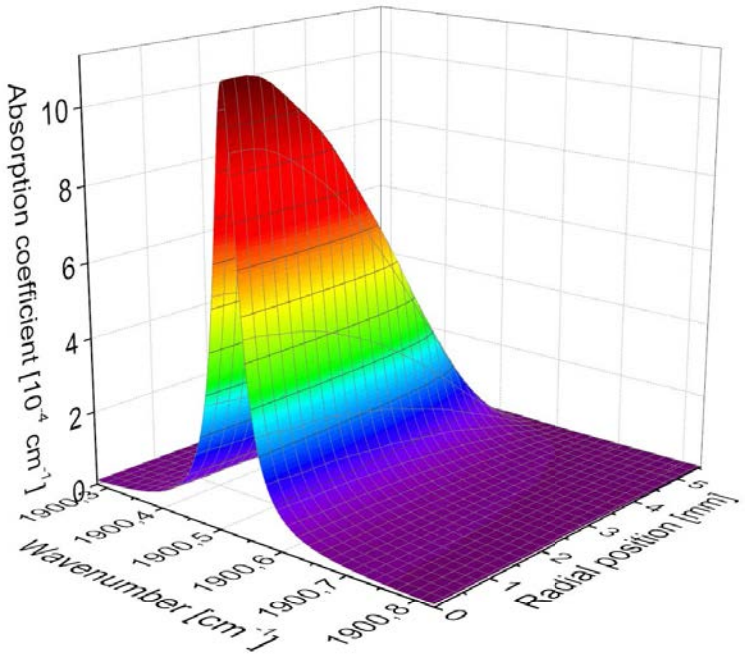

Figure E.1: Spectral absorption coefficient cf line 2, from simulation.

Then, we apply the forward Abel transform (equation 3.14, section 3.4.1) to figure E.1. This is in practice achieved by integrating along chords at various wavenumber positions and we obtain the simulated absorbance profile of figure E.2-left. A good agreement is found between measurements and simulations.

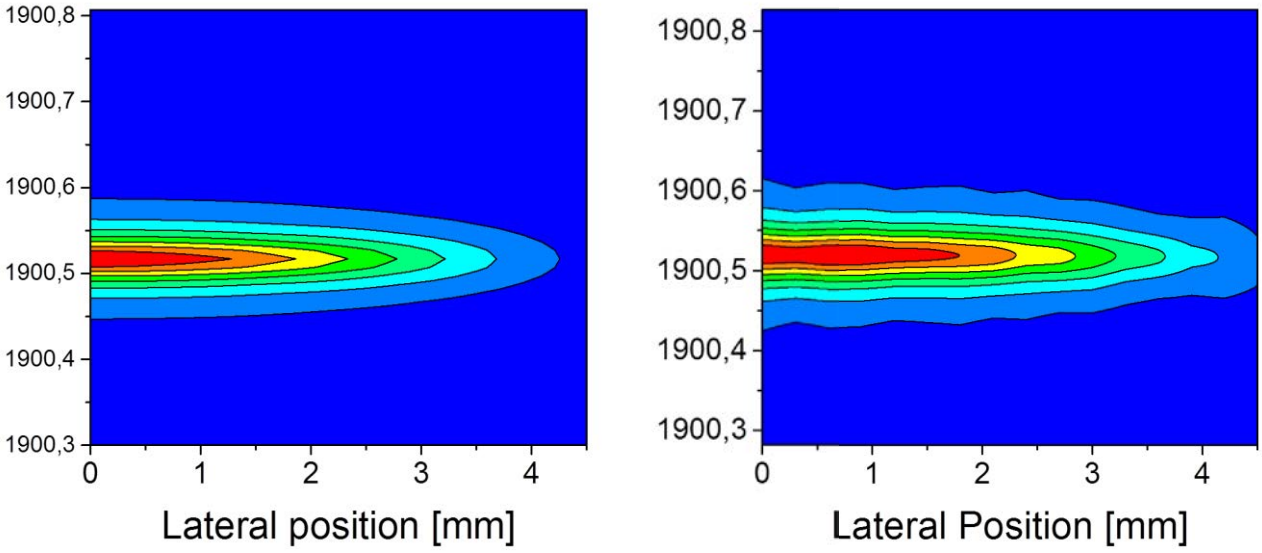

Figure E.2: Comparison between reconstructed absorbance profiles (left) and experimental data (right) for line 2.

A comparison between experimental and simulated absorbance spectra is provided for two lateral locations (at discharge center and at 3.9 mm distance from axis) in figure E.3. At discharge center the simulation overestimates the peak absorbance but everywhere else the simulation fits the measurement data well. At 3.9-mm distance from axis, the measurement and simulation are in good agreement over the whole profile.

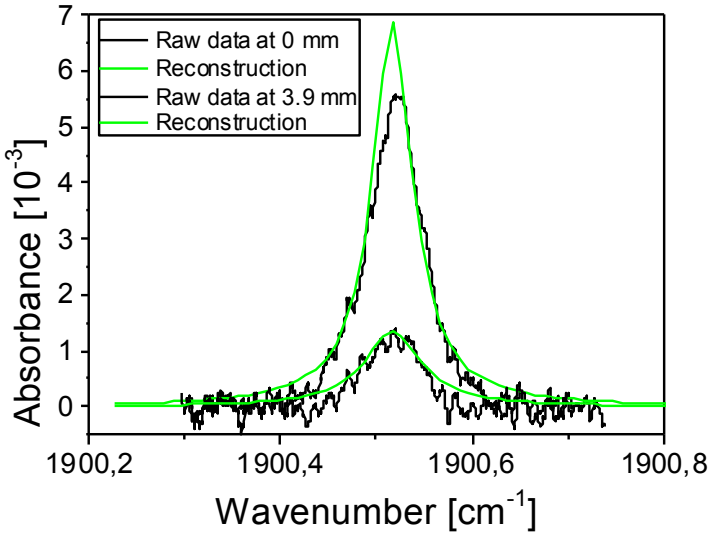

Figure E.3: Comparison between simulated absorbance profiles and experimental data for line 2 at discharge center and at 3.9 mm distance from axis.

At line center, i.e. at 1900.517 cm^{-1}, exactly, the relative contribution of the various radii to the total absorbance at lateral position 0 and 2 mm, respectively are shown in figure E.4 and E.5, respectively. These results are depicted in terms of percentage of cumulated headcounts. At lateral position 0 mm (discharge center), 50 % of the total measured absorbance is obtained by integrating over the small absorbance "elements" from radii between 0 and 1.5 mm. This means that one quarter of the radial spread of NO (up to 5.5 mm) represents half of the total measured absorbance. A similar result is obtained at lateral position 2 mm since the radial portion between 2 and 3 mm represents more than 60 % of the total recorded absorbance at 2 mm.
We can conclude that even though NO is accumulated due to flow recirculation, the measured NO densities are more likely affected by the near vicinity of the discharge rather than the accumulated species far from discharge center.

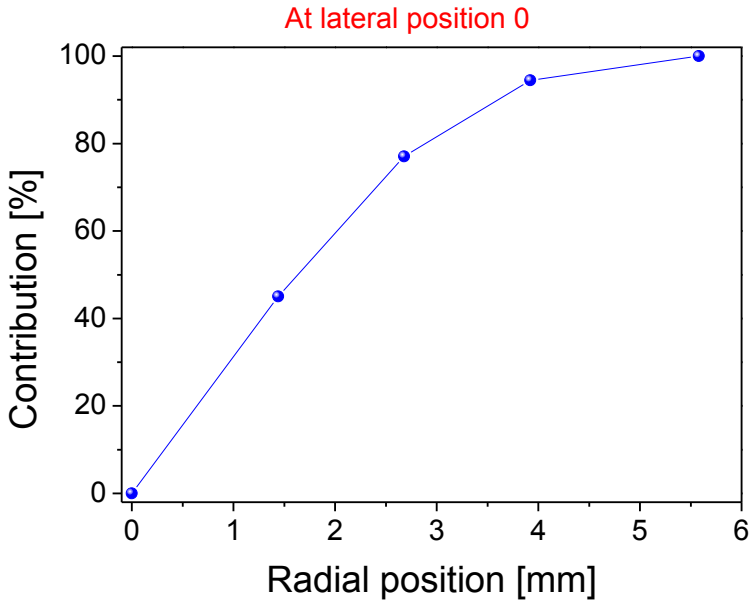

Figure E.4: Evaluation of the contribution of the different radial portions in and around the discharge, in terms of percentage at 1900.517 cm^{-1} and at lateral position 0.

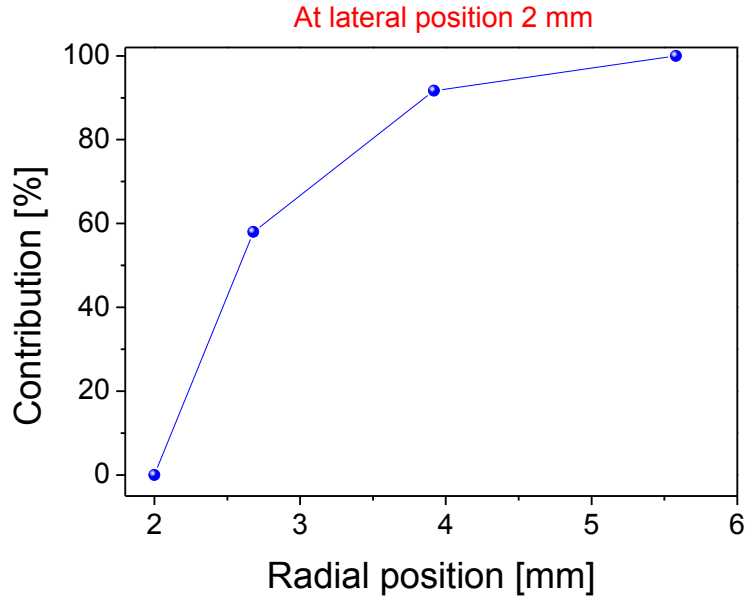

Figure E.5: Evaluation of the contribution of the radial portions around the discharge, in terms of percentage at 1900.517 cm^{-1} and at lateral position 2 mm.